

Detecting trends of stratospheric ozone and tropospheric water vapour at mid-latitudes using measurements from multiple techniques

Inaugural dissertation
of the Faculty of Science,
University of Bern

presented by

Leonie Bernet

from Germany

Supervisor of the doctoral thesis:

PD Dr. Klemens Hocke
Institute of Applied Physics

Detecting trends of stratospheric ozone and tropospheric water vapour at mid-latitudes using measurements from multiple techniques

Inaugural dissertation
of the Faculty of Science,
University of Bern

presented by

Leonie Bernet

from Germany

Supervisor of the doctoral thesis:

PD Dr. Klemens Hocke
Institute of Applied Physics

Accepted by the Faculty of Science.

The Dean:

Bern, 13.11.2020

Prof. Dr. Zoltan Balogh



Except where otherwise noted, the content of this work is licensed under the Creative Commons Attribution 4.0 International license (<https://creativecommons.org/licenses/by/4.0/>). This license lets others distribute, remix, adapt, and build upon the work, even commercially, as long as they give appropriate credit, provide a link to the license, and indicate if changes were made.

This document was typeset using the typographic style `classicthesis` developed by André Miede and Ivo Pletikosić. The style was inspired by Robert Bringhurst's book on typography "*The Elements of Typographic Style*". The package is available at <https://bitbucket.org/amiede/classicthesis/>.

© Leonie Bernet, Detecting trends of stratospheric ozone and tropospheric water vapour at mid-latitudes using measurements from multiple techniques, PhD thesis, Institute of Applied Physics, University of Bern, Bern, Switzerland, second edition, November 2020.

SUMMARY

This thesis investigates and quantifies changes in stratospheric ozone and tropospheric water vapour at mid-latitudes since the mid-1990s. Recent studies have shown that estimates of such changes from various ground-based measurement techniques are not always consistent. A possible reason for these differences may be inhomogeneities in the data. Data inhomogeneities arise from modifications in the instrument setup, measurement failures, problems or adjustments in the calibration and retrieval procedures, or from temporal sampling biases. To explain differences in observed changes, data inhomogeneities have first to be identified by intercomparing various datasets. In a second step, the inhomogeneities can be considered in the trend estimation to obtain optimal estimates of the true changes.

This thesis aims to obtain more consistent trend estimates of stratospheric ozone profiles and tropospheric water vapour at mid-latitudes. For this purpose, we compared ozone and integrated water vapour (IWV) time series from various measurement techniques. The observations were intercompared to identify anomalies, biases, and inhomogeneities in the data. Trends in recent decades were then estimated by considering these irregularities in the trend estimation. To this end, two advanced trend analysis methods were tested and applied on the data. The trend models use the full error covariance matrix of the observations, which can be adapted to account for data correlations and inhomogeneities.

We used stratospheric ozone observations measured by ground-based microwave radiometers, lidars, and ozonesondes, as well as satellite and reanalysis model data. We found good agreement between various ozone datasets. However, we also identified some anomalies and inhomogeneities in the ozone data and showed that they affect the trend estimates. Stratospheric ozone trend profiles are presented for northern (central Europe) and southern mid-latitudes (New Zealand). In both hemispheres, we observe a recovery in ozone concentrations in the upper stratosphere after the turn-around of ozone-depleting substances (ODSs) in 1997. We found trends that generally lie between 1 % and 3 % per decade, providing a confirmation of ozone recovery in the upper stratosphere as expected from reduced ODS emissions. In the lower stratosphere, we found inconsistent trends, suggesting that further research on lower-stratospheric ozone changes is required.

Observations of IWV were used from a microwave radiometer, from a Fourier-transform infrared spectrometer, from a network of ground

stations of the Global Navigation Satellite System (GNSS), and from reanalysis model data. We present trends derived from these IWV measurements in Switzerland. They show that IWV increased by 2 % to 5 % per decade since 1995, which is generally consistent with rising temperature. Also, we show that the advanced trend model used is well suited to reduce trend biases caused by GNSS-antenna updates.

In conclusion, this thesis presents optimized trends of stratospheric ozone and IWV for recent decades at mid-latitudes. Further, it helps to better understand inconsistencies between trend estimates from multiple techniques by investigating the effect of data irregularities on the trends. Consequently, the results of this thesis contribute to a better understanding of ozone and water vapour changes in a changing climate.

CONTENTS

1	INTRODUCTION	1
I THEORETICAL BACKGROUND		
2	OZONE AND WATER VAPOUR IN THE ATMOSPHERE	5
2.1	Stratospheric ozone	5
2.2	Tropospheric water vapour	15
3	MEASURING OZONE AND WATER VAPOUR IN THE ATMOSPHERE	19
3.1	Radiative transfer	20
3.2	Techniques to measure stratospheric ozone	23
3.3	Techniques to measure integrated water vapour	28
II DATA AND METHODOLOGY		
4	DATASETS	35
4.1	Ozone datasets	35
4.2	Integrated water vapour datasets	41
5	ATMOSPHERIC TREND ANALYSIS	45
5.1	Linear regression	45
5.2	Trend models	48
III RESULTS AND DISCUSSION		
6	STRATOSPHERIC OZONE TRENDS IN CENTRAL EUROPE	55
6.1	Research approach	56
6.2	Summary of the study	57
7	STRATOSPHERIC OZONE TRENDS AT LAUDER, NEW ZEALAND	61
7.1	Research approach	61
7.2	Summary of the study	63
8	TRENDS OF INTEGRATED WATER VAPOUR IN SWITZERLAND	67
8.1	Research approach	68
8.2	Summary of the study	69
9	CONCLUSIONS	71
9.1	Recommendations and outlook	72
BIBLIOGRAPHY		75
ACRONYMS		91
ACKNOWLEDGMENTS		95
APPENDIX		
A	PUBLICATIONS	99
A.1	Study on ozone trends in central Europe	99
A.2	Study on ozone trends in Lauder, New Zealand	121

A.3	Study on water vapour trends in Switzerland	136
B	MISCELLANEOUS	159
B.1	List of publications	159
B.2	Declaration of consent	161

1 | INTRODUCTION

Stratospheric ozone and tropospheric water vapour are atmospheric trace gases that play essential roles in the climate system. Small changes in their concentration can have large effects on chemical processes, dynamics, and the radiative balance in the atmosphere. They are therefore defined as essential climate variables (ECVs) by the World Meteorological Organization (WMO). To understand and predict the evolution of the climate system, it is indispensable to constantly measure and monitor these ECVs.

Stratospheric ozone is expected to increase in response to reduced emissions of ozone-depleting substance (ODS) after the implementation of the Montreal Protocol. Recent studies agree on a healing of the Antarctic "ozone hole" and on global recovery of ozone concentrations in the upper stratosphere (e.g. WMO, 2018a), which demonstrates the success of the protocol. However, various ground-based datasets do not agree on the magnitude and uncertainties of the trends, especially in the lower stratosphere (SPARC/IO₃C/GAW, 2019). Tropospheric water vapour is also expected to increase, due to global temperature rise. However, increasing water vapour trends are still not detected with confidence and show large regional differences, especially above continents (e.g. Bindoff et al., 2013; Chen and Liu, 2016). The main reason for these uncertainties in ozone and water vapour trends are their slow changes with time. Such small changes may be masked by natural variability and are thus difficult to detect. Further, inhomogeneities in measurements might lead to physically inconsistent patterns and falsify trend estimates. To obtain optimal estimates of the true changes, it is therefore important to analyse measured time series carefully, to identify inhomogeneities, and to account for them in the trend analyses.

The underlying aim of this thesis is to obtain more consistent trend estimates of stratospheric ozone and tropospheric water vapour at mid-latitudes. To reach this aim, various ground-based time series are compared comprehensively to assess the quality and stability of the data. Particularly, we compare coincident measurements from multiple ground-based techniques, extended by satellite and reanalyses data, which makes it possible to detect inhomogeneities and biases in the data. Advanced trend analysis methods that consider data uncertainties are then applied to obtain optimal estimates of the true ozone and

water vapour trends. This helps to clarify the question whether ozone and water vapour increase in observed measurements as expected from anthropogenic emissions of ODSs and greenhouse gases (GHGs).

This thesis is divided in three parts. Part I summarizes the role of ozone and water vapour in the atmosphere and describes how to measure them. This includes a chapter about the theoretical background and the current state of research concerning the most important atmospheric and climatic processes in which ozone and water vapour are involved (Chapter 2). Various techniques to measure ozone and water vapour in the atmosphere are then described in Chapter 3.

Part II presents the datasets (Chapter 4) used and introduces the methodology for the estimation of atmospheric trends (Chapter 5).

Part III consists of three different studies published in or submitted to peer-reviewed journals. The first study presents ground-based ozone trends in central Europe and investigates how anomalous observations can be incorporated into the analysis of stratospheric ozone trends (Chapter 6). A related study is presented in Chapter 7, which concentrates on ozone measurements and trends in the southern hemisphere. The third study presents trends of integrated water vapour in Switzerland based on various ground-based measurement techniques (Chapter 8).

Finally, Chapter 9 summarizes and discusses the outcome of the thesis and gives an outlook for future studies. The publications are attached in the appendix (Appendix A).

Part I

THEORETICAL BACKGROUND

This part provides theoretical background about ozone and water vapour in the atmosphere, reviews the current state of research, and summarizes various measurement techniques to measure the concentration of both gases.

2

OZONE AND WATER VAPOUR IN THE ATMOSPHERE

The atmosphere is a thin layer around the earth and the medium of life on the earth surface. It is composed to 78.09% of nitrogen (N_2), to 20.95% of oxygen (O_2) and to 0.93% of argon (Ar). Multiple species, so called trace gases, build the remaining gaseous constituents. Water vapour is the most abundant trace gas, but its concentration varies highly with season and location (<1% to 3%). Other trace gases such as carbon dioxide (CO_2), methane (CH_4) or ozone (O_3) have abundances smaller than 0.05%. Despite their small amount, these trace gases are crucial for chemical processes and the radiative balance in the atmosphere.

Several of them are essential to characterize the climate system. They are therefore part of the group of ECVs, as defined by the WMO. Small changes in the concentration of these gases can already have large effects on the earth system and life on earth. Measuring and monitoring ECVs is therefore required to understand and predict the evolution of the climate system.

The evolution of two of these ECVs is the topic of this thesis: stratospheric ozone and tropospheric water vapour. This chapter describes the most important processes and the current state of research concerning the role of both gases in the climate system.

2.1 STRATOSPHERIC OZONE

Ozone has multiple functions in the atmosphere; it is involved in radiative, chemical and dynamical processes. It is a pollutant in the troposphere, absorbs harmful ultraviolet (UV) radiation in the stratosphere and also acts as a GHG. Ozone is a gas with high reactivity, that has strong oxidizing capacities. It therefore plays an important role in oxidizing numerous chemical species in the atmosphere.

Ozone in the troposphere is problematic for plants and human beings, because it is harmful already at low concentration. Tropospheric ozone mostly results from photochemical reactions with nitrogen oxides and organic compounds that originate from the combustion of fossil fuels.

This thesis concentrates on ozone in the stratosphere, where about 90% of the atmospheric ozone resides. Ozone mainly absorbs radiation between 240 nm and 320 nm and builds a protective shield in the stratosphere which protects life from harmful UV radiation. The UV absorption leads to a vertical distribution of ozone with maximum concentration in terms of number density at around 20 km and in terms of volume mixing ratio (VMR) at around 35 km (Fig. 2.1). This altitude is determined by a balance between the photochemical production driven from above and decreasing air density with height (Brasseur, 1999). The UV absorption by ozone is responsible for an increase in temperature with height in the stratosphere (Fig. 2.1). Ozone is involved in multiple chemical reactions in the stratosphere. The basics of ozone-related chemical processes in the stratosphere are summarized in the following.

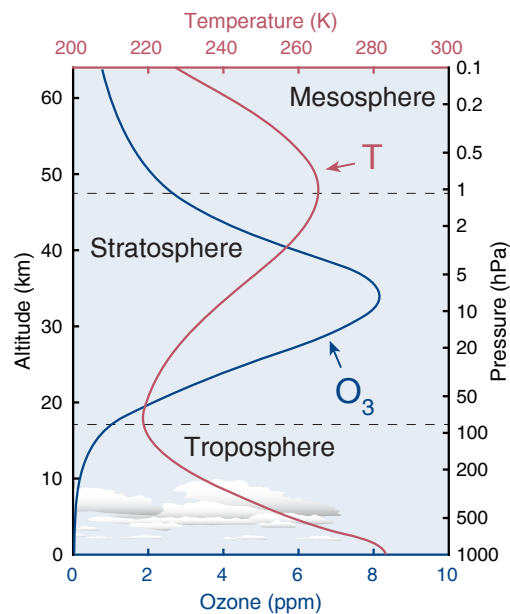
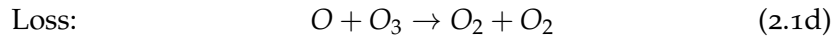
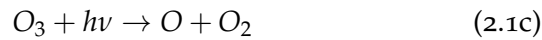
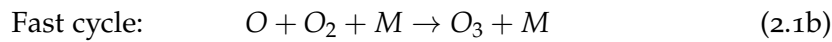
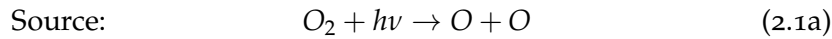


Figure 2.1: Typical ozone (O_3) volume mixing ratio (VMR) in parts per million (ppm) and temperature (T) profiles at mid-latitudes, obtained from ground-based radiometer measurements in Bern, Switzerland.

2.1.1 Stratospheric ozone chemistry

Ozone in the stratosphere is formed by photochemical mechanisms that are described by the pure oxygen chemistry. The basic principle of pure oxygen chemistry has first been presented by Chapman (1930). It includes the fast and continuous formation and destruction of atomic oxygen (O) and ozone (O_3), which are commonly referred to as *odd*

oxygen. The odd oxygen cycle with its source and loss reactions, also called *Chapman cycle*, are given by:



where M represents a collision partner that is inert, generally O_2 or N_2 . Within the Chapman cycle, odd oxygen is formed and destroyed in several steps. First, molecular oxygen (O_2) is split into atomic oxygen through photodissociation by UV radiation (Eq. 2.1a). By colliding with another oxygen molecule and the collision partner M , ozone is then formed (Eq. 2.1b). This photochemical ozone production depends on solar irradiation and the availability of a collision partner, and is thus largest in the tropical stratosphere. The collision partner is required to conserve the energy of momentum and it absorbs the excess energy of the collision. This reaction is substantial for atmospheric ozone, as it is the only known reaction that forms ozone in the atmosphere (Brasseur and Solomon, 2005b). Further, it leads to the release of kinetic energy, which is responsible for the positive temperature gradient with height in the stratosphere (Bekki and Savarino, 2016). Next, the ozone molecule is split apart by UV radiation, forming atomic oxygen in its ground state (^3P) or in its excited state (^1D) (Eq. 2.1c). Equation 2.1b and Eq. 2.1c are fast so that O and O_3 are continuously produced and destroyed, which leads to a stable concentration of odd oxygen. Finally, odd oxygen is removed again by Eq. 2.1d, forming two oxygen molecules.

In the 1960s, scientists realized that the loss of odd oxygen via Eq. 2.1d was not sufficient in balancing the production of odd oxygen to explain observed ozone concentrations (Crutzen, 1999). The Chapman cycle thus overestimates the amount of stratospheric ozone, and other ozone destructive mechanisms are necessary to explain the observed ozone concentrations. It was soon found that, in addition to the pure oxygen chemistry, catalytic cycles are important for stratospheric ozone destruction. In these reactions, a catalyst species X reacts with ozone (Eq. 2.2a), and is then rebuilt by the reaction with atomic oxygen (Eq. 2.2b):



In this way, the catalyst is not consumed and can destroy ozone recurrently. These catalysts can be of natural or of anthropogenic origin. The most important catalytic cycles for ozone destruction are reactions with hydrogen compounds (HO_x), first presented by Bates and Nicolet (1950), reactions with nitrogen compounds (NO_x) (Crutzen, 1970),

and reactions with chlorine compounds (ClO_x). Chlorine compounds mainly result from anthropogenic emissions of chlorofluorocarbons (CFCs) (see Section 2.1.3). Their substantial risk to destroy the ozone layer has first been pointed out by Molina and Rowland (1974).

The ozone destruction by catalytic cycles is interrupted through the formation of reservoir species (ClONO_2 and HCl). These species have longer live times than the active catalysts and deactivate the catalytic ozone destruction. However, in polar winter conditions, this deactivation can be interrupted through reactions of the reservoir species on polar stratospheric cloud (PSC) particles. The reactions on PSC particles lead to the removal of active nitrogen through sedimentation of PSC particles, which further enhances the ClO_x cycle. During polar night, active chlorine is accumulated. As soon as sunlight comes back in late winter, the active chlorine destroys large amounts of ozone (Brasseur and Solomon, 2005b). This causes strong ozone depletion in Antarctic late winter and early spring, known as the Antarctic ozone hole, as first presented by Farman et al. (1985).

Stratospheric ozone chemistry involves multiple additional chemical cycles. The complex dependencies are presented in detail in various textbooks, for example in Brasseur and Solomon (2005a).

2.1.2 Stratospheric ozone at mid-latitudes

The global distribution of stratospheric ozone is strongly influenced by transport through the mean stratospheric circulation. Ozone production is largest in the tropics, and ozone rich air is transported from the tropical stratosphere towards the winter pole. In the last mid-century, A. W. Brewer (1949) and G. M. B. Dobson (1956) suggested that air rises in the tropics, transporting dry and ozone rich stratospheric air towards higher latitudes. This circulation is called Brewer-Dobson circulation (BDC). As a result of the BDC, total column concentrations are largest in spring at mid- to high latitudes of the winter hemisphere, as illustrated in Fig. 2.2. The BDC is driven by planetary Rossby-waves that propagate into the winter stratosphere where they break, inducing a poleward flow. Detailed explanations can be found for example in Holton et al. (1995) and Plumb (2002). A measure to estimate how fast the BDC transports air from the tropics towards a specific location is the mean age of stratospheric air. The age of air can be inferred from observations of long-lived trace gases (e.g. SF_6), suggesting ages of 4 to 6 years in the lower stratosphere at mid-latitudes (Haenel et al., 2015; Karpechko et al., 2018; Stiller et al., 2012).

At mid-latitudes (35° to 60° latitudes), stratospheric ozone concentrations are determined by a balance between photochemistry and transport. Whereas upper-stratospheric ozone is dominated by photochemistry, ozone in the lower stratosphere is influenced by both

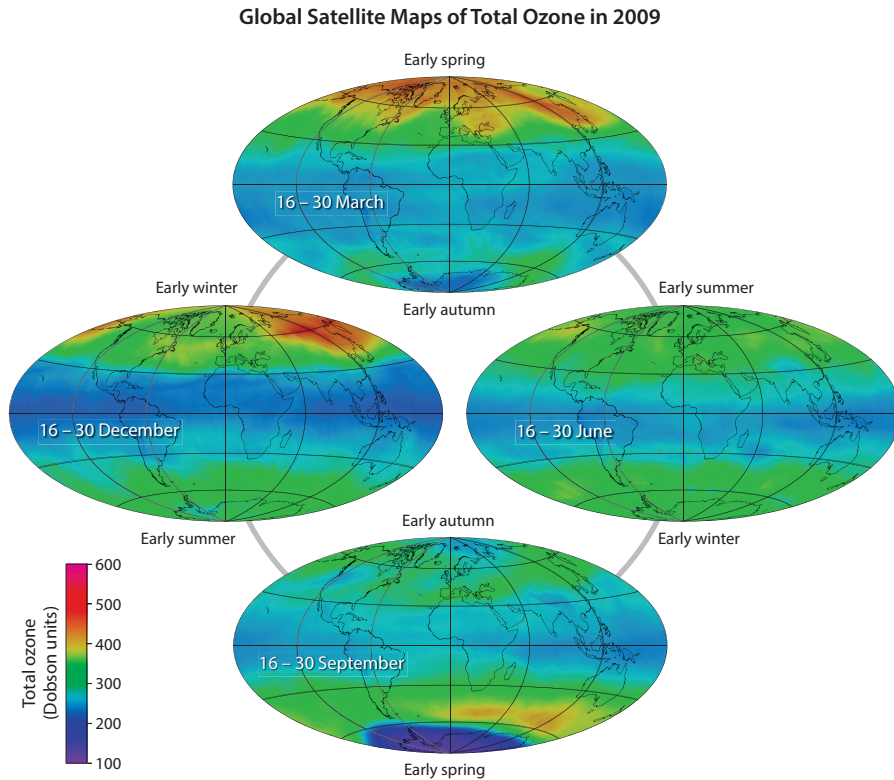


Figure 2.2: Global distribution of total ozone averaged over 2 weeks for the four seasons in 2009 from satellite measurements. In that year, a strong Antarctic ozone hole is visible in September.

— *Salawitch et al. (2019), Figure Q3-1*

chemistry and dynamics (Chipperfield, 2012). This includes large-scale transport from the tropics as described above, but also polar dynamics and small-scale mixing processes. For example, mid-latitude ozone concentrations can be strongly disturbed by the displacement or splitting of the polar vortex, transporting polar air to mid-latitudes (e.g. Godin et al., 2002). Further, variations in the tropopause height, which are related to tropospheric circulation or climate change, also affect ozone concentrations. For example, an inverse relationship between total column ozone and tropopause height was reported by Varotsos et al. (2004). Further, Steinbrecht et al. (1998) hypothesized that around one third of the pre-1997 ozone depletion at Hohenpeissenberg, Germany, could be explained by changes in the tropopause height.

Other significant natural contributions to the concentration of ozone are changing circulation patterns that are influenced by the quasi-biennial oscillation (QBO) (e.g. Tweedy et al., 2017) or the El Niño Southern Oscillation (ENSO) (e.g. Diallo et al., 2018). Further, the 11-year solar cycle affects ozone photochemistry, with increased heating and photolysis rates in the tropics at solar maximum (Ball et al., 2019a). However, the solar-ozone response is still subject to uncertainties,

as shown by Maycock et al. (2016). Nevertheless, Wuebbles (1984) showed that the solar cycle has the largest effect among the natural contributions on ozone trends. Also, Moreira et al. (2016) showed that the solar cycle has a large contribution to ozone variability recorded by a ground-based radiometer in Bern, Switzerland. Finally, volcanic eruptions can have a big effect on stratospheric ozone, leading to strong ozone depletion.

Mid-litudinal total column ozone has a strong annual cycle, with a maximum in spring when the transport from the tropics is largest. A minimum occurs in autumn, because photochemical destruction is large during summer and transport from the tropics is small. At northern mid-latitudes, Moreira et al. (2016) found a seasonal cycle with an amplitude of around 16 % in the middle stratosphere based on ground-based radiometer measurements. However, this regular cycle can be disturbed by the mentioned natural variabilities from year to year. Generally, this interannual variability is larger on the northern hemisphere due to larger planetary wave activity than on the southern hemisphere, related to the asymmetric land-sea distribution. Further, an hemispherical asymmetry exists in the BDC, with stronger transport in the northern winter hemisphere (e.g. Konopka et al., 2015). Finally, the diurnal cycle of stratospheric ozone at northern mid-latitudes was found to be between 3 % to 6 % due to diurnal variation in photochemistry and dynamics (Schanz et al., 2014; Studer et al., 2014).

2.1.3 Stratospheric ozone trends

Past ozone decline

Anthropogenic emissions of ODSs are responsible for a strong global decline in stratospheric ozone observed since the 1980s. The use of ODSs in industrial and consumer products led to a substantial increase of chlorofluorocarbon (CFC) emissions from the middle 20th century, as shown in Fig. 2.3a. The international response to the strong increase in ODS emissions was the Montreal protocol on Substances that Deplete the Ozone Layer, which was signed in 1987 and entered into force in 1989. The Montreal protocol and its successive adjustments and amendments aimed to phase out emissions of ODSs. As a result of this international agreement, the ODS emissions declined from the late 1980s on (Fig. 2.3a). Further, the equivalent effective stratospheric chlorine (EESC), that had been continuously increasing since the 1960s, started to decrease after reaching a maximum in the late 1990s (Fig. 2.3b). The EESC (or EECl in Fig. 2.3b) is a quantity to measure the total ozone-depleting capacity of chlorine- and bromine-containing molecules in the atmosphere based on surface ODS concentrations. As a response to increased ODSs in the atmosphere, ozone declined

around the globe, as shown by the total ozone measurements in Fig. 2.3c. Moreover, extreme depletion was observed over Antarctica in each spring (Fig. 2.3d) and occasionally over the Arctic, related to reactions on PSC particles as described above. As a consequence of the reduced ODS emissions after the Montreal Protocol, ozone stopped to decline around the year 2000 (Fig. 2.3c), which will be discussed in the following.

Present ozone changes

In recent years, different factors have been indicating that stratospheric ozone started to recover. The clearest indications occur in regions that are most sensitive to changing stratospheric chlorine concentrations (Steinbrecht et al., 2018). This includes the upper stratosphere, where significant ozone increase starting in the late 1990s have been detected using datasets of multiple different measurement techniques. This has been summarized in the latest Scientific Assessment of Ozone Depletion of the WMO/United Nations Environment Programme (UNEP) (Braesicke et al., 2018) and the Long-term Ozone Trends and Uncertainties in the Stratosphere (LOTUS) report (SPARC/IO₃C/GAW, 2019). Furthermore, Antarctic ozone is highly sensitive to changes in ODSs, and the severe ozone hole over the Antarctic has started to recover (Kuttippurath and Nair, 2017; Pazmiño et al., 2018; Solomon et al., 2016; Strahan and Douglass, 2018; Strahan et al., 2019).

In less sensitive regions, however, the ozone recovery is more difficult to observe, especially in total ozone column data (Weber et al., 2018) or in the lower stratosphere. It is even discussed whether ozone continues to decline in the lower stratosphere (Ball et al., 2018; 2019b; 2020; Chipperfield et al., 2018; Wargan et al., 2018). Nevertheless, consensus exists that the significant ozone decline observed in the 1980s has generally stopped and that the Montreal Protocol has thus been successful (Steinbrecht et al., 2018).

In the upper stratosphere, where photochemistry dominates ozone production, two processes are mainly responsible for the detected ozone increase (Pawson et al., 2014b; Steinbrecht et al., 2018). The first process is related to the decline of anthropogenic emissions of ODSs. The decreased emissions have led to less chlorine species in the stratosphere, which slows down the catalytic ozone destruction. The second process is due to cooling of the stratosphere caused by increased GHG emissions. GHGs molecules can get excited and de-excited either through the absorption of infrared (IR) radiation or through molecular collisions. The GHGs, mainly CO₂, warm the troposphere because they absorb IR radiation emitted from the earth surface. The CO₂ molecules get excited and the energy is either radiated back and "trapped" by other GHG molecules, or transformed to kinetical energy through collisions, which means that temperature increases. In the stratosphere,

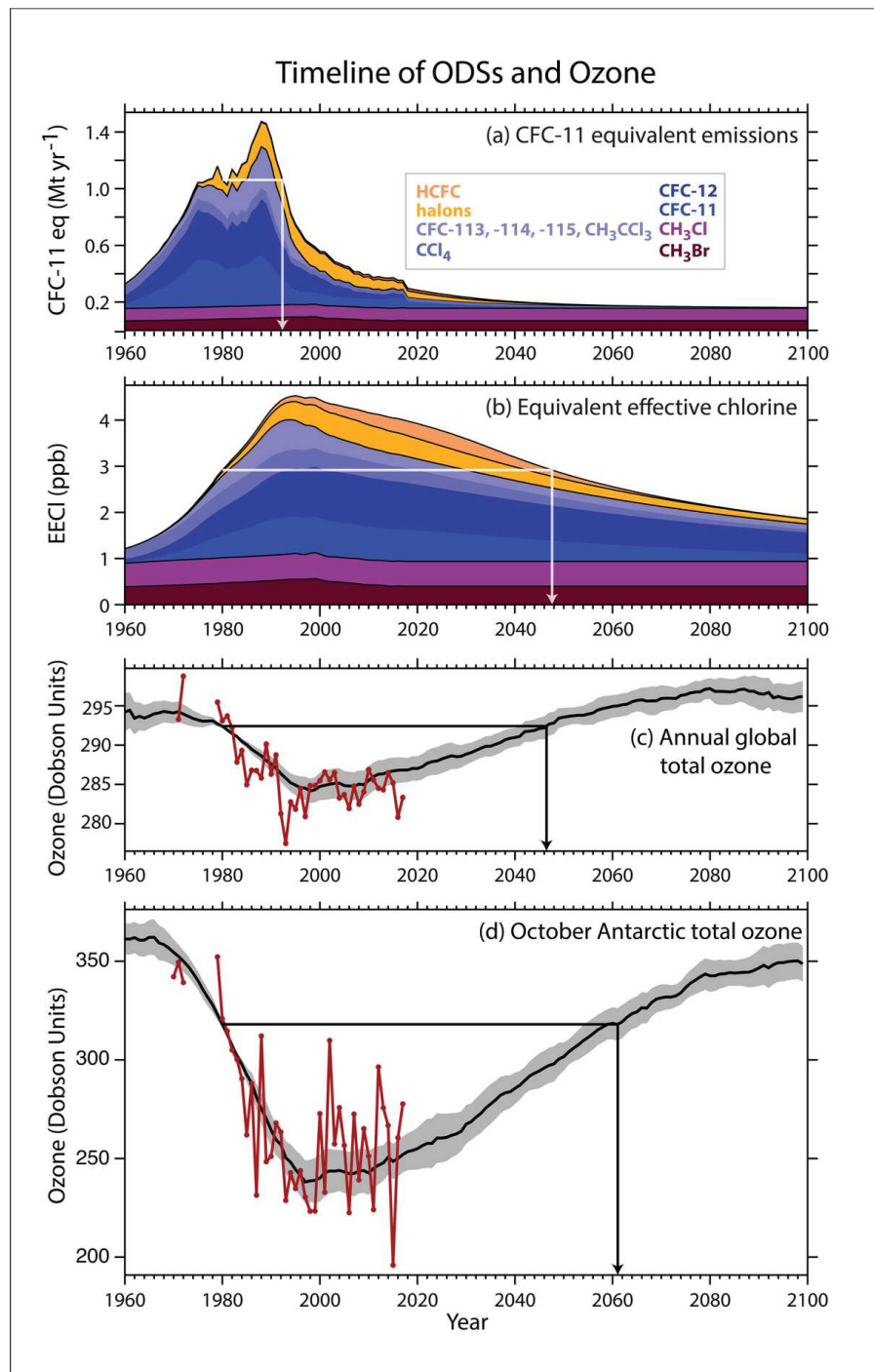


Figure 2.3: Observed and projected changes in (a) emissions of ozone-depleting substances (ODSs), (b) equivalent effective stratospheric chlorine (EECl) emissions, (c) global total column ozone (60°N to 60°S) observations (black) and model output (red), and (d) Antarctic spring total ozone (observations and model). ODS emissions in panel (a) are given in units of equivalent CFC-11, which is the most prominent chlorofluorocarbon (CFC). Future projections assume a greenhouse gas increase according to the RCP6.0 scenario (IPCC, 2014). The arrows indicate values in 1980 and the observed or projected date of return to 1980 values.

— WMO (2018a), Figure ES-1

less molecules are available for collisions. Further, less IR radiation reaches the stratosphere. Therefore, CO₂ molecules are mostly excited through molecular collisions. The excited CO₂ molecules then de-excite by emitting IR radiation that escapes towards space rather than transforming the energy into kinetic energy through collisions. In the stratosphere, kinetic energy is therefore transformed to radiative energy that escapes to space, which cools the stratosphere. This process leads to a cooling of the stratosphere with increasing GHG emissions (e.g. Fels et al., 1980). The cooling slows down ozone destruction cycles in the upper stratosphere that are strongly temperature dependent. Stratospheric cooling thus contributes to upper-stratospheric ozone recovery.

Stratospheric cooling has been reported for example by model and observational data, with a cooling between 0.25 K to 0.8 K per decade in the last four decades (Maycock et al., 2018; Steiner et al., 2020). However, stratospheric temperature changes are not only related to increasing GHGs, but also closely linked with ozone changes and changes in the circulation and dynamics (e.g. Maycock et al., 2018). Indeed, the cooling slowed down after 1997 because cooling associated with ozone depletion was reduced with ongoing ozone recovery (Maycock et al., 2018; Solomon et al., 2017; Steiner et al., 2020).

Expected future ozone changes

The ozone layer is expected to recover in the next decades due to decreasing ODSs. However, the recovery will be slow compared to the fast ozone decline in the past (Steinbrecht et al., 2018). This is due to the long lifetime of ODSs, leading to a slow decline of stratospheric chlorine compared to the prior fast increase (see Fig. 2.3b).

Globally, pre-1980 total ozone levels are currently estimated to occur around 2042 to 2051 (Braesicke et al., 2018), as illustrated in Fig. 2.3c. Afterwards, even higher ozone concentrations are expected. The main reason for this super-recovery is the increased transport of ozone rich air through the BDC. Climate models predict that the BDC will accelerate with climate change by 2% to 3.2% depending on the GHG emission scenario (Butchart and Scaife, 2001; Butchart, 2014). In the last decades, an increase in the BDC of 2% was derived from lower-stratospheric temperature observations by Fu et al. (2015) and Karpechko et al. (2018). Further, age of air trends derived from observations of stratospheric trace gases are negative in the lower stratosphere, indicating younger air due to faster transport (Hegglin et al., 2014; Karpechko et al., 2018; Ray et al., 2014). However, BDC changes are difficult to observe in available measurements (Butchart, 2014) and the sign of BDC trends in the middle and upper stratosphere remains still uncertain (Karpechko et al., 2018).

At northern mid-latitudes, pre-1980 levels in total ozone are expected between 2020 and 2044 (Braesicke et al., 2018). This broad time range illustrates that large uncertainties in ozone recovery remain. Uncertainties about the time of recovery do not only arise from uncertainties in the strengthening of the BDC, but also from uncertainties in other expected dynamical changes and how ozone responds to them. For example, models are inconsistent in the response of the QBO to climate change (Richter et al., 2020). Moreover, processes that further decrease ozone balance the described ozone increase due to increasing BDC. For example, the tropopause height is expected to increase with climate change (e.g. Hu and Vallis, 2019), which reduces the total ozone column. Also, the mixing of ozone-poor tropical lower-stratospheric air with mid-latitudinal air has been increasing, leading to decreasing lower-stratospheric ozone at mid-latitudes (Ball et al., 2020). Moreover, methane (CH₄) and nitrous oxide (N₂O) are involved in catalytic ozone destruction; ozone recovery thus depends also from their future anthropogenic emissions (Braesicke et al., 2018). Increased methane emissions increase the amount of water vapour in the stratosphere (Yue et al., 2019), which may further cool the lower stratosphere (Ball et al., 2020; Maycock et al., 2011), and enhance the formation of PSCs and related ozone loss in polar regions (e.g. Kirk-Davidoff et al., 1999; Stenke and Grewe, 2005).

To summarize, it is expected that the continuous GHG emissions will lead to an increase of ozone concentrations beyond the natural level of the 1960s (WMO, 2018b). However, this is subject to large uncertainties because multiple other processes affect ozone concentrations. Consequently, despite the success of the Montreal protocol in stopping ozone depletion, it is indispensable to continue observing stratospheric ozone and assessing its changes with great accuracy.

Challenges in ozone trend detection

Detecting stratospheric ozone trends can be a difficult task. The long-term changes are often small and may be masked by natural variability or uncertainties in the data. Further, short measurement records and autocorrelation increases uncertainties when estimating trends (Steinbrecht et al., 2018). Also, trends detected by different instruments or by different trend models may differ (SPARC/IO₃C/GAW, 2019; Strahan et al., 2019). In recent years, not all datasets agreed on magnitude and uncertainties of ozone trends at all altitudes, as it was already presented in WMO's Scientific Assessment of Ozone Depletion in 2014 (Pawson et al., 2014a). A comprehensive study by Harris et al. (2015) even concluded that it was too early to report a significant ozone increase in the upper stratosphere (SPARC/IO₃C/GAW, 2019). These differences laid the foundation for the project on Long-term Ozone Trends and Uncertainties in the Stratosphere (LOTUS), which aims to

"revisit the causes of differences in the conclusions regarding the significance of post-turnaround ozone trends [...]" (SPARC/IO₃C/GAW, 2019, p. 2). The ozone studies presented in this thesis (Chapters 6 and 7) also contribute to this aim.

2.2 TROPOSPHERIC WATER VAPOUR

Terrestrial water cycles between various reservoirs within the earth system, forming the hydrosphere. This includes the earth mantle, the oceans, ice sheets, fresh water, glaciers and the atmosphere. The smallest reservoir of the hydrosphere is the atmosphere; its mass is only 0.001 % of the total mass of water on earth (Wallace and Hobbs, 2006c). However, exchange rates are largest in the atmosphere, with residence times on the scale of days (Wallace and Hobbs, 2006c). Water enters the atmosphere through evaporation from water surfaces and soil water, sublimation from ice surfaces and transpiration from vegetation. The water molecule has a strong electric dipole moment, so that large energy amounts are required or released by the phase changes between vapour, liquid and ice. This transition between states is crucial, because it enables water to transfer energy from the earth surface to the atmosphere through evaporation (e.g. from oceans) and condensation (e.g. cloud formation). In form of latent heat, energy is then redistributed around the globe. Water vapour is the basis for the formation of clouds and precipitation. Furthermore, water vapour controls the energy balance of the earth, directly because it is a strong GHG, and indirectly by the formation of clouds that influence the radiative budget. Finally, it also controls optical properties of the atmosphere by influencing size and composition of aerosols.

Globally, a balance between evaporation and precipitation exist. Over continents, however, moist air is transported from the oceans so that precipitation generally exceeds evaporation. Depending on the regional climate, the volume concentration of water vapour in the atmosphere varies largely. It can reach up to 4 % close to the surface in warm, tropical regions, whereas it can be far below 1 % in cold, dry regions (Ahrens, 2009). A typical vertical distribution of water vapour at mid-latitudes in the troposphere is shown in Fig. 2.4. Most of the water vapour is concentrated in the first kilometers, whereas stratospheric air contains water vapour on the order of a few parts per million (ppm) by volume. The tropopause acts as a cold trap for atmospheric water vapour which explains the dryness of the stratosphere. However, water vapour can enter the stratosphere due to convective overshooting of ice particles. A further source of stratospheric water vapour is methane that enters the stratosphere and that is subsequently oxidized.

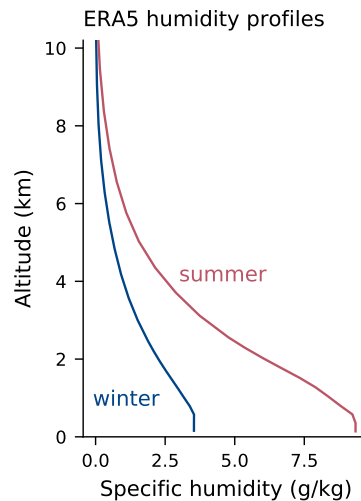


Figure 2.4: Typical profiles of specific humidity for mid-latitudinal summer and winter. The profiles show mean values of ECMWF reanalysis, 5th generation (ERA5) data from 1995 to 2018 at Bern.
— Generated using Copernicus Climate Change Service Information

The global distribution of water vapour scales with temperature but is also highly dependent on circulation and weather patterns. A typical distribution is shown in Fig. 2.5, which shows the total, vertically integrated amount of water vapour (total precipitable water vapour, or integrated water vapour (IWV)) from satellite measurements. Water vapour amounts are largest in the Intertropical Convergence Zone (ITCZ) and decrease towards the poles, with typical values of around 15 mm in northern mid-latitudinal spring.

2.2.1 Water vapour and climate

Water vapour plays a crucial role in the earth's climate, because it is the most abundant GHG in the atmosphere. Through the absorption of IR radiation, the molecules are transformed to an excited state, and will de-excite through molecular collisions. Further, cloud droplets and ice crystals absorb IR radiation that is partly re-emitted towards the surface. Consequently, the troposphere is warmed by around 33 °C compared to an atmosphere without water vapour, which makes the earth surface habitable. This natural greenhouse effect is enhanced by anthropogenic emissions of other GHGs, mainly CO₂. According to the Intergovernmental Panel on Climate Change (IPCC), surface temperature data report a global warming of 0.85 °C over the period 1880 to 2012 (IPCC, 2013). Further, the IPCC concludes that "human influence on the climate system is clear" (IPCC, 2013, p. 15), which

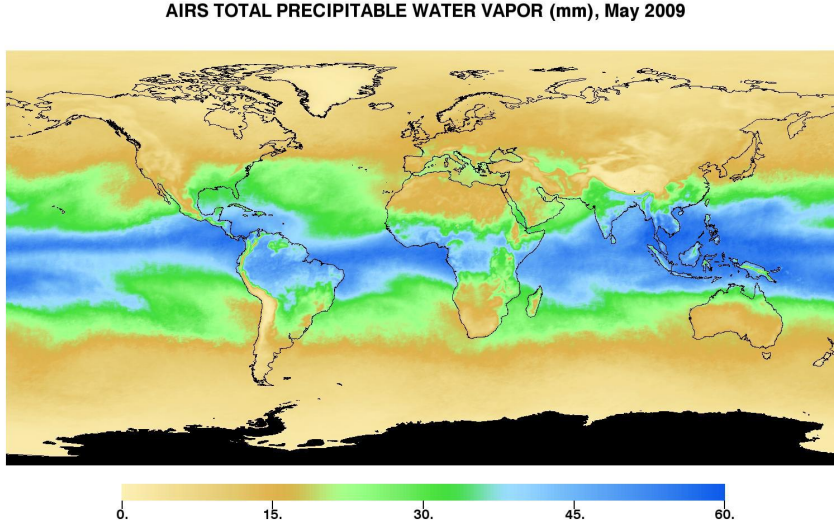


Figure 2.5: Typical global distribution of total precipitable water vapour, showing measurements from the Atmospheric Infrared Sounder (AIRS) on NASA’s Aqua satellite in May 2009.

— NASA/JPL AIRS Project

<https://airs.jpl.nasa.gov/resources/174/global-total-precipitable-water-vapor-for-may-2009/>

is a strong political statement on the anthropogenic origin of climate change.

Water vapour is strongly coupled with temperature, with increasing amounts for rising temperature. This coupling results in a positive feedback, as illustrated in Fig. 2.6. When the temperature increases due to increased anthropogenic GHG emissions (initial change), evaporation and the amount of atmospheric water vapour increase. Consequently, the GHG effect is enhanced, which further increases the temperature. This positive water vapour feedback enhances anthropogenic climate change caused by GHG emissions. Indeed, it increases the surface temperature sensitivity to changes in CO₂ emissions by almost a factor of two (e.g. Held and Soden, 2000).

When humid air is saturated, it is in equilibrium with liquid water and the vapour pressure e equals the saturation vapour pressure e_s . In this case, the relative humidity (RH) would be 100% ($RH = \frac{e}{e_s}$). The saturation vapour pressure is, in ideal cases, only temperature dependent, and increases with rising temperature. Its fractional change resulting from a small change in temperature (dT) is given by the approximated form of the Clausius–Clapeyron equation:

$$\frac{de_s}{e_s} \approx \frac{L_v}{R_v T^2} dT, \quad (2.3)$$

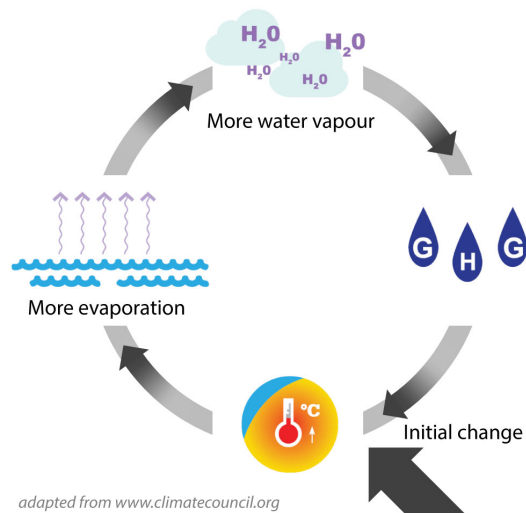


Figure 2.6: Schema to illustrate the water vapour feedback.

— Adapted from www.climatecouncil.org.au/resources/so-what-exactly-is-a-feedback-loop/

with the latent heat of evaporation $L_v = 2.5 \times 10^6 \text{ Jkg}^{-1}$, the gas constant for water vapour $R_v = 461 \text{ JK}^{-1}\text{kg}^{-1}$, and the actual temperature T . On global average, this corresponds to a water vapour change of around 7% for each degree increase in temperature (Trenberth et al., 2003), under the assumption that RH remains constant (Möller, 1963). Even though it has been shown that RH is generally insensitive to climate changes (e.g. Held and Soden, 2000), it is discussed that RH is not constant with time everywhere, especially over land due to insufficient moistening (Collins et al., 2013; Sherwood et al., 2010). Nevertheless, it was found that the magnitude of the observed tropospheric water vapour increase over the past 40 years corresponds globally to the observed temperature change, and that RH remained approximately constant over the same time period (Stocker et al., 2013). This is, however, not always the case on regional scales, and local water vapour trend analyses are thus important.

3 | MEASURING OZONE AND WATER VAPOUR IN THE ATMOSPHERE

Various techniques exist to measure trace gases in the atmosphere. The amount of ozone and water vapour varies highly in space, both horizontally and vertically. Depending on the interest of altitude, coverage and temporal resolution, different techniques are appropriate. One can distinguish in situ measurements and remote sensing techniques (Fig. 3.1). Whereas in situ instruments carried on balloons, air planes or rockets measure directly at the location of interest, ground-based and space-borne remote sensing rely on the atmospheric emission and absorption of electromagnetic radiation, generally described by the theory of radiative transfer.

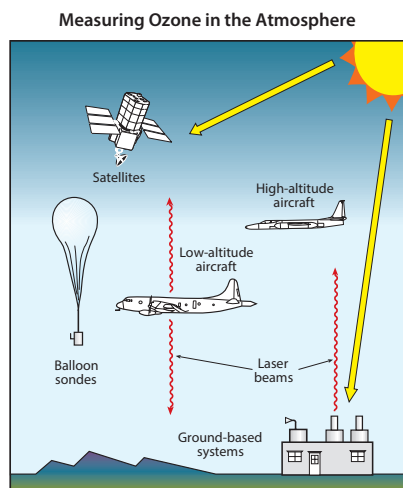


Figure 3.1: Techniques to measure ozone in the atmosphere.

— Salawitch *et al.* (2019), Figure Q4-1

Depending on the frequency, the atmosphere is more opaque or more transparent for electromagnetic radiation. In specific atmospheric windows, radiation can therefore pass through the atmosphere and can be used at the surface to infer information about its composition (Fig. 3.2). The spectrum of the atmospheric transmittance is important for the design of ground-based remote sensing instruments.

Ground-based measurements are complementary to satellite measurements. They provide information on diurnal cycle and short-term fluctuations of atmospheric parameters and species at a specific location. Ground-based instruments can measure for many decades with

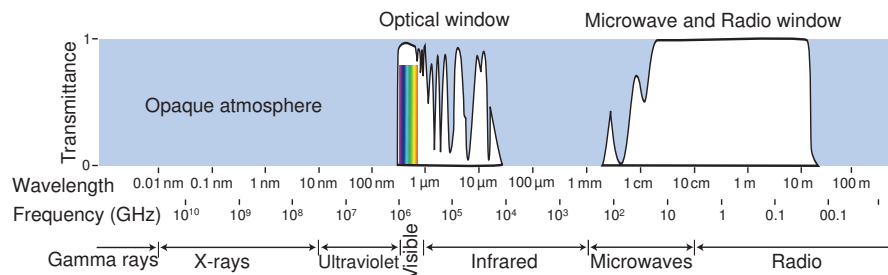


Figure 3.2: Atmospheric transmission and atmospheric windows.

— Adapted from Christian and Roy (2017), copyright Cambridge University Press. Reproduced with permission of the licensor through PLSclear.

no or small instrumental changes. This stability is essential to assess long-term changes in atmospheric trace gases. Furthermore, the ground-based data can be used for validation of satellite missions. On the other hand, satellites provide a unique insight into the global distribution of atmospheric parameters and species.

To make the detection of global long-term changes with high-quality and consistent ground-based measurements possible, a cooperative network with standard data requirements is necessary. The Network for the Detection of Atmospheric Composition Change (NDACC) responds to this purpose. NDACC is an international, global network, providing a platform for ground-based and balloon-borne measurements of atmospheric composition (De Mazière et al., 2018). Since 1991, the network provides measurements of multiple trace gas species from different measurement techniques, with the objective of detecting and understanding long-term changes in atmospheric composition. All ground-based ozone instruments used in our studies are part of NDACC. More details about NDACC can be found in De Mazière et al. (2018) and on the NDACC webpage (NDACC, 2020)

The following sections describe some basic notions of radiative transfer and give an overview of ozone and water vapour measurement techniques that provide data used in this thesis.

3.1 RADIATIVE TRANSFER

The underlying principle of remote sensing is the interaction of electromagnetic radiation with matter, described as radiative transfer. In the atmosphere, this includes interaction (absorption, emission and scattering) with molecules, aerosols or cloud droplets. The main sources of radiation in the atmosphere are solar radiation, radiation from thermal emission of the earth, and thermal emission from the atmosphere itself.

Radiation that passes through the atmosphere is attenuated by absorption or scattering on gas molecules and particles. The change in intensity dI_λ of a beam of radiation along a distance dz in the atmosphere is described by the *Beer-Lambert Law* (Wallace and Hobbs, 2006b):

$$dI_\lambda = -I_\lambda k_\lambda n \sigma dz \quad (3.1)$$

where k_λ is the absorption and scattering efficiency, n is the number density, and σ is the particle cross section.

Depending on the wavelength and the measurement technique used, absorption or scattering may be more relevant. For techniques such as microwave radiometry or Fourier-transform infrared spectrometry (FTIR), molecular absorption and emission are relevant whereas scattering can be neglected. For the lidar technique, scattering has also to be considered. The principle of absorption, emission and scattering is briefly summarized in the following. The description of absorption and emission (Section 3.1.1) concentrates on radiative transfer in the microwave part of the electromagnetic spectrum, because data from several microwave radiometers are used in this thesis.

3.1.1 Absorption and emission

An object of temperature T emits thermal radiation at all frequencies. For an idealized body in thermal equilibrium, the thermal emission is described as blackbody radiation. The emission is only determined by the temperature of the blackbody. The total radiation intensity B_ν emitted by a blackbody for a given frequency interval $d\nu$ is described by the *Planck function* (Janssen, 1993):

$$B_\nu(T) d\nu = \frac{2h\nu^3}{c^2(e^{\frac{h\nu}{kT}} - 1)} d\nu, \quad (3.2)$$

where T is the temperature of the blackbody, h is the Planck's constant ($h = 6.626 \times 10^{-34}$ J s), c is the speed of light ($c = 2.998 \times 10^8$ m s⁻¹ in a vacuum) and k is the Boltzmann's constant ($k = 1.38 \times 10^{-23}$ J K⁻¹). The term $h\nu$ describes the quantized energy carried by a photon. Real bodies do generally not emit blackbody radiation. Their emission is scaled with a frequency dependent emissivity. To maintain thermal equilibrium, the emissivity of a body always equals its absorptivity (*Kirchoff's law*).

For the microwave part of the electromagnetic spectrum, the exponent $\frac{h\nu}{kT}$ approaches zero ($h\nu \ll kT$), so that the Planck function can be approximated by the so-called *Rayleigh-Jeans approximation* (Janssen,

1993). With the Rayleigh-Jeans approximation, Eq. 3.2 simplifies and the intensity has a linear relationship to the temperature:

$$B_\nu(T) = \frac{2h\nu^3}{c^2(e^{\frac{h\nu}{kT}} - 1)} \approx \frac{2kT\nu^2}{c^2} = \frac{2kT}{\lambda^2}. \quad (3.3)$$

This temperature within the Rayleigh-Jeans limit is usually referred to as *brightness temperature* T_b .

The wavelength of microwave radiation is long compared to the size of air molecules and the scattering efficiency is thus very small. When scattering is neglected, the net change of intensity within a radiation beam that passes through an atmospheric slice dz is given by the emission of the medium, determined by the Planck function (Eq. 3.2), minus the absorption in the medium according to the Beer-Lambert law (Eq. 3.1). This is known as the *Schwarzschild equation*, where both terms are scaled with the absorption coefficient k_a :

$$dI_\nu = (k_a B_\nu(T) - k_a I_\nu) dz \quad (3.4)$$

When integrating over the whole atmospheric height (0 to z_1), this gives the *radiative transfer equation (RTE)*:

$$I_\nu(z=0) = I_\nu(z_1)e^{-\tau_\nu(z_1)} + \int_0^{z_1} B_\nu(T)k_a e^{-\tau_\nu(z)} dz \quad (3.5)$$

The RTE describes the radiative intensity determined by the emission and the absorption in the medium for a pencil of radiation that passes through the atmosphere. The absorption coefficient k_a depends not only on temperature and the number density of the species, but also on the line shape function, and includes therefore altitude information of the absorbing species (compare Section 3.2.1). The term $e^{-\tau_\nu(z)}$ is the *transmittance* (t) through the atmosphere, describing the radiation remaining in the pencil, where τ is the *optical depth* (cumulative attenuation along the atmospheric path). If the Rayleigh-Jeans limit applies, the net change of intensity when passing through the atmosphere is described by the simplified form of the RTE, commonly used in microwave radiometry:

$$T_b(\nu, z_0) = T_0 e^{-\tau_\nu(z_1)} + \int_{z_0}^{z_1} T(z) e^{-\tau_\nu(z)} k_a dz \quad (3.6)$$

where T_0 is the brightness temperature of the cosmic background radiation, $T(z)$ is the physical temperature at height z , z_0 is the surface, and z_1 is the upper boundary of the atmosphere.

3.1.2 Scattering

Extinction of radiation when passing through the atmosphere does not only occur through absorption, but also through scattering. Scattering

describes the redirection of energy, instead of changing the molecular energy level when a photon collides with a molecule (Salby, 1996). The scattering efficiency is considered when radiation passes through the atmosphere, as described by k_λ in Eq. 3.1. It depends on the molecule or particle size and on the wavelength of radiation. It is negligible if the particle size is much smaller than the wavelength.

3.2 TECHNIQUES TO MEASURE STRATOSPHERIC OZONE

The history of stratospheric ozone measurements is a fascinating development in the last century, starting with simple UV measurements and leading to the complete identification of the stratospheric ozone layer and the discovery of the ozone hole. A brief historical overview is given in the following. A comprehensive overview of the history of stratospheric ozone measurements is given for example in Brönnimann (2013) and Dobson (1968).

First information about stratospheric ozone was obtained by measuring UV radiation at ground. In 1920, Fabry and Buisson (1921) measured during two weeks UV radiation in Marseille, France and derived from the atmospheric absorption the amount of ozone in the atmosphere. Routine ozone measurements started in 1924, when G. M. B. Dobson designed a weather-proof instrument to measure total column ozone, the Dobson spectrophotometer (Dobson et al., 1926). After first measurements in Oxford, England, more instruments were built and distributed at several stations in Europe, one of which is Arosa in Switzerland. Around ten years later, in 1933, first information about the vertical ozone distribution was obtained, when the so-called "Umkehr" method was applied on measurements from the Dobson spectrophotometer in Arosa (Götz et al., 1933). This method uses consecutive zenith measurements of scattered radiation during sunrise or sunset, when the path of solar radiation through the atmosphere changes rapidly. Depending on the solar angle, the amount of scattered solar radiation measured at ground varies. The intensity of radiation that is scattered downwards to the instrument after having crossed the whole stratosphere is smaller for wavelengths that are absorbed by ozone than for longer wavelengths. For radiation scattered downwards directly from above the ozone layer, this wavelength dependent difference is smaller. This difference in absorption for different solar zenith angles gives information about the altitude where most ozone absorption occurs (Brönnimann, 2013; Götz et al., 1934). With this method, the altitude of the ozone layer was estimated for the first time to be around 20 km at Arosa (Götz et al., 1933). Soon after, first

balloon-borne ozone measurements confirmed these observations (E. Regener and V. H. Regener, 1934).

The long-term and global monitoring of ozone was not the focus of these first stratospheric ozone measurements. Nevertheless, first international measurements were already performed in the 1930s. A continuous international network with regular standard ozone measurements was then established during the International Geophysical Year in 1957 (Brönnimann, 2013; Dobson, 1968; Komhyr et al., 1989). The network was coordinated by the WMO, who established the Global Ozone Observing System (GO₃OS), which was later merged into the current Global Atmosphere Watch (GAW) programme of the WMO (WMO, 2020). This made uniform and comparable ozone observations possible and it was an important step towards long-term monitoring of the ozone layer. Regular routine measurements with ozonesondes started in the 1960s, and first ozone measurements from satellites are available since the 1970s (Brönnimann, 2013).

New ground-based remote sensing techniques to measure ozone profiles were developed in the following decades. They are generally automated and make continuous long-term measurements of ozone profiles at a specific location possible. Two examples for ground-based remote sensing of ozone profiles are microwave radiometers and lidars. The measurement principle of both techniques is described in more detail in the following. Further, ozonesondes and satellite ozone measurements are briefly introduced. The instruments and datasets used in this thesis are later presented in Chapter 4.

3.2.1 Ozone microwave radiometry

Microwave radiometry is a passive remote sensing technique that measures radiation emitted from the atmosphere to infer information about its composition or its thermodynamic state. It uses radiation in the microwave part of the electromagnetic spectrum from approximately 3 GHz to 3000 GHz (10 cm to 0.1 mm). The principle of microwave radiometry is described in detail for example in Janssen (1993).

In microwave radiometry, we are interested in the intensity of radiation emitted by a molecule. Molecules that possess an electric or magnetic dipole absorb and emit microwave radiation due to rotational transitions between energetic states. Each molecular species has its own absorption and emission spectrum characterized by molecule-specific spectral lines. The strength of the emitted spectral lines can then be used to derive information about the atmospheric composition.

Figure 3.3 shows the emission lines of oxygen, ozone and water vapour in the microwave spectrum. The shape of the spectral lines is determined by broadening of the central line. Broadening means that

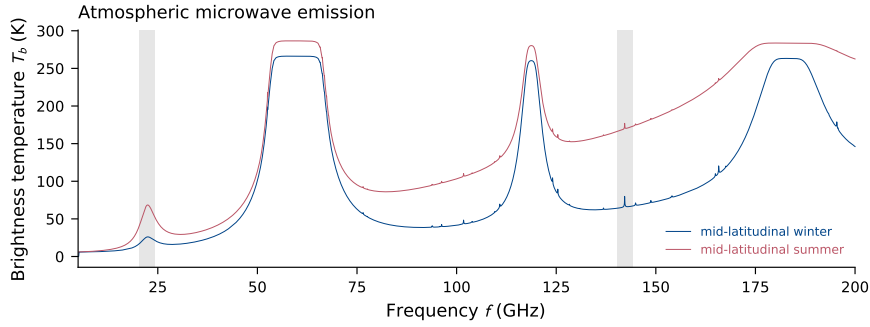


Figure 3.3: Atmospheric emissions from oxygen, ozone and water vapour for typical summer and winter mid-latitude conditions, simulated with the Atmospheric Radiative Transfer Simulator 2 (ARTS2). The grey bars show the water vapour emission line at 22.235 GHz and the ozone emission line at 142.175 GHz, both used by microwave radiometers presented in this thesis. The strong lines at 60 GHz and 118 GHz are oxygen lines, and the line at 183 GHz results from water vapour emissions.

— Simulation run by E. Sauvageat, IAP, University of Bern

a molecule does not only absorb and emit at the transition-specific frequency, but also at adjacent frequencies (Petty, 2006). It is crucial for remote sensing because it contains altitude information of the molecular emissions. Spectral line broadening arises from pressure broadening, Doppler broadening and natural broadening. The latter, which is due to uncertainty in the lifetime of excited states, can be neglected in atmospheric research. Doppler broadening is due to the molecular motion, which leads to a Doppler shift of the emitted radiation. For the emission line at 142.175 GHz that is often used to retrieve ozone, Doppler broadening is only dominant in the upper mesosphere, where pressure is small. Below, pressure broadening dominates the line shape. Pressure broadening occurs due to intermolecular collisions that disturb the natural molecular transitions, leading to absorption and emission at frequencies that deviate from the molecule-specific central frequency. The molecular collisions are highly pressure dependent, and the line shape due to pressure broadening can therefore be used to obtain information about the vertical distribution of the molecule concentration.

A microwave radiometer (MWR) at ground measures the superposition of differently broadened emission lines, which can be used to infer altitude resolved profiles of a specific species. For this, the RTE (Eq. 3.6) is solved, in which the absorption coefficient k_a contains altitude information about the species. However, the solution is not unique, and a priori knowledge of the vertical distribution of the species is needed. The most likely vertical distribution of the species

can then be inferred with an optimal estimation technique using a radiative transfer model to simulate the observed spectral line.

3.2.2 Lidar remote sensing

Lidar (light detection and ranging) is an active remote sensing technique that infers physical properties in the atmosphere from absorption and scattering on atmospheric gases, liquids and solids (Leblanc et al., 2013). The lidar system contains a laser that emits short pulses of monochromatic light. The light is scattered by the atmospheric molecules and the backscattered signal is partly measured by a telescope at ground. The amount of the backscattered radiation and the travel time of the photons can then be used to infer information about the atmosphere. This includes information about the amount and vertical distribution of specific molecules as well as temperature, air density, wind speed and wind direction (Leblanc et al., 2013). The power P of the detected lidar signal from a distance r can be described in a simple form by:

$$P(r) = KG(r)\beta(r)t(r), \quad (3.7)$$

where K describes the system performance, $G(r)$ the measurement geometry, $\beta(r)$ the backscatter coefficient, and $t(r)$ the transmittance along the path (Wandinger, 2005).

To retrieve ozone profiles, differential absorption lidars (DIALs) are used (Schotland, 1974). They emit laser pulses at two specific wavelengths, of which one is strongly absorbed by ozone molecules and the other one is weakly absorbed. The ratio of the backscattered signal at both wavelengths and the signal travel time then give information about the concentration of ozone in the atmosphere. More information on DIAL systems can be found for example in Gimmestad (2005) and Ismail and Browell (2015).

3.2.3 Balloon-borne soundings

Ozonesondes are sensors that are carried by meteorological balloons to measure ozone concentration while ascending through the atmosphere. The most common ozonesonde sensor is the Electrochemical concentration cell (ECC) (Komhyr, 1969), but also Brewer-Mast (Brewer and Milford, 1960) ozonesondes are still in use. The sondes consist of two electrolytic cells containing potassium iodide in an aqueous solution, between which an electric current flows dependent on the ozone concentration in the sampled air (Wallace and Hobbs, 2006a).

To calibrate ozonesonde profiles of different soundings, the profiles are generally normalized with a correction factor (CF). The CF is the

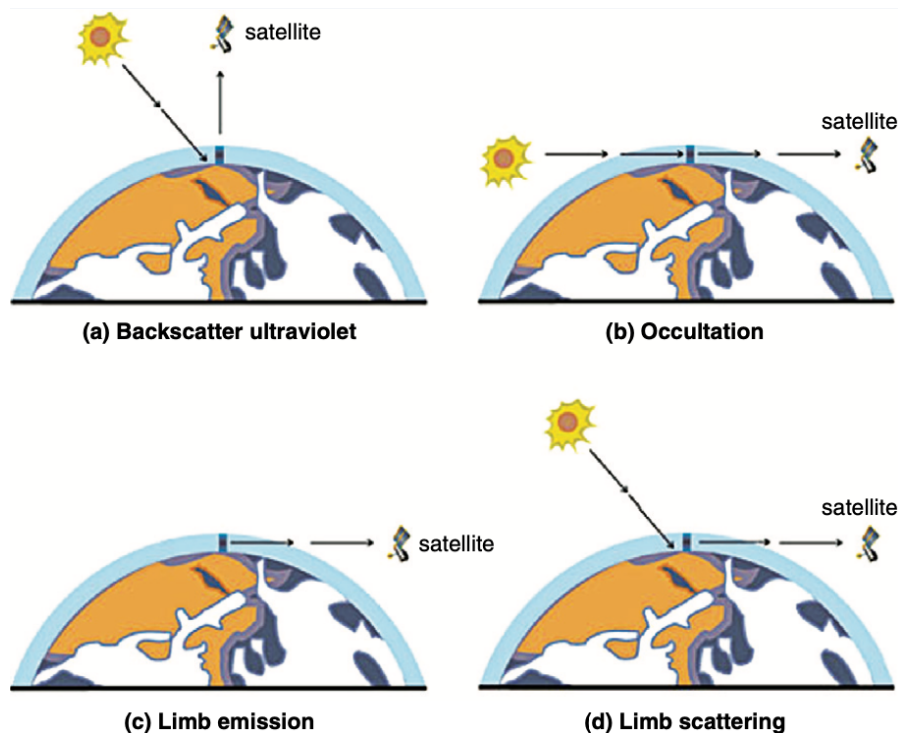


Figure 3.4: Schematic overview of four passive satellite measurement techniques used to measure ozone profiles.

— This figure was published in Wallace and Hobbs (2006a), copyright Elsevier. Courtesy of P. Newman, NASA Goddard Space Flight Center.

ratio of total column ozone measured by a reference instrument to the total integrated ozone from the sonde. When determining trends from ozonesonde data, changes in the CF might introduce an artificial trend. Further, it has been shown that manufacturer changes or small changes in sensor type can lead to large inhomogeneities in long-term sounding records (e.g. Deshler et al., 2008; Hassler et al., 2014; SPARC/IO₃C/GAW, 2019). Careful homogenization of ozonesonde records is therefore required, which has been performed recently at around 30 stations worldwide (SPARC/IO₃C/GAW, 2019).

3.2.4 Satellite-based remote sensing

Since the 1970s, multiple satellite measurements have been providing ozone measurements. Ozone profiles can be retrieved from backscatter ultraviolet (BUV), occultation, limb emission, or limb scattering measurements (Fig. 3.4). For example, a series of nine Solar Backscatter Ultraviolet Radiometer (SBUV) instruments on NASA and NOAA satellite platforms have been providing long-term ozone time series since 1970 (SPARC/IO₃C/GAW, 2019). Three consecutive Stratospheric Aerosol and Gas (SAGE) instruments use the solar occultation technique to retrieve ozone profiles since 1979 (Hassler et al., 2014). The limb

emission technique is used by the Microwave Limb Sounder (MLS) on the Aura satellite. Aura MLS measurements are used in this thesis as described in Section 4.1.4. An overview of available ozone satellite instruments and merged satellite products is given for example in Hassler et al. (2014) and SPARC/IO₃C/GAW (2019).

3.3 TECHNIQUES TO MEASURE INTEGRATED WATER VAPOUR

The amount of water vapour in the troposphere varies highly in space and time. Regional variability can be large because water vapour availability depends on humidity supply, temperature, and transport processes, as described in Section 2.2. To account for this large spatial variability, measurements with high horizontal resolution are required. Satellite measurements provide global coverage, but they often lack regional variability because of their poor horizontal resolution. To overcome this problem, ground-based measurements are ideal, providing dense measurement networks. Further, the long-term stability and continuity of ground-based instruments is optimal for trend estimation of water vapour.

The longest ground-based records of humidity profiles are given by radiosondes. Radiosondes have been the standard technique for atmospheric measurements since the mid 20th century. First radiosondes have been launched around 1930 and they became an operational tool for many national weather services in the 1940s (DuBois et al., 2002). Radiosondes thus provide important long-term in situ profile measurements of temperature, pressure and humidity. However, they have some disadvantages such as limited temporal resolution, high costs, and logistical difficulties. Dense measurement networks are therefore usually not possible.

Ground-based remote sensing instruments are less labour intensive than radiosondes and provide continuous water vapour measurements with a higher temporal resolution. The total water vapour amount can for example be measured by Fourier-transform infrared (FTIR) spectrometers or MWRs. FTIRs are ideal to measure many trace gases at the same time, because they cover a broad spectral range. However, FTIR measurements are normally based on sunlight absorption. Generally, they thus retrieve data only in cloud-free daylight conditions, even though moonlight operation is possible for some instruments. In contrast, MWRs can retrieve data in cloudy conditions and during light precipitation. This all-weather and all-daytime capability is a strong advantage of MWRs. Another all-weather technique to derive water vapour data is the use of ground-based receivers of the Global Navigation Satellite System (GNSS), that measure the delayed signal

from GNSS satellites. The advantage of this technique is that dense receiver networks at low costs exist that are ideal to study regional differences in water vapour.

This thesis concentrates on measurements of the total water vapour amount, vertically integrated over the whole atmospheric column, the integrated water vapour (IWV). IWV is given in mm, which is the total mass of water vapour on a surface of one square meter (kgm^{-2}) divided by the density of liquid water (1000 kgm^{-3}). Because most of the atmospheric water vapour resides close to the surface (compare Fig. 2.4), the total amount of water vapour in the atmospheric column (IWV) is a good measure for tropospheric concentrations.

IWV measurements from three remote sensing techniques are used in the thesis to derive IWV changes in Switzerland: MWR, FTIR, and GNSS. The measurement principle of those techniques is therefore described in the following. Instrument- and data-specific information are given later in Chapter 4.

3.3.1 IWV microwave radiometry

To retrieve integrated water vapour, passive MWRs measure the emission of water vapour molecules due to rotational transitions. They use specific microwave frequency channels, for example close to the water vapour emission line at 22.235 GHz.

To derive IWV from a measured radiation intensity, we use the Rayleigh-Jeans approximation of the radiative transfer equation (Eq. 3.6). For the retrieval of integrated values, Eq. 3.6 can be rewritten, assuming that the whole troposphere is an isothermal layer of the mean temperature T_m (Ingold et al., 1998):

$$T_b = T_0 e^{-\tau} + T_m (1 - e^{-\tau}). \quad (3.8)$$

The opacity of the atmosphere at a given frequency i is then given by

$$\tau_i = -\ln \left(\frac{T_{b,i} - T_{m,i}}{T_0 - T_{m,i}} \right). \quad (3.9)$$

The opacity depends linearly on the atmospheric water content and can be used to derive IWV and integrated liquid water (ILW) (Hocke et al., 2017; Mätzler and Morland, 2009):

$$\tau_i = a_i + b_i \text{IWV} + c_i \text{ILW}. \quad (3.10)$$

The constants a_i and b_i are statistical coefficients, derived from nearby radiosonde measurements and fine-tuned with clear-sky radiometer measurements (Mätzler and Morland, 2009). The coefficient c_i is the Rayleigh mass absorption coefficient of liquid water.

3.3.2 Fourier-transform infrared spectrometry

Fourier-transform infrared (FTIR) spectrometers use the absorption of solar infrared radiation by molecules in the atmosphere to retrieve more than 25 atmospheric constituents simultaneously (M. Schneider et al., 2013). The rotational-vibrational absorption lines by molecules such as ozone, water vapour, methane or carbon dioxide between 2.2 and 14.3 μm give information about the total column density of the species. Due to the pressure broadening of each individual absorption line, the lines contain also some information about the vertical distribution of the molecules. FTIR measurements require a constant solar input, and can thus be performed only during clear-sky conditions. Even though night-time retrievals using lunar absorption measurements are possible (e.g. Palm et al., 2010), their signal to noise ratio is low and most FTIRs can only retrieve during daylight. The temporal resolution is of several minutes (M. Schneider et al., 2013). The two main components of an FTIR are a solar tracker that captures the direct solar beam, and a high resolution Fourier-transform spectrometer that converts the observed intensity fluctuations into a spectrum.

Compared to other atmospheric species, retrieving IWV from FTIR measurements is more challenging. Standard retrieval methods are often not suitable because of the large vertical gradient and the high temporal variability of IWV. A method to retrieve IWV has first been presented by M. Schneider et al. (2006) and has been optimized by Sussmann et al. (2009), using the absorption lines between 11.7 and 11.9 μm .

3.3.3 GNSS ground stations

A dense network of ground-based Global Navigation Satellite System (GNSS) receivers exist worldwide, coordinated by the International GNSS Service (IGS). They receive dual-frequency L-band (1 to 2 GHz) signals from GNSS satellites. The GNSS satellites are placed in medium earth orbit (MEO) at around 20 000 km, ensuring the availability of at least four satellites at the same time around the world (Jin et al., 2014c). In the last decades, different GNSSs have been established, with the main aim to use them for positioning, navigation and timing. This includes the US-American Global Positioning System (GPS), the Russian Global'naya Navigatsionnaya Sputnikovaya Sistema (GLONASS), Galileo from the European Union, and the Chinese BeiDou Navigation Satellite System.

Besides the use for positioning and timing, the GNSS signal can be used for atmospheric sciences. When the signal passes through the atmosphere, it changes speed and direction due to the variation in air density. This so-called atmospheric refraction, described by

the refractivity, leads to a retardation of the signal. Integrating the refractivity along the whole path gives the total path delay of the signal in meter (Jin et al., 2014b). The retardation caused in the ionized atmosphere (above approximately 60 km) is called ionospheric delay, whereas the retardation in the "neutral" atmosphere below is called tropospheric delay (Jin et al., 2014a). The tropospheric delay along the path from the satellite to the receiver can be used to infer the total amount of atmospheric water vapour (IWV). The contribution of the ionosphere is removed by an ionospheric correction.

To obtain IWV from the tropospheric delay, the zenith total delay (ZTD) recorded by ground GNSS receivers is used. The ZTD is obtained from the tropospheric delay along each satellite–receiver path (slant delay) by applying a mapping function that accounts for the position and elevation angle. Typical ZTD values are around 2 m (Strang and Borre, 1997). For further processing, the ZTD is divided into a wet and a dry component. The dry component (zenith hydrostatic delay (ZHD)) is responsible for 90% of the delay (Strang and Borre, 1997). It can be determined using surface pressure (from weather stations, meteorological weather models, or reanalysis models) and gravitational acceleration (Saastamoinen, 1972). The remaining wet component (zenith wet delay (ZWD)) is closely related to IWV, which can then be calculated with some additional temperature information (Bevis et al., 1992). The procedure is described in detail by Guerova et al. (2003), Hagemann et al. (2002) and Heise et al. (2009), and the method to derive IWV used in this thesis is given in Bernet et al. (2020c) (Appendix A.3).

The measured ZTD is highly sensitive to changes in the GNSS antenna setup or the environment. An antenna update can lead to small height differences, which can result in jumps in the ZTD data. Also, changes in the radomes, receivers or cables may lead to biases in the data. Furthermore, changes in the environment around the antenna (e.g. tree cuts or new buildings) can influence the signal (Bernet et al., 2020b; Pacione et al., 2017). Vey et al. (2009) found jumps in IWV data after radome updates of a similar magnitude as expected from climate-related changes. Identifying and handling such changes is therefore essential for trend analyses.

Part II

DATA AND METHODOLOGY

This part presents the ozone and water vapour datasets used in the thesis, and introduces the methodology of trend analysis.

4 | DATASETS

Long-term datasets from various ground-based remote sensing techniques measuring stratospheric ozone and IWV are intercompared in this thesis. In addition, satellite data from the Microwave Limb Sounder (MLS) on the Aura satellite and reanalysis model data are used. Reanalyses are chemistry-climate or weather models that reconstruct the best estimate of the real atmospheric state by assimilating observations into the model. We used IWV and stratospheric ozone data from two reanalysis products, ERA5 and MERRA-2. ERA5 is the latest atmospheric reanalysis from the European Centre for Medium Range Weather Forecasts (ECMWF) (Hersbach et al., 2020), and MERRA-2 is the Modern-Era Retrospective analysis for Research and Applications, version 2 from National Aeronautics and Space Administration (NASA)'s Global Modelling and Assimilation Office (GMAO) (Gelaro et al., 2017). An overview of the ground-based measurement sites with the instruments used in this thesis is given in Table 4.1 and described in more detail in the following.

4.1 OZONE DATASETS

To estimate stratospheric ozone trends, we use ozone profile data from microwave radiometers (MWRs), lidars, and ozonesondes from different measurement sites, which are all part of the Network for the Detection of Atmospheric Composition Change (NDACC) (Table 4.1). In the first study (Chapter 6), we compare Ground-based Millimeter-wave Ozone Spectrometer (GROMOS) data at Bern with ozone profiles from three other stations in central Europe (Fig. 4.1a) and satellite data (Aura MLS). In the second study (Chapter 7), data from the southern hemispheric station Lauder in New Zealand (Fig. 4.1b) are used and compared with Aura MLS and ERA5.

4.1.1 Microwave radiometers

We use data from three different ozone MWRs: the Microwave Ozone Profiling Instrument (MOPI) located in Lauder as described in Bernet et al. (2020a) (Appendix A.2) and references therein (e.g. Nedoluha et al., 2015), the Stratospheric Ozone Monitoring Radiometer (SOMORA)

STATION	INSTRUMENT	SPECIES	SAMPLING RATE
Bern (CH) 46.95° N, 7.44° E; 577 m	GROMOS	O ₃	30 min to 1 h
	TROWARA	IWV	1 h
	GNSS (ExWi)	IWV	1 h
Payerne (CH) 46.8° N, 7.0° E; 491 m	SOMORA	O ₃	30 min to 1 h
	Ozonesonde	O ₃	13/month
	GNSS	IWV	1 h
Jungfraujoch (CH) 46.55° N, 7.98° E; 3580 m	FTIR	IWV	8/month
	GNSS	IWV	1 h
Hohenpeissenberg (DE) 47.8° N, 11.0° E; 980 m	Lidar	O ₃	8/month
	Ozonesonde	O ₃	10/month
Haute Provence (FR) 43.9° N, 5.7° E; 650 m	Lidar	O ₃	11/month
	Ozonesonde	O ₃	4/month
Lauder (NZ) 45° S, 169.7° E; 370 m	Lidar	O ₃	5/month
	MOPI	O ₃	6 h

Table 4.1: Information about measurement stations, instruments, and datasets used in this thesis. The sampling rate only refers to the data and study period used and may be different in other data versions or study periods. Sampling given per month indicates the number of measurement days per month. Additional GNSS stations are shown in Fig. 4.9.

located in Payerne as described in Bernet et al. (2019a) (Appendix A.1) and references therein (e.g. Maillard Barras et al., 2015), and GROMOS located in Bern. The principle to retrieve ozone from MWR measurements was described in Section 3.2.1. GROMOS is a special focus in the first study of this thesis (Chapter 6) and therefore described in more detail in the following.

The ozone radiometer GROMOS

The Ground-based Millimeter-wave Ozone Spectrometer (GROMOS) is located on the roof of the university building Exakte Wissenschaften (ExWi) in Bern (Fig. 4.2). It has been measuring continuously since November 1994. The instrument measures emission due to rotational transitions of ozone molecules at 142.175 GHz with an elevation angle of 40°. Measurements from the sky are performed through a blue styrofoam window, which is generally transparent to microwave radi-

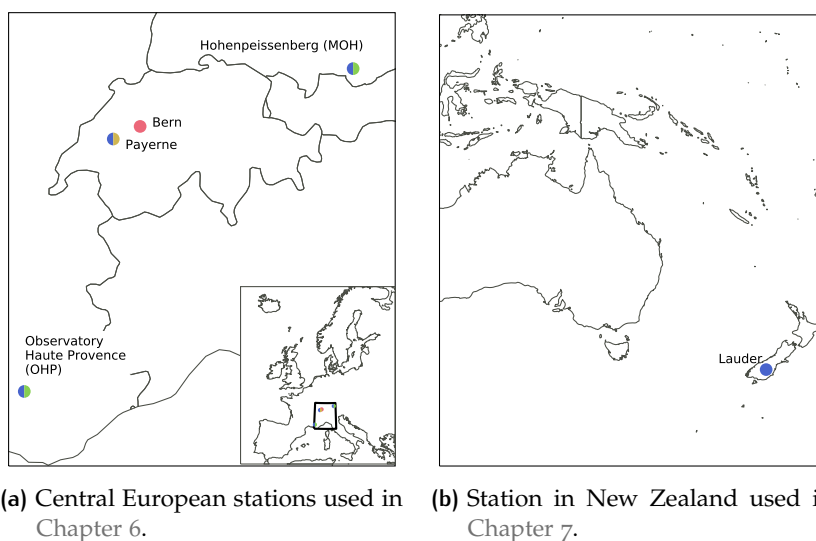


Figure 4.1: Maps showing NDACC stations that provide ozone measurements used in this thesis.

ation. They are alternated with measurements from a cold and a hot load to continuously calibrate the received signal. The signal is guided through a quasi-optical system where it is filtered and down-converted with a local oscillator to an intermediate frequency of 3.7 GHz, which is then analysed by a fast Fourier-transform spectrometer (FFTS).

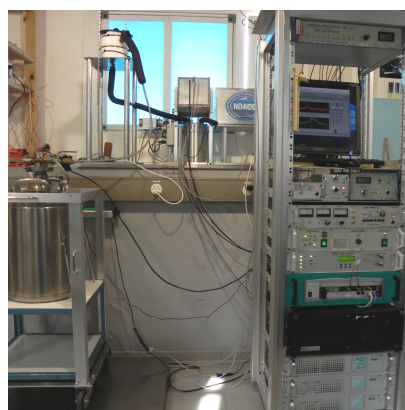


Figure 4.2: The GROMOS radiometer in a temperature-controlled room at the University of Bern.

To retrieve ozone profiles from the measured spectrum, the measurements are integrated over 30 minutes. The measured spectrum is compared to a spectrum simulated with the Atmospheric Radiative Transfer Simulator 2 (ARTS₂, Buehler et al. (2018)). By using an a priori profile as a first guess for the vertical ozone distribution, the best estimate of an ozone VMR profile is obtained with an optimal

estimation method according to Rodgers (2000). The profiles provide independent information between approximately 20 and 52 km (Moreira et al., 2015) with a vertical resolution of ~ 15 km to 20 km in the stratosphere (Fig. 4.3d). The vertical smoothing of the retrieved ozone profiles is described by the averaging kernels (AVKs) (Fig. 4.3b).

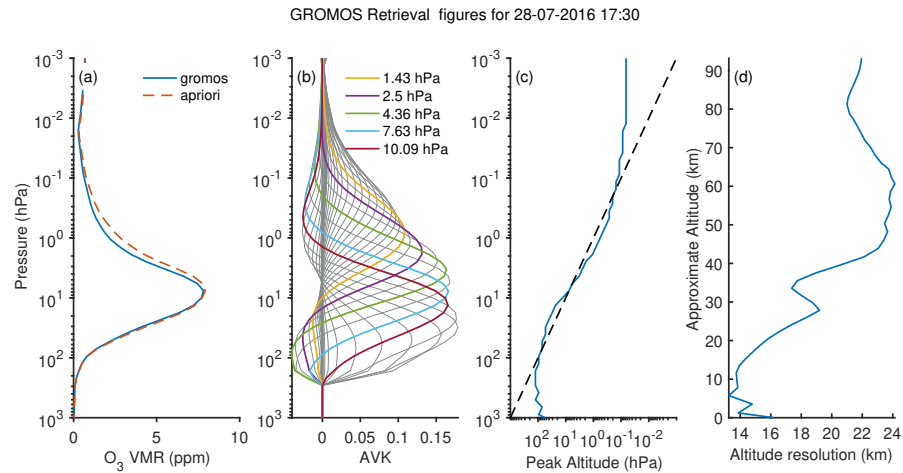


Figure 4.3: Characteristics of a typical ozone VMR profile retrieved from GROMOS measurements. (a) Retrieved and a priori profile, (b) averaging kernels (AVKs), (c) peak of the AVKs, (d) altitude resolution (full width at half maximum of the AVKs).

The instrumental and retrieval setup used in our study (version 2021) have been described in detail by Moreira (2017) and Moreira et al. (2015). Before October 2009, a filter bench (FB) was used instead of the FFTS, and measurements were integrated for one hour. Using overlapping measurements of almost two years, all retrieved ozone profiles before 2009 were homogenized as described in Moreira et al. (2015). The AVKs before and after the spectrometer upgrade are slightly different. To investigate the influence of this change on the ozone profiles, we applied the mean GROMOS AVKs before and after the upgrade to a constant ozone profile. The difference between the resulting convolved profiles represents the effect of the changing AVKs after the spectrometer upgrade (Fig. 4.4). We observe that this difference profile looks similar to the mean difference profile that was applied for harmonization by Moreira et al. (2015), also shown in Fig. 4.4. The profile used for the harmonization has larger amplitudes in the peaks, indicating that additional differences are also corrected for (Bernet et al., 2019b). We therefore conclude that the applied harmonization corrects for the effect of changing AVKs.

Microwave radiation is almost not affected by clouds and GROMOS ozone retrievals are thus possible in almost all weather conditions, except during heavy rain. Furthermore, the measurements do not depend on solar radiation, and the instrument measures during day

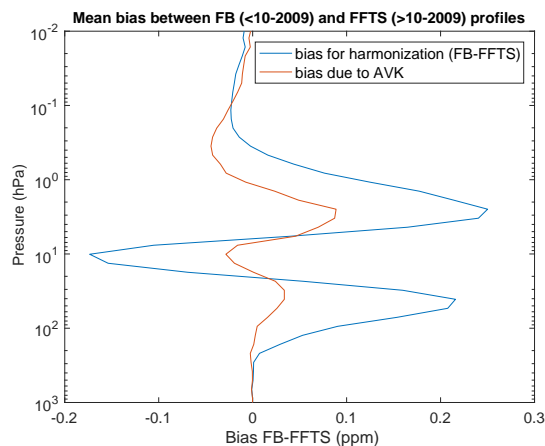


Figure 4.4: Difference between averaged filter bench (FB) profiles (before October 2009) and fast Fourier-transform spectrometer (FFTS) profiles (after October 2009) averaged during the overlapping measurement period. The profile was used for the harmonization of FB data according to Moreira et al. (2015). The orange line (bias due to AVK) indicates the difference that is only caused by the difference in averaging kernels. — Bernet et al. (2019b)

and night. Consequently, a long-term continuous time series of retrieved ozone profiles with (half-)hourly resolution is available at Bern (Fig. 4.5). The continuous measurements with few, harmonized changes in the measurement setup make the time series ideal for trend estimation.

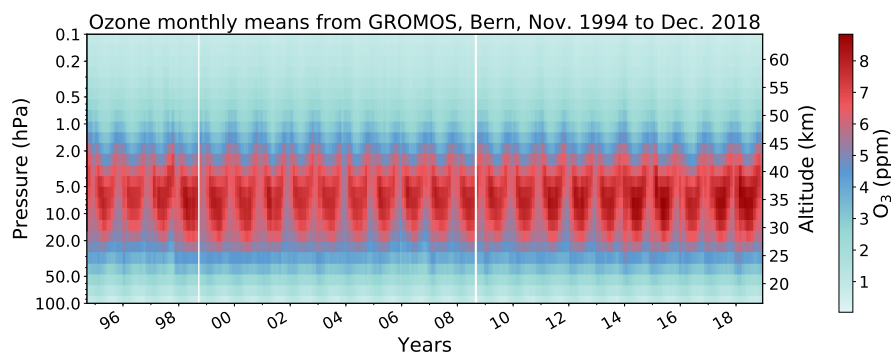


Figure 4.5: GROMOS ozone VMRs from 1994 to 2018. White vertical lines indicate months with missing data.

4.1.2 Lidars

We use measurements from DIAL lidars at Hohenpeissenberg, at the Observatory of Haute Provence (OHP), and at Lauder. The lidars emit laser pulses at 308 nm and 353 nm or 355 nm to derive ozone concentrations from the backscattered signal (see Section 3.2.2). The

instruments are described in Bernet et al. (2019a) (Appendix A.1) and Bernet et al. (2020c) (Appendix A.2) and references therein. Additional instrument-specific information about the lidars used can be found in Steinbrecht et al. (2009b) and Werner et al. (1983) (Hohenpeissenberg), Godin-Beekmann et al. (2003) and Nair et al. (2012) (OHP), and in Brinksmas et al. (1997) and Swart et al. (1994) (Lauder).

The lidars provide ozone number density profiles between approximately 15 and 40 km with high vertical resolution. They operate in clear-sky nights only and measure on average during between five and eleven nights per month, depending on the location (Fig. 4.6 and Table 4.1).

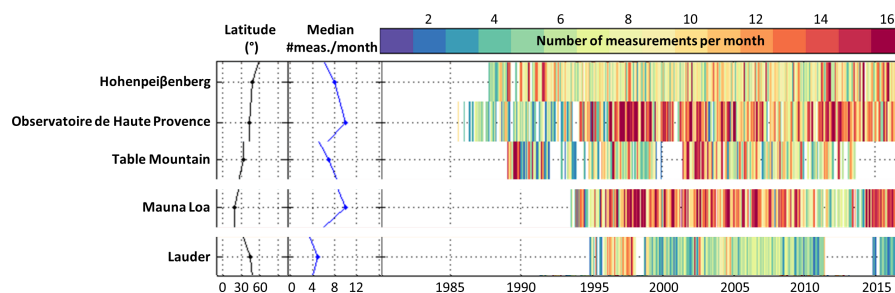


Figure 4.6: Number of ozone lidar measurements per month for NDACC stations. Measurements from three of the stations are used in this thesis (Hohenpeissenberg, Observatory of Haute Provence, and Lauder). The two panels on the left indicate the station latitude and the median number of measurements per month.

— SPARC/IO₃C/GAW (2019), Figure 2.3

4.1.3 Ozonesondes

In this thesis, ozonesonde records from Payerne, Hohenpeissenberg, and OHP are used. Ozonesondes at Hohenpeissenberg use a Brewer-Mast sensor, whereas the ozonesondes at OHP use ECCs. The Payerne ozonesonde was initially a Brewer-Mast sonde, but was upgraded to ECC in autumn 2002 (Jeannet et al., 2007). The soundings are generally launched one to three times per week, with on average 4 to 13 profiles per month (Table 4.1). We use profiles up to an altitude of 30 km, above which the balloon generally bursts. Measurement uncertainties lie within 5%, with largest differences between soundings in the lower stratosphere (e.g. Hassler et al., 2014). All ozonesonde profiles used in this study were normalized with collocated total column ozone measurements (Bernet et al., 2019a), as described in Section 3.2.3. The correction factor (CF) of the three ozonesonde time series is shown in Fig. 4.7.

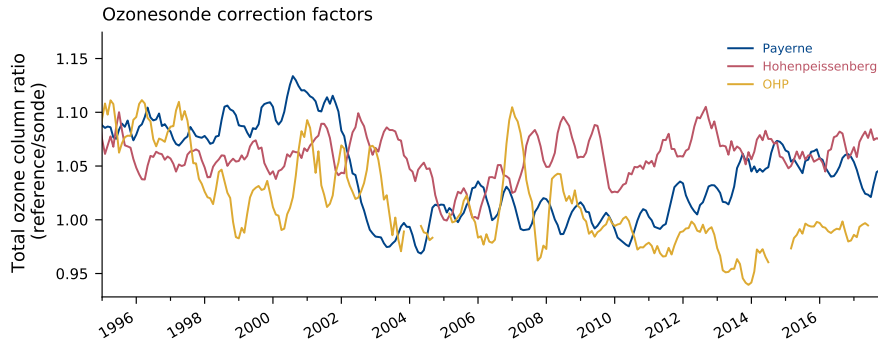


Figure 4.7: Monthly means of the correction factor (CF) of the three ozonesonde time series used in this thesis, smoothed with a moving window of five month. The CF is the ratio of total column ozone of a reference instrument and the total column ozone derived from the ozonesonde.

4.1.4 Aura MLS satellite data

Satellite measurements used in this thesis come from the Microwave Limb Sounder (MLS) on board NASA's EOS (Earth Observing System) Aura satellite (Waters et al., 2006). The satellite is in a near-polar, sun-synchronous orbit at around 700 km altitude, passing a specific location on earth twice a day. The MLS instrument measures thermal microwave limb emissions from the atmosphere since August 2004. Aura MLS measures thermal emissions in a broad spectral region to retrieve vertical profiles of ozone and multiple other chemical species in the stratosphere and mesosphere. For ozone retrievals, thermal emissions at 240 GHz are used (Livesey et al., 2018). Aura MLS ozone data have been validated by Froidevaux et al. (2008).

Hubert et al. (2016) showed that stratospheric ozone data from Aura MLS are stable with no drifts between 20 and 40 km. Furthermore, good agreement with ground-based measurements of ozone profiles have been shown (e.g. Moreira et al., 2017). We use quality-checked Aura MLS data version 4.2 according to Livesey et al. (2018).

4.2 INTEGRATED WATER VAPOUR DATASETS

To derive IWV trends in Switzerland, water vapour measurements are used from a radiometer, an FTIR spectrometer and a network of GNSS stations. Details about the two instruments and the GNSS network are given in the following.

4.2.1 The water radiometer TROWARA

The water vapour MWR used in this thesis is the Tropospheric Water Radiometer (TROWARA). It has been measuring IWV and ILW since November 1994 on the roof of the ExWi university building in Bern. The retrieval principle was described in Section 3.3.1. The initial setup of the instrument is described in Peter and Kämpfer (1992). Additional instrument upgrades were performed in 2002 and 2004 (Morland et al., 2006; Morland, 2002). Being first installed outside, it was moved inside the building in November 2002 to reduce the temperature variability and avoid rain drops on the lens (Morland, 2002). From then on, the instrument receives the radiation through a styrofoam window (Fig. 4.8a). To account for possible data jumps and to fill data gaps arising from the instrument upgrades, data before 2008 were harmonized (Morland et al., 2009) and data gaps were filled with IWV data derived from the collocated GROMOS instrument. For TROWARA, frequency channels at 21.39 GHz and 31.5 GHz are used. The channel at 21.39 GHz is close to the water vapour line at 22.235 GHz and is thus sensitive to water vapour, whereas the channel at 31.5 GHz is more sensitive to liquid water.

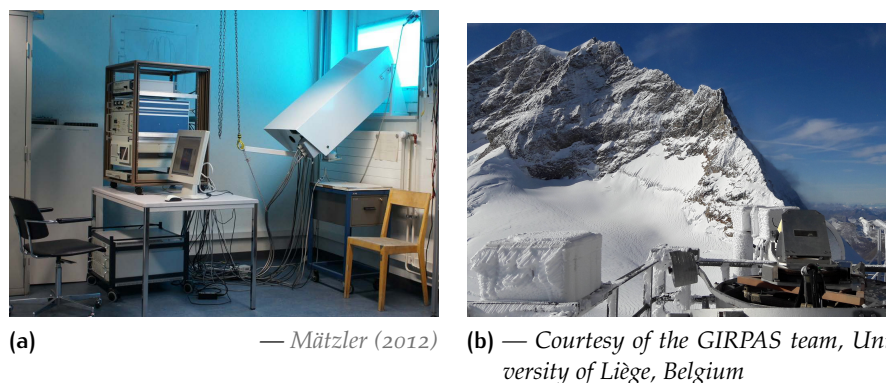


Figure 4.8: (a) TROWARA radiometer at the University of Bern, and (b) solar tracker of the FTIR at Jungfraujoch.

4.2.2 FTIR spectrometer

We use IWV data from FTIR spectrometer measurements at the high altitude research station Jungfraujoch (Table 4.1). A home-made instrument, operated by the University of Liège, was installed at Jungfraujoch in 1984 and completed in 1990 by a commercial Bruker IFS120HR instrument (Sussmann et al., 2009). In 2002, the Bruker instrument replaced the former instrument definitely. The measurement principle is described in Section 3.3.2 and instrumental details are given by Zander et al. (2008). The solar tracker of the instrument at Jungfraujoch is shown in Fig. 4.8b. The FTIR measurements require a constant

solar input and are thus strongly weather dependent. On average, the FTIR provides IWV measurements at eight days per month within our study period.

4.2.3 GNSS

We use GNSS ZTD data in Switzerland from the Automated GNSS Network for Switzerland (AGNES) and from a few additional stations (Bernet et al., 2020c). The AGNES network consists of 31 measurement stations. It is maintained by the Swiss Federal Office of Topography (swisstopo) and was established in 2001 (Brockmann et al., 2001a; b; Brockmann, 2001; D. Schneider et al., 2000). The current status of all stations is consistently reported on a monitor webpage (Swisstopo, 2019). In early years, only GPS receivers were used. However, most of the antennas and receivers were enhanced to GPS and GLONASS in 2008 and to multi-GNSS (including Galileo and BeiDou signals) in spring 2015 (Brockmann et al., 2016). The stations used in this thesis are shown in Fig. 4.9.

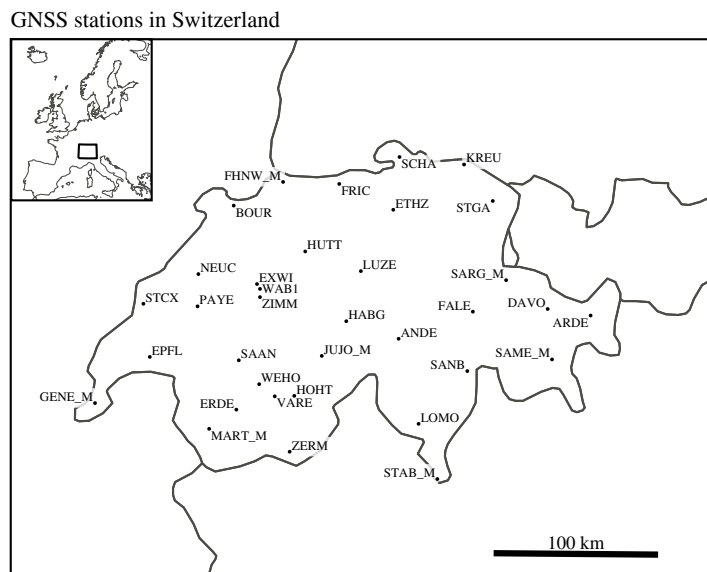


Figure 4.9: GNSS stations in Switzerland as used in Chapter 8. The station abbreviations are defined in Table 1 of Bernet et al. (2020c) (Appendix A.3). — Bernet et al. (2020c)

GNSS ZTD data are processed to obtain IWV as described in Section 3.3.3 and in Bernet et al. (2020c) (Appendix A.3). The derived IWV data are stored in the database Studies in Atmospheric Radiative Transfer and Water Vapour Effects (STARTWAVE, 2020). In 2014, all GNSS data have been reprocessed by swisstopo in the frame of the second EUREF (International Association of Geodesy Reference Frame Sub-Commission for Europe) Permanent Network (EPN) reprocessing

campaign as described in Pacione et al. (2017). For the reprocessed data, new versions of the antenna model, the mapping function, and the tropospheric a priori model are used (Brockmann, 2015). The differences between the old, unprocessed GNSS data and the newly reprocessed data are illustrated in Fig. 4.10. Shown are the monthly differences between TROWARA IWV data and the mean IWV of some selected GNSS stations around Bern, using unprocessed and reprocessed GNSS data. As comparison, the difference between TROWARA and MERRA-2 reanalysis data at Bern are also shown. The figure presents a clear step change in the unprocessed GNSS data in 2014. Moreover, it shows that the reprocessing substantially improved the GNSS IWV data before 2014, with very good agreement to TROWARA and MERRA-2 after the reprocessing. This illustrates the importance of uniform processing of GNSS data. In this thesis (Chapter 8), we only use the reprocessed GNSS data.

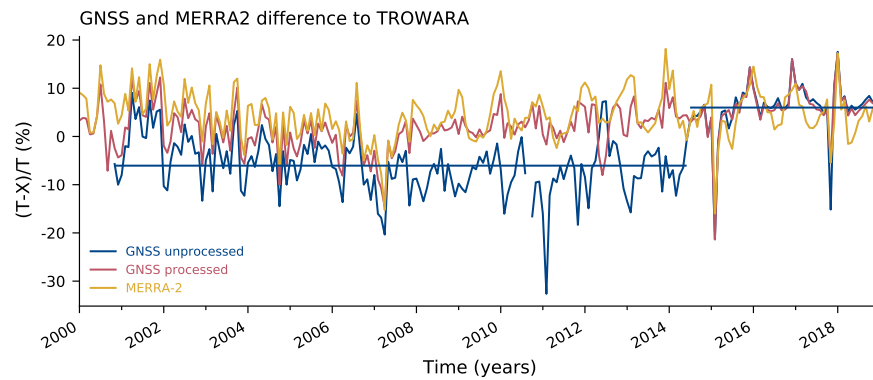


Figure 4.10: Monthly relative differences between TROWARA data at Bern and the IWV mean from selected nearby GNSS stations (BOUR, PAYE, NEUC, LUZE, ETHZ, ZIMM). Differences to the old, unprocessed GNSS data (blue) and the new, reprocessed GNSS data (red) are shown. Additionally, differences between TROWARA and MERRA-2 reanalysis data are shown (yellow). The horizontal blue lines show the mean of the unprocessed GNSS data before and after the reprocessing in 2014.

5

ATMOSPHERIC TREND ANALYSIS

The most common technique for atmospheric trend detection are multiple linear regression (MLR) techniques. This chapter gives a short introduction into linear regression and presents two trend methods that are used to determine ozone and water vapour trends within this thesis.

5.1 LINEAR REGRESSION

The principle of linear regression is to model the relationship between a dependent and one or more independent variables, mostly based on the method of least-squares. The principle is described in detail for example in Wilks (1995) or Schuenemeyer and Drew (2010), and it is summarized in the following.

5.1.1 Simple linear regression

The most basic case of regression is the simple linear regression (SLR). SLR is used to describe the linear relationship between an independent explanatory variable x , which is also called a predictor, and a dependent response variable y , also called predictand (Wilks, 1995). The relationship of the two variables is described by a linear function that produces the least error when y is predicted for a given x :

$$\hat{y}(x) = a + bx. \quad (5.1)$$

The symbol $\hat{}$ describes a predicted or estimated value. The case is illustrated in Fig. 5.1. Generally, the best fit is obtained by minimizing the sum of the squared residuals r_i (least-squares method). The residuals r_i describe the difference between the predicted and the true values:

$$r_i = y_i - \hat{y}(x_i), \quad (5.2)$$

and the residuals sum of squares is given by

$$\sum_{i=1}^n (y_i - \hat{y}_i)^2 = \sum_{i=1}^n (y_i - (a + bx_i))^2, \quad (5.3)$$

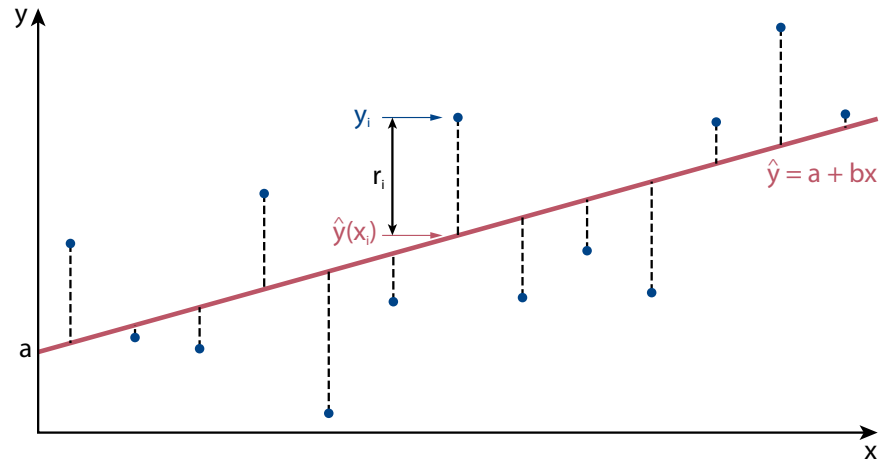


Figure 5.1: Illustration of simple linear regression with a least-square fit. The straight red line minimizes the squared sum of the residuals r_i .

which is in matrix notation:

$$\sum_{i=1}^n (y_i - \hat{y}_i)^2 = (y_i - (a + bx_i))^T (y_i - (a + bx_i)). \quad (5.4)$$

Minimizing Eq. 5.4 by setting its derivatives with respect to a and b to zero leads to the values of the regression coefficients a (intercept) and b (slope).

It is assumed that the residuals are independent random variables, with a mean of zero and a constant variance. This means that they scatter around the regression line with equal variance for each x . This is a central point of linear regression, and estimating the variance of the residuals makes statistical inferences about the quality of the regression model possible (Wilks, 1995). The goodness of the regression fit can be judged by evaluating the mean squared error of the residuals, or by the coefficient of determination (R^2), whereby R^2 describes the proportion of the total variation in y that is accounted for by the regression (Wilks, 1995).

5.1.2 Multiple linear regression

In multiple linear regression (MLR), more than one predictor describes the response variable y . The principle is the same as for SLR, but more regression coefficients are added to Eq. 5.1. Similar as for SLR, the residuals sum of squares (Eq. 5.4) is then reduced to derive the regression parameters.

MLR is commonly used in atmospheric sciences to determine trends from atmospheric observations. However, the standard MLR is not

adequate for this purpose because of insufficient treatment of uncertainties and correlations. Indeed, atmospheric measurements always contain some uncertainty about the measured value, which is not considered in a standard MLR. More advanced MLR techniques that account for measurement uncertainties are therefore needed. Further, measurement errors may be clustered and correlated in time, for example due to irregular sampling (von Clarmann et al., 2010). This is not consistent with the assumption of independent residuals as described above. Advanced MLR techniques should therefore also account for correlated clusters in the measurement errors. These issues are discussed in the following section.

5.1.3 Advanced multiple linear regression for atmospheric trends

For atmospheric trend determination, $y(x)$ generally represents a measurement at time x . Each measurement has an uncertainty, and the regression can be optimized by considering it in the regression fit. More weight is given to measurements that are more precise, and less weight to more uncertain measurements. Further, nearby responses are often correlated. Therefore, the measurement uncertainties and the correlation between residuals has to be considered. Applying this to the residuals sum of squares from Eq. 5.4 gives the *cost function* χ^2 (von Clarmann et al., 2010):

$$\chi^2 = (y_i - \hat{y}(x_i))^T S_y^{-1} (y_i - \hat{y}(x_i)), \quad (5.5)$$

where S_y is the covariance matrix of y . The diagonal elements of S_y contain the variance of the measurements, whereas the off-diagonal elements represent the covariance between neighbouring measurements.

If the regression fit would be perfect, all residuals would lie within their uncertainties, so that each weighted element of Eq. 5.5 would be smaller than one. The cost function would then be smaller than the degrees of freedom (DOF), which are defined as the number of data points minus the number of fitted variables. Consequently, this *normalized cost function* defined as

$$\chi_{norm}^2 = \frac{\chi^2}{DOF} \quad (5.6)$$

can be used to identify the goodness of the regression fit and the number of required iterations. For ideal fits, χ_{norm}^2 is smaller than unity.

5.2 TREND MODELS

To estimate trends of stratospheric ozone and IWV, we use two different multiple linear regression models. The first model has been developed by T. von Clarmann at the Karlsruhe Institute of Technology (KIT) and is described in von Clarmann et al. (2010). It is further referred to as KIT model. The second model has been developed within the LOTUS project. It is described in SPARC/IO₃C/GAW (2019) and further referred to as LOTUS model.

5.2.1 The KIT multiple linear regression

In the KIT model, the regression function given in Eq. 5.7 predicts the values \hat{y} with a monthly time vector t as independent variable. For ozone trends, several proxies that influence stratospheric ozone are used, such as the quasi-biennial oscillation (QBO), the solar activity and the El Niño Southern Oscillation (ENSO). The regression function for ozone with the regression coefficients a to h is given by:

$$\begin{aligned} \hat{y}(t) = & a + b \cdot t \\ & + c \cdot \text{QBO}_{30\text{hPa}}(t) + d \cdot \text{QBO}_{50\text{hPa}}(t) \\ & + e \cdot \text{F}_{10.7}(t) \\ & + f \cdot \text{MEI}(t) \\ & + \sum_{n=1}^4 \left(g_n \cdot \sin\left(\frac{2\pi t}{l_n}\right) + h_n \cdot \cos\left(\frac{2\pi t}{l_n}\right) \right). \end{aligned} \quad (5.7)$$

$\text{QBO}_{30\text{hPa}}$ and $\text{QBO}_{50\text{hPa}}$ represent the normalized Singapore winds at 30 hPa and 50 hPa, used as indices of the QBO. The solar activity is represented by the solar flux ($\text{F}_{10.7}$) measured at a wavelength of 10.7 cm. The influence of ENSO is considered by the Multivariate ENSO Index (MEI), that combines six meteorological variables measured over the tropical Pacific (Wolter and Timlin, 1998). An example for these proxy contribution to ozone is shown in Fig. 5.2. In addition, four periodic oscillations with different wave periods l_n are used to account for annual ($l_1 = 12$ months) and semi-annual ($l_2 = 6$ months) oscillation, and for two overtones of the annual cycle ($l_3 = 4$ months and $l_4 = 3$ months). From Eq. 5.7, the cost function is computed according to Eq. 5.5 and the regression coefficients are determined by minimizing the cost function.

Uncertainty consideration in the trend model

To account for the uncertainties of the measurements, the error covariance matrix S_y is considered in the cost function (Eq. 5.5). It weights the residuals with the monthly uncertainties of the data. Using the measurement uncertainties in S_y will generally lead to larger, more

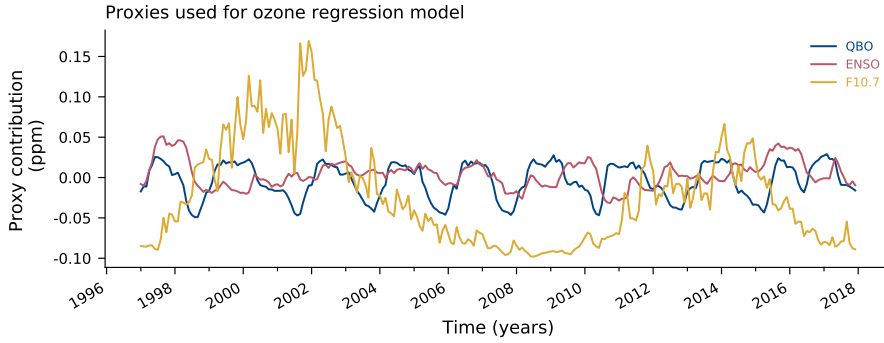


Figure 5.2: Example for proxy contribution to ozone. Shown are the contribution to ozone at 10 hPa for ozone data from GROMOS.

realistic trend uncertainties and can also change the trend values itself due to different weighting of the initial data.

The covariance matrix is composed of several parts, given by

$$S_y = S_{instr} + S_{autocorr} + S_{bias}. \quad (5.8)$$

S_{instr} contains the monthly uncertainty estimates of the measurements. $S_{autocorr}$ accounts for residuals autocorrelated in time which are caused by atmospheric variation not described by the trend model. Finally, S_{bias} describes uncertainties of a possible bias. The composition of the covariance matrix is illustrated in Fig. 5.3. The diagonal elements in S_{instr} contain the squared estimated monthly uncertainties (red). The off-diagonal elements of S_{instr} are set to zero, assuming initially no error correlation between the measurements in time. Also, $S_{autocorr}$ is initially set to zero. In case that χ_{norm}^2 (Eq. 5.6) is larger than one, the off diagonal elements of $S_{autocorr}$ are filled within an iterative process with autocorrelation coefficients derived from the residuals of the regression fit (orange). The mean variance of $S_{autocorr}$ is then scaled such that χ_{norm}^2 becomes unity. These additional uncertainties in $S_{autocorr}$ represent atmospheric variability that were initially not considered by the regression model, which improves the regression fit.

Accounting for biases and anomalies

The strength of the KIT trend model is that it can account for inhomogeneities in the data (von Clarmann et al., 2010). Data can be inhomogeneous due to changes in the measurement setup, due to non-uniform spatial or temporal sampling, or due to unknown instrumental issues. Such inhomogeneities or anomalous periods can falsify the trends.

Anomalous periods can be considered in the trend model by increasing the monthly uncertainties of these periods in S_{instr} (green in Fig. 5.3). However, an even more effective way to account for anomalies would

$$S_y = \begin{bmatrix} 0.1^2 & AC & & \dots & AC \\ AC & 0.1^2 & & & \vdots \\ & & \ddots & & \\ \vdots & & & \text{blue area} & \\ AC & \dots & & \begin{bmatrix} 0.3^2 & 5^2 & 5^2 \\ 5^2 & 0.3^2 & 5^2 \\ 5^2 & 5^2 & 0.4^2 \end{bmatrix} & \end{bmatrix}$$

S_{instr}
 $S_{autocorr}$
 Correction by increased uncertainty
 Correction by correlated block (S_{bias})

Figure 5.3: Exemplary illustration of the covariance matrix S_y used in the KIT regression model. The blue area represents a biased subset.

be to fit a bias for a biased data subset. A biased subset can occur after an instrumental change, or it can correspond to a measurement block with anomalous observations. A straightforward approach that is similar to a bias fit was presented by von Clarmann et al. (2001) and von Clarmann et al. (2010). The proposed method consists of adding a fully correlated block to the part of S_{bias} that corresponds to the biased subset. For each subset, the block in S_{bias} is set to the square of the estimated bias uncertainty of this block (purple in Fig. 5.3). This process makes a fit of the bias possible. It is mathematically equivalent to adding the bias as an additional regression fit variable, with the advantage that no additional fit variable needs to be included in the regression (von Clarmann et al., 2001).

Depending on the value chosen as bias uncertainty, the bias is estimated more or less from the data itself. For small bias uncertainties, the bias will be close to the a priori value (which would be a bias of zero), whereas it will be estimated completely from the given data for large bias uncertainty values. The approach has been applied to correct for possible biases after instrumental or retrieval changes (Bernet et al., 2020a; c; Eckert et al., 2014) or to account for anomalous periods in an instrumental time series (Bernet et al., 2019a).

5.2.2 The LOTUS regression model

The LOTUS model (USask ARG and LOTUS Group, 2017) is based on the regression model used by Damadeo et al. (2014) and is described extensively in SPARC/IO₃C/GAW (2019). It results from a number of sensitivity tests to find out best practices in terms of the proxies used. It was optimized for global analyses of satellite data. Proxies that describe local variability have thus not been analysed (SPARC/IO₃C/GAW, 2019). Further optimization for local ground-based trends is therefore still possible.

Similar to the KIT model, the LOTUS model minimizes a cost function, in which autocorrelations are determined within an iterative process until the autocorrelation coefficient has converged. The LOTUS regression function uses similar predictors as the KIT regression (Eq. 5.7), including ENSO, QBO, solar cycle, and four periodic oscillations to account for the annual cycle. In addition, it also uses a proxy for aerosol optical depth, that accounts for example for volcanic eruptions, and tropopause pressure as a proxy for tropospheric expansion.

The LOTUS cost function also includes a covariance matrix, which makes uncertainty consideration possible. However, this has not been used in the final trend results of the LOTUS report (SPARC/IO₃C/GAW, 2019), due to the difficulty of correcting for non-constant variances in the data (heteroscedasticity correction). This may be a problem when using merged datasets with abrupt changes in the sampling frequency. In this thesis, we test the LOTUS regression with weighting, but further investigations might be required in the LOTUS model adjustment to use this feature.

A more detailed description of the model is given at https://arg.usask.ca/docs/LOTUS_regression/, where the regression model is publicly available as a python software package.

Part III

RESULTS AND DISCUSSION

This part presents and discusses three studies about ozone and water vapour trends that have been published in or submitted to peer-reviewed journals.

6 | STRATOSPHERIC OZONE TRENDS IN CENTRAL EUROPE

This chapter summarizes the study published in Bernet et al. (2019a) (Appendix A.1).

Broad consensus exists today that ozone has stopped declining in the upper stratosphere in response to the turnaround of ODSs emissions, as described in Section 2.1.3 (e.g. Newchurch et al., 2003; Reinsel et al., 2005; Shepherd et al., 2014; SPARC/IO₃C/GAW, 2019; Steinbrecht et al., 2006; 2009a; Stolarski and Frith, 2006; WMO, 2014; 2018b; Zanis et al., 2006). However, not all datasets agree on magnitude and uncertainties of the trends. In order to detect true ozone trends, it is critical to find the origin of differences in trends and in their uncertainties. Trend differences may result from the different characteristics of the datasets. They differ in stability, accuracy, temporal and spatial sampling, and in spatial smoothing properties (SPARC/IO₃C/GAW, 2019). Stability changes can be due to ageing of an instrument, merging of datasets or changes in the instrument setup, the calibration, or the retrieval procedure. They lead to biases in the data that influence the trends, especially when they occur towards the beginning or the end of the dataset (e.g. Bai et al., 2017).

Several of these problems have been addressed in recent studies using satellite ozone products. The influence of sampling patterns on trends has been discussed by Millán et al. (2016) and Damadeo et al. (2018). Satellite drifts have been identified by Hubert et al. (2016), which were not considered in the comprehensive satellite trend estimates of WMO (2014) or Harris et al. (2015). Other satellite trend studies considered drifts or biases to avoid their influence on trends (e.g. Bourassa et al., 2018; Eckert et al., 2014), or used satellite data with no or small drifts only (e.g. Sofieva et al., 2017; Steinbrecht et al., 2017). The WMO ozone assessment of 2018 used updated, partly reprocessed versions of satellite datasets (Braesicke et al., 2018). Further efforts to detect steps and biases in satellite data have been made by Ball et al. (2017). Their Bayesian method uses different satellite datasets to result in an optimal merged ozone composite, but it has not yet been applied on ground-based data. Further advances with robust merged satellite and ground-based ozone data are planned within the ISSI project "Towards a Universal Framework for Merging Atmospheric

Observations from the Ground and Space" (<https://www.issibern.ch/teams/mergeatmosobserve/>, last access on 28.07.2020).

Similar challenges occur when estimating trends from ground-based records. Even though ground-based measurements are generally less subject to drifts than satellite measurements because they can constantly be maintained, other difficulties occur with ground-based measurements. The data variability between different ground-based ozone instruments is larger than for satellites, not only due to strong regional variability, but also due to differences between instrument types. Moreover, changes in the instrumental setup may lead to biases that might not always be well documented. Consequently, ground-based ozone datasets need careful analysis before estimating trends. Biases due to instrumental changes or anomalies in the time series due to instrumental artifacts have to be corrected.

Several studies presented ground-based ozone trends at northern mid-latitudes (e.g. Braesicke et al., 2018; Harris et al., 2015; Nair et al., 2015; 2013; SPARC/IO₃C/GAW, 2019; Steinbrecht et al., 2009a; 2017), but none of them considered biases in the ground-based datasets that might influence resulting trends. Moreira et al. (2015) presented GROMOS trends and found significant positive trends in the upper stratosphere. In recent years, GROMOS showed some anomalies that might be responsible for larger trends than observed in other datasets. This was shown for example by Steinbrecht et al. (2017), who presented an update of satellite and ground-based ozone trend profiles. They showed that the microwave ozone trends at northern mid-latitudes (including GROMOS and SOMORA data) deviate from the other trends between 20 and 30 km. This differences in trend estimates from MWRs, together with the problem of trend differences as described above, was the motivation for the study presented in this chapter.

The study aims

1. to understand differences between GROMOS trend profiles and trends from other ground-based instruments,
2. to present an approach to handle anomalous observations in ground-based ozone time series when estimating trends.

6.1 RESEARCH APPROACH

To achieve the first aim of the study, we identified anomalies in the GROMOS time series by comparing GROMOS data to other ground-based datasets in central Europe and Aura MLS. The other instruments include lidars (Section 4.1.2), ozonesondes (Section 4.1.3), and another MWR (Section 4.1.1) at stations in southern Germany, southern France and Switzerland. We compared coincident profiles from 1995 to 2017

and defined anomalies in the GROMOS data as soon as three instruments showed differences larger than 10 % at a specific altitude.

To account for the anomalous observations in the GROMOS data, we used the approach of dependent uncertainties and bias fitting as explained in Section 5.2.1 and illustrated in Fig. 6.1. We increased the uncertainties in the covariance matrix (case II) and set a fully correlated block (case III) to the anomalous periods. This improves the trend estimate substantially (Fig. 6.1b).

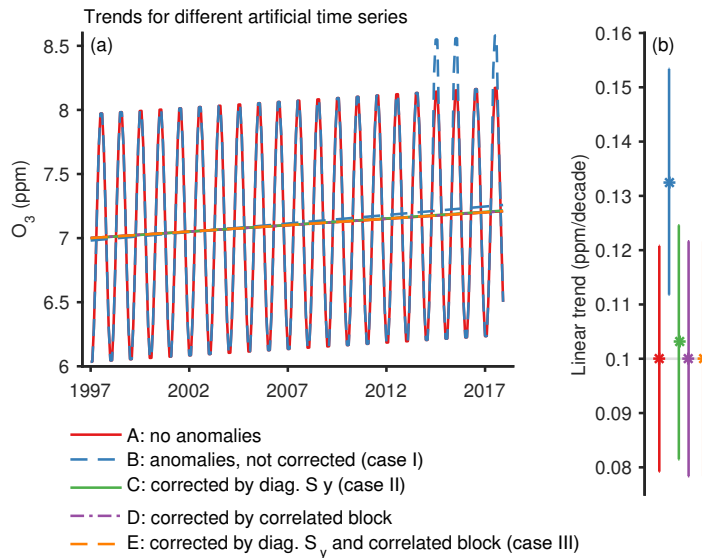


Figure 6.1: (a) Artificial ozone time series with a trend of 0.1 ppm per decade and (b) the corresponding trends. The weighting and correction applied lead to different trend estimates, as shown in panel (b).

— Adapted from Bernet *et al.* (2019a)

Furthermore, we investigated how differences in sampling rates and trend period lengths affect the trend. For this purpose, we varied the sampling or length of GROMOS data and derived trends for these data subsets. Finally, we compared the corrected GROMOS trends with trend profiles from the other instruments to investigate their agreement.

6.2 SUMMARY OF THE STUDY

We computed the relative differences between GROMOS and each of the other datasets (Fig. 6.2). The figure reveals some anomalies in the GROMOS data that we identified as described above. The origin of these anomalies could not be identified yet. It might be due to instrumental artifacts, for example due to problems in the calibration, instabilities in the spectrometer channels, ice formation on the cold load, or deficiencies in the tropospheric correction. In future,

an improved GROMOS retrieval version with optimized calibration and retrieval processes is planned, which might correct for these anomalies.

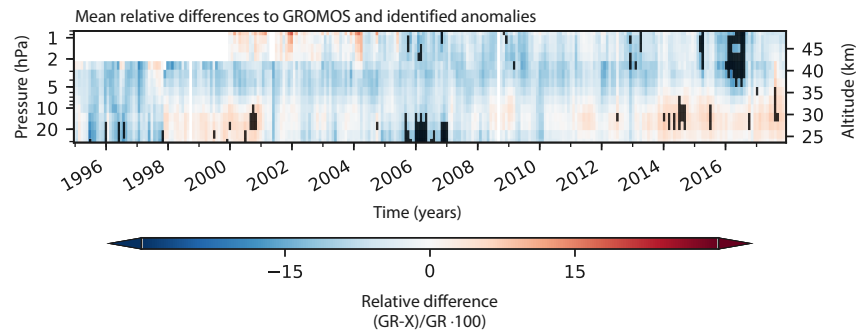


Figure 6.2: Mean differences between GROMOS and the other instruments in central Europe. Identified GROMOS anomalies are shown in black. — Adapted from Bernet *et al.* (2019a)

In a next step, we considered the anomalies in the covariance matrix of the GROMOS measurements when estimating the trends. This leads to different trend profiles, as shown in Fig. 6.3. The optimized trend profile (case III) shows a trend of 2.2 % per decade in the middle and lower stratosphere and peaks at around 4 hPa (≈ 37 km) with a trend of 2.7 % per decade. This corrected trend profile is consistent with the satellite-based trends presented by Steinbrecht *et al.* (2017). Figure 6.3 further shows that the trend peak at around 4 hPa is only marginally affected by the different corrections and thus rather robust.

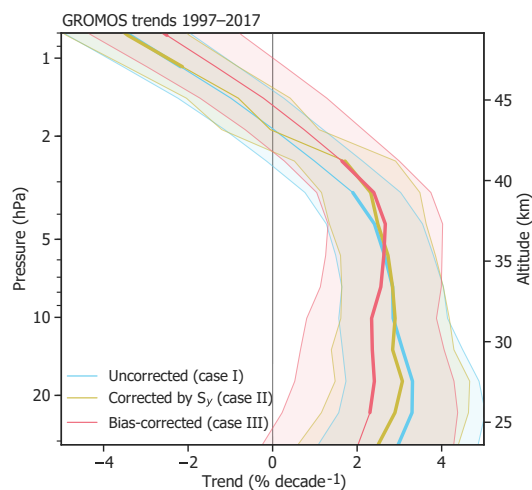


Figure 6.3: GROMOS trends, uncorrected and corrected for observed anomalies, with 2-standard-deviation uncertainties. Bold lines indicate trends that are significantly different from zero at 95 % confidence interval. — Adapted from Bernet *et al.* (2019a)

In addition, we present a short investigation how sampling patterns and the choice of the trend period influence GROMOS ozone trend estimates. Investigating the sampling rate is relevant, because lidar measurements are restricted to clear-sky nights, and might thus depend on location and season (Hatzaki et al., 2014; Steinbrecht et al., 2006). We found that selecting different night measurements can lead to trend differences of around 1 % per decade. However, the differences lie within the trend uncertainties, which is consistent with Maillard Barras et al.’s (2020) study. Based on ground-based MWR and model trend estimates, they found that significant trend differences can not be attributed to temporal sampling differences.

Moreover, we showed that the starting year of the trend period affects the trend estimate. The later the trend period starts, the larger the trend value is, which is consistent with results presented in Harris et al.’s (2015) study. These results suggest that the true trend might not be linear or that some interannual variations might not be captured by the trend model.

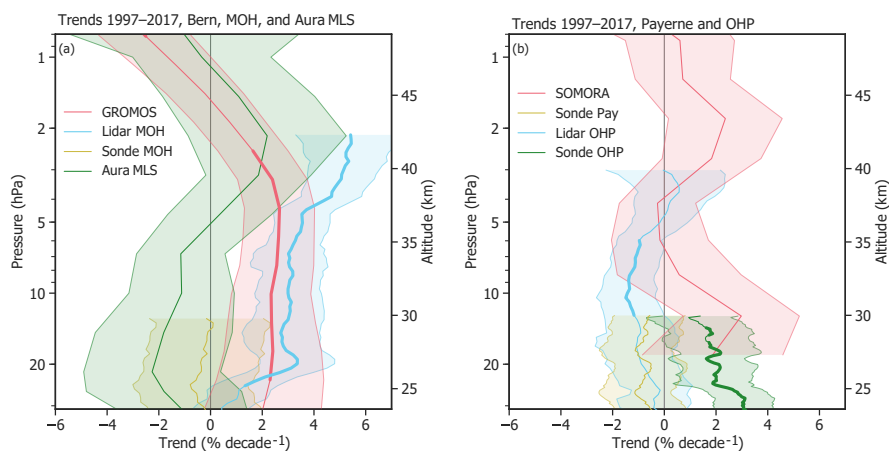


Figure 6.4: Ozone trends from ground-based instruments in central Europe and from Aura MLS data. GROMOS and SOMORA are MWRs located in Bern and Payerne; lidar and ozonesonde data are from Payerne, Hohenpeissenberg (MOH) and from the observatory of Haute Provence (OHP). Trends start in 1997, except for SOMORA (2000) and Aura MLS (2005).

— Adapted from Bernet et al. (2019a)

Finally, we compared our corrected GROMOS trend with trends derived from the other datasets in central Europe (Fig. 6.4). The datasets mostly agree on positive trends of 1 % to 3 % in the upper stratosphere, but differ in the lower stratosphere. The observed upper-stratospheric ozone trends are consistent with mainly satellite-based results at northern mid-latitudes from various studies (e.g. Ball et al., 2017; Frith et al., 2017; Sofieva et al., 2017; SPARC/IO₃C/GAW, 2019; Steinbrecht et al., 2017). The observed disagreement in lower-stratospheric trends

shows that further corrections for e.g. instrumental changes might be necessary. Further, it reflects the ongoing discussion on uncertain lower-stratospheric ozone trends, as mentioned in Section 2.1.3 (e.g. Ball et al., 2018; Chipperfield et al., 2018). We attribute the observed differences between the trend profiles to a combination of unconsidered drifts, different sampling rates, spatial distance of the measurement stations, and different starting years.

In summary, our results show that anomalies in ground-based time series affect stratospheric ozone trends. By comparing stratospheric ozone measurements from multiple techniques, we found anomalies in the GROMOS time series. We showed that accounting for these anomalies in the trend estimation improves the GROMOS trend. Further, our trend estimates confirm that ozone is recovering in the upper stratosphere over central Europe. Moreover, our conflicting results in the lower stratosphere emphasize the need for further investigations concerning lower-stratospheric ozone trends.

The study was published in *Atmospheric Chemistry and Physics* in April 2019 (see Appendix A.1).

FULL CITATION:

L. Bernet, T. von Clarmann, S. Godin-Beekmann, G. Ancellet, E. Maillard Barras, R. Stübi, W. Steinbrecht, N. Kämpfer and K. Hocke (Apr. 2019a). Ground-based ozone profiles over central Europe: incorporating anomalous observations into the analysis of stratospheric ozone trends. In: *Atmospheric Chemistry and Physics* 19.7, pp. 4289–4309. ISSN: 1680-7324. DOI: [10.5194/acp-19-4289-2019](https://doi.org/10.5194/acp-19-4289-2019)

7

STRATOSPHERIC OZONE TRENDS AT LAUDER, NEW ZEALAND

This chapter summarizes the study as given in Bernet et al. (2020a) (Appendix A.2).

Stratospheric ozone measurements on the southern hemisphere are rare. Further, ozone recovery in the middle and lower stratosphere is still not clear, as discussed previously (e.g. Section 2.1.3). Long-term and stable measurements at the NDACC station at Lauder in New Zealand are therefore invaluable. Recently, Lauder stratospheric ozone data have been used to derive trends in Steinbrecht et al.'s (2017) study and in the LOTUS report (SPARC/IO₃C/GAW, 2019). Steinbrecht et al. (2017) found upper-stratospheric ozone trends in the southern hemisphere between 0 and 4 % per decade, and small insignificant trends below. Similar results are reported in SPARC/IO₃C/GAW (2019), but with negative ozonesonde and FTIR trends at Lauder below 20 hPa. However, the time series of various ground-based instruments at Lauder have not been compared in detail to identify possible inhomogeneities. Nevertheless, this is required to assess their suitability for trend estimation. Moreover, the studies did not investigate how potential inhomogeneities in the data affect the trend estimates. Also, the data uncertainties have not been considered when estimating stratospheric ozone trends from ground-based data at Lauder.

The aim of the study presented here is

1. to verify whether Lauder ground-based time series are suitable for trend estimation,
2. to show whether data inhomogeneities and data uncertainties affect the trend estimates,
3. to compare trend results obtained from two different trend regression models.

7.1 RESEARCH APPROACH

The first aim of the study is achieved by comparing ground-based MWR (Section 4.1.1) and lidar data (Section 4.1.2) at Lauder with coincident Aura MLS data (Section 4.1.4) and ERA5 data. This makes

it possible to identify inhomogeneities in the data and to judge on the data quality for trend estimation.

To achieve the second and third aim of the study, two different regression models were used: the KIT model (von Clarmann et al. (2010), Section 5.2.1) and the LOTUS model (SPARC/IO₃C/GAW (2019), Section 5.2.2). To consider the data uncertainties when estimating trends, we weight the KIT regression with the monthly uncertainties of the data. In the LOTUS model, this weighting was not applied for the final trend results in the LOTUS report (SPARC/IO₃C/GAW, 2019). We therefore present weighted ground-based LOTUS trends at Lauder for the first time. To weight the regression, the diagonal elements of the error covariance matrix are set to the uncertainties of the different datasets (Section 5.2.1). The uncertainty profiles used are shown in Fig. 7.1. They consist of the measurement uncertainty (random and systematic errors) and the standard error of the monthly means.

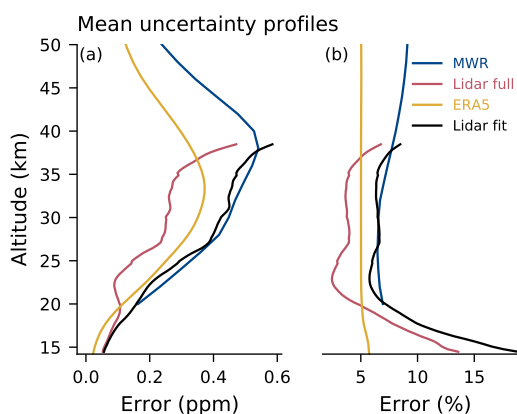


Figure 7.1: Mean uncertainty profiles used for the Lauder trends in (a) parts per million (ppm) and (b) percent.

In addition to the weighting, we use a bias correction in the KIT model. For this, a constant block in the error covariance matrix was set to the estimated bias uncertainty of the biased subblock, as described in Section 5.2.1. This process enables a fit of a potential bias from the data itself. Following this approach, the trend of lidar and ERA5 data was then estimated by correcting for observed inhomogeneities. We show lidar trends derived from the full data (*lidar full*), but also from lidar data with a seasonal fit (*lidar fit*) according to Wilhelm et al. (2019). This fit was applied because the sparse temporal lidar sampling might distort the monthly means.

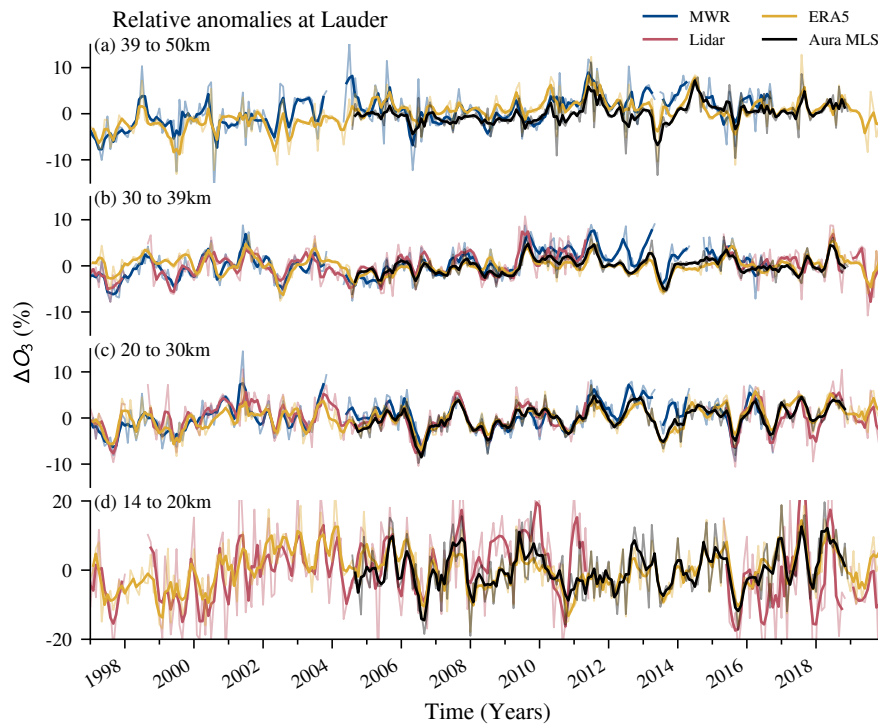


Figure 7.2: Monthly ozone anomalies at Lauder for MWR, lidar, Aura MLS, and ERA5 data for four altitude ranges. The anomalies describe the deviation from the monthly mean climatology from 1997 to 2019 ($(\text{data} - \text{climatology}) / \text{climatology}$). Bold lines show smoothed data with a moving window of three months.

— *Bernet et al. (2020a)*

7.2 SUMMARY OF THE STUDY

The comparison of the various datasets at Lauder reveals a remarkably good agreement on ozone anomalies (Fig. 7.2). The ozone anomalies show that ozone in Lauder varies naturally by around 10% in the middle and upper stratosphere. Only in the lower stratosphere variations are larger (Fig. 7.2d), which is expected due to larger dynamical influences in the lower stratosphere. The agreement of various datasets on the ozone anomalies indicates that the anomalies are of natural origin.

By comparing coincident profiles of MWR, lidar, and ERA5 data, we identified changes in ERA5 data in 2004 and in 2015, and small lidar changes after a data gap in 2014. Furthermore, we found that ERA5 substantially underestimates ozone in the upper stratosphere (40 km to 50 km).

We found that using weighted LOTUS regression (Fig. 7.3b) changes the trend estimates compared to the unweighted estimates (Fig. 7.3a). The weighted regression leads to a close agreement between the

weighted MWR and lidar trends (Fig. 7.3b). However, the weighted lidar trend without seasonal fit ("lidar full") varies vertically in Fig. 7.3b. Further investigations about LOTUS model adjustments might thus be required when using the weighted LOTUS regression. When using the KIT model, we observe that the lidar and ERA₅ trends better agree with the MWR trends in case that the identified inhomogeneities were considered (Fig. 7.3d), compared to the uncorrected trends (Fig. 7.3c).

Generally, the Lauder data report ozone trends in the middle and upper stratosphere between 0% and 5% per decade, whereas the lidar and MWR agree on trends between 2% and 3% per decade in this altitude region. These results are consistent with earlier studies (e.g. Nair et al., 2015; SPARC/IO₃C/GAW, 2019; Vigouroux et al., 2015).

To summarize, we showed that the Lauder datasets agree well, and that the Lauder MWR and lidar data are suitable for trend estimates. Further, our analyses showed that treating data inhomogeneities and data uncertainties in the regression affects the calculated trends. In addition, both trend models (KIT and LOTUS) deliver similar ozone trend profiles. However, the consideration of uncertainties and inhomogeneities affect the trends differently.

The study was submitted to *Remote Sensing* in October 2020 (see Appendix A.2).

FULL CITATION:

L. Bernet, I. Boyd, G. Nedoluha, R. Querel, D. Swart and K. Hocke (2020a). Validation and trend analysis of stratospheric ozone data from ground-based observations at Lauder, New Zealand. In: *Remote Sensing* in review, pp. 1–14

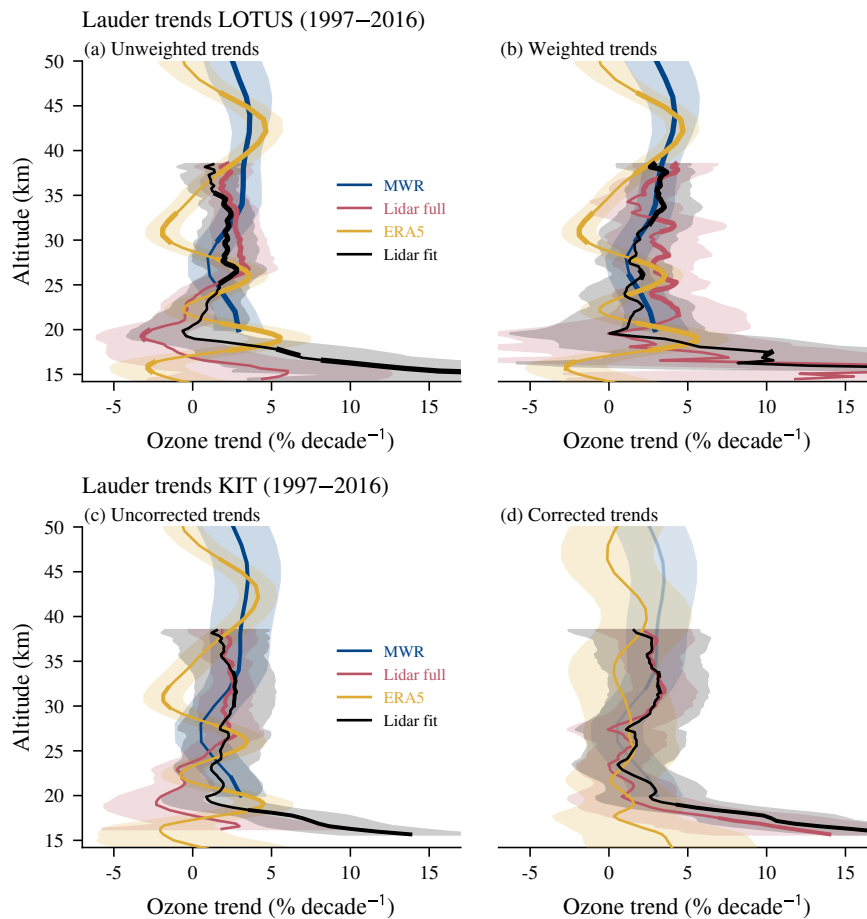


Figure 7.3: Ozone trends at Lauder for MWR, lidar (full and with seasonal fit), and ERA₅ data, using (a) the unweighted LOTUS regression, (b) the weighted LOTUS regression, (c) the KIT regression, and (d) the KIT regression with bias correction. The shading represents 2-standard-deviation uncertainties.

— Adapted from Bernet et al. (2020a)

8

TRENDS OF INTEGRATED WATER VAPOUR IN SWITZERLAND

This chapter summarizes the study published in Bernet et al. (2020c) (Appendix A.3).

Atmospheric water vapour is closely linked to temperature according to the Clausius–Clapeyron relation, as described in Section 2.2.1. Several studies showed spatial correlations between changes in IWV and temperature, especially over oceans (e.g. Trenberth et al., 2005; Wang et al., 2016; Wentz and Schabel, 2000). Other studies report that large regional differences exist, and that water vapour scales not everywhere to temperature as expected (e.g. Chen and Liu, 2016; O’Gorman and Muller, 2010; Wagner et al., 2006; Wang et al., 2016). Multiple studies using satellite data report global IWV trends between 1 and 2 % per decade (e.g. Hartmann et al., 2013; Ho et al., 2018; Zhang et al., 2018). However, they also report large spatial trend differences between various regions. Regional analyses of IWV changes are thus required. Satellite data have some limitations for regional IWV trend analyses, not only due to their limited spatial resolution, but also because of missing harmonization across changing satellite platforms (e.g. Hartmann et al., 2013). Stable long-term measurements from ground are therefore ideal for regional IWV trend analyses.

IWV trends from ground-based GNSS measurements in Europe have been presented by Alshawaf et al. (2017) and Nilsson and Elgered (2008), who observed differences between trends at various stations. In Switzerland, IWV trends at some single stations have been discussed (Hicks-Jalali et al., 2020; Hocke et al., 2011; 2016; Morland et al., 2009; Nyeki et al., 2019; Sussmann et al., 2009), but most of them used shorter time series than available today. An update is essential, especially because of the strong temperature increase in Switzerland in recent years (NCCS, 2018). Moreover, none of these studies presents IWV trends from ground-based measurements for the whole of Switzerland.

Therefore, the aims of the study described in this chapter are

1. to present ground-based IWV trends in Switzerland obtained from multiple techniques and reanalyses data,
2. to verify whether water vapour increases as expected from observed temperature changes.

8.1 RESEARCH APPROACH

To achieve the first aim of the study, we compared data from the MWR TROWARA (Section 4.2.1), from a FTIR spectrometer (Section 4.2.2), from the Swiss GNSS network (Section 4.2.3), and from reanalysis model data, and determined trends for all datasets. We used the KIT trend model as described in Section 5.2.1. To obtain optimal estimates of the IWV trends, we considered instrumental jumps in the GNSS data when estimating trends. For this, a constant block was set in the measurement covariance matrix so that the trend programme fits a bias to the subset of data after the instrumental change (see Section 5.2.1). The approach of bias correction is illustrated in Fig. 8.1. This correction is important, because GNSS measurements are highly sensitive to changes in the setup, as discussed in Section 3.3.3. Jumps in the GNSS data occur for example after antenna changes but also after changes in the environment surrounding the station (Pacione et al., 2017).

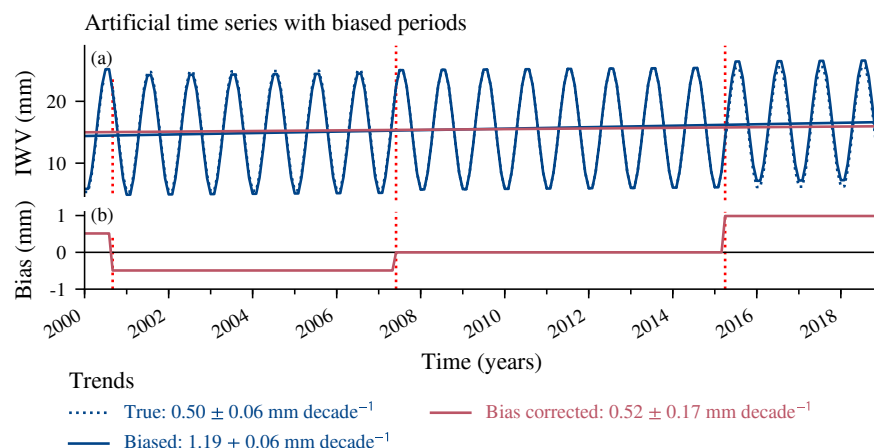


Figure 8.1: Illustration of the bias correction with an artificial time series, with added biases after virtual instrument changes (vertical red dashed lines). Panel (b) shows biases that have been fit from the data. The bias-corrected trend is substantially improved compared to the biased, uncorrected trend. — *Bernet et al. (2020c)*

To respond to the second aim of the study, we derived the theoretical change in IWV from reanalysis temperature data. We determined the fractional change in saturation vapour pressure for a given temperature change according to Eq. 2.3. The temperature change within the study period was determined from reanalyses data. The resulting change in saturation vapour pressure represents the change in water vapour that is only due to temperature changes, assuming that the relative humidity (RH) remains constant. Comparing these values with observed IWV changes gives therefore information about the validity of the temperature–water vapour correlation in Switzerland.

8.2 SUMMARY OF THE STUDY

We compared IWV data from TROWARA with GNSS stations around Bern and reanalysis data. The comparison showed a good agreement within 5 % between TROWARA and the other datasets. Further, we validated for the first time the long-term IWV time series from the FTIR spectrometer at Jungfraujoch with collocated GNSS measurements (Fig. 8.2). The results indicate an FTIR agreement of 15 % with coincident GNSS data, with a small dry bias of GNSS data compared to FTIR. This dry bias at Jungfraujoch was also observed in previous studies (Guerova et al., 2003; Haefele et al., 2004; Morland et al., 2006; Nyeki et al., 2005) and is probably due to the missing GNSS antenna calibration before 2016. Indeed, we found that the bias was reduced to 4 % after a GNSS antenna update in 2016. Furthermore, the comparison illustrates an FTIR clear-sky bias of around 1 mm due to the measurement restrictions to clear-sky conditions (Fig. 8.2c).

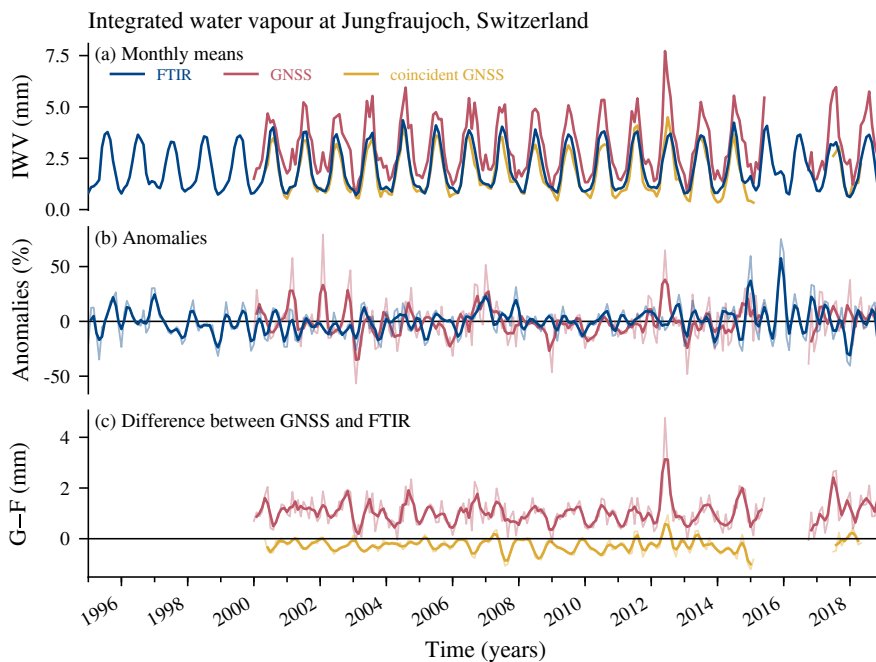


Figure 8.2: (a) Monthly means of IWV at Jungfraujoch from the FTIR spectrometer and GNSS measurements, for all and coincident GNSS measurements. (b) Anomalies from the climatology ($(\text{data} - \text{climatology}) / \text{climatology}$) for FTIR data and fully sampled GNSS data. (c) Differences between GNSS (G) and FTIR (F) data for all and coincident GNSS data. Bold lines show smoothed data with a moving mean window of three months.

— *Bernet et al. (2020c)*

The derived IWV trends for all GNSS stations in Switzerland report generally an increase in IWV between 2 to 5 % per decade, but vary between different stations, especially in mountainous regions (Fig. 8.3).

Over the whole year, only three stations show negative trends that are, however, insignificant. Significant positive trends are observed at six stations, mostly in summer.

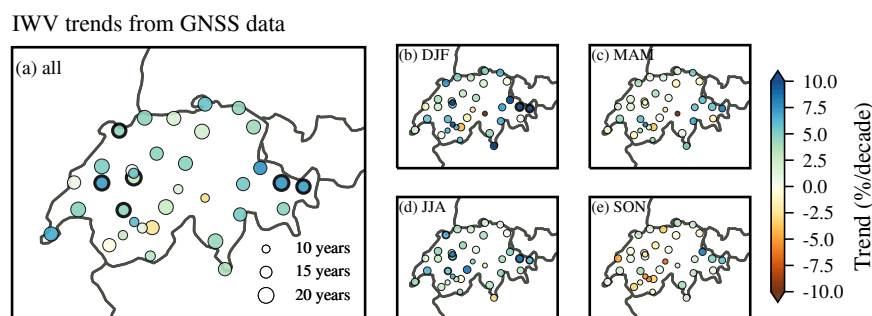


Figure 8.3: IWV trends from GNSS data in Switzerland for (a) the whole year, and the four seasons (b) to (e). The marker size indicates the length of the GNSS time series, bold edges mark stations with trends that are significantly different from zero (95% confidence).
— Bernet *et al.* (2020c)

Finally, we showed that the IWV increase generally follows the observed temperature changes, except in winter. However, the winter trends are not significantly different from zero, which prevents us from drawing solid conclusions about temperature-related IWV changes in winter. Moreover, we found positive, but insignificant RH trends from ERA5 data in winter, suggesting that the assumption of constant RH might not always be valid. This makes it more challenging to attribute changes in IWV to temperature changes.

In summary, we showed that water vapour in Switzerland mostly increased during the last decades, which is consistent with observed warming trends. Furthermore, we presented regional IWV trends in Switzerland and showed that the bias correction within the KIT trend model is well suited to reduce biases due to GNSS antenna updates. Our results illustrate that homogeneously reprocessed GNSS data enable monitoring regional water vapour changes in a changing climate.

The study was published in *Atmospheric Chemistry and Physics* in October 2020 (see Appendix A.3).

FULL CITATION:

L. Bernet, E. Brockmann, T. von Clarmann, N. Kämpfer, E. Mahieu, C. Mätzler, G. Stober and K. Hocke (2020c). Trends of atmospheric water vapour in Switzerland from ground-based radiometry, FTIR and GNSS data. In: *Atmospheric Chemistry and Physics* 20.19, pp. 11223–11244. DOI: [10.5194/acp-20-11223-2020](https://doi.org/10.5194/acp-20-11223-2020)

9

CONCLUSIONS

This thesis had the aim of obtaining consistent trends of stratospheric ozone and integrated water vapour (IWV) at mid-latitudes derived from ground-based measurements. For this purpose, we intercompared data from multiple ground-based techniques together with reanalysis model and Aura *MLS* satellite data. This made it possible to identify anomalies, biases and inhomogeneities in the data. We found that such irregularities affect trend estimates, and presented an approach to account for them when estimating trends. Using this approach, we presented optimized ozone and IWV trend estimates over almost three decades.

The thesis consists of three studies on stratospheric ozone and IWV trends. In the first study, we identified anomalies in ozone measurements of the *GROMOS* radiometer and introduced the approach to account for these anomalies when estimating trends. The approach is based on von Clarmann et al.'s (2010) work and consists in adapting the full observational covariance matrix in the *KIT* regression model to account for anomalous observations. As a result, we obtained an improved *GROMOS* trend estimate. Furthermore, we presented stratospheric ozone trends over central Europe obtained from microwave radiometers, lidars, and ozonesondes. These trends were generally consistent with satellite ozone trends from other studies. We detected an ozone recovery in the upper stratosphere while trends in the lower stratosphere were not always consistent.

In the second study, we presented ozone measurements from ground-based lidar and *MWR*, *Aura MLS*, and *ERA5* reanalysis data at Lauder, New Zealand. We observed that all datasets agree on a number of anomalies, indicating that they are due to natural variability. Moreover, we showed that although ground-based ozone data at Lauder are suitable for trend estimation, the consideration of data inhomogeneities and data uncertainties affect the ozone trend estimates. We found positive ozone trends at Lauder in the upper stratosphere, consistent with other studies. Furthermore, we compared the *KIT* and the *LOTUS* trend models and found a good agreement between both, although some differences occur at specific altitudes.

In the final study, we presented IWV trends in Switzerland based on *MWR*, *FTIR*, *GNSS*, and reanalysis data. We found that water vapour

generally increased as expected from observed temperature changes. However, the IWV trends vary regionally, especially in mountainous regions. Moreover, we showed that the dense GNSS measurement network has the potential to monitor regional IWV changes and presented bias-corrected GNSS trends. To correct for biases caused by GNSS antenna updates, we used correlated blocks in the covariance matrix within the KIT regression, which was successfully tested with an artificial time series.

The approach to account for anomalies and inhomogeneities when estimating trends is a step towards improved trend estimates of stratospheric ozone and IWV. Generally, it is relevant for many areas in climate research, as instrumental problems are a common challenge when determining long-term trends. Whereas biases and drifts have been considered in several satellite ozone trend studies (e.g. Bourassa et al., 2018; Eckert et al., 2014), ground-based ozone trends (e.g. SPARC/IO₃C/GAW, 2019; Steinbrecht et al., 2017) were generally not corrected for biases or data inhomogeneities. Further, the comprehensive LOTUS report presents ground-based ozone trends (SPARC/IO₃C/GAW, 2019), but does not investigate how data uncertainties and inhomogeneities affect the resulting trend estimates. This thesis filled these gaps by presenting stratospheric ozone trends that account for inhomogeneities and uncertainties in the data. In addition, applying the approach on GNSS based IWV data showed that bias-corrected GNSS-derived trends provide a reliable source to estimate regional IWV changes. This is important, because many studies revealed that IWV trends and their relation to temperature changes differ regionally (e.g. Chen and Liu, 2016; Wang et al., 2016).

To conclude, this thesis presented and intercompared stratospheric ozone and IWV observations from multiple measurement techniques. Natural and instrument-specific anomalies could be distinguished in order to obtain optimized trend estimates that account for instrument-specific inhomogeneities. Therefore, the approach presented in this thesis helps to clarify inconsistencies between trends from different ground-based datasets. Consequently, the thesis contributes to a better understanding of the evolution of ozone and water vapour in a changing climate.

9.1 RECOMMENDATIONS AND OUTLOOK

This thesis has focused on selected ground-based remote sensing datasets at mid-latitudes. The analysis could be extended to further datasets in future studies. In the study on European ozone trends, we used the bias correction only for GROMOS trends. It would be interesting to apply this approach also to the other ground-based datasets in

central Europe. Moreover, the Lauder ozone study could be extended by including additional collocated ground-based measurements (FTIR, ozonesondes, and Umkehr data) and by comparing the ground-based trends with coincident satellite trends.

Our study on IWV trends proved the quality of the GNSS derived IWV data. However, some updates in the IWV algorithm might further improve the IWV data, including improved mean temperature estimates and updated refractivity coefficients (e.g. Bock et al., 2020). Moreover, it would be interesting to further analyse the correlation between changes in temperature profile measurements and observed IWV changes, using data from radiosondes or microwave radiometers.

The results of this thesis build the basis for new investigations and further improvements to obtain optimal ozone trend estimates from ground-based MWRs. We identified anomalies in the GROMOS time series and observed trend differences to the SOMORA radiometer. These observations led to a new PhD project that aims to homogenize the time series of the two microwave radiometers. For this purpose, the calibration and retrieval procedures are currently improved and harmonized.

Possible areas for further research could be the detailed analysis of lower-stratospheric ozone to explain the differences in observed trends. For this purpose, it would be interesting to analyse changes in the tropopause height (using e.g. temperature measurements) and how it affects ozone at a specific measurement station. Finally, it is relevant to investigate ground-based ozone trends also outside of mid-latitudes. To this end, I will investigate total ozone trends in the Arctic from ground-based measurements within a postdoctoral research stay at the NILU institute in Oslo, Norway.

BIBLIOGRAPHY

- A. W. Brewer (Oct. 1949). Evidence for a world circulation provided by the measurements of helium and water vapour distribution in the stratosphere. In: *Quarterly Journal of the Royal Meteorological Society* 75.326, pp. 351–363. ISSN: 00359009. DOI: [10.1002/qj.49707532603](https://doi.org/10.1002/qj.49707532603).
- Ahrens, C. D. (2009). Meteorology Today: An Introduction to Weather, Climate, and the Environment Ninth Edition. In: *Meteorology Today: An Introduction to Weather, Climate, and the Environment Ninth Edition*. ISBN: 9780495555735.
- Alshawaf, F., K. Balidakis, G. Dick, S. Heise and J. Wickert (2017). Estimating trends in atmospheric water vapor and temperature time series over Germany. In: *Atmospheric Measurement Techniques* 10.9, pp. 3117–3132. DOI: [10.5194/amt-10-3117-2017](https://doi.org/10.5194/amt-10-3117-2017).
- Bai, K., N.-B. Chang, R. Shi, H. Yu and W. Gao (2017). An inter-comparison of multi-decadal observational and reanalysis data sets for global total ozone trends and variability analysis. In: *Journal of Geophysical Research: Atmospheres* 122.13, pp. 1–21. ISSN: 2169897X. DOI: [10.1002/2016JD025835](https://doi.org/10.1002/2016JD025835).
- Ball, W. T., E. V. Rozanov, J. Alsing, D. R. Marsh, F. Tummon, D. J. Mortlock, D. Kinnison and J. D. Haigh (2019a). The Upper Stratospheric Solar Cycle Ozone Response. In: *Geophysical Research Letters* 46.3, pp. 1831–1841. ISSN: 19448007. DOI: [10.1029/2018GL081501](https://doi.org/10.1029/2018GL081501).
- Ball, W. T., J. Alsing, D. J. Mortlock, E. V. Rozanov, F. Tummon and J. D. Haigh (2017). Reconciling differences in stratospheric ozone composites. In: *Atmospheric Chemistry and Physics* 17.March, pp. 12269–12302. DOI: [10.5194/acp-2017-142](https://doi.org/10.5194/acp-2017-142).
- Ball, W. T., J. Alsing, D. J. Mortlock, J. Staehelin, J. D. Haigh, T. Peter, F. Tummon, R. Stübi, A. Stenke, J. Anderson, A. Bourassa, S. M. Davis, D. Degenstein, S. M. Frith, L. Froidevaux, C. Roth, V. Sofieva, R. Wang, J. Wild, P. Yu, J. R. Ziemke and E. V. Rozanov (2018). Evidence for continuous decline in lower stratospheric ozone offsetting ozone layer recovery. In: *Atmospheric Chemistry and Physics* 18, pp. 1379–1394. DOI: [10.5194/acp-18-1379-2018](https://doi.org/10.5194/acp-18-1379-2018).
- Ball, W. T., J. Alsing, J. Staehelin, S. M. Davis, L. Froidevaux and T. Peter (2019b). Stratospheric ozone trends for 1985–2018: Sensitivity to recent large variability. In: *Atmospheric Chemistry and Physics* 19.19, pp. 12731–12748. ISSN: 16807324. DOI: [10.5194/acp-19-12731-2019](https://doi.org/10.5194/acp-19-12731-2019).
- Ball, W. T., G. Chiodo, M. Abalos, J. Alsing and A. Stenke (Aug. 2020). Inconsistencies between chemistry–climate models and observed lower stratospheric ozone trends since 1998. In: *Atmospheric Chemistry and Physics* 20.16, pp. 9737–9752. ISSN: 1680-7324. DOI: [10.5194/acp-20-9737-2020](https://doi.org/10.5194/acp-20-9737-2020).
- Bates, D. R. and M. Nicolet (Sept. 1950). The photochemistry of atmospheric water vapor. In: *Journal of Geophysical Research* 55.3, pp. 301–327. ISSN: 01480227. DOI: [10.1029/JZ055i003p00301](https://doi.org/10.1029/JZ055i003p00301).
- Bekki, S. and J. Savarino (2016). Ozone and Stratospheric Chemistry. In: *Encyclopedia of Geochemistry*. January, pp. 1–12. ISBN: 978-3-319-39193-9. DOI: [10.1007/978-3-319-39193-9_207-1](https://doi.org/10.1007/978-3-319-39193-9_207-1).
- Bernet, L., I. Boyd, G. Nedoluha, R. Querel, D. Swart and K. Hocke (2020a). Validation and trend analysis of stratospheric ozone data from ground-based observations at Lauder, New Zealand. In: *Remote Sensing* in review, pp. 1–14.
- Bernet, L., E. Brockmann, T. von Clarmann, N. Kämpfer, E. Mahieu, C. Mätzler, G. Stober and K. Hocke (2020b). Interactive comment on “Trends of atmospheric water vapour in Switzerland from ground-based radiometry, FTIR and GNSS data”. In: *Atmospheric Chemistry and Physics Discussions*. DOI: <https://doi.org/10.5194/acp-2020-77-AC1,.>

- Bernet, L., E. Brockmann, T. von Clarmann, N. Kämpfer, E. Mahieu, C. Mätzler, G. Stober and K. Hocke (2020c). Trends of atmospheric water vapour in Switzerland from ground-based radiometry, FTIR and GNSS data. In: *Atmospheric Chemistry and Physics* 20.19, pp. 11223–11244. DOI: [10.5194/acp-20-11223-2020](https://doi.org/10.5194/acp-20-11223-2020).
- Bernet, L., T. von Clarmann, S. Godin-Beekmann, G. Ancellet, E. Maillard Barras, R. Stübi, W. Steinbrecht, N. Kämpfer and K. Hocke (Apr. 2019a). Ground-based ozone profiles over central Europe: incorporating anomalous observations into the analysis of stratospheric ozone trends. In: *Atmospheric Chemistry and Physics* 19.7, pp. 4289–4309. ISSN: 1680-7324. DOI: [10.5194/acp-19-4289-2019](https://doi.org/10.5194/acp-19-4289-2019).
- (2019b). Interactive comment on “Ozone trend profiles in the stratosphere: combining ground-based data over Central Europe to consider uncertainties” by Leonie Bernet et al. In: *Atmospheric chemistry and physics Discussion*. DOI: <https://doi.org/10.5194/acp-2018-1213-AC1>.
- Bevis, M., S. Businger, T. A. Herring, C. Rocken, R. A. Anthes and R. H. Ware (1992). GPS meteorology: Remote sensing of atmospheric water vapor using the global positioning system. In: *Journal of Geophysical Research* 97.D14, pp. 15787–15801. ISSN: 0148-0227. DOI: [10.1029/92JD01517](https://doi.org/10.1029/92JD01517).
- Bindoff, N., P. Stott, K. AchutaRao, M. Allen, N. Gillett, D. Gutzler, K. Hansingo, G. Hegerl, Y. Hu, S. Jain, I. Mokhov, J. Overland, J. Perlwitz, R. Sebbari and X. Zhang (2013). Detection and Attribution of Climate Change: from Global to Regional. In: *Climate Change 2013: The Physical Science Basis. Contribution of Working Group I to the Fifth Assessment Report of the Intergovernmental Panel on Climate Change*. Ed. by T. Stocker, D. Qin, G.-K. Plattner, M. Tignor, S. Allen, J. Boschung, A. Nauels, Y. Xia, V. Bex and P. Midgley. Cambridge, United Kingdom and New York, NY, USA: Cambridge University Press, pp. 867–952. DOI: [10.1017/CB09781107415324.022](https://doi.org/10.1017/CB09781107415324.022).
- Bock, O., R. Pacione, F. Ahmed, A. Araszkievicz, Z. Baldysz, K. Balidakis, C. Barroso, S. Bastin, S. Beirle, J. Berckmans, J. Böhm, J. Bogusz, M. Bos, E. Brockmann, M. Cadeddu, B. Chimani, J. Douša, G. Elgered, M. Eliaš, R. Fernandes, M. Figurski, E. Fionda, M. Gruszczynska, G. Guerova, J. Guijarro, C. Hackman, R. Heinkelmann, J. Jones, S. Zengin Kazancı, A. Klos, D. Landskron, J. P. Martins, V. Mattioli, B. Mircheva, S. Nahmani, R. T. Nilsson, T. Ning, G. Nykiel, A. Parracho, E. Pottiaux, A. Ramos, P. Rebischung, A. Sá, W. Dorigo, H. Schuh, G. Stankunavicius, K. Stepniak, H. Valentim, R. V. Malderen, P. Viterbo, P. Willis and A. Xaver (2020). Use of GNSS Tropospheric Products for Climate Monitoring (Working Group 3). In: *Advanced GNSS Tropospheric Products for Monitoring Severe Weather Events and Climate*. Ed. by J. Jones et al. Springer Nature Switzerland AG. ISBN: 9783030139018. DOI: [10.1007/978-3-030-13901-8_5](https://doi.org/10.1007/978-3-030-13901-8_5).
- Bourassa, A. E., C. Z. Roth, D. J. Zawada, L. A. Rieger, C. A. McLinden and D. A. Degenstein (2018). Drift-corrected Odin-OSIRIS ozone product: Algorithm and updated stratospheric ozone trends. In: *Atmospheric Measurement Techniques* 11.1, pp. 489–498. ISSN: 18678548. DOI: [10.5194/amt-11-489-2018](https://doi.org/10.5194/amt-11-489-2018).
- Braesicke, P., Neu, J. (Lead authors), V. Fioletov, S. Godin-Beekmann, D. Hubert, I. Petropavlovskikh, M. Shiotani, W. Ball, K.-L. Chang, R. Damadeo, S. Dhomse, S. Frith, A. Gaudel, B. Hassler, R. Hossaini, S. Kremser, S. Misios, O. Morgenstern, R. Salawitch, V. Sofieva, K. Tourpali, O. Tweedy and D. Zawada (2018). Update on Global ozone: past, present, and Future. In: *Scientific Assessment of Ozone Depletion: 2018*. Geneva, Switzerland: Global Ozone Research and Monitoring Project–Report No. 58, World Meteorological Organization. Chap. 3. URL: https://www.esrl.noaa.gov/csl/assessments/ozone/2018/%20downloads/Chapter3%5C_20180zoneAssessment.pdf.
- Brasseur, G. P. (1999). Middle Atmospheric Ozone. In: *Atmospheric Chemistry and Global Change*. New York: Oxford University Press. Chap. 14, pp. 487–514. ISBN: 0195105214.
- Brasseur, G. P. and S. Solomon (2005a). *Aeronomy of the Middle Atmosphere: Chemistry and Physics of the Stratosphere and Mesosphere*. 3rd ed. Vol. 32. Atmospheric and Oceanographic Sciences Library. Dordrecht: Springer Netherlands. ISBN: 978-1-4020-3284-4. DOI: [10.1007/1-4020-3824-0](https://doi.org/10.1007/1-4020-3824-0).

- (2005b). ‘Composition and Chemistry’. In: *Aeronomy of the Middle Atmosphere*. Dordrecht: Springer Netherlands, pp. 265–442. ISBN: 978-1-4020-3824-2. DOI: [10.1007/1-4020-3824-0_5](https://doi.org/10.1007/1-4020-3824-0_5).
- Brewer, A. W. and J. R. Milford (1960). ‘The Oxford-Kew Ozone Sonde’. In: *Proceedings of the Royal Society of London. Series A, Mathematical and Physical Sciences*. Vol. 256. 1287. Royal Society, pp. 470–495. URL: <http://www.jstor.org/stable/2413928>.
- Brinksma, E. J., D. P. J. Swart, J. B. Bergwerff, Y. J. Meijer and F. T. Ormel (1997). RIVM Stratospheric Ozone Lidar at NDSC Station Lauder: Routine Measurements and Validation During the OPAL Campaign. In: *Advances in Atmospheric Remote Sensing with Lidar* December 1994, pp. 529–532. DOI: [10.1007/978-3-642-60612-0_128](https://doi.org/10.1007/978-3-642-60612-0_128).
- Brockmann, E. (2015). *Reprocessed GNSS tropospheric products at swisstopo*. GNSS4SWEC workshop, Thessaloniki, May 11-14 2015.
- Brockmann, E., S. Grünig, R. Hug, D. Schneider, A. Wiget and U. Wild (2001a). National Report of Switzerland Introduction and first applications of a Real-Time Precise Positioning Service using the Swiss Permanent Network. In: *Subcommission for the European Reference Frame (EUREF). EUREF Publication No. 10*. Ed. by J. Torres and H. Hornik. Frankfurt am Main 2002: Mitteilungen des Bundesamtes für Kartographie und Geodäsie, Vol. 23, pp. 272–276. URL: http://www.euref.eu/symposia/book2001/nr%5C%5C%5C_28.PDF.
- Brockmann, E., G. Guerova and M. Troller (2001b). Swiss Activities in Combining GPS with Meteorology. In: *Subcommission for the European Reference Frame (EUREF). EUREF Publication No. 10*. Ed. by J. Torres and H. Hornik. Frankfurt am Main 2002: Mitteilungen des Bundesamtes für Kartographie und Geodäsie, Vol. 23, pp. 95–99. URL: http://www.euref.eu/symposia/book2001/2%5C_6.pdf.
- Brockmann, E., D. Andrey, D. Ineichen, L. Kislig, J. Liechti, S. Lutz, C. Misslin, S. Schaer and U. Wild (2016). Automated GNSS Network Switzerland (AGNES). In: International Foundation HFSJG, Activity Report 2016. URL: https://www.hfsjg.ch/wordpress/reports/2016/%20137%5C_Swisstopo%5C_Brockmann.pdf.
- Brockmann, E. (2001). ‘Positionierungsdienste und Geodaten des Schweizerischen Bundesamtes für Landestopographie’. In: *Tagungsband - POSNAV 2001, DGON-Symposium Positionierung und Navigation: 6. bis 8. März 2001, Dresden*. Bonn: DGON.
- Brönnimann, S. (2013). *Ozon in der Atmosphäre*. Bern, Switzerland: Geographica Bernensia, Verlag Paul Haupt. ISBN: 3258064377.
- Buehler, S. A., J. Mendrok, P. Eriksson, A. Perrin, R. Larsson and O. Lemke (Apr. 2018). ARTS, the Atmospheric Radiative Transfer Simulator – version 2.2, the planetary toolbox edition. In: *Geoscientific Model Development* 11.4, pp. 1537–1556. ISSN: 1991-9603. DOI: [10.5194/gmd-11-1537-2018](https://doi.org/10.5194/gmd-11-1537-2018).
- Butchart, N. and A. A. Scaife (2001). Removal of chlorofluorocarbons by increased mass exchange between the stratosphere and troposphere in a changing climate. In: *Nature* 410.6830, pp. 799–802. ISSN: 00280836. DOI: [10.1038/35071047](https://doi.org/10.1038/35071047).
- Butchart, N. (2014). Reviews of Geophysics The Brewer-Dobson circulation. In: *Rev. Geophys* 52, pp. 157–184. ISSN: 19449208. DOI: [10.1002/2013RG000448](https://doi.org/10.1002/2013RG000448).
- Chapman, S. (1930). A Theory of Atmospheric Ozone. In: *Royal Meteorological Society Memoirs* 3, pp. 103–125.
- Chen, B. and Z. Liu (2016). Global water vapor variability and trend from the latest 36 year (1979 to 2014) data of ECMWF and NCEP reanalyses, radiosonde, GPS, and microwave satellite. In: *Journal of Geophysical Research* 121.19, pp. 11442–11462. ISSN: 21562202. DOI: [10.1002/2016JD024917](https://doi.org/10.1002/2016JD024917).
- Chipperfield, M. P. (2012). Mid-latitude Ozone Depletion. In: *Stratospheric Ozone Depletion and Climate Change*. Ed. by R. Müller. Cambridge: Royal Society of Chemistry. Chap. 6, pp. 169–189. DOI: [10.1039/9781849733182-00169](https://doi.org/10.1039/9781849733182-00169).
- Chipperfield, M. P., S. Dhomse, R. Hossaini, W. Feng, M. L. Santee, M. Weber, J. P. Burrows, J. D. Wild, D. Loyola and M. Coldewey-Egbers (2018). On the Cause of Recent Variations in Lower Stratospheric Ozone. In: *Geophysical Research Letters* 45, pp. 5718–5726. ISSN: 00948276. DOI: [10.1029/2018GL078071](https://doi.org/10.1029/2018GL078071).

- Christian, C. and J.-R. Roy (2017). 'Telescopes'. In: *A Question and Answer Guide to Astronomy*. 2nd ed. Cambridge University Press, pp. 253–272. DOI: [10.1017/9781316681558.009](https://doi.org/10.1017/9781316681558.009).
- Collins, M., R. Knutti, J. Arblaster, J. Dufresne, T. Fichefet, P. Friedlingstein, X. Gao, W. Gutowski, T. Johns, G. Krinner, M. Shongwe, C. Tebaldi, A. Weaver and M. Wehner (2013). Long-term Climate Change: Projections, Commitments and Irreversibility. In: *Climate Change 2013: The Physical Science Basis. Contribution of Working Group I to the Fifth Assessment Report of the Intergovernmental Panel on Climate Change*. Ed. by T. Stocker, D. Qin, G.-K. Plattner, M. Tignor, S. Allen, J. Boschung, A. Nauels, Y. Xia, V. Bex and P. Midgley. Cambridge, United Kingdom and New York, NY, USA: Cambridge University Press. Chap. 12, pp. 1029–1136. DOI: [10.1017/CB09781107415324.024](https://doi.org/10.1017/CB09781107415324.024).
- Crutzen, P. J. (1999). Global Problems of Atmospheric Chemistry — The Story of Man's Impact on Atmospheric Ozone. In: *Atmospheric Environmental Research*. Ed. by D. Möller. Berlin, Heidelberg: Springer Berlin Heidelberg. Chap. 1, pp. 3–30. ISBN: 978-3-642-58382-7. DOI: [10.1007/978-3-642-58382-7_1](https://doi.org/10.1007/978-3-642-58382-7_1).
- (Apr. 1970). The influence of nitrogen oxides on the atmospheric ozone content. In: *Quarterly Journal of the Royal Meteorological Society* 96.408, pp. 320–325. ISSN: 00359009. DOI: [10.1002/qj.49709640815](https://doi.org/10.1002/qj.49709640815).
- Damadeo, R. P., J. M. Zawodny and L. W. Thomason (2014). Reevaluation of stratospheric ozone trends from SAGE II data using a simultaneous temporal and spatial analysis. In: *Atmospheric Chemistry and Physics* 14.24, pp. 13455–13470. ISSN: 16807324. DOI: [10.5194/acp-14-13455-2014](https://doi.org/10.5194/acp-14-13455-2014).
- Damadeo, R. P., J. M. Zawodny, E. E. Remsburg and K. A. Walker (2018). The Impact of Non-uniform Sampling on Stratospheric Ozone Trends Derived from Occultation Instruments. In: *Atmospheric Chemistry and Physics* 18.1, pp. 535–554. DOI: [10.5194/acp-2017-575](https://doi.org/10.5194/acp-2017-575).
- De Mazière, M., A. M. Thompson, M. J. Kurylo, J. D. Wild, G. Bernhard, T. Blumensstock, G. O. Braathen, J. W. Hannigan, J.-c. Lambert, T. Leblanc, T. J. McGee, G. Nedoluha, I. Petropavlovskikh, G. Seckmeyer, P. C. Simon, W. Steinbrecht and S. E. Strahan (Apr. 2018). The Network for the Detection of Atmospheric Composition Change (NDACC): history, status and perspectives. In: *Atmospheric Chemistry and Physics* 18.7, pp. 4935–4964. ISSN: 1680-7324. DOI: [10.5194/acp-18-4935-2018](https://doi.org/10.5194/acp-18-4935-2018).
- Deshler, T., J. L. Mercer, H. G. J. Smit, R. Stubi, G. Levrat, B. J. Johnson, S. J. Oltmans, R. Kivi, A. M. Thompson, J. Witte, J. Davies, F. J. Schmidlin, G. Brothers and T. Sasaki (2008). Atmospheric comparison of electrochemical cell ozonesondes from different manufacturers, and with different cathode solution strengths: The Balloon Experiment on Standards for Ozonesondes. In: *Journal of Geophysical Research Atmospheres* 113.4, pp. 1–17. ISSN: 01480227. DOI: [10.1029/2007JD008975](https://doi.org/10.1029/2007JD008975).
- Diallo, M., M. Riese, T. Birner, P. Konopka, R. Müller, M. I. Hegglin, M. L. Santee, M. Baldwin, B. Legras and F. Ploeger (2018). Response of stratospheric water vapor and ozone to the unusual timing of El Niño and the QBO disruption in 2015–2016. In: *Atmospheric Chemistry and Physics* 18.17, pp. 13055–13073. ISSN: 16807324. DOI: [10.5194/acp-18-13055-2018](https://doi.org/10.5194/acp-18-13055-2018).
- Dobson, G. M. B. (Mar. 1968). Forty Years' Research on Atmospheric Ozone at Oxford: a History. In: *Applied Optics* 7.3, p. 387. ISSN: 0003-6935. DOI: [10.1364/AO.7.000387](https://doi.org/10.1364/AO.7.000387).
- Dobson, G. M. B., D. N. Harrison and F. A. Lindemann (1926). Measurements of the amount of ozone in the earth's atmosphere and its relation to other geophysical conditions. In: *Proceedings of the Royal Society of London. Series A, Containing Papers of a Mathematical and Physical Character* 110.A, pp. 660–693. ISSN: 0950-1207. DOI: [10.1098/rspa.1926.0040](https://doi.org/10.1098/rspa.1926.0040).
- DuBois, J. L., R. P. Multhaus and C. A. Ziegler (2002). The Invention and Development of the Radiosonde with a Catalog of Upper-Atmospheric Telemetering Probes in the National Museum of American History, Smithsonian Institution. In: *Smithsonian Studies in History and Technology* 53, pp. 1–78. ISSN: 00810258. DOI: [10.5479/si.00810258.53.1](https://doi.org/10.5479/si.00810258.53.1).

- Eckert, E., T. von Clarmann, M. Kiefer, G. P. Stiller, S. Lossow, N. Glatthor, D. A. Degenstein, L. Froidevaux, S. Godin-Beekmann, T. Leblanc, S. McDerimid, M. Pastel, W. Steinbrecht, D. P. J. Swart, K. A. Walker and P. F. Bernath (2014). Drift-corrected trends and periodic variations in MIPAS IMK/IAA ozone measurements. In: *Atmospheric Chemistry and Physics* 14.5, pp. 2571–2589. ISSN: 16807324. DOI: [10.5194/acp-14-2571-2014](https://doi.org/10.5194/acp-14-2571-2014).
- Fabry, C. and H. Buisson (1921). A study of the ultra-violet end of the solar spectrum. In: *Astrophysical Journal* LIV.5, pp. 297–322. ISSN: 1098-6596. DOI: [10.1017/CB09781107415324.004](https://doi.org/10.1017/CB09781107415324.004).
- Farman, J. C., B. G. Gardiner and J. D. Shanklin (1985). Large losses of total ozone in Antarctica reveal seasonal ClO_x/NO_x interaction. In: *Nature* 315.6016, pp. 207–210. ISSN: 0028-0836. DOI: [10.1038/315207a0](https://doi.org/10.1038/315207a0).
- Fels, S. B., J. D. Mahlman, M. D. Schwarzkopf and R. W. Sinclair (Oct. 1980). Stratospheric Sensitivity to Perturbations in Ozone and Carbon Dioxide: Radiative and Dynamical Response. In: *Journal of the Atmospheric Sciences* 37.10, pp. 2265–2297. ISSN: 0022-4928. DOI: [10.1175/1520-0469\(1980\)037<2265:SSTPI0>2.0.CO;2](https://doi.org/10.1175/1520-0469(1980)037<2265:SSTPI0>2.0.CO;2).
- Frith, S. M., R. S. Stolarski, N. A. Kramarova and R. D. McPeters (2017). Estimating Uncertainties in the SBUV Version 8.6 Merged Profile Ozone Dataset. In: *Atmospheric Chemistry and Physics* 17.June, pp. 14695–14707. ISSN: 1680-7375. DOI: [10.5194/acp-2017-412](https://doi.org/10.5194/acp-2017-412).
- Froidevaux, L., Y. B. Jiang, A. Lambert, N. J. Livesey, W. G. Read, J. W. Waters, E. V. Browell, J. W. Hair, M. A. Avery, T. J. McGee, L. W. Twigg, G. K. Sumnicht, K. W. Jucks, J. J. Margitan, B. Sen, R. A. Stachnik, G. C. Toon, P. F. Bernath, C. D. Boone, K. A. Walker, M. J. Filipiak, R. S. Harwood, R. A. Fuller, G. L. Manney, M. J. Schwartz, W. H. Daffer, B. J. Drouin, R. E. Cofield, D. T. Cuddy, R. F. Jarnot, B. W. Knosp, V. S. Perun, W. V. Snyder, P. C. Stek, R. P. Thurstans and P. A. Wagner (2008). Validation of Aura Microwave Limb Sounder stratospheric ozone measurements. In: *Journal of Geophysical Research* 113.D15, D15S20. ISSN: 0148-0227. DOI: [10.1029/2007JD008771](https://doi.org/10.1029/2007JD008771).
- Fu, Q., P. Lin, S. Solomon and D. L. Hartmann (Oct. 2015). Observational evidence of strengthening of the Brewer-Dobson circulation since 1980. In: *Journal of Geophysical Research: Atmospheres* 120.19, p. 238. ISSN: 2169-897X. DOI: [10.1002/2015JD023657](https://doi.org/10.1002/2015JD023657).
- G. M. B. Dobson (Aug. 1956). Origin and distribution of the polyatomic molecules in the atmosphere. In: *Proceedings of the Royal Society of London. Series A. Mathematical and Physical Sciences* 236.1205, pp. 187–193. ISSN: 0080-4630. DOI: [10.1098/rspa.1956.0127](https://doi.org/10.1098/rspa.1956.0127).
- Gelaro, R., W. McCarty, M. J. Suárez, R. Todling, A. Molod, L. Takacs, C. A. Randles, A. Darmenov, M. G. Bosilovich, R. Reichle, K. Wargan, L. Coy, R. Cullather, C. Draper, S. Akella, V. Buchard, A. Conaty, A. M. da Silva, W. Gu, G. K. Kim, R. Koster, R. Lucchesi, D. Merkova, J. E. Nielsen, G. Partyka, S. Pawson, W. Putman, M. Rienecker, S. D. Schubert, M. Sienkiewicz and B. Zhao (2017). The Modern-Era Retrospective Analysis for Research and Applications, version 2 (MERRA-2). In: *Journal of Climate* 30.14, pp. 5419–5454. ISSN: 08948755. DOI: [10.1175/JCLI-D-16-0758.1](https://doi.org/10.1175/JCLI-D-16-0758.1).
- Gimmestad, G. G. (2005). Differential-Absorption Lidar for Ozone and Industrial Emissions. In: *Lidar Range-Resolved Optical Remote Sensing of the Atmosphere*. Ed. by C. Weitkamp. New York: Springer-Verlag. Chap. 7, pp. 187–212. DOI: [10.1007/0-387-25101-4_7](https://doi.org/10.1007/0-387-25101-4_7).
- Godin, S., M. Marchand, A. Hauchecorne and F. Lefèvre (2002). Influence of arctic polar ozone depletion on lower stratospheric ozone amounts at haute-provence observatory (43.92°N, 5.71 °E). In: *Journal of Geophysical Research Atmospheres* 107.20, p. 8272. ISSN: 01480227. DOI: [10.1029/2001JD000516](https://doi.org/10.1029/2001JD000516).
- Godin-Beekmann, S., J. Porteneuve and A. Garnier (2003). Systematic DIAL lidar monitoring of the stratospheric ozone vertical distribution at Observatoire de Haute-Provence (43.92°N, 5.71°E). In: *Journal of Environmental Monitoring* 5.1, pp. 57–67. ISSN: 14640325. DOI: [10.1039/b205880d](https://doi.org/10.1039/b205880d).

- Götz, F. W. P., G. M. B. Dobson and A. R. Meetham (Aug. 1933). Vertical Distribution of Ozone in the Atmosphere. In: *Nature* 132.3329, p. 281. DOI: [10.1038/132281a0](https://doi.org/10.1038/132281a0).
- Götz, F. W. P., A. R. Meetham and G. M. B. Dobson (1934). The vertical distribution of ozone in the Atmosphere. In: *Quarterly Journal of the Royal Meteorological Society* 65.281, pp. 314–319. ISSN: 1477870X. DOI: [10.1002/qj.49706528107](https://doi.org/10.1002/qj.49706528107).
- Guerova, G., E. Brockmann, J. Quiby, F. Schubiger and C. Mätzler (2003). Validation of NWP Mesoscale Models with Swiss GPS Network AGNES. In: *Journal of Applied Meteorology* 42.1, pp. 141–150. ISSN: 0894-8763. DOI: [10.1175/1520-0450\(2003\)042<0141:vonmmw>2.0.co;2](https://doi.org/10.1175/1520-0450(2003)042<0141:vonmmw>2.0.co;2).
- Haefele, P., L. Martin, M. Becker, E. Brockmann, J. Morland, S. Nyeki, C. Mätzler and M. Kirchner (2004). 'Impact of radiometric water vapor measurements on troposphere and height estimates by GPS'. In: *Proceedings of the 17th International Technical Meeting of the Satellite Division of the Institute of Navigation, ION GNSS 2004*. Long Beach, CA, pp. 2289–2302.
- Haenel, F. J., G. P. Stiller, T. von Clarmann, B. Funke, E. Eckert, N. Glatthor, U. Grabowski, S. Kellmann, M. Kiefer, A. Linden and T. Reddmann (2015). Reassessment of MIPAS age of air trends and variability. In: *Atmospheric Chemistry and Physics* 15.22, pp. 13161–13176. ISSN: 16807324. DOI: [10.5194/acp-15-13161-2015](https://doi.org/10.5194/acp-15-13161-2015).
- Hagemann, S., L. Bengtsson and G. Gendt (2002). *On the determination of atmospheric water vapour from GPS measurements*. Tech. rep. 340. Hamburg, Germany: Max Planck Institute for Meteorology. URL: https://epub.sub.uni-hamburg.de/epub/volltexte/2010/5300/pdf/max_scirep_340.pdf.
- Harris, N. R. P., B. Hassler, F. Tummon, G. E. Bodeker, D. Hubert, I. Petropavlovskikh, W. Steinbrecht, J. Anderson, P. K. Bhartia, C. D. Boone, A. Bourassa, S. M. Davis, D. Degenstein, A. Delcloo, S. M. Frith, L. Froidevaux, S. Godin-Beekmann, N. Jones, M. J. Kurylo, E. Kyrölä, M. Laine, S. T. Leblanc, J.-C. Lambert, B. Liley, E. Mahieu, A. Maycock, M. de Mazière, A. D. Parrish, R. Querel, K. H. Rosenlof, C. Roth, C. Sioris, J. Staehelin, R. S. Stolarski, R. Stübi, J. Tamminen, C. Vigouroux, K. A. Walker, H. J. Wang, J. Wild and J. M. Zawodny (2015). Past changes in the vertical distribution of ozone - Part 3: Analysis and interpretation of trends. In: *Atmospheric Chemistry and Physics* 15.17, pp. 9965–9982. ISSN: 16807324. DOI: [10.5194/acp-15-9965-2015](https://doi.org/10.5194/acp-15-9965-2015).
- Hartmann, D., A. K. Tank, M. Rusticucci, L. Alexander, S. Brönnimann, Y. Charabi, F. Dentener, E. Dlugokencky, D. Easterling, A. Kaplan, B. Soden, P. Thorne, M. Wild and P.M. Zhai (2013). Observations: Atmosphere and Surface. In: *Climate Change 2013: The Physical Science Basis. Contribution of Working Group I to the Fifth Assessment Report of the Intergovernmental Panel on Climate Change*. Ed. by T. Stocker, D. Qin, G.-K. Plattner, M. Tignor, S. Allen, J. Boschung, A. Nauels, Y. Xia, V. Bex and P. Midgley. Cambridge, United Kingdom and New York, NY, USA: Cambridge University Press. Chap. 2, pp. 159–254. DOI: [10.1017/CB09781107415324.008](https://doi.org/10.1017/CB09781107415324.008).
- Hassler, B., I. Petropavlovskikh, J. Staehelin, T. August, P. K. Bhartia, C. Clerbaux, D. Degenstein, M. De Mazière, B. M. Dinelli, A. Dudhia, G. Dufour, S. M. Frith, L. Froidevaux, S. Godin-Beekmann, J. Granville, N. R. P. Harris, K. Hoppel, D. Hubert, Y. Kasai, M. J. Kurylo, E. Kyrölä, P. F. Levelt, C. T. McElroy, R. D. McPeters, R. Munro, H. Nakajima, A. D. Parrish, P. Raspollini, E. E. Remsberg, K. H. Rosenlof, A. Rozanov, T. Sano, Y. Sasano, M. Shiotani, H. G. J. Smit, G. P. Stiller, J. Tamminen, D. W. Tarasick, J. Urban, R. J. van der A, J. P. Veefkind, C. Vigouroux, T. von Clarmann, C. von Savigny, K. A. Walker, M. Weber, J. Wild and J. M. Zawodny (2014). Past changes in the vertical distribution of ozone - Part 1: Measurement techniques, uncertainties and availability. In: *Atmospheric Measurement Techniques* 7.5, pp. 1395–1427. ISSN: 18678548. DOI: [10.5194/amt-7-1395-2014](https://doi.org/10.5194/amt-7-1395-2014).
- Hatzaki, M., H. A. Flocas, I. Simmonds, J. Kouroutzoglou, K. Keay and I. Rudeva (2014). Seasonal aspects of an objective climatology of anticyclones affecting the mediterranean. In: *Journal of Climate* 27.24, pp. 9272–9289. ISSN: 08948755. DOI: [10.1175/JCLI-D-14-00186.1](https://doi.org/10.1175/JCLI-D-14-00186.1).
- Hegglin, M. I., D. A. Plummer, T. G. Shepherd, J. F. Scinocca, J. Anderson, L. Froidevaux, B. Funke, D. Hurst, A. Rozanov, J. Urban, T. Von Clarmann, K. A. Walker,

- H. J. Wang, S. Tegtmeier and K. Weigel (2014). Vertical structure of stratospheric water vapour trends derived from merged satellite data. In: *Nature Geoscience* 7.10, pp. 768–776. ISSN: 17520908. DOI: [10.1038/NGEO2236](https://doi.org/10.1038/NGEO2236).
- Heise, S., G. Dick, G. Gendt, T. Schmidt and J. Wickert (2009). Integrated water vapor from IGS ground-based GPS observations: Initial results from a global 5-min data set. In: *Annales Geophysicae* 27.7, pp. 2851–2859. ISSN: 09927689. DOI: [10.5194/angeo-27-2851-2009](https://doi.org/10.5194/angeo-27-2851-2009).
- Held, I. M. and B. J. Soden (Nov. 2000). Water vapor feedback and global warming. In: *Annual Review of Energy and the Environment* 25.1, pp. 441–475. ISSN: 1056-3466. DOI: [10.1146/annurev.energy.25.1.441](https://doi.org/10.1146/annurev.energy.25.1.441).
- Hersbach, H., B. Bell, P. Berrisford, S. Hirahara, A. Horányi, J. Muñoz-Sabater, J. Nicolas, C. Peubey, R. Radu, D. Schepers, A. Simmons, C. Soci, S. Abdalla, X. Abellan, G. Balsamo, P. Bechtold, G. Biavati, J. Bidlot, M. Bonavita, G. De Chiara, P. Dahlgren, D. Dee, M. Diamantakis, R. Dragani, J. Flemming, R. Forbes, M. Fuentes, A. Geer, L. Haimberger, S. Healy, R. J. Hogan, E. Hólm, M. Janisková, S. Keeley, P. Laloyaux, P. Lopez, C. Lupu, G. Radnoti, P. de Rosnay, I. Rozum, F. Vamborg, S. Villaume and J. N. Thépaut (2020). The ERA5 global reanalysis. In: *Quarterly Journal of the Royal Meteorological Society* June, pp. 1999–2049. ISSN: 1477870X. DOI: [10.1002/qj.3803](https://doi.org/10.1002/qj.3803).
- Hicks-Jalali, S., R. J. Sica, G. Martucci, E. Maillard Barras, J. Voirin and A. Haeefe (Aug. 2020). A Raman lidar tropospheric water vapour climatology and height-resolved trend analysis over Payerne, Switzerland. In: *Atmospheric Chemistry and Physics* 20.16, pp. 9619–9640. ISSN: 1680-7324. DOI: [10.5194/acp-20-9619-2020](https://doi.org/10.5194/acp-20-9619-2020).
- Ho, S. P., L. Peng, C. Mears and R. A. Anthes (2018). Comparison of global observations and trends of total precipitable water derived from microwave radiometers and COSMIC radio occultation from 2006 to 2013. In: *Atmospheric Chemistry and Physics* 18.1, pp. 259–274. ISSN: 16807324. DOI: [10.5194/acp-18-259-2018](https://doi.org/10.5194/acp-18-259-2018).
- Hocke, K., N. Kämpfer, C. Gerber and C. Mätzler (Feb. 2011). A complete long-term series of integrated water vapour from ground-based microwave radiometers. In: *International Journal of Remote Sensing* 32.3, pp. 751–765. ISSN: 13665901. DOI: [10.1080/01431161.2010.517792](https://doi.org/10.1080/01431161.2010.517792).
- Hocke, K., F. Navas Guzmán, F. Cossu and C. Mätzler (2016). Cloud Fraction of Liquid Water Clouds above Switzerland over the Last 12 Years. In: *Climate* 4, p. 48. ISSN: 2225-1154. DOI: [10.3390/cli4040048](https://doi.org/10.3390/cli4040048).
- Hocke, K., F. Navas-Guzmán, L. Moreira, L. Bernet and C. Mätzler (Oct. 2017). Oscillations in atmospheric water above Switzerland. In: *Atmospheric Chemistry and Physics* 17.19, pp. 12121–12131. DOI: [10.5194/acp-17-12121-2017](https://doi.org/10.5194/acp-17-12121-2017).
- Holton, J. R., P. H. Haynes, M. E. McIntyre, A. R. Douglass, R. B. Rood and L. Pfister (1995). Stratosphere-troposphere exchange. In: *Rev. Geophys.* 33.4, p. 403. ISSN: 8755-1209. DOI: [10.1029/95RG02097](https://doi.org/10.1029/95RG02097).
- Hu, S. and G. K. Vallis (2019). Meridional structure and future changes of tropopause height and temperature. In: *Quarterly Journal of the Royal Meteorological Society* 145.723, pp. 2698–2717. ISSN: 1477870X. DOI: [10.1002/qj.3587](https://doi.org/10.1002/qj.3587).
- Hubert, D., J.-C. Lambert, T. Verhoelst, J. Granville, A. Keppens, J. L. Baray, A. E. Bourassa, U. Cortesi, D. A. Degenstein, L. Froidevaux, S. Godin-Beekmann, K. W. Hoppel, B. J. Johnson, E. Kyrölä, T. Leblanc, G. Lichtenberg, M. Marchand, C. T. McElroy, D. Murtagh, H. Nakane, T. Portafaix, R. Querel, J. M. Russell, J. Salvador, H. G. J. Smit, K. Stebel, W. Steinbrecht, K. B. Strawbridge, R. Stübi, D. P. J. Swart, G. Taha, D. W. Tarasick, A. M. Thompson, J. Urban, J. A. E. Van Gijssel, R. Van Malderen, P. Von Der Gathen, K. A. Walker, E. Wolfram and J. M. Zawodny (2016). Ground-based assessment of the bias and long-term stability of 14 limb and occultation ozone profile data records. In: *Atmospheric Measurement Techniques* 9.6, pp. 2497–2534. ISSN: 18678548. DOI: [10.5194/amt-9-2497-2016](https://doi.org/10.5194/amt-9-2497-2016).
- Ingold, T., R. Peter and N. Kämpfer (1998). Weighted mean tropospheric temperature and transmittance determination at millimeter-wave frequencies for ground-based applications. In: *Radio Science* 33.4, pp. 905–918. DOI: [10.1002/zaac.200400263](https://doi.org/10.1002/zaac.200400263).

- IPCC (2013). Summary for Policymakers. In: *Climate Change 2013: The Physical Science Basis. Contribution of Working Group I to the Fifth Assessment Report of the Intergovernmental Panel on Climate Change*. Ed. by T. Stocker, D. Qin, G.-K. Plattner, M. Tignor, S. Allen, J. Boschung, A. Nauels, Y. Xia, V. Bex and P. Midgley. Cambridge, United Kingdom and New York, NY, USA: Cambridge University Press, pp. 1–30. DOI: [10.1017/CB09781107415324.004](https://doi.org/10.1017/CB09781107415324.004).
- (2014). *Climate Change 2014: Synthesis Report. Contribution of Working Groups I, II and III to the Fifth Assessment Report of the Intergovernmental Panel on Climate Change*. Ed. by Core Writing Team, R. Pachauri and L. Meyer. Geneva, Switzerland, p. 151. ISBN: 978-92-9169-143-2.
- Ismail, S. and E. V. Browell (2015). Lidar: Differential Absorption Lidar. In: *Encyclopedia of Atmospheric Sciences: Second Edition*. Second Edi. Vol. 3. Elsevier, pp. 277–288. ISBN: 9780123822260. DOI: [10.1016/B978-0-12-382225-3.00204-8](https://doi.org/10.1016/B978-0-12-382225-3.00204-8).
- Janssen, M. A. (Jan. 1993). *Atmospheric Remote Sensing by Microwave Radiometry*. Wiley seri. Vol. 36. 1. John Wiley & Sons, Inc.
- Jeannot, P., R. Stübi, G. Levrat, P. Viatte and J. Staehelin (June 2007). Ozone balloon soundings at Payerne (Switzerland): Reevaluation of the time series 1967–2002 and trend analysis. In: *Journal of Geophysical Research* 112.D11, p. D11302. ISSN: 0148-0227. DOI: [10.1029/2005JD006862](https://doi.org/10.1029/2005JD006862).
- Jin, S., E. Cardellach and F. Xie (2014a). GNSS Atmospheric and Multipath Delays. In: *GNSS remote sensing : theory, methods and applications*. Chap. 2, pp. 17–30. DOI: [10.1007/978-94-007-7482-7_2](https://doi.org/10.1007/978-94-007-7482-7_2).
- (2014b). Ground GNSS Atmospheric Sensing. In: *GNSS remote sensing : theory, methods and applications*. Vol. 19. Chap. 3, pp. 33–60. DOI: [10.1007/978-94-007-7482-7_3](https://doi.org/10.1007/978-94-007-7482-7_3).
- (2014c). Introduction to GNSS. In: *GNSS remote sensing : theory, methods and applications*. Chap. 1, pp. 3–16. DOI: [10.1007/978-94-007-7482-7_1](https://doi.org/10.1007/978-94-007-7482-7_1).
- Karpechko, A. Y., Maycock, A. C. (Lead authors), M. Abalos, H. Akiyoshi, J. M. Arblaster, C. I. Garfinkel, K. H. Rosenhof and M. Sigmond (2018). Stratospheric Ozone Changes and Climate. In: *Scientific Assessment of Ozone Depletion: 2018*. Geneva, Switzerland: Global Ozone Research and Monitoring Project–Report No. 58, World Meteorological Organization. Chap. 5. URL: https://www.esrl.noaa.gov/csd/assessments/ozone/2018/report/%20Chapter5%5C_2018OzoneAssessment.pdf.
- Kirk-Davidoff, D. B., E. J. Hintsä, J. G. Anderson and D. W. Keith (Nov. 1999). The effect of climate change on ozone depletion through changes in stratospheric water vapour. In: *Nature* 402.6760, pp. 399–401. ISSN: 0028-0836. DOI: [10.1038/46521](https://doi.org/10.1038/46521).
- Komhyr, W. D. (1969). Electrochemical concentration cells for gas analysis. In: *Annales de Géophysique* 25, pp. 203–210.
- Komhyr, W. D., R. D. Grass and R. K. Leonard (1989). Dobson spectrophotometer 83: a standard for total ozone measurements, 1962–1987. In: *Journal of Geophysical Research* 94.D7, pp. 9847–9861. ISSN: 01480227. DOI: [10.1029/JD094iD07p09847](https://doi.org/10.1029/JD094iD07p09847).
- Konopka, P., F. Ploeger, M. Tao, T. Birner and M. Riese (2015). Hemispheric asymmetries and seasonality of mean age of air in the lower stratosphere: Deep versus shallow branch of the Brewer-Dobson circulation. In: *Journal of Geophysical Research* 120.5, pp. 2053–2066. ISSN: 21562202. DOI: [10.1002/2014JD022429](https://doi.org/10.1002/2014JD022429).
- Kuttippurath, J. and P. J. Nair (2017). The signs of Antarctic ozone hole recovery. In: *Scientific Reports* 7.585. DOI: [10.1038/s41598-017-00722-7](https://doi.org/10.1038/s41598-017-00722-7).
- Leblanc, T., T. Trickl and H. Vogelmann (2013). Lidar. In: *Monitoring Atmospheric Water Vapour. Ground-Based Remote Sensing and In-situ Methods*. Ed. by N. Kämpfer. New York, NY: Springer New York. Chap. 7, pp. 113–158. DOI: [10.1007/978-1-4614-3909-7_7](https://doi.org/10.1007/978-1-4614-3909-7_7).
- Livesey, N. J., W. G. Read, P. A. Wagner, L. Froidevaux, A. Lambert, G. L. Manney, L. F. M. Valle, H. C. Pumphrey, M. L. Santee, M. J. Schwartz, S. Wang, R. A. Fuller, R. F. Jarnot, B. W. Knosp, E. Martinez and R. R. Lay (2018). *Earth Observing System (EOS) Aura Microwave Limb Sounder (MLS) Version 4.2x level 2 data quality and description document*. Tech. rep. Pasadena, California, USA: Jet Propulsion Laboratory,

- California Institute of Technology. URL: https://mls.jpl.nasa.gov/data/v4-2_data_quality_document.pdf.
- Maillard Barras, E., A. Haefele, R. Stübi and D. Ruffieux (2015). A method to derive the Site Atmospheric State Best Estimate (SASBE) of ozone profiles from radiosonde and passive microwave data. In: *Atmospheric Measurement Techniques Discussions*, pp. 3399–3422. DOI: [10.5194/amtd-8-3399-2015](https://doi.org/10.5194/amtd-8-3399-2015).
- Maillard Barras, E., A. Haefele, L. Nguyen, F. Tummon, W. Ball, E. Rozanov, R. Rüfenacht, K. Hocke, L. Bernet, N. Kämpfer, G. Nedoluha and I. Boyd (2020). Study of the dependence of stratospheric ozone long-term trends on local solar time. In: *Atmospheric Chemistry and Physics* 20, pp. 8453–8471. ISSN: 1680-7316. DOI: <https://doi.org/10.5194/acp-20-8453-2020>.
- Mätzler, C. (2012). *Application Note on TROWARA Data*. Tech. rep. Bern, Switzerland: University of Bern, Institute of Applied Physics. URL: <https://boris.unibe.ch/17922/>.
- Mätzler, C. and J. Morland (2009). Refined physical retrieval of integrated water vapor and cloud liquid for microwave radiometer data. In: *IEEE Transactions on Geoscience and Remote Sensing* 47.6, pp. 1585–1594. ISSN: 01962892. DOI: [10.1109/TGRS.2008.2006984](https://doi.org/10.1109/TGRS.2008.2006984).
- Maycock, A. C., K. P. Shine and M. M. Joshi (2011). The temperature response to stratospheric water vapour changes. In: *Quarterly Journal of the Royal Meteorological Society* 137.657, pp. 1070–1082. ISSN: 00359009. DOI: [10.1002/qj.822](https://doi.org/10.1002/qj.822).
- Maycock, A. C., K. Matthes, S. Tegtmeier, R. Thiéblemont and L. Hood (2016). The representation of solar cycle signals in stratospheric ozone-Part 1: A comparison of recently updated satellite observations. In: *Atmospheric Chemistry and Physics* 16.15, pp. 10021–10043. ISSN: 16807324. DOI: [10.5194/acp-16-10021-2016](https://doi.org/10.5194/acp-16-10021-2016).
- Maycock, A. C., W. J. Randel, A. K. Steiner, A. Y. Karpechko, J. Christy, R. Saunders, D. W. Thompson, C. Z. Zou, A. Chrysanthou, N. Luke Abraham, H. Akiyoshi, A. T. Archibald, N. Butchart, M. Chipperfield, M. Dameris, M. Deushi, S. Dhomse, G. Di Genova, P. Jöckel, D. E. Kinnison, O. Kirner, F. Ladstädter, M. Michou, O. Morgenstern, F. O'Connor, L. Oman, G. Pitari, D. A. Plummer, L. E. Revell, E. Rozanov, A. Stenke, D. Vioni, Y. Yamashita and G. Zeng (2018). Revisiting the Mystery of Recent Stratospheric Temperature Trends. In: *Geophysical Research Letters* 45.18, pp. 9919–9933. ISSN: 19448007. DOI: [10.1029/2018GL078035](https://doi.org/10.1029/2018GL078035).
- Millán, L. F., N. J. Livesey, M. L. Santee, J. L. Neu, G. L. Manney and R. A. Fuller (May 2016). Case Studies of the Impact of Orbital Sampling on Stratospheric Trend Detection and Derivation of Tropical Vertical Velocities: Solar Occultation versus Limb Emission Sounding. In: *Atmospheric Chemistry and Physics* 16.18, pp. 11521–11534. ISSN: 1680-7375. DOI: [10.5194/acp-2016-356](https://doi.org/10.5194/acp-2016-356).
- Molina, M. J. and F. S. Rowland (1974). Stratospheric sink for chlorofluoromethanes: chlorine atom-catalysed destruction of ozone. In: *Nature* 249.5460, pp. 810–812. ISSN: 00280836. DOI: [10.1038/249810a0](https://doi.org/10.1038/249810a0).
- Möller, F. (1963). On the influence of changes in the CO₂ concentration in air on the radiation balance of the Earth's surface and on the climate. In: *Journal of Geophysical Research* 68.13, pp. 3877–3886. DOI: [10.1029/jz068i013p03877](https://doi.org/10.1029/jz068i013p03877).
- Moreira, L. (2017). Trends and oscillations in middle atmospheric ozone observed by a ground-based microwave radiometer. Ph.D. Thesis. University of Bern, Switzerland.
- Moreira, L., K. Hocke, E. Eckert, T. Von Clarmann and N. Kämpfer (2015). Trend analysis of the 20-year time series of stratospheric ozone profiles observed by the GROMOS microwave radiometer at Bern. In: *Atmospheric Chemistry and Physics* 15.19, pp. 10999–11009. ISSN: 16807324. DOI: [10.5194/acp-15-10999-2015](https://doi.org/10.5194/acp-15-10999-2015).
- Moreira, L., K. Hocke and N. Kämpfer (2017). Comparison of ozone profiles and influences from the tertiary ozone maximum in the night-to-day ratio above Switzerland. In: *Atmospheric Chemistry and Physics* 17.17, pp. 10259–10268. ISSN: 1680-7375. DOI: [10.5194/acp-2017-274](https://doi.org/10.5194/acp-2017-274).
- Moreira, L., K. Hocke, F. Navas-Guzmán, E. Eckert, T. von Clarmann and N. Kämpfer (Mar. 2016). The natural oscillations in stratospheric ozone observed by the

- GROMOS microwave radiometer at the NDACC station Bern. In: *Atmospheric Chemistry and Physics* 16.16, pp. 10455–10467. ISSN: 1680-7375. DOI: [10.5194/acp-2016-66](https://doi.org/10.5194/acp-2016-66).
- Morland, J., C. M. Coen, K. Hocke, P. Jeannet and C. Mätzler (2009). Tropospheric water vapour above Switzerland over the last 12 years. In: *Atmospheric Chemistry and Physics* 9.16, pp. 5975–5988. ISSN: 16807324. DOI: [10.5194/acp-9-5975-2009](https://doi.org/10.5194/acp-9-5975-2009).
- Morland, J., B. Deuber, D. G. Feist, L. Martin, S. Nyeki, N. Kämpfer, C. Mätzler, P. Jeannet and L. Vuilleumier (June 2006). The STARTWAVE atmospheric water database. In: *Atmos. Chem. Phys.* 6.8, pp. 2039–2056. ISSN: 1680-7324. DOI: [10.5194/acp-6-2039-2006](https://doi.org/10.5194/acp-6-2039-2006).
- Morland, J. (2002). TROWARA - Tropospheric Water Vapour Radiometer. Radiometer review and new calibration model. Tech. rep. Bern, Switzerland: University of Bern.
- Nair, P. J., L. Froidevaux, J. Kuttippurath, J. M. Zawodny, J. M. Russell, W. Steinbrecht, H. Claude, T. Leblanc, J. A. Van Gijsel, B. Johnson, D. P. Swart, A. Thomas, R. Querel, R. Wang and J. Anderson (2015). Subtropical and midlatitude ozone trends in the stratosphere: Implications for recovery. In: *Journal of Geophysical Research Atmospheres* 120.14, pp. 7247–7257. ISSN: 21698996. DOI: [10.1002/2014JD022371](https://doi.org/10.1002/2014JD022371).
- Nair, P. J., S. Godin-Beekmann, L. Froidevaux, L. E. Flynn, J. M. Zawodny, J. M. Russell, A. Pazmiño, G. Ancellet, W. Steinbrecht, H. Claude, T. Leblanc, S. McDermid, J. A. E. Van Gijsel, B. Johnson, A. Thomas, D. Hubert, J.-C. Lambert, H. Nakane and D. P. J. Swart (2012). Relative drifts and stability of satellite and ground-based stratospheric ozone profiles at NDACC lidar stations. In: *Atmospheric Measurement Techniques* 5.6, pp. 1301–1318. ISSN: 18671381. DOI: [10.5194/amt-5-1301-2012](https://doi.org/10.5194/amt-5-1301-2012).
- Nair, P. J., S. Godin-Beekmann, J. Kuttippurath, G. Ancellet, F. Goutail, A. Pazmiño, L. Froidevaux, J. M. Zawodny, R. D. Evans, H. J. Wang, J. Anderson and M. Pastel (2013). Ozone trends derived from the total column and vertical profiles at a northern mid-latitude station. In: *Atmospheric Chemistry and Physics* 13.20, pp. 10373–10384. ISSN: 16807316. DOI: [10.5194/acp-13-10373-2013](https://doi.org/10.5194/acp-13-10373-2013).
- NCCS (2018). CH2018 - Climate Scenarios for Switzerland. In: Zurich: National Centre for Climate Services, p. 24. ISBN: 978-3-9525031-3-3.
- NDACC (2020). *Network for the Detection of Atmospheric Composition Change*. URL: <http://www.ndaccdemo.org>.
- Nedoluha, G. E., I. S. Boyd, A. Parrish, R. M. Gomez, D. R. Allen, L. Froidevaux, B. J. Connor and R. R. Querel (June 2015). Unusual stratospheric ozone anomalies observed in 22 years of measurements from Lauder, New Zealand. In: *Atmospheric Chemistry and Physics* 15.12, pp. 6817–6826. ISSN: 1680-7324. DOI: [10.5194/acp-15-6817-2015](https://doi.org/10.5194/acp-15-6817-2015).
- Newchurch, M. J., E.-S. Yang, D. M. Cunnold, G. C. Reinsel, J. M. Zawodny and J. M. Russell (2003). Evidence for slowdown in stratospheric ozone loss: First stage of ozone recovery. In: *Journal of Geophysical Research: Atmospheres* 108.D16, p. 4507. ISSN: 2156-2202. DOI: [10.1029/2003JD003471](https://doi.org/10.1029/2003JD003471).
- Nilsson, T. and G. Elgered (2008). Long-term trends in the atmospheric water vapor content estimated from ground-based GPS data. In: *Journal of Geophysical Research Atmospheres* 113.19. ISSN: 01480227. DOI: [10.1029/2008JD010110](https://doi.org/10.1029/2008JD010110).
- Nyeki, S., L. Vuilleumier, J. Morland, A. Bokoye, P. Viatte, C. Mätzler and N. Kämpfer (2005). A 10-year integrated atmospheric water vapor record using precision filter radiometers at two high-alpine sites. In: *Geophysical Research Letters* 32, p. L23803. ISSN: 00948276. DOI: [10.1029/2005GL024079](https://doi.org/10.1029/2005GL024079).
- Nyeki, S., S. Wacker, C. Aebi, J. Gröbner, G. Martucci and L. Vuilleumier (Oct. 2019). Trends in surface radiation and cloud radiative effect at four Swiss sites for the 1996–2015 period. In: *Atmospheric Chemistry and Physics* 19.20, pp. 13227–13241. ISSN: 1680-7324. DOI: [10.5194/acp-19-13227-2019](https://doi.org/10.5194/acp-19-13227-2019).
- O’Gorman, P. A. and C. J. Muller (2010). How closely do changes in surface and column water vapor follow Clausius-Clapeyron scaling in climate change simulations? In: *Environmental Research Letters* 5.2. ISSN: 17489326. DOI: [10.1088/1748-9326/5/2/025207](https://doi.org/10.1088/1748-9326/5/2/025207).

- Pacione, R., A. Araszkiwicz, E. Brockmann and J. Dousa (2017). EPN-Repro2: A reference GNSS tropospheric data set over Europe. In: *Atmospheric Measurement Techniques* 10.5, pp. 1689–1705. ISSN: 18678548. DOI: [10.5194/amt-10-1689-2017](https://doi.org/10.5194/amt-10-1689-2017).
- Palm, M., C. Melsheimer, S. Noël, J. Notholt, J. Burrows and O. Schrems (2010). Integrated water vapor above Ny Ålesund, Spitsbergen: a multisensor intercomparison. In: *Atmospheric Chemistry and Physics Discussions* 8.6, pp. 21171–21199. ISSN: 1680-7375. DOI: [10.5194/acpd-8-21171-2008](https://doi.org/10.5194/acpd-8-21171-2008).
- Pawson, S., Steinbrecht, W. (Lead Authors), A. J. Charlton-Perez, M. Fujiwara, Kapechko, A. Yu., Petropavlovskikh, I., Urban, J. and M. Weber (2014a). Update on Global Ozone: Past, Present, and Future, Chapter 2. In: *Scientific Assessment of Ozone Depletion: 2014, Global Ozone Research and Monitoring Project – Report No. 55*. Geneva, Switzerland: World Meteorological Organization.
- Pawson, S., Steinbrecht, W. (Lead authors), A. J. Charlton-Perez, M. Fujiwara, A. Y. Karpechko, I. Petropavlovskikh, J. Urban, M. Weber, M. I. Hegglin, D. E. Kinnison, D. Loyola, C. A. McLinden, L. D. Oman, D. A. Plummer, L. E. Revell, T. Sakazaki, W. Seviour, S. Tegtmeier, R. J. van der A and J. Wild (2014b). Update on global ozone: Past, present, and future. In: *Scientific Assessment of Ozone Depletion: 2014*. Vol. 416. 55. Geneva, Switzerland: Global Ozone Research and Monitoring Project – Report No. 55, World Meteorological Organization. Chap. 2. URL: https://www.esrl.noaa.gov/csl/assessments/ozone/2014/report/%20chapter2%5C_20140zoneAssessment.pdf.
- Pazmiño, A., S. Godin-Beekmann, A. Hauchecorne, C. Claud, S. Khaykin, F. Goutail, E. Wolfram, J. Salvador and E. Quel (May 2018). Multiple symptoms of total ozone recovery inside the Antarctic vortex during austral spring. In: *Atmos. Chem. Phys.* 18.10, pp. 7557–7572. ISSN: 1680-7324. DOI: [10.5194/acp-18-7557-2018](https://doi.org/10.5194/acp-18-7557-2018).
- Peter, R. and N. Kämpfer (1992). Radiometric Determination of Water Vapor and Liquid Water and Its Validation With Other Techniques. In: *Journal of Geophysical Research* 97.D16, pp. 18173–18183.
- Petty, G. W. (2006). Absorption by Atmospheric Gases. In: *A First Course in Atmospheric Radiation*. 2nd ed. Madison, Wisconsin: Sundog Publishing. Chap. 9, pp. 236–279. ISBN: 978-0-9729033-1-8.
- Plumb, R. A. (2002). Stratospheric transport. In: *Journal of the Meteorological Society of Japan* 80.4 B, pp. 793–809. ISSN: 00261165. DOI: [10.2151/jmsj.80.793](https://doi.org/10.2151/jmsj.80.793).
- Ray, E. A., F. L. Moore, K. H. Rosenlof, S. M. Davis, C. Sweeney, P. Tans, T. Wang, J. W. Elkins, H. Bönisch, A. Engel, S. Sugawara, T. Nakazawa and S. Aoki (Dec. 2014). Improving stratospheric transport trend analysis based on SF 6 and CO 2 measurements. In: *Journal of Geophysical Research: Atmospheres* 119.24, pp. 14, 110–14, 128. ISSN: 2169897X. DOI: [10.1002/2014JD021802](https://doi.org/10.1002/2014JD021802).
- Regener, E. and V. H. Regener (1934). Aufnahme des ultravioletten Sonnenspektrums in der Stratosphäre und vertikale Ozonverteilung. In: *Physikalische Zeitschrift* 35, pp. 788–793.
- Reinsel, G. C., A. J. Miller, E. C. Weatherhead, L. E. Flynn, R. M. Nagatani, G. C. Tiao and D. J. Wuebbles (2005). Trend analysis of total ozone data for turnaround and dynamical contributions. In: *Journal of Geophysical Research D: Atmospheres* 110.16, p. D16306. ISSN: 01480227. DOI: [10.1029/2004JD004662](https://doi.org/10.1029/2004JD004662).
- Richter, J. H., N. Butchart, Y. Kawatani, A. C. Bushell, L. Holt, F. Serva, J. Anstey, I. R. Simpson, S. Osprey, K. Hamilton, P. Braesicke, C. Cagnazzo, C.-C. Chen, R. R. Garcia, L. J. Gray, T. Kerzenmacher, F. Lott, C. McLandress, H. Naoe, J. Scinocca, T. N. Stockdale, S. Versick, S. Watanabe, K. Yoshida and S. Yukimoto (2020). Response of the Quasi-Biennial Oscillation to a warming climate in global climate models. In: *Quarterly Journal of the Royal Meteorological Society* March 2019, pp. 1–29. ISSN: 0035-9009. DOI: [10.1002/qj.3749](https://doi.org/10.1002/qj.3749).
- Rodgers, C. D. (2000). *Inverse Methods for Atmospheric Sounding: Theory and Practice*. Ed. by F. W. Taylor. Singapore: World Scientific Publishing Co. Pte. Ltd.
- Saastamoinen, J. (Mar. 1972). Atmospheric Correction for the Troposphere and Stratosphere in Radio Ranging Satellites. In: *The Use of Artificial Satellites for Geodesy*.

- Ed. by S. W. Henriksen et al. Vol. 15. Washington, D.C.: Geophys. Monogr. Ser., pp. 247–251. DOI: [10.1029/GM015p0247](https://doi.org/10.1029/GM015p0247).
- Salawitch, R. J., (Lead Author), D. W. Fahey, M. I. Hegglin, L. A. McBride, W. R. Tribett and S. J. Doherty (2019). *Twenty Questions and Answers About the Ozone Layer: 2018 Update*. Geneva, Switzerland: World Meteorological Organization. ISBN: 978-1-7329317-2-5.
- Salby, M. L. (1996). Chapter 8 Atmospheric radiation. In: *International Geophysics*. Ed. by M. L. Salby. Vol. 61. International Geophysics. Academic Press. Chap. 8, pp. 198–257. DOI: [10.1016/S0074-6142\(96\)80045-3](https://doi.org/10.1016/S0074-6142(96)80045-3).
- Schanz, A., K. Hocke and N. Kämpfer (2014). Daily ozone cycle in the stratosphere: Global, regional and seasonal behaviour modelled with the Whole Atmosphere Community Climate Model. In: *Atmospheric Chemistry and Physics* 14.14, pp. 7645–7663. ISSN: 16807324. DOI: [10.5194/acp-14-7645-2014](https://doi.org/10.5194/acp-14-7645-2014).
- Schneider, D., E. Brockmann, U. Marti, A. Schlatter and U. Wild (2000). 'National Report of Switzerland Introduction of a Precise Swiss Positioning Service "swipos" and Progress in the Swiss National Height Network "LHN95"'. In: *Report on the Symposium of the IAG Subcommission for Europe (EUREF) held in Tromsø, 22 - 24 June 2000*. Ed. by J. Torres, pp. 315–322.
- Schneider, M., P. Demoulin, R. Sussmann and J. Notholt (2013). Fourier Transform Infrared Spectrometry. In: *Monitoring Atmospheric Water Vapour. Ground-Based Remote Sensing and In-situ Methods*. Ed. by N. Kämpfer. New York, NY: Springer New York. Chap. 6, pp. 95–111. DOI: [10.1007/978-1-4614-3909-7_6](https://doi.org/10.1007/978-1-4614-3909-7_6).
- Schneider, M., F. Hase and T. Blumenstock (2006). Water vapour profiles by ground-based FTIR spectroscopy: Study for an optimised retrieval and its validation. In: *Atmospheric Chemistry and Physics* 6.3, pp. 811–830. ISSN: 16807324. DOI: [10.5194/acp-6-811-2006](https://doi.org/10.5194/acp-6-811-2006).
- Schotland, R. M. (1974). Errors in the Lidar Measurement of Atmospheric Gases by Differential Absorption. In: *Journal of Applied Meteorology* 13.1, pp. 71–77. ISSN: 0021-8952. DOI: [10.1175/1520-0450\(1974\)013<0071:EITLMO>2.0.CO;2](https://doi.org/10.1175/1520-0450(1974)013<0071:EITLMO>2.0.CO;2).
- Schuenemeyer, J. H. and L. J. Drew (2010). Regression. In: *Statistics for Earth and Environmental Scientists*. Hoboken, New Jersey: John Wiley & Sons, Ltd. Chap. 4, pp. 99–149. ISBN: 9780470650707. DOI: [10.1002/9780470650707.ch4](https://doi.org/10.1002/9780470650707.ch4).
- Shepherd, T. G., D. A. Plummer, J. F. Scinocca, M. I. Hegglin, V. E. Fioletov, M. C. Reader, E. Remsberg, T. von Clarmann and H. J. Wang (2014). Reconciliation of halogen-induced ozone loss with the total-column ozone record. In: *Nature Geoscience* 7.6, pp. 443–449. ISSN: 1752-0894. DOI: [10.1038/ngeo2155](https://doi.org/10.1038/ngeo2155).
- Sherwood, S. C., W. Ingram, Y. Tsushima, M. Satoh, M. Roberts, P. L. Vidale and P. A. O’Gorman (2010). Relative humidity changes in a warmer climate. In: *Journal of Geophysical Research Atmospheres* 115.9, pp. 1–11. ISSN: 01480227. DOI: [10.1029/2009JD012585](https://doi.org/10.1029/2009JD012585).
- Sofieva, V. F., E. Kyrölä, M. Laine, J. Tamminen, D. Degenstein, A. Bourassa, C. Roth, D. Zawada, M. Weber, A. Rozanov, N. Raipoe, G. P. Stiller, A. Laeng, T. von Clarmann, K. A. Walker, P. Sheese, D. Hubert, M. van Roozendaal, C. Zehner, R. P. Damadeo, J. Zawodny, N. Kramarova and P. K. Bhartia (2017). Merged SAGE II, Ozone_cci and OMPS ozone profiles dataset and evaluation of ozone trends in the stratosphere. In: *Atmospheric Chemistry and Physics* 17, pp. 12533–12552. ISSN: 1680-7375. DOI: [10.5194/acp-2017-598](https://doi.org/10.5194/acp-2017-598).
- Solomon, S., D. Ivy, M. Gupta, J. Bandoro, B. Santer, Q. Fu, P. Lin, R. R. Garcia, D. Kinnison and M. Mills (2017). Mirrored changes in Antarctic ozone and stratospheric temperature in the late 20th versus early 21st centuries. In: *Journal of Geophysical Research: Atmospheres* 122.16, pp. 8940–8950. ISSN: 21698996. DOI: [10.1002/2017JD026719](https://doi.org/10.1002/2017JD026719).
- Solomon, S., D. J. Ivy, D. Kinnison, M. J. Mills, R. R. Neely and A. Schmidt (July 2016). Emergence of healing in the Antarctic ozone layer. In: *Science* 353.6296, pp. 269–274. ISSN: 0036-8075. DOI: [10.1126/science.aae0061](https://doi.org/10.1126/science.aae0061).
- SPARC/IO₃C/GAW (2019). SPARC/IO₃C/GAW Report on Long-term Ozone Trends and Uncertainties in the Stratosphere. In: ed. by I. Petropavlovskikh, S. Godin-

- Beekmann, D. Hubert, R. P. Damadeo, B. Hassler and V. F. Sofieva. SPARC Report No. 9, GAW Report No. 241, WCRP-17/2018. DOI: [10.17874/f899e57a20b](https://doi.org/10.17874/f899e57a20b).
- STARTWAVE (2020). *Studies in Atmospheric Radiative Transfer and Water Vapour Effects*. URL: <http://www.iapmw.unibe.ch/research/projects/STARTWAVE/>.
- Steinbrecht, W., H. Claude, U. Köhler and K. P. Hoinka (1998). Correlations between tropopause height and total ozone: Implications for long-term changes. In: *Journal of Geophysical Research Atmospheres* 103.D15, pp. 19183–19192. ISSN: 01480227. DOI: [10.1029/98JD01929](https://doi.org/10.1029/98JD01929).
- Steinbrecht, W., H. Claude, F. Schönenborn, I. S. McDermid, T. Leblanc, S. Godin, T. Song, D. P. J. Swart, Y. J. Meijer, G. E. Bodeker, B. J. Connor, N. Kämpfer, K. Hocke, Y. Calisesi, N. Schneider, J. de la Noë, a. D. Parrish, I. S. Boyd, C. Brühl, B. Steil, M. a. Giorgetta, E. Manzini, L. W. Thomason, J. M. Zawodny, M. P. McCormick, J. M. Russell, P. K. Bhartia, R. S. Stolarski and S. M. Hollandsworth-Frith (2006). Long-term evolution of upper stratospheric ozone at selected stations of the Network for the Detection of Stratospheric Change (NDSC). In: *Journal of Geophysical Research* 111.D10, pp. 1–18. ISSN: 0148-0227. DOI: [10.1029/2005JD006454](https://doi.org/10.1029/2005JD006454).
- Steinbrecht, W., H. Claude, F. Schönenborn, I. S. McDermid, T. Leblanc, S. Godin-Beekmann, P. Keckhut, A. Hauchecorne, J. A. E. Van Gijssel, D. P. J. Swart, G. E. Bodeker, A. D. Parrish, I. S. Boyd, N. Kämpfer, K. Hocke, R. S. Stolarski, S. M. Frith, L. W. Thomason, E. E. Remsberg, C. von Savigny, A. Rozanov and J. P. Burrows (2009a). Ozone and temperature trends in the upper stratosphere at five stations of the Network for the Detection of Atmospheric Composition Change. In: *International Journal of Remote Sensing* 30.15-16, pp. 3875–3886. ISSN: 0143-1161. DOI: [10.1080/01431160902821841](https://doi.org/10.1080/01431160902821841).
- Steinbrecht, W., L. Froidevaux, R. Fuller, R. Wang, J. Anderson, C. Roth, A. Bourassa, D. Degenstein, R. Damadeo, J. Zawodny, S. M. Frith, R. McPeters, P. Bhartia, J. Wild, C. Long, S. Davis, K. Rosenlof, V. Sofieva, K. Walker, N. Raupoe, A. Rozanov, M. Weber, A. Laeng, T. von Clarmann, G. Stiller, N. Kramarova, S. Godin-Beekmann, T. Leblanc, R. Querel, D. Swart, I. Boyd, K. Hocke, N. Kämpfer, E. Maillard Barras, L. Moreira, G. Nedoluha, C. Vigouroux, T. Blumenstock, M. Schneider, O. García, N. Jones, E. Mahieu, D. Smale, M. Kotkamp, J. Robinson, I. Petropavlovskikh, N. Harris, B. Hassler, D. Hubert and F. Tummon (2017). An update on ozone profile trends for the period 2000 to 2016. In: *Atmospheric Chemistry and Physics* 17, pp. 10675–10690. ISSN: 1680-7375. DOI: [10.5194/acp-17-10675-2017](https://doi.org/10.5194/acp-17-10675-2017).
- Steinbrecht, W., M. I. Hegglin, N. Harris and M. Weber (2018). Is global ozone recovering? In: *Comptes Rendus - Geoscience* 350.7, pp. 368–375. ISSN: 16310713. DOI: [10.1016/j.crte.2018.07.012](https://doi.org/10.1016/j.crte.2018.07.012).
- Steinbrecht, W., T. J. McGee, L. W. Twigg, H. Claude, F. Schönenborn, G. K. Sumnicht and D. Silbert (2009b). Intercomparison of stratospheric ozone and temperature profiles during the October 2005 Hohenpeißenberg Ozone Profiling Experiment (HOPE). In: *Atmospheric Measurement Techniques* 2.1, pp. 125–145. ISSN: 18678548. DOI: [10.5194/amt-2-125-2009](https://doi.org/10.5194/amt-2-125-2009).
- Steiner, A. K., F. Ladstädter, W. J. Randel, A. C. Maycock, Q. Fu, C. Claud, H. Gleisner, L. Haimberger, S.-P. Ho, P. Keckhut, T. Leblanc, C. Mears, L. M. Polvani, B. D. Santer, T. Schmidt, V. Sofieva, R. Wing and C.-Z. Zou (Oct. 2020). Observed Temperature Changes in the Troposphere and Stratosphere from 1979 to 2018. In: *Journal of Climate* 33.19, pp. 8165–8194. ISSN: 0894-8755. DOI: [10.1175/JCLI-D-19-0998.1](https://doi.org/10.1175/JCLI-D-19-0998.1).
- Stenke, A. and V. Grewe (2005). Simulation of stratospheric water vapor trends: Impact on stratospheric ozone chemistry. In: *Atmospheric Chemistry and Physics* 5.5, pp. 1257–1272. ISSN: 16807316. DOI: [10.5194/acp-5-1257-2005](https://doi.org/10.5194/acp-5-1257-2005).
- Stiller, G. P., T. von Clarmann, F. Haenel, B. Funke, N. Glatthor, U. Grabowski, S. Kellmann, M. Kiefer, A. Linden, S. Lossow and M. López-Puertas (2012). Observed temporal evolution of global mean age of stratospheric air for the 2002 to 2010 period. In: *Atmospheric Chemistry and Physics* 12.7, pp. 3311–3331. ISSN: 16807316. DOI: [10.5194/acp-12-3311-2012](https://doi.org/10.5194/acp-12-3311-2012).

- Stocker, T., D. Qin, G.-K. Plattner, L. Alexander, S. Allen, N. Bindoff, F.-M. Bréon, J. Church, U. Cubasch, S. Emori, P. Forster, P. Friedlingstein, N. Gillett, J. Gregory, D. Hartmann, E. Jansen, B. Kirtman, R. Knutti, K. K. Kumar, P. Lemke, J. Marotzke, V. Masson-Delmotte, G. Meehl, I. Mokhov, S. Piao, V. Ramaswamy, D. Randall, M. Rhein, M. Rojas, C. Sabine, D. Shindell, L. Talley, D. Vaughan and S.-P. Xie (2013). Technical Summary. In: *Climate Change 2013: The Physical Science Basis. Contribution of Working Group I to the Fifth Assessment Report of the Intergovernmental Panel on Climate Change*. Ed. by T. Stocker, D. Qin, G.-K. Plattner, M. Tignor, S. Allen, J. Boschung, A. Nauels, Y. Xia, V. Bex and P. Midgley. Cambridge, United Kingdom and New York, NY, USA: Cambridge University Press, pp. 31–116. DOI: [10.1017/CB09781107415324.005](https://doi.org/10.1017/CB09781107415324.005).
- Stolarski, R. S. and S. M. Frith (2006). Search for evidence of trend slow-down in the long-term TOMS/SBUV total ozone data record: the importance of instrument drift uncertainty. In: *Atmospheric Chemistry and Physics* 6, pp. 4057–4065. ISSN: 1680-7316. DOI: [10.5194/acpd-6-3883-2006](https://doi.org/10.5194/acpd-6-3883-2006).
- Strahan, S. E. and A. R. Douglass (2018). Decline in Antarctic Ozone Depletion and Lower Stratospheric Chlorine Determined From Aura Microwave Limb Sounder Observations. In: *Geophysical Research Letters* 45.1, pp. 382–390. ISSN: 19448007. DOI: [10.1002/2017GL074830](https://doi.org/10.1002/2017GL074830).
- Strahan, S. E., A. R. Douglass and M. R. Damon (2019). Why Do Antarctic Ozone Recovery Trends Vary? In: *Journal of Geophysical Research: Atmospheres* 124.15, pp. 8837–8850. ISSN: 21698996. DOI: [10.1029/2019JD030996](https://doi.org/10.1029/2019JD030996).
- Strang, G. and K. Borre (1997). Global Positioning System. In: *Linear Algebra, Geodesy, and GPS*. Wellesley, MA: Wellesley-Cambridge Press, pp. 447–480. ISBN: 0961408863.
- Studer, S., K. Hocke, A. Schanz, H. Schmidt and N. Kämpfer (2014). A climatology of the diurnal variations of stratospheric and mesospheric ozone over Bern, Switzerland. In: *Atmospheric Chemistry and Physics* 14.2009, pp. 5905–5919. ISSN: 1680-7375. DOI: [10.5194/acpd-13-22445-2013](https://doi.org/10.5194/acpd-13-22445-2013).
- Sussmann, R., T. Borsdorff, M. Rettinger, C. Camy-Peyret, P. Demoulin, P. Duchatelet, E. Mahieu and C. Servais (2009). Technical Note: Harmonized retrieval of column-integrated atmospheric water vapor from the FTIR network – First examples for long-term records and station trends. In: *Atmospheric Chemistry and Physics* 9.22, pp. 8987–8999. ISSN: 16807324. DOI: [10.5194/acp-9-8987-2009](https://doi.org/10.5194/acp-9-8987-2009).
- Swart, D. P., J. Spakman and H. B. Bergwerff (1994). 'RIVM's Stratospheric Ozone Lidar for NDSC Station Lauder: System Description and First Results'. In: *Abstracts of Papers of the 17th International Laser Radar Conference*. Sendai, Japan, pp. 405–408. URL: https://laser-sensing.jp/ILRC17%5C_1994%5C_Sendai/pdfs/%20405%5C_Swart.pdf.
- Swisstopo (2019). *Automated GNSS Network for Switzerland (AGNES)*. URL: <http://pnac.swisstopo.admin.ch/pages/en/agnes.html>.
- Trenberth, K. E., A. Dai, R. M. Rasmussen and D. B. Parsons (Sept. 2003). The Changing Character of Precipitation. In: *Bull. Am. Meteorol. Soc.* 84.9, pp. 1205–1218. ISSN: 0003-0007. DOI: [10.1175/BAMS-84-9-1205](https://doi.org/10.1175/BAMS-84-9-1205).
- Trenberth, K. E., J. Fasullo and L. Smith (2005). Trends and variability in column-integrated atmospheric water vapor. In: *Climate Dynamics* 24.7-8, pp. 741–758. ISSN: 09307575. DOI: [10.1007/s00382-005-0017-4](https://doi.org/10.1007/s00382-005-0017-4).
- Tweedy, O. V., N. A. Kramarova, S. E. Strahan, P. A. Newman, L. Coy, W. J. Randel, M. Park, D. W. Waugh and S. M. Frith (June 2017). Response of trace gases to the disrupted 2015–2016 quasi-biennial oscillation. In: *Atmospheric Chemistry and Physics* 17.11, pp. 6813–6823. ISSN: 1680-7324. DOI: [10.5194/acp-17-6813-2017](https://doi.org/10.5194/acp-17-6813-2017).
- USask ARG and LOTUS Group (2017). *LOTUS regression*. URL: https://arg.usask.ca/docs/LOTUS%5C_regression/.
- Varotsos, C., C. Cartalis, A. Vlamakis, C. Tzanis and I. Keramitsoglou (2004). The long-term coupling between column ozone and tropopause properties. In: *Journal of Climate* 17.19, pp. 3843–3854. ISSN: 08948755. DOI: [10.1175/1520-0442\(2004\)017<3843:TLCBCO>2.0.CO;2](https://doi.org/10.1175/1520-0442(2004)017<3843:TLCBCO>2.0.CO;2).

- Vey, S., R. Dietrich, M. Fritsche, A. Rülke, P. Steigenberger and M. Rothacher (2009). On the homogeneity and interpretation of precipitable water time series derived from global GPS observations. In: *Journal of Geophysical Research Atmospheres* 114.10, p. D10101. ISSN: 01480227. DOI: [10.1029/2008JD010415](https://doi.org/10.1029/2008JD010415).
- Vigouroux, C., T. Blumenstock, M. Coffey, Q. Errera, O. García, N. B. Jones, J. W. Hannigan, F. Hase, B. Liley, E. Mahieu, J. Mellqvist, J. Notholt, M. Palm, G. Persson, M. Schneider, C. Servais, D. Smale, L. Thölix and M. De Mazière (2015). Trends of ozone total columns and vertical distribution from FTIR observations at eight NDACC stations around the globe. In: *Atmospheric Chemistry and Physics* 15.6, pp. 2915–2933. ISSN: 16807324. DOI: [10.5194/acp-15-2915-2015](https://doi.org/10.5194/acp-15-2915-2015).
- von Clarmann, T., U. Grabowski and M. Kiefer (2001). On the role of non-random errors in inverse problems in radiative transfer and other applications. In: *Journal of Quantitative Spectroscopy and Radiative Transfer* 71.1, pp. 39–46. ISSN: 00224073. DOI: [10.1016/S0022-4073\(01\)00010-3](https://doi.org/10.1016/S0022-4073(01)00010-3).
- von Clarmann, T., G. P. Stiller, U. Grabowski, E. Eckert and J. Orphal (2010). Technical note: Trend estimation from irregularly sampled, correlated data. In: *Atmospheric Chemistry and Physics* 10.14, pp. 6737–6747. ISSN: 16807316. DOI: [10.5194/acp-10-6737-2010](https://doi.org/10.5194/acp-10-6737-2010).
- Wagner, T., S. Beirle, M. Grzegorski and U. Platt (2006). Global trends (1996–2003) of total column precipitable water observed by Global Ozone Monitoring Experiment (GOME) on ERS-2 and their relation to near-surface temperature. In: *Journal of Geophysical Research Atmospheres* 111.12, p. D12102. ISSN: 01480227. DOI: [10.1029/2005JD006523](https://doi.org/10.1029/2005JD006523).
- Wallace, J. M. and P. V. Hobbs (2006a). Atmospheric Chemistry. In: *Atmospheric Science*. Ed. by J. M. Wallace and P. V. Hobbs. 2nd ed. San Diego: Academic Press. Chap. 5, pp. 153–207. ISBN: 978-0-12-732951-2. DOI: <https://doi.org/10.1016/B978-0-12-732951-2.50010-7>.
- (2006b). *Atmospheric Science - An introductory survey*. Elsevier Inc. ISBN: 9788578110796. DOI: [10.1017/CB09781107415324.004](https://doi.org/10.1017/CB09781107415324.004).
- (2006c). The Earth System. In: *Atmospheric Science*. Ed. by J. M. Wallace and P. V. Hobbs. 2nd ed. San Diego: Academic Press. Chap. 2, pp. 25–61. ISBN: 978-0-12-732951-2. DOI: <https://doi.org/10.1016/B978-0-12-732951-2.50007-7>.
- Wandinger, U. (2005). Introduction to Lidar. In: *Lidar Range-Resolved Optical Remote Sensing of the Atmosphere*. Ed. by C. Weitkamp. New York: Springer-Verlag. Chap. 1, pp. 1–18. DOI: [10.1007/0-387-25101-4_1](https://doi.org/10.1007/0-387-25101-4_1).
- Wang, J., A. Dai and C. Mears (2016). Global water vapor trend from 1988 to 2011 and its diurnal asymmetry based on GPS, radiosonde, and microwave satellite measurements. In: *Journal of Climate* 29.14, pp. 5205–5222. ISSN: 08948755. DOI: [10.1175/JCLI-D-15-0485.1](https://doi.org/10.1175/JCLI-D-15-0485.1).
- Wargan, K., C. Orbe, S. Pawson, J. R. Ziemke, L. D. Oman, M. A. Olsen, L. Coy and K. Emma Knowland (May 2018). Recent Decline in Extratropical Lower Stratospheric Ozone Attributed to Circulation Changes. In: *Geophysical Research Letters* 45.10, pp. 5166–5176. ISSN: 00948276. DOI: [10.1029/2018GL077406](https://doi.org/10.1029/2018GL077406).
- Waters, J. W., L. Froidevaux, R. S. Harwood, R. F. Jarnot, H. M. Pickett, W. G. Read, P. H. Siegel, R. E. Cofield, M. J. Filipiak, D. A. Flower, J. R. Holden, G. K. Lau, N. J. Livesey, G. L. Manney, H. C. Pumphrey, M. L. Santee, D. L. Wu, D. T. Cuddy, R. R. Lay, M. S. Loo, V. S. Perun, M. J. Schwartz, P. C. Stek, R. P. Thurstans, M. A. Boyles, K. M. Chandra, M. C. Chavez, G. S. Chen, B. V. Chudasama, R. Dodge, R. A. Fuller, M. A. Girard, J. H. Jiang, Y. Jiang, B. W. Knosp, R. C. Labelle, J. C. Lam, K. A. Lee, D. Miller, J. E. Oswald, N. C. Patel, D. M. Pukala, O. Quintero, D. M. Scaff, W. Van Snyder, M. C. Tope, P. A. Wagner and M. J. Walch (2006). The Earth Observing System Microwave Limb Sounder (EOS MLS) on the aura satellite. In: *IEEE Transactions on Geoscience and Remote Sensing* 44.5, pp. 1075–1092. ISSN: 01962892. DOI: [10.1109/TGRS.2006.873771](https://doi.org/10.1109/TGRS.2006.873771).
- Weber, M., M. Coldewey-Egbers, V. E. Fioletov, S. M. Frith, J. D. Wild, J. P. Burrows, C. S. Long and D. Loyola (Feb. 2018). Total ozone trends from 1979 to 2016 derived from five merged observational datasets – the emergence into ozone recovery.

- In: *Atmospheric Chemistry and Physics* 18.3, pp. 2097–2117. ISSN: 1680-7324. DOI: [10.5194/acp-18-2097-2018](https://doi.org/10.5194/acp-18-2097-2018).
- Wentz, F. J. and M. Schabel (2000). Precise climate monitoring using complementary satellite data sets. In: *Nature* 403.6768, pp. 414–416. ISSN: 00280836. DOI: [10.1038/35000184](https://doi.org/10.1038/35000184).
- Werner, J., K. W. Rothe and H. Walther (1983). Monitoring of the stratospheric ozone layer by laser radar. In: *Applied Physics B Photophysics and Laser Chemistry* 32.3, pp. 113–118. ISSN: 07217269. DOI: [10.1007/BF00688815](https://doi.org/10.1007/BF00688815).
- Wilhelm, S., G. Stober and P. Brown (2019). Climatologies and long-term changes in mesospheric wind and wave measurements based on radar observations at high and mid latitudes. In: *Annales Geophysicae* 37.5, pp. 851–875. ISSN: 14320576. DOI: [10.5194/angeo-37-851-2019](https://doi.org/10.5194/angeo-37-851-2019).
- Wilks, D. S. (1995). Statistical Weather Forecasting. In: *Statistical Methods in the Atmospheric Sciences, An Introduction*. San Diego: Academic Press. Chap. 6, pp. 159–232. ISBN: 9780080541723.
- WMO (2014). Scientific Assessment of Ozone Depletion: 2014. In: Geneva, Switzerland: World Meteorological Organization, Global Ozone Research and Monitoring Project - Report No. 55, p. 416. ISBN: 9789966076014.
- (2018a). Executive Summary: Scientific Assessment of Ozone Depletion: 2018. In: *Scientific Assessment of Ozone Depletion: 2018*. Geneva, Switzerland: World Meteorological Organization, Global Ozone Research and Monitoring Project - Report No. 58, p. 67.
- (2018b). Scientific Assessment of Ozone Depletion: 2018. In: Geneva, Switzerland: World Meteorological Organization, Global Ozone Research and Monitoring Project - Report No. 58, p. 588. ISBN: 9781732931718.
- (2020). *World Meteorological Organization, Global Atmosphere Watch Programme*. URL: <https://public.wmo.int/en/programmes/global-atmosphere-%20watch-programme>.
- Wolter, K. and M. S. Timlin (1998). Measuring the strength of ENSO events: How does 1997/98 rank? In: *Weather* 53.9, pp. 315–324. DOI: [10.1002/j.1477-8696.1998.tb06408.x](https://doi.org/10.1002/j.1477-8696.1998.tb06408.x).
- Wuebbles, D. J. (1984). ‘Trends in ozone and temperature structure: comparison of theory and measurements’. In: *Atmospheric Ozone, Proceedings of the Quadrennial Ozone Symposium*. Ed. by C. S. Zerefos and A. Ghazi. Halkidiki, Greece, pp. 87–91.
- Yue, J., J. Russell, Q. Gan, T. Wang, P. Rong, R. Garcia and M. Mlynczak (2019). Increasing Water Vapor in the Stratosphere and Mesosphere After 2002. In: *Geophysical Research Letters* 46.22, pp. 13452–13460. ISSN: 19448007. DOI: [10.1029/2019GL084973](https://doi.org/10.1029/2019GL084973).
- Zander, R., E. Mahieu, P. Demoulin, P. Duchatelet, G. Roland, C. Servais, M. D. Mazière, S. Reimann and C. P. Rinsland (2008). Our changing atmosphere: Evidence based on long-term infrared solar observations at the Jungfraujoch since 1950. In: *Science of the Total Environment* 391.2-3, pp. 184–195. ISSN: 00489697. DOI: [10.1016/j.scitotenv.2007.10.018](https://doi.org/10.1016/j.scitotenv.2007.10.018).
- Zanis, P., E. Maillard, J. Staehelin, C. Zerefos, E. Kosmidis, K. Tourpali and I. Wohltmann (2006). On the turnaround of stratospheric ozone trends deduced from the reevaluated Umkehr record of Arosa, Switzerland. In: *Journal of Geophysical Research Atmospheres* 111, p. D22307. ISSN: 01480227. DOI: [10.1029/2005JD006886](https://doi.org/10.1029/2005JD006886).
- Zhang, Y., J. Xu, N. Yang and P. Lan (May 2018). Variability and Trends in Global Precipitable Water Vapor Retrieved from COSMIC Radio Occultation and Radiosonde Observations. In: *Atmosphere* 9.174. ISSN: 2073-4433. DOI: [10.3390/atmos9050174](https://doi.org/10.3390/atmos9050174).

ACRONYMS

AGNES	Automated GNSS Network for Switzerland
AVK	averaging kernel
BDC	Brewer-Dobson circulation
BeiDou	BeiDou Navigation Satellite System
CF	correction factor
CFC	chlorofluorocarbon
DIAL	differential absorption lidar
ECC	Electrochemical concentration cell
ECMWF	European Centre for Medium Range Weather Forecasts
ECV	essential climate variable
EESC	equivalent effective stratospheric chlorine
ENSO	El Niño Southern Oscillation
ERA5	ECMWF reanalysis, 5th generation
ExWi	Building of the University of Bern
FB	filter bench
FFTS	fast Fourier-transform spectrometer
FTIR	Fourier-transform infrared
GAW	Global Atmosphere Watch
GHG	greenhouse gas
GLONASS	Global'naya Navigatsionnaya Sputnikovaya Sistema
GNSS	Global Navigation Satellite System
GPS	Global Positioning System
GROMOS	Ground-based Millimeter-wave Ozone Spectrometer
IGS	International GNSS Service
ILW	integrated liquid water
IPCC	Intergovernmental Panel on Climate Change
IR	infrared
IWV	integrated water vapour
KIT	Karlsruhe Institute of Technology
LOTUS	Long-term Ozone Trends and Uncertainties in the Stratosphere
MEI	Multivariate ENSO Index
MEO	medium earth orbit

MERRA-2	Modern-Era Retrospective analysis for Research and Applications, version 2
MLR	multiple linear regression
MLS	Microwave Limb Sounder
MOPI	Microwave Ozone Profiling Instrument
MWR	microwave radiometer
NASA	National Aeronautics and Space Administration
NDACC	Network for the Detection of Atmospheric Composition Change
NOAA	National Oceanic and Atmospheric Administration
ODS	ozone-depleting substance
OHP	Observatory of Haute Provence
PSC	polar stratospheric cloud
QBO	quasi-biennial oscillation
RH	relative humidity
RTE	radiative transfer equation
SBUV	Solar Backscatter Ultraviolet Radiometer
SLR	simple linear regression
SOMORA	Stratospheric Ozone Monitoring Radiometer
swisstopo	Swiss Federal Office of Topography
TROWARA	Tropospheric Water Radiometer
UNEP	United Nations Environment Programme
UV	ultraviolet
VMR	volume mixing ratio
WMO	World Meteorological Organization
ZHD	zenith hydrostatic delay
ZTD	zenith total delay
ZWD	zenith wet delay

ACKNOWLEDGMENTS

I would like to thank everyone who contributed to this thesis and who supported me during the last four years. Particularly, I would like to thank:

Klemens Hocke for the excellent supervision and support, for the insights and the good ideas, and for having always been available to answer my questions.

Niklaus Kämpfer for the inputs in the beginning of my thesis, Axel Murk for the interest and for having taken over the group lead, and Gunter Stober for the new energy and ideas brought to the group.

The Oeschger Centre for Climate Change Research for providing excellent networking and exchanging possibilities, and Peter Stucki for answering all my questions concerning the Graduate School of Climate Sciences.

Franziska Schranz for the good office and travel company, for the fruitful discussions over all these years and for having reviewed this thesis. Jonas Hagen for the inspiring discussions and for the excellent sysadmin support during all the years. Martin Lainer for the sysadmin support in my first years. Eric Sauvageat for having reviewed parts of this thesis and for the good company within my last year. H el ene for the regular, relaxing, and inspiring lunch breaks during all these years.

All colleagues from the microwave group at the institute for the good company and enjoyable coffee-, tea-, and lunch-breaks.

Andres Luder, Niklaus Jaussi, and Daniel Weber for the excellent instrument maintenance, without which the continuous measurements would not be possible.

The secretaries Beatrice Thut and Simone Corry, and the former secretaries Franziska St ampfli and Yvette Eggenschwiler for their always kind and good assistance.

Thomas von Clarmann, Sophie Godin-Beekmann, and Daan Hubert for their inputs, support, and helpful discussions.

Gabriele Stiller for accepting to serve as external referee for this thesis, and Stefan Br onnimann for agreeing on chairing the defence.

The Swiss National Science Foundation for funding my PhD.

My family. Thank you that you have always supported me in all my decisions. My friends in Switzerland, Germany, Hungary and France for always being there for me. And Etienne. Thank you for everything, for your understanding and your support, for your graphical assistance, for your patience, for your music, and for being there for me.

APPENDIX

A.1 STUDY ON OZONE TRENDS IN CENTRAL EUROPE

The following article was published in *Atmospheric Chemistry and Physics* in April 2019 (<https://doi.org/10.5194/acp-19-4289-2019>).

FULL CITATION:

L. Bernet, T. von Clarmann, S. Godin-Beekmann, G. Ancellet, E. Maillard Barras, R. Stübi, W. Steinbrecht, N. Kämpfer and K. Hocke (Apr. 2019a). Ground-based ozone profiles over central Europe: incorporating anomalous observations into the analysis of stratospheric ozone trends. In: *Atmospheric Chemistry and Physics* 19.7, pp. 4289–4309. ISSN: 1680-7324. DOI: [10.5194/acp-19-4289-2019](https://doi.org/10.5194/acp-19-4289-2019)

Atmos. Chem. Phys., 19, 4289–4309, 2019
https://doi.org/10.5194/acp-19-4289-2019
© Author(s) 2019. This work is distributed under
the Creative Commons Attribution 4.0 License.



Ground-based ozone profiles over central Europe: incorporating anomalous observations into the analysis of stratospheric ozone trends

Leonie Bernet^{1,2}, Thomas von Clarmann³, Sophie Godin-Beekmann⁴, Gérard Ancellet⁴, Eliane Maillard Barras⁵, René Stübi⁵, Wolfgang Steinbrecht⁶, Niklaus Kämpfer^{1,2}, and Klemens Hocke^{1,2}

¹Institute of Applied Physics, University of Bern, Bern, Switzerland

²Oeschger Centre for Climate Change Research, University of Bern, Bern, Switzerland

³Karlsruhe Institute of Technology, Institute of Meteorology and Climate Research, Karlsruhe, Germany

⁴Centre National de la Recherche Scientifique, Université de Versailles Saint-Quentin-en-Yvelines, Guyancourt, France

⁵MeteoSwiss, Payerne, Switzerland

⁶Deutscher Wetterdienst, Hohenpeissenberg, Germany

Correspondence: Leonie Bernet (leonie.bernet@iap.unibe.ch)

Received: 19 November 2018 – Discussion started: 4 December 2018

Revised: 14 March 2019 – Accepted: 15 March 2019 – Published: 3 April 2019

Abstract. Observing stratospheric ozone is essential to assess whether the Montreal Protocol has succeeded in saving the ozone layer by banning ozone depleting substances. Recent studies have reported positive trends, indicating that ozone is recovering in the upper stratosphere at mid-latitudes, but the trend magnitudes differ, and uncertainties are still high. Trends and their uncertainties are influenced by factors such as instrumental drifts, sampling patterns, discontinuities, biases, or short-term anomalies that may all mask a potential ozone recovery. The present study investigates how anomalies, temporal measurement sampling rates, and trend period lengths influence resulting trends. We present an approach for handling suspicious anomalies in trend estimations. For this, we analysed multiple ground-based stratospheric ozone records in central Europe to identify anomalous periods in data from the GROund-based Millimetre-wave Ozone Spectrometer (GROMOS) located in Bern, Switzerland. The detected anomalies were then used to estimate ozone trends from the GROMOS time series by considering the anomalous observations in the regression. We compare our improved GROMOS trend estimate with results derived from the other ground-based ozone records (lidars, ozonesondes, and microwave radiometers), that are all part of the Network for the Detection of Atmospheric Composition Change (NDACC). The data indicate positive trends of 1 % decade⁻¹ to 3 % decade⁻¹ at an altitude of about 39 km

(3 hPa), providing a confirmation of ozone recovery in the upper stratosphere in agreement with satellite observations. At lower altitudes, the ground station data show inconsistent trend results, which emphasize the importance of ongoing research on ozone trends in the lower stratosphere. Our presented method of a combined analysis of ground station data provides a useful approach to recognize and to reduce uncertainties in stratospheric ozone trends by considering anomalies in the trend estimation. We conclude that stratospheric trend estimations still need improvement and that our approach provides a tool that can also be useful for other data sets.

1 Introduction

After the large stratospheric ozone decrease due to ozone depleting substances (ODSs) (Molina and Rowland, 1974; Chubachi, 1984; Farman et al., 1985), signs of an ozone recovery have been reported in recent years (e.g. WMO, 2018; SPARC/IO3C/GAW, 2019). Implementing the Montreal Protocol (1987) has succeeded in reducing ODS emissions so that the total chlorine concentration has been decreasing since 1997 (Jones et al., 2011). As a consequence, stratospheric ozone concentrations over Antarctica have started to increase again, as shown by recent studies (Solomon et al.,

2016; Kuttippurath and Nair, 2017; Pazmiño et al., 2018; Strahan and Douglass, 2018). Outside of the polar regions, however, differences in ozone recovery are observed depending on altitude and latitude. The question as to whether ozone is recovering in the lower stratosphere is still controversial (Ball et al., 2018; Chipperfield et al., 2018; Stone et al., 2018; Wargan et al., 2018), whereas broad consensus exists that stratospheric ozone has stopped declining in the upper stratosphere since the end of the 1990s (Newchurch et al., 2003; Reinsel et al., 2005; Steinbrecht et al., 2006; Stolarski and Frith, 2006; Zanis et al., 2006; Steinbrecht et al., 2009a; Shepherd et al., 2014; WMO, 2014, 2018; SPARC/IO3C/GAW, 2019). Recently estimated trends for upper stratospheric ozone are positive, but they are still different in magnitude and significance because detecting a small trend is a difficult task. Many factors influence stratospheric ozone such as variations in atmospheric dynamics, solar irradiance, or volcanic aerosols and the increase of greenhouse gases (WMO, 2014). Further, ozone trends might be masked by natural variability.

Other important sources for trend uncertainties are instrumental drifts, abrupt changes, biases, or sampling issues, e.g. due to instrumental differences in sampling patterns or in vertical or temporal resolution. Satellite drifts have been included in trend uncertainties in several studies (e.g. Stolarski and Frith, 2006; Frith et al., 2017). Possible statistical methods to consider abrupt changes in a time series are, for example, presented by Bates et al. (2012). Biases in ozone data sets can lead to important differences in trend estimates, especially when they occur at the beginning or the end of the considered trend period (e.g. Bai et al., 2017). The influence of non-uniform sampling patterns on trends was illustrated by Millán et al. (2016). Also Damadeo et al. (2018) showed that accounting for temporal and spatial sampling biases and diurnal variability changes satellite-based trends.

To account for several of the mentioned factors that influence trend estimates, different approaches were published following the Scientific Assessment of Ozone Depletion of the World Meteorological Organization (WMO) in 2014 (WMO, 2014), with the aim to reduce uncertainties in trend estimates. Drifts in single satellite data sets were, for example, considered in the studies by Eckert et al. (2014) or Bourassa et al. (2018), whereas Sofieva et al. (2017) used only stable satellite products with no or small drifts. The study of Steinbrecht et al. (2017) summarizes recent trend estimates using only updated satellite data sets with small drifts. The drifts were mainly identified by Hubert et al. (2016) and were not considered in the trend estimates by Harris et al. (2015) or WMO (2014). Steinbrecht et al. also used data from a large range of ground stations, but possible biases or anomalies in these ground-based data were not considered. The resulting ground-based trends consequently show some important differences and were not used in their final merged trend profile. Ball et al. (2017) used an advanced trend estimation method that considers steps in satellite time series or

biases due to measurement artefacts. Their Bayesian method uses a priori information about the different satellite data sets and results in an optimal merged ozone composite, but it has not yet been applied to ground-based data.

The studies presented above agree on positive ozone trends in the upper stratosphere with some differences in magnitude and show varying trends in the middle and lower stratosphere. This agreement is more difficult to observe in ground-based data sets, in which the data variability is larger due to strong regional variability (Steinbrecht et al., 2017; WMO, 2014). Because of this larger variability, considering instrumental biases or regional anomalies is of special importance for trend estimations derived from ground-based data. In addition to Steinbrecht et al. (2017) and WMO (2014), several other studies presented ground-based trends of stratospheric ozone profiles (e.g. Steinbrecht et al., 2009a; Nair et al., 2013, 2015; Harris et al., 2015; SPARC/IO3C/GAW, 2019), but biases in the data sets that might influence the resulting trends have not been considered yet.

The present study proposes an approach to handle the problem of anomalous observations in time series by considering the anomalies when estimating trends. For this purpose, we present the updated data set of the ground-based microwave radiometer GROMOS (GROUND-based Millimetre-wave Ozone Spectrometer) located in Bern, Switzerland. We determine its trends with a multilinear parametric trend model (von Clarmann et al., 2010) by considering anomalies and uncertainties in the time series, resulting in an improved trend estimate. To identify such anomalies in the GROMOS data set, we compare the GROMOS data with other ground-based data sets (lidars, ozonesondes, and microwave radiometers) in central Europe (Sect. 3). We define anomalies as periods in which the data deviates from the other data sets. Before applying our trend approach to the GROMOS time series (Sect. 4.3), we tested it with an artificial time series (Sect. 4.2). Not only anomalies in a time series influence resulting trends, but also sampling patterns and the choice of the trend period. We therefore present a short analysis of temporal sampling rate and trend period length based on the GROMOS data set (Sect. 4.3.1 and 4.3.2). Finally, we compare the improved GROMOS trend with the trends from the other data sets used (Sect. 4.4).

2 Ozone data sets

The stratospheric ozone profile data used in the present study come from different ground-based instruments that measure in central Europe (Table 1). They are all part of the Network for the Detection of Atmospheric Composition Change (NDACC, 2019). In addition, we used data from the Microwave Limb Sounder (MLS) on board the Aura satellite (Aura/MLS). All data from the different stations are compared to data from the GROMOS radiometer located in Bern, Switzerland (46.95° N, 7.44° E; 574 m above sea level

(a.s.l.). The aerological station (MeteoSwiss) in Payerne, Switzerland (46.8° N, 7.0° E; 491 m a.s.l.), is located 40 km south-west of Bern, which ensures comparable stratospheric measurements. The Meteorological Observatory Hohenpeisenberg (MOH; Germany; 47.8° N, 11.0° E; 980 m a.s.l.) is located 290 km north-east of Bern, and the Observatory of Haute Provence (OHP; France; 43.9° N, 5.7° E; 650 m a.s.l.) lies 360 km south-west of Bern. Even if stratospheric trace gases generally show small horizontal variability, the distance between the different stations, especially between MOH and OHP, may lead to some differences in measured ozone.

2.1 Microwave radiometers

We use data from two microwave radiometers, both located in Switzerland. They measure the 142 GHz line where ozone molecules emit microwave radiation due to rotational transitions. The spectral line measured is pressure-broadened and thus contains information about the vertical distribution of ozone molecules. To obtain a vertical ozone profile, the received radiative intensity is compared to the spectrum simulated by the Atmospheric Radiative Transfer Simulator 2 (ARTS2; Eriksson et al., 2011). By using an optimal estimation method according to Rodgers (2000), the best estimate of the vertical profile of ozone volume mixing ratio is then retrieved from the measured spectrum. This is done using the software tool Qpack2, which together with ARTS2 provides an entire retrieval environment (Eriksson et al., 2005).

The GROUND-based Millimetre-wave Ozone Spectrometer (GROMOS) located in Bern is the main focus of this study (Kämpfer, 1995; Peter, 1997). GROMOS has been measuring ozone spectra continuously since November 1994. Before October 2009, the measurements were performed by means of a filter bench (FB) with an integration time of 1 h. Since October 2009, a fast Fourier transform spectrometer (FFTS) with an integration time of 30 min has been used. An overlap measurement period of almost 2 years (October 2009 to July 2011) was used to homogenize the FB data, by subtracting the mean bias profile averaged over the whole overlap period ($FB_{\text{mean}} - FFTS_{\text{mean}}$) from all FB profiles (Moreira et al., 2015). These homogenized ozone data are available on the NDACC web page (<ftp://ftp.cpc.ncep.noaa.gov/ndacc/station/bern/hdf/mwave/>, last access: 28 March 2019). The FFTS retrieval used in the present study (version 2021) uses variable errors in the a priori covariance matrix of around 30 % in the stratosphere and 70 % in the mesosphere and a constant measurement error of 0.8 K (Moreira, 2017). The retrieved profiles have a vertical resolution of ~ 15 to 25 km in the stratosphere. We concentrate in this study on the middle and upper stratosphere between 31 hPa (≈ 24 km) and 0.8 hPa (≈ 49 km), where the retrieved ozone is quasi-independent of the a priori information. This is assured by limiting the altitude range to the altitudes where the area of the averaging kernels (measurement response) is larger

than 0.8, which means that more than 80 % of the information comes from the observation rather than from the a priori data (Rodgers, 2000). More information about the homogenization as well as the parameters used in the retrieval can be found in Moreira et al. (2015). Besides the described data harmonization to account for the instrument upgrade, we performed some additional data corrections. Because the stratospheric signal is weak in an opaque and humid troposphere, we discarded measurements when the atmospheric transmittance was smaller than 0.3. Excluding measurements in such a way should not result in a sampling bias because tropospheric humidity is uncorrelated to stratospheric ozone. Also, the data have been corrected for outliers at each pressure level by removing values that exceed 4 times the standard deviation within a 3-day moving median window. Profiles were excluded completely when more than 50 % of their values were missing (e.g. due to outlier detection). Furthermore, we omitted profiles in which the instrumental system temperature showed outliers exceeding 4 times the standard deviation within a 30-day moving median window.

The second microwave radiometer used in this study is the Stratospheric Ozone MONitoring RAdiometer (SOMORA). It was built in 2000 as an update of the GROMOS radiometer and has been located in Payerne since 2002. Some instrumental changes were performed at the beginning of 2005 (front-end change) and in October 2010, when the acousto-optical spectrometer of SOMORA was upgraded to an FFTS (Mailard Barras et al., 2015). The data have been harmonized to account for the spectrometer change. The instrument covers an altitude range from 25 to 60 km with a temporal resolution of 30 min to 1 h. In this study, we consider SOMORA data at an altitude range between 18 hPa (≈ 27 km) and 0.8 hPa (≈ 49 km). For more information about SOMORA, refer to Calisesi (2003) concerning the instrumental setup and Mailard Barras et al. (2009, 2015) concerning the operational version of the ozone retrievals used in the present study.

2.2 Lidars

We use data from two differential absorption lidar (DIAL; Schotland, 1974) instruments in Germany and France. The instruments emit laser pulses at two different wavelengths, one of which is absorbed by ozone molecules and the other which is not. Comparing the backscattered signal at these two wavelengths provides information on the vertical ozone distribution in the atmosphere. The lidars can only retrieve ozone profiles during clear-sky nights due to scattering on cloud particles and the interference with sunlight.

The lidar at the Meteorological Observatory Hohenpeisenberg (MOH) has been operating since 1987, emitting laser pulses at 308 and 353 nm (Werner et al., 1983; Steinbrecht et al., 2009b). On average, it retrieves eight night profiles a month. In this study we limit the data to the altitude range in which the measurement error averaged over the whole study period is below 10 % (below 42 km or 2 hPa). The lower alti-

Table 1. Information about measurement stations, instruments, and data used in the present study.

Station	Instrument	Altitude range	Measurement rate	Analysis period (mm/yyyy)
Bern, Switzerland 46.95 ° N, 7.44 ° E; 574 m	GROMOS	31–0.8 hPa	30 min to 1 h	01/1995–12/2017
Payerne, Switzerland 46.8° N, 7.0° E; 491 m	SOMORA	31–0.8 hPa	30 min to 1 h	01/2000–12/2017
	Ozonesonde	24–30 km	13 profiles month ^{-1a}	01/1995–12/2017
Hohenpeissenberg, Germany 47.8° N, 11.0° E; 980 m	Lidar	24–42.3 km	8 profiles month ^{-1a}	01/1995–12/2017
	Ozonesonde	24–30 km	10 profiles month ^{-1a}	01/1995–12/2017
Haute Provence, France 43.9° N, 5.7° E; 650 m	Lidar	24–39.9 km	11 profiles month ^{-1a}	01/1995–12/2017
	Ozonesonde	24–30 km	4 profiles month ^{-1a}	01/1995–12/2017
Aura satellite, above Bern 46.95 ± 1° N, 7.44 ± 8° E	MLS	31–0.8 hPa	Two overpasses day ⁻¹	08/2004–12/2017 ^b

^a Averaged number of profiles per month in the analysed period. ^b For the trend calculations, data from January 2005 to December 2017 are used.

tude limit was set to the chosen limit of GROMOS at 31 hPa (≈ 24 km).

The Observatory of Haute Provence (OHP) operates a lidar that has been measuring in its current setup since the end of 1993 (Godin-Beekmann et al., 2003). The lidar emits laser pulses at 308 nm and 355 nm, as first described by Godin et al. (1989). The instrument measures on average 11 profiles per month. We use OHP lidar profiles below 40 km (≈ 2.7 hPa) for which the averaged measurement error remains below 10%. As a lower altitude limit, we use 31 hPa (≈ 24 km) to be consistent with the GROMOS limits. More detailed information about the lidars and ozonesondes used can be found, for example, in Godin et al. (1999) and Nair et al. (2011, 2012).

2.3 Ozonesondes

The three mentioned observatories at Payerne, MOH, and OHP also provide weekly ozonesonde measurements. The ozonesonde measurements in Payerne are usually performed three times a week at 11:00 UTC (Jeannet et al., 2007), resulting in 13 profiles per month on average. The meteorological balloon carried a Brewer Mast sonde (BM; Brewer and Milford, 1960) until September 2002, which was then replaced by an electrochemical concentration cell (ECC; Komhyr, 1969). The profiles are normalized using concurrent total column ozone from the Dobson spectrometer at Arosa, Switzerland (46.77° N, 9.7° E; 1850 m a.s.l.; Favaro et al., 2002). If the Dobson data are not available, forecast ozone column estimates based on GOME-2 (Global Ozone Monitoring Experiment-2) data are used (<http://www.temis.nl/uvradiation/nrt/uvindex.php>, last access: 28 March 2019).

Ozone soundings at MOH are performed two to three times per week with a BM sonde (on average 10 profiles per month). Three different radiosonde types have been used

since 1995, all carrying a BM ozonesonde, without major changes in its performance since 1974 (Steinbrecht et al., 2016). The profiles are normalized by on-site Dobson or Brewer spectrophotometers and, if not available, by satellite data (Steinbrecht et al., 2016).

At OHP, ECC ozonesondes have been used since 1991 with several instrumental changes (Gaudel et al., 2015). The data were normalized with total column ozone measured by a Dobson spectrophotometer until 2007 and an ultraviolet–visible SAOZ (Système d'Analyse par Observation Zénithale) spectrometer afterwards (Guirlet et al., 2000; Nair et al., 2011). In our analysed period, four profiles are available on average per month.

Ozonesonde data are limited to altitudes up to ~ 30 km, above which the balloon usually bursts. Therefore, we used ozonesonde profiles only below 30 km, which is a threshold value for Brewer Mast ozonesondes with precision and accuracy below $\pm 5\%$ (Smit and Kley, 1996). For normalization, the correction factor (CF), which is the ratio of total column ozone from the reference instrument to the total ozone from the sonde, has been applied to all ozonesonde profiles. At all measurement stations, we discarded profiles when their CF was larger than 1.2 or smaller than 0.8 (Harris et al., 1998; Smit and ASOPOS Panel, 2013). We further excluded profiles with extreme jumps or constant ozone values, as well as profiles with constant or decreasing altitude values.

2.4 Aura/MLS

The microwave limb sounder (MLS) on the Aura satellite, launched in mid-2004, measures microwave emission from the Earth in five broad spectral bands (Parkinson et al., 2006). It provides profiles of different trace gases in the atmosphere, with a vertical resolution of ~ 3 km. Stratospheric ozone is retrieved by using the spectral band centred at 240 GHz. We

used ozone data from Aura/MLS version 4.2 above Bern with a spatial coincidence of $\pm 1^\circ$ latitude and $\pm 8^\circ$ longitude, where the satellite passes twice a day (around 02:00 and 13:00 UTC). More information about the MLS instrument and the data product can be found, e.g. in Waters et al. (2006). We chose the Aura/MLS data for our study because there are no drifts between 20 and 40 km (Hubert et al., 2016).

3 Time series comparison

To identify potential anomalies in the GROMOS data, we compared the data with the other described data sets in the time period from January 1995 to December 2017, except for some instruments that cover a shorter time period (Table 1).

3.1 Comparison methodology

To compare GROMOS with the other instruments, the different data sets have been processed to compare consistent quantities and have been smoothed to the GROMOS grid. Taking relative differences between the data sets made it possible to identify anomalous periods in the GROMOS time series.

3.1.1 Data processing

In this study we concentrate on the altitude range between 31 and 0.8 hPa, in which the a priori contribution to GROMOS profiles is low (see Sect. 2.1). We therefore limit all instrument data to this altitude range and divide it into three parts. For convenience, they will be referred to as the lower stratosphere between 31 and 13 hPa (≈ 24 to 29 km), the middle stratosphere between 13 and 3 hPa (≈ 29 to 39 km), and the upper stratosphere between 3 and 0.8 hPa (≈ 39 to 49 km). The limits for the upper stratosphere agree with the common definition (e.g. Ramaswamy et al., 2001), whereas the lower and middle stratosphere defined here are usually referred to as the middle stratosphere in other studies.

Most of the instruments provide volume mixing ratios (VMRs) of ozone in parts per million (ppm). In cases that the data were given in number density (molecules cm^{-3}), the VMR was calculated with the air pressure and temperature provided by the same instrument for ozonesondes or co-located ozone- or radiosonde data for lidars. For lidar measurements, these sonde temperature and pressure profiles are completed above the balloon burst by operational model data from the National Center for Environmental Prediction (NCEP) at OHP and by lidar temperature measurements and extrapolated radiosonde pressure data at MOH.

The GROMOS, SOMORA, and Aura/MLS profiles have a constant pressure grid, which is not the case for the lidar and ozonesonde data. The lidar and ozonesonde data were therefore linearly interpolated to a regular spaced altitude grid of 100 m for the ozonesonde at OHP and Payerne and 300 m for the lidars and the ozonesonde at MOH. The mean profile of

the interpolated pressure data then built the new pressure grid for the ozone data. These interpolated lidar and ozonesonde data are used for the trend estimations. For the direct comparison with GROMOS, the data were adapted to the GROMOS grid, which is described in the next section (Sect. 3.1.2). Our figures generally show both pressure and geometric altitude. The geometric altitude is approximated by the mean altitude grid from GROMOS, which is determined for each retrieved profile from operational model data of the European Centre for Medium-Range Weather Forecasts (ECMWF).

3.1.2 GROMOS comparison and anomalies

The vertical resolution of GROMOS and SOMORA is usually coarser than for the other instruments. When comparing profiles directly with GROMOS profiles, the different vertical resolution of the instruments has to be considered. Smoothing the profiles of the different instruments by GROMOS' averaging kernels makes it possible to compare the profiles with GROMOS without biases due to resolution or a priori information (Tsou et al., 1995). The profiles with higher vertical resolution than GROMOS were convolved by the averaging kernel matrix according to Connor et al. (1991), with

$$\mathbf{x}_{\text{conv}} = \mathbf{x}_a + \mathbf{AVK}(\mathbf{x}_h - \mathbf{x}_{a,h}), \quad (1)$$

where \mathbf{x}_{conv} is the resulting convolved profile, \mathbf{x}_a is the a priori profile used in the GROMOS retrieval, $\mathbf{x}_{a,h}$ is the same a priori profile but interpolated to the grid of the highly resolved measurement, \mathbf{x}_h is the profile of the highly resolved instrument, and \mathbf{AVK} is the corresponding averaging kernel matrix from GROMOS. The rows of the \mathbf{AVK} have been interpolated to the grid of the highly resolved instrument and scaled to conserve the vertical sensitivity (Keppens et al., 2015). The SOMORA profiles have a similar vertical resolution as profiles from GROMOS and were thus not convolved because this would require a more advanced comparison method as proposed by Rodgers and Connor (2003) or Calisesi et al. (2005). GROMOS and SOMORA have a higher temporal resolution than the other instruments. For SOMORA, only profiles coincident in time with GROMOS have been selected. For the other instruments, a mean of GROMOS data at the time of the corresponding measurement was used, with a time coincidence of ± 30 min. Only for the lidars were GROMOS data averaged over the whole lidar measurement time (usually one night).

For comparison with GROMOS we computed relative differences between the monthly mean values of the different data sets and the monthly mean of the coincident GROMOS profiles. The relative difference (RD) for a specific month i has been calculated by subtracting the monthly ozone value of the data set (X_i) from the corresponding GROMOS monthly mean (GR_i), using the GROMOS monthly mean as a reference:

$$\text{RD}_{i,X} = (\text{GR}_i - X_i)/\text{GR}_i \cdot 100. \quad (2)$$

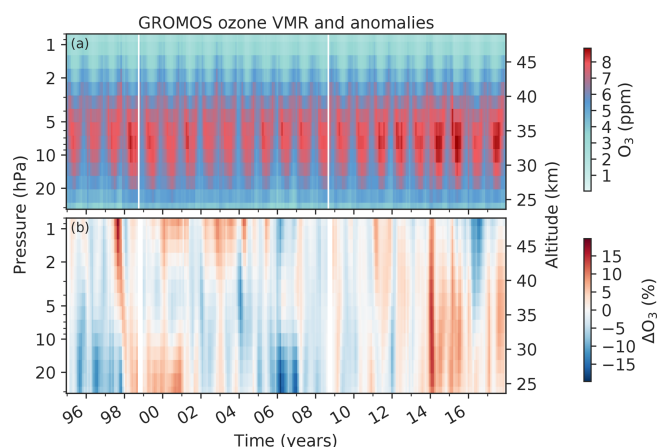


Figure 1. (a) Monthly means of ozone volume mixing ratio (VMR) measured by GROMOS (Ground-based Millimetre-wave Ozone Spectrometer) at Bern from January 1995 to December 2017. The white lines indicate months for which no measurements were available due to instrumental issues. (b) Deviation from GROMOS monthly mean climatology (1997 to 2017), smoothed by a moving median window of 3 months.

Based on the relative differences we identified periods in which GROMOS differs from the other instruments. To identify these anomalies we used a debiased relative difference (RD_{debiased}), given by

$$RD_{\text{debiased},i,X} = RD_{i,X} - \overline{RD}_X, \quad (3)$$

where \overline{RD}_X is the mean relative difference of GROMOS to the data set X over the whole period. This made it possible to ignore a potential constant offset of the instruments and to concentrate on periods with temporally large differences to GROMOS. When this debiased relative difference was larger than 10 % for at least three instruments, the respective month was identified as an anomaly in the GROMOS data. Above 2 hPa, for which only SOMORA and Aura/MLS data are available, both data sets need to have a debiased relative difference to GROMOS larger than 10 % to be identified as an anomaly.

3.2 GROMOS time series

The monthly means of the GROMOS time series (Fig. 1a) clearly depict the maximum of ozone VMR between 10 hPa and 5 hPa and the seasonal ozone variation, with increased spring–summer ozone in the middle stratosphere and increased autumn–winter values in the upper stratosphere (Moreira et al., 2016). Figure 1b shows GROMOS’ relative deviations from the monthly climatology (monthly means over the whole period 1995 to 2017). This ozone deviation is calculated by the ratio of the deseasonalized monthly means (difference between each individual monthly mean and the corresponding climatology of this month) and the monthly climatology. We observe some periods in which GROMOS

data deviate from their usual values, mostly distinguishable between the lower–middle stratosphere and the upper stratosphere. In the lower–middle stratosphere we observe negative anomalies (less ozone than usual) in 1995 to 1997 and 2005 to 2006 and positive anomalies (more ozone than usual) in 1998 to 2000, in 2014 to 2015, and in 2017. In the upper stratosphere the data show negative anomalies in 2016 and positive anomalies in 2000 and 2002 to 2003. Strong but short-term positive anomalies are visible in 1997 in the upper stratosphere and at the beginning of 2014. The positive anomaly in the upper stratosphere in 1997 is due to some missing data in November 1997 because of an instrumental upgrade, leading to a larger monthly mean value than usual. Besides this we did not detect any systematic instrumental issues in the GROMOS data that could explain the anomalies. Therefore, we compare the GROMOS data with the presented ground-based data sets, as well as with Aura/MLS data, to check whether the observed anomalies are due to natural variability or due to unexplained instrumental issues.

3.3 Comparison of different data sets

We compared GROMOS with ground-based and Aura/MLS data and averaged them over three altitude ranges (Fig. 2). The different data sets have been smoothed with the averaging kernels of GROMOS to make a direct comparison possible, as described in Sect. 3.1.2. Due to the similar vertical resolution of GROMOS and SOMORA, the SOMORA profiles have not been smoothed by GROMOS’ averaging kernels, despite differences between their a priori data and averaging kernels. This might lead to larger differences between GROMOS and SOMORA than between GROMOS and the other instruments. To avoid an instrument not covering the full range of one of the three altitude ranges, all ozonesonde data have been cut at 30 km (≈ 11.5 hPa), all lidar data at 3 hPa (≈ 39 km), and all SOMORA data below 13 hPa (≈ 29 km) for this analysis. The different instrument time series shown in Fig. 2 only contain data that are coincident with GROMOS measurements as described in Sect. 3.1.2, whereas the GROMOS data shown here represent the complete GROMOS time series with its high temporal sampling. This might lead to some sampling differences that are not considered in this figure.

The different data sets agree well, showing, however, periods in which some instruments deviate more from GROMOS than others. In the upper stratosphere (Fig. 2a), GROMOS and SOMORA agree well most of the time, but GROMOS reports slightly less ozone than SOMORA and also smaller values than Aura/MLS. A step change between SOMORA and GROMOS is visible in 2005, which might be related to the SOMORA front-end change in 2005. In the middle stratosphere (Fig. 2b), both lidars exceed the other instrument data in the last years, starting in 2004 at OHP and in 2010 at MOH. Similar deviations of the MOH and OHP li-

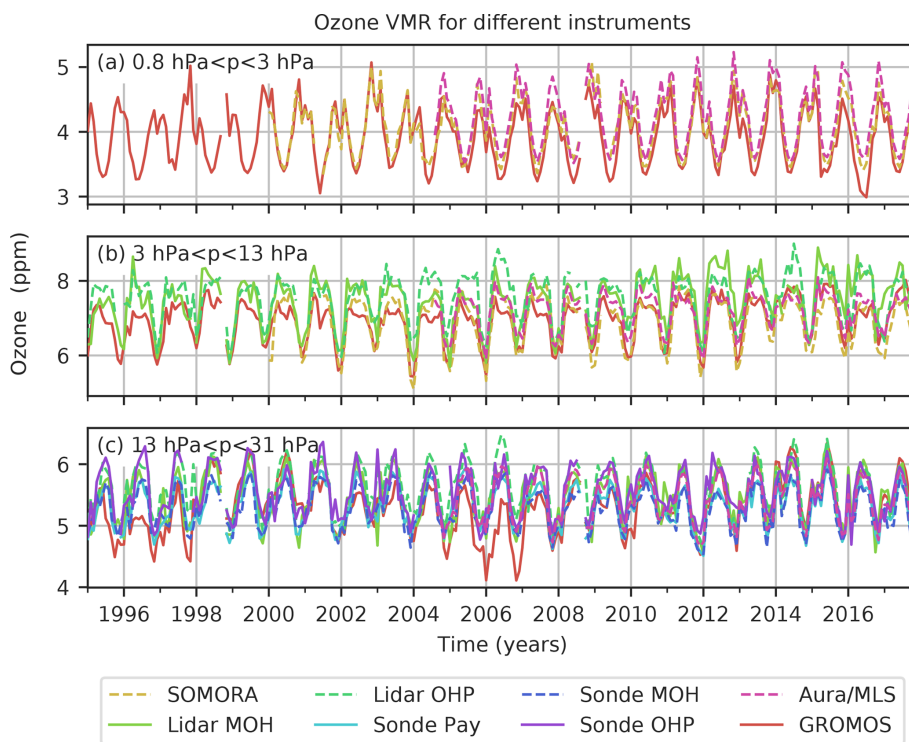


Figure 2. Monthly means of ozone VMR from the microwave radiometers GROMOS (Bern) and SOMORA (Payerne), the lidars at the observatories of Hohenpeissenberg (MOH) and Haute Provence (OHP), and the ozonesonde measurements at MOH, OHP, and Payerne, as well as Aura/MLS data above Bern. The data have been averaged over three altitude ranges.

dars have also been observed by Steinbrecht et al. (2017), as can be seen in the latitudinal lidar averages of their study.

Differences between the data sets in the lower stratosphere can be better seen in Fig. 3. The monthly relative differences of time coincident pairs of GROMOS (GR) and the convolved data set X are shown, with GROMOS data as reference values (Eq. 2). The mean relative difference of all instruments compared to GROMOS (black line in Fig. 3) generally lies within $\sim \pm 10\%$. However, there are some periods with larger deviations, in which GROMOS measures less ozone than the other instruments (negative relative difference) in 1995 to 1997 and in 2006 in the lower stratosphere and in 2016 in the middle and upper stratosphere. We further observe that the relative difference between GROMOS and the OHP ozonesonde shows some important peaks in the last decade, indicating that the sonde often measures more ozone than GROMOS. The ozonesonde data seem to have some outlier profiles. When comparing the monthly means of coincident pairs, these outliers are even more visible because only a small number of OHP ozonesonde profiles are available per month (only four profiles on average).

For a broader picture, the same relative differences to GROMOS are shown in Fig. 4, but each panel represents an individual instrument, and all altitude levels are shown. The anomalies for which at least three data sets (or two above 2 hPa) deviate by more than 10% from GROMOS (as de-

scribed in Sect. 3.1.2) are shown in the lowest panel in black. In addition to the negative anomalies observed already in the other figures (e.g. in 2006 in the lower stratosphere and in 2016 in the upper stratosphere), we also observe positive anomalies in the lower–middle stratosphere in 2000 and 2014. The negative anomalies in 1995 to 1997 in the lower stratosphere that we observed in Fig. 3 were only partly detected as anomalies with our anomaly criteria.

To summarize our comparison results, we observed some periods with anomalies compared to GROMOS' climatology (Fig. 1). Some of these anomalies were also observed when comparing GROMOS to the different data sets (Figs. 2, 3, and 4). This implies that the source of the anomalies is local variations in Bern or instrumental issues of GROMOS rather than broad atmospheric variability. We can thus conclude that the observed negative GROMOS anomalies in the lower stratosphere in 2006 and in the upper stratosphere in 2016 are biases in the GROMOS time series. The same is the case for the positive anomalies in 2000 and 2014 in the lower and middle stratosphere and also for some summer months in 2015, 2016, and 2017. In contrast to these confirmed anomalies, the GROMOS anomalies in the lower stratosphere in 1995 to 1997 (negative) and 1998 and 1999 (positive) as observed in Fig. 1 are small when comparing to the other instruments and are thus only confirmed for a few months by our anomaly detection. The biased periods in the upper

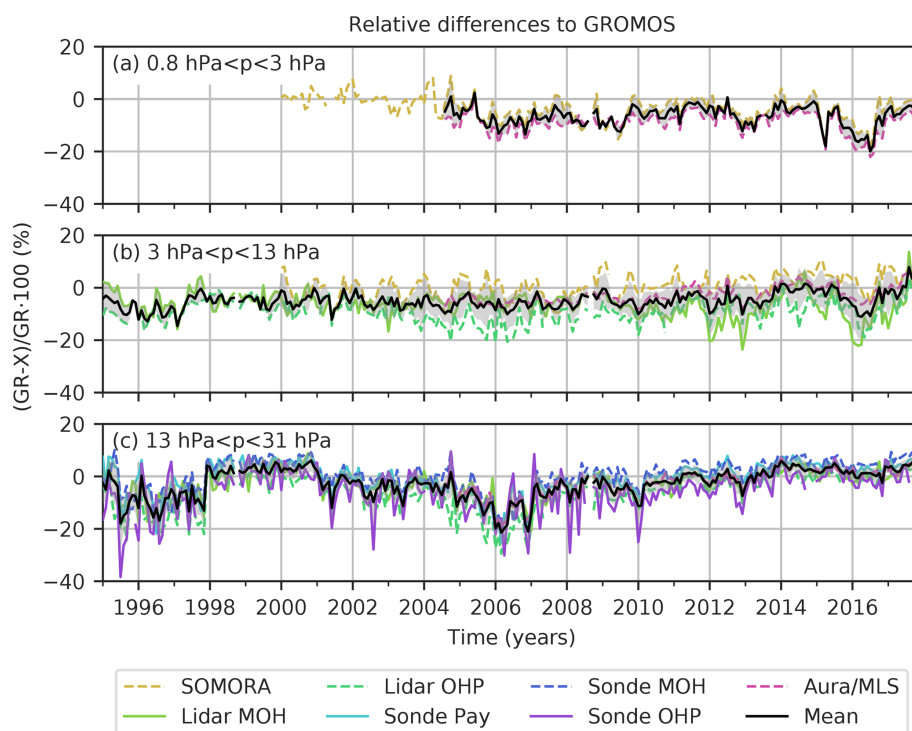


Figure 3. Relative differences (RD) of monthly means between GROMOS and coincident pairs of SOMORA, lidars (MOH, OHP), ozonesondes (Payerne, MOH, OHP), and Aura/MLS, averaged over three altitude ranges. The relative difference (RD) is given by $(GR - X)/GR \cdot 100$, where GR represents GROMOS monthly means and X represents monthly means of the other data sets. The black lines show the mean values of all RDs, and the grey shaded areas show its standard deviation.

stratosphere in 2000 and 2002 to 2003 (positive anomalies) were not confirmed by comparing GROMOS to SOMORA and might thus be real ozone variations. However, we have to keep in mind that fewer instruments (only SOMORA and Aura/MLS) provide data for comparison above 2 hPa, which makes the anomaly detection less robust at these altitudes, especially prior to the start of Aura/MLS measurements in 2004. Our results are consistent with those reported by Moreira et al. (2017). They compared GROMOS with Aura/MLS data and also observed positive deviations of GROMOS in the middle stratosphere in 2014 and 2015 as well as a negative deviation in the upper stratosphere in 2016. Hubert et al. (2019) found similar anomalies in the GROMOS time series by comparing ground-based data sets to several satellite products (see also SPARC/IO3C/GAW, 2019). Some of our detected biased periods were also found by Steinbrecht et al. (2009a) who compared different ground-based instruments, for example, the GROMOS anomaly in 2006. They attribute the observed biases to sampling differences but also to irregularities in some data sets. In fact, our results confirm irregularities in the GROMOS time series, which are probably due to instrumental issues of GROMOS and not only due to sampling differences.

4 Ozone trend estimations

Ozone trends are estimated in the present study by using a multilinear parametric trend model (von Clarmann et al., 2010). By comparing the GROMOS data to the other data sets as described above (Sect. 3.3), we have confirmed some anomalous periods in the GROMOS time series. To improve the GROMOS trend estimates, we now use these detected anomalies and consider them in the regression fit. In the following, the trend model (Sect. 4.1) will first be applied to an artificial time series to test and illustrate the approach of considering anomalies in the regression (Sect. 4.2). It will then be applied on GROMOS data (Sect. 4.3) before comparing the resulting GROMOS trends to trends from the other instruments (Sect. 4.4).

4.1 Trend model

To estimate stratospheric ozone trends, we applied the multilinear parametric trend model from von Clarmann et al. (2010) to the monthly means of all individual data sets. The model fits the following regression function:

$$y(t) = a + b \cdot t + c \cdot \text{QBO}_{30\text{hPa}}(t) + d \cdot \text{QBO}_{50\text{hPa}}(t) + e \cdot \text{F10.7}(t)$$

$$+ f \cdot \text{MEI}(t) + \sum_{n=1}^4 \left(g_n \cdot \sin\left(\frac{2\pi t}{l_n}\right) + h_n \cdot \cos\left(\frac{2\pi t}{l_n}\right) \right), \quad (4)$$

where $y(t)$ represents the estimated ozone time series, t is the monthly time vector, and a to h are coefficients that are fitted in the trend model. $\text{QBO}_{30\text{hPa}}$ and $\text{QBO}_{50\text{hPa}}$ are the normalized Singapore winds at 30 and 50 hPa, used as indices of the quasi-biennial oscillation (QBO, available at <http://www.geo.fu-berlin.de/met/ag/strat/produkte/qbo/singapore.dat>, last access: 28 March 2019). F10.7 is the solar flux at a wavelength of 10.7 cm used to represent the solar activity (measured in Ottawa and Penticton, Canada; National Research Council of Canada, 2019). The El Niño Southern Oscillation (ENSO) is considered by the Multivariate ENSO Index (MEI), that combines six meteorological variables measured over the tropical Pacific (Wolter and Timlin, 1998). The F10.7 data and the MEI data are available via <https://www.esrl.noaa.gov/psd/data/climateindices/list/> (last access: 28 March 2019). In addition to the described natural oscillations, we used four periodic oscillations with different wavelengths l_n to account for annual ($l_1 = 12$ months) and semi-annual ($l_2 = 6$ months) oscillation as well as two further overtones of the annual cycle ($l_3 = 4$ months and $l_4 = 3$ months).

The strength of the model from von Clarmann et al. (2010) used in our study is that it can consider inhomogeneities in data sets, by considering a full error covariance matrix (\mathbf{S}_y) when reducing the cost function (χ^2). Inhomogeneous data can originate from changes in the measurement system (e.g. changes in calibration standards or merging of data sets with different instrumental modes), from irregularities in spatial or temporal sampling, or from unknown instrumental issues. Such inhomogeneities lead to groups of temporally correlated data errors, that can, if not considered, change significance and slope of the estimated trend (von Clarmann et al., 2010). The study of von Clarmann et al. (2010) presents an approach to consider known or suspected inhomogeneities in the trend analysis. They divide the data into multiple subsets which are assumed to be biased with respect to each other and which are characterized by diagonal blocks in the data covariance matrix. We use their method and code in our trend analyses to account for inhomogeneities. The inhomogeneities are in our case anomalies in some months that we identified as described in Sect. 3.1.2.

The total uncertainty of the data set is represented by a full error covariance matrix \mathbf{S}_y that describes covariances between the measurements in time for each pressure level. The covariance matrix is for each instrument given by

$$\mathbf{S}_y = \mathbf{S}_{\text{instr}} + \mathbf{S}_{\text{autocorr}} + \mathbf{S}_{\text{bias}}, \quad (5)$$

where $\mathbf{S}_{\text{instr}}$ gives the monthly uncertainty estimates for the instrument, $\mathbf{S}_{\text{autocorr}}$ accounts for residuals autocorrelated in time which are caused by atmospheric variation not captured

by the trend model, and \mathbf{S}_{bias} describes the bias uncertainties when a bias is considered. The diagonal elements of $\mathbf{S}_{\text{instr}}$ are set to the monthly means of the measurement uncertainties for each instrument. For lidar data this is on average 4 % for the OHP lidar and 6 % at MOH between ~ 20 and 40 km, with smallest uncertainties in the middle stratosphere. For the ozonesonde, the uncertainty is assumed to be 5 % for all ECC sondes and 10 % for BM sondes (Harris et al., 1998; Smit and ASOPOS Panel, 2013). For SOMORA we use uncertainties composed of smoothing and observational error, ranging from 1 % to 2 % in the middle stratosphere and 2 % to 7 % in the upper stratosphere. The Aura/MLS uncertainties used range between 2 % and 5 % throughout the stratosphere. For GROMOS we use uncertainty estimates as described by Moreira et al. (2015), composed of the standard error ($\sigma/\sqrt{\text{DOF}}$, with standard deviation σ and degrees of freedom DOF) of the monthly means, an instrumental uncertainty (measurement noise), and an estimated systematic instrument uncertainty obtained from cross-comparison. The resulting uncertainty values are approximately 5 % in the middle stratosphere, 6 % to 8 % in the lower stratosphere, and 6 % to 7 % in the upper stratosphere. The off-diagonal elements of $\mathbf{S}_{\text{instr}}$ are set to zero, assuming no error correlation between the measurements in time. The additional covariance matrix $\mathbf{S}_{\text{autocorr}}$, which is added to $\mathbf{S}_{\text{instr}}$, is first also set to zero. In a second iteration, autocorrelation coefficients are inferred from residuals of the initial trend fit. The mean variance of $\mathbf{S}_{\text{autocorr}}$ is scaled such that the χ^2 divided by the degrees of freedom of the trend fit with the new \mathbf{S}_y becomes unity. The degrees of freedom are the number of data points minus the number of fitted variables. The latter are the number of the coefficients of the trend model plus the number of relevant correlation terms inferred by the procedure described above. This additional covariance matrix $\mathbf{S}_{\text{autocorr}}$ represents contributions to the fit residuals which are not caused by data errors but by phenomena that are not represented by the trend model. $\mathbf{S}_{\text{autocorr}}$ is only considered if the initial normalized χ^2 is larger than unity, which is not the case if the assumed data errors are larger than the fit residuals (Stiller et al., 2012). The more sophisticated uncertainty estimates that we use for GROMOS are larger than the residuals in the first regression fit ($\chi^2 < 1$), which means that the time correlated residuals ($\mathbf{S}_{\text{autocorr}}$) are not considered for the GROMOS trend. For all the other instruments, however, correlated residuals are considered because we use simple instrumental uncertainties that are usually smaller than the fitted residuals.

To account for the anomalies in the time series when estimating the trends we adapted \mathbf{S}_y in two steps. First, we increased the uncertainties for months and altitudes for which anomalies were identified (using the method described in Sect. 3.1.2). For this purpose, we set the diagonal elements of $\mathbf{S}_{\text{instr}}$ for the respective month i to a value obtained from the mean difference to all instruments ($\text{RD}_{\text{debiased},i}$) and the mean GROMOS ozone value. Assuming, for example, that GROMOS deviates from all instruments on average by 10 %

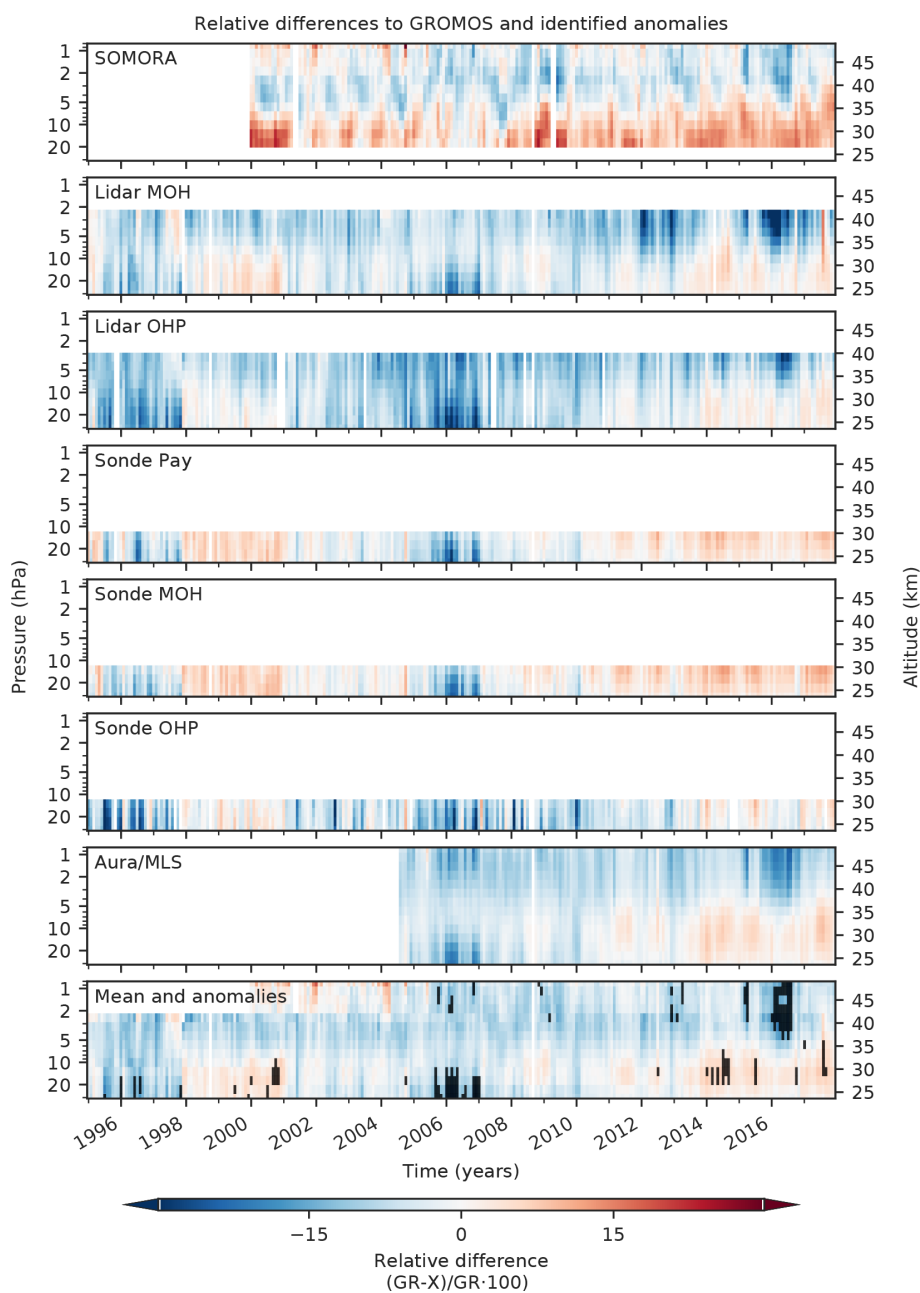


Figure 4. Relative differences (RDs) of monthly means between GROMOS and SOMORA, lidars (MOH and OHP), ozonesondes (Payerne, MOH, OHP), and Aura/MLS. The lowest panel shows the mean of all RDs. The black areas in the lowest panel show periods in which at least three data sets (or two data sets above 2 hPa) have a debiased relative difference (RD_{debiased}) larger than 10 %.

in August 2014 at 10 hPa, the overall mean August value at this altitude would be 7 ppm. In this case we would assume an uncertainty of 0.7 ppm for this biased month at this altitude level. In a second step, we account for biases in the data subsets in which anomalies were detected. For this, a fully correlated block composed of the squared estimated bias uncertainties is added to the part of S_{bias} that is concerned by anomalies. For example, to account for a bias in the summer months of 2014, a fixed bias uncertainty is added to all vari-

ances and covariances of these months in S_{bias} . Considering the bias in this way is mathematically equivalent to treating the bias as an additional fit variable that is fitted to the regression model with an optimal estimation method, as shown by von Clarmann et al. (2001). The value chosen for the bias uncertainty determines how much the bias is estimated from the data itself. For small values, the bias will be close to the a priori value, which would be a bias of zero; for large values it will be estimated completely from the given data. The bias

can thus be estimated from the data itself, which makes the method more robust because it does not depend on an a priori choice of the bias (Stiller et al., 2012). In a sensitivity test we found that assuming an uncertainty value of 5 ppm for the correlated block permits a reliable fit, whereby the bias is fitted independently of the a priori zero bias.

The described procedure for anomaly consideration is only applied to the GROMOS time series, whereas the other trend estimates were not corrected for anomalies. Our ozone trend estimates always start in January 1997, which is the most likely turning point for ozone recovery due to the decrease of ODSs (Jones et al., 2011), and all end in December 2017. Exceptions are the trends from SOMORA and Aura/MLS. The SOMORA trend starts in January 2000 when the instrument started to measure ozone. Aura/MLS covers the shortest trend period, starting only in January 2005. The trends are always given in $\% \text{ decade}^{-1}$, which is determined at each altitude level from the regression model output in ppm decade^{-1} by dividing it for each data set by its ozone mean value of the whole period. We declare a trend to be significantly different from zero at a 95 % confidence interval, as soon as its absolute value exceeds twice its uncertainty. This statistically inferred confidence interval is based on the assumed instrumental uncertainties. Unknown drifts of the data sets, however, are not considered in this claim.

4.2 Artificial time series analysis

The trend programme from von Clarmann et al. (2010) can handle uncertainties in a flexible way, which makes it possible to account for anomalies in a time series, as described above (Sect. 4.1). To investigate how anomalies can be best considered in the trend programme, we first test the programme with a simple artificial time series and then try to use the specific features of the trend programme to immunize it against anomalies. The artificial time series used for this purpose consists of monthly ozone values from January 1997 to December 2017 and is given by

$$y(t) = a + b \cdot t + g \cdot \sin\left(\frac{2\pi t}{l_n}\right) + h \cdot \cos\left(\frac{2\pi t}{l_n}\right), \quad (6)$$

with the monthly time vector t , a constant ozone value $a = 7 \text{ ppm}$, and a trend of $0.1 \text{ ppm decade}^{-1}$, i.e. $b = 0.1/120 \text{ ppm per month}$. We consider a simple seasonal oscillation with an amplitude $A = 1 \text{ ppm}$ such that $A^2 = g^2 + h^2$ (e.g. $g = h = -\sqrt{0.5} \text{ ppm}$) and a wavelength $l_n = 12$ months. The uncertainty was assumed to be 0.1 ppm for each monthly ozone value, which was considered in the diagonal elements of S_y . No noise was superimposed to the data. This artificial time series (shown in Fig. 5a) is later on referred to as case A. The estimated trend for this simple time series corresponds quasi-perfectly to the assumed time series' trend ($0.1 \text{ ppm decade}^{-1}$), which proves that the trend programme works well. The residuals are of order 10^{-6} and increase towards the start and end of the time series (Fig. 5b).

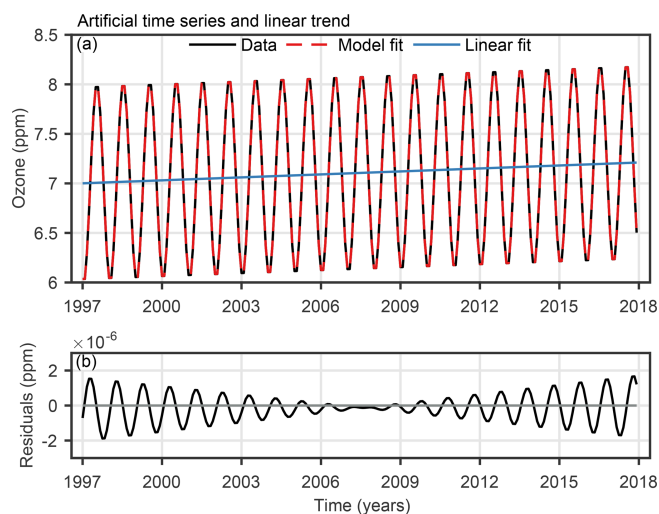


Figure 5. (a) Artificial ozone time series (composed of a simple seasonal cycle and a linear trend) and its model fit and linear trend estimation. (b) Trend model residuals (data – model fit).

To investigate how the trend programme reacts to anomalies in the time series, we performed the following sensitivity study. We increased the monthly ozone values in the summer months (June, July, August) of 2014, 2015, and 2017 by 5 % ($\approx 0.4 \text{ ppm}$). Since we are interested in the net effect of the anomalies, again no noise was superimposed on the test data. The same error covariance matrix S_y as in case A has been used. For this modified time series (case B), we observe a trend of $\sim 0.13 \text{ ppm decade}^{-1}$ instead of the expected $\sim 0.1 \text{ ppm decade}^{-1}$ (Fig. 6 and Table 2). Assuming that a real time series contains such suspicious anomalies due to, for example, instrumental issues, they would distort the true trend.

A simple way to handle such anomalies would be to omit anomalous data in the time series. This, however, would increase trend uncertainties and lead to a loss of important information. Therefore, we use the presented approach to handle anomalous observations in the time series when estimating the trend. To account for these anomalies in the trend estimation, we make use of the fact that the user of the trend programme has several options to manipulate the error covariance matrix S_y . In a first attempt we decreased the weight of the anomalies in the time series by increasing their uncertainties (diagonal elements of S_y) and set the uncertainties of the affected summer months to 0.36 ppm (case C in Fig. 6 and Table 2). This uncertainty value corresponds to 5 % of the overall mean ozone value. The uncertainty of the months without anomalies remained 0.1 ppm . No additional error correlations between the anomaly-affected data points were considered. The impact of the anomaly is already reduced from about 33 % to about 3 %. The estimated error of the trend has slightly increased because, with this mod-

Table 2. Summary of the artificial ozone time series and the different model parameters used to correct the trend estimation for artificially added anomalies.

Case	Parameters in the artificial time series		Parameters in the trend programme			
	True trend	Added anomalies	Monthly uncert. ^a	Uncert. for anomalies ^b	Bias uncert. ^c	Estimated trend
A	0.1 ppm decade ⁻¹	–	0.1 ppm	–	–	0.100 ± 0.010 ppm decade ⁻¹
B	0.1 ppm decade ⁻¹	5 %	0.1 ppm	–	–	0.133 ± 0.010 ppm decade ⁻¹
C	0.1 ppm decade ⁻¹	5 %	0.1 ppm	0.36 ppm	–	0.103 ± 0.011 ppm decade ⁻¹
D	0.1 ppm decade ⁻¹	5 %	0.1 ppm	–	5 ppm	0.100 ± 0.011 ppm decade ⁻¹
E	0.1 ppm decade ⁻¹	5 %	0.1 ppm	0.36 ppm	5 ppm	0.100 ± 0.011 ppm decade ⁻¹

^a Uncertainty considered in the diagonal elements of the covariance matrix S_y . ^b Uncertainty considered in the diagonal elements of S_y for months with anomalies. ^c Bias uncertainty considered in the off-diagonal elements of S_y for months with anomalies, set as a correlated block.

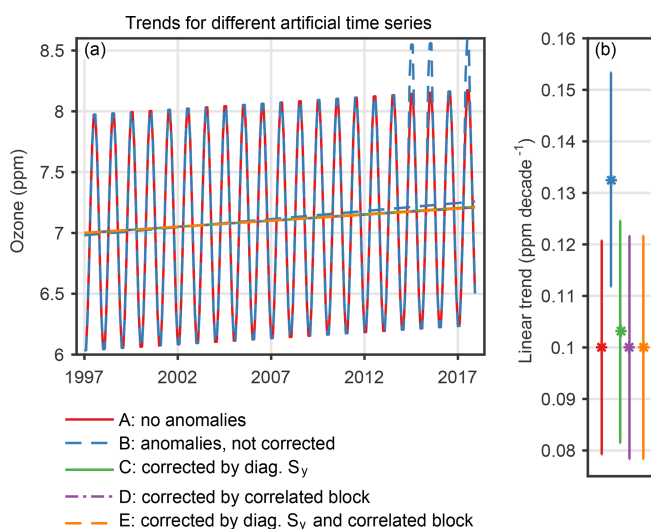


Figure 6. (a) Ozone time series and linear trends for the same artificial ozone time series as in Fig. 5 (case A). Anomalies were added to the time series in the summer months 2014, 2015, and 2017 in case B. Different corrections have been applied to account for those anomalies in the trend fit, represented by cases C to E. (b) Linear trend estimates for the time series without anomalies (case A) and the time series with added anomalies, for which the anomalies were considered in different ways (cases C, D, E) or not considered at all (case B). The error bars show 2 standard deviation (σ) uncertainties.

ified covariance matrix which represents larger data errors, the data set contains less information.

In a next step, we added a correlated block to the covariance matrix for the months containing anomalies and applied the S_y once without (case D) and once with (case E) the increased diagonal elements of S_y . Adding the correlated block to S_y corresponds to an unknown bias of the data subset that is affected by anomalies and leads to a free fit of the bias magnitude. This bias is represented in S_y as a fully correlated block of (5 ppm)². It has an expectation value of zero and an uncertainty of 5 ppm. With this approach (cases D and E), the trend obtained from the anomaly-affected data is almost identical to the trend obtained from the original data

(case A). This implies that the trend estimation has successfully been immunized against the anomaly.

In summary, we found that the trend estimates based on anomaly-affected data are largely improved by consideration of the anomalies in the covariance matrix, while without this, a largely erroneous trend is found. For this purpose it is not necessary to know the magnitude of the systematic anomaly. It is only necessary to know which of the data points are affected. We further found that the trend estimate is closer to its true value when higher uncertainties are chosen (diagonal elements of S_y or correlated block in S_y ; not shown). This can be explained by the fact that the additional uncertainties represented by S_y allow the bias to vary as in an optimal estimation scheme in which the bias is a fit variable itself (von Clarmann et al., 2001). When estimating the bias, the larger the bias uncertainty is, the less confidence is accounted to the a priori knowledge about the bias (that would be a bias of zero), and the bias is then determined directly from the data as if it were an additionally fitted variable. Based on our test with the artificial time series, we conclude that our method succeeds in handling suspicious anomalies in a time series, leading to an estimated trend close to the trend that would be expected without anomalies.

4.3 GROMOS trends

The GROMOS time series has been used for trend estimations in Moreira et al. (2015), who found a significant positive trend in the upper stratosphere. In recent years, GROMOS showed some anomalies leading to larger trends than expected in the middle atmosphere, as, for example, shown by Steinbrecht et al. (2017) or SPARC/IO3C/GAW (2019). These larger trends motivated us to improve GROMOS trend estimates by accounting for the observed anomalies. In the following, we present the trend profiles of the GROMOS time series by considering the detected anomalies in the trend programme with the different correction methods that were introduced in Sect. 4.1. In a first step, we estimated the trend without considering anomalies in the data (case I in Fig. 7). The uncertainties of the data that are used as diagonal elements in S_y range between 5 % and 8 % and are composed

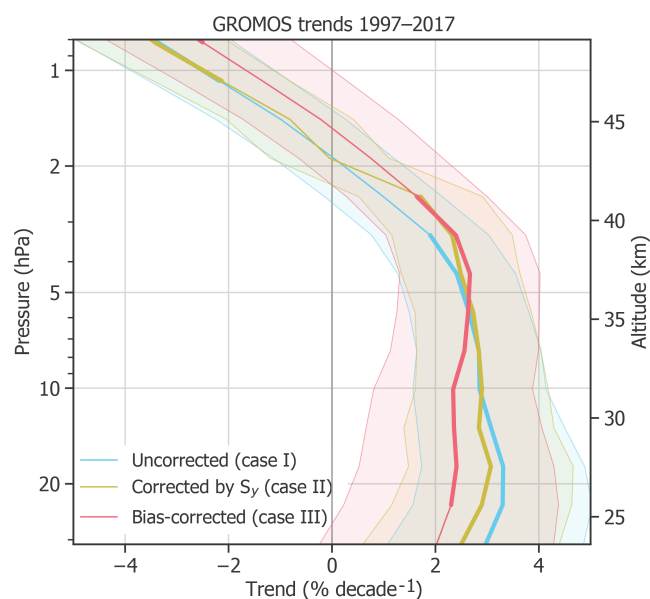


Figure 7. GROMOS ozone trends from January 1997 to December 2017, without considering anomalies (case I), considering anomalies in the diagonal elements of S_y (case II), and considering a correlated bias block for anomalies (case III). The shaded areas show 2σ uncertainties, whereas the bold lines represent altitudes at which the trend profile is significantly different from zero at a 95 % confidence interval ($|\text{trend}| > 2\sigma$).

as proposed by Moreira et al. (2015) (see Sect. 4.1). In a second step (case II), we increased the uncertainties (diagonal elements of S_y) for the months and altitudes that were detected as anomalies. The uncertainties for these anomalous data have been set to a value obtained from the difference to the other data sets (RD_{debiased}), as described in Sect. 4.1. Finally, we considered a fully correlated block for the periods in which anomalies were detected to fit a bias (case III). The bias uncertainty was set to 5 ppm at all altitudes, which ensures that the bias is fully estimated from the data. The diagonal elements of S_y stayed the same as in case II.

The trend profiles in Fig. 7 report an uncorrected GROMOS ozone trend (case I) of about $3\% \text{ decade}^{-1}$ in the middle stratosphere from 31 to 5 hPa, which decreases above to around $-4\% \text{ decade}^{-1}$ at 0.8 hPa. Correcting the trend by increasing the uncertainty for months with anomalies (case II) decreases the trend slightly in the lower stratosphere, but the differences are small. Using a correlated block in the covariance matrix to estimate the bias of each anomaly in an optimized way (case III) decreases the trend by around $1\% \text{ decade}^{-1}$ in the lower stratosphere. The trend profile of this optimized trend estimation has a trend of $2.2\% \text{ decade}^{-1}$ in the lower and middle stratosphere and peaks at approximately 4 hPa with a trend of $2.7\% \text{ decade}^{-1}$. The corrected trend profile is consistent with recent satellite-based ozone trends (e.g. Steinbrecht et al., 2017) in the middle

stratosphere. In the upper stratosphere it decreases again to $-2.4\% \text{ decade}^{-1}$ at 0.8 hPa.

All these different GROMOS trend estimates, considering anomalies in different ways, show a significant positive trend of $\sim 2.5\% \text{ decade}^{-1}$ at around 4 hPa (≈ 37 km) and a trend decrease above. This agreement indicates that the trend at these altitudes is only marginally affected by the identified anomalies and is rather robust. We can thus conclude that the trend of around $2.5\% \text{ decade}^{-1}$ is a sign for an ozone recovery in the altitude range of 35 to 40 km. This result is consistent with trends derived from merged satellite data sets as, for example, found in Ball et al. (2017), Frith et al. (2017), Sofieva et al. (2017), or Steinbrecht et al. (2017), even though the GROMOS trend peak is observed at slightly lower altitudes. A possible reason for this difference in the trend peak altitude might be related to the averaging kernels of the current GROMOS retrieval version. We observe that after the instrument upgrade in 2009, the averaging kernels peak at higher altitudes than expected, indicating that the information is retrieved from slightly higher altitudes (~ 2 to 4 km). It is therefore possible that the trend peak altitude does not exactly correspond to the true peak altitude. The instrumental upgrade in 2009 led to a change in the averaging kernels. This change, however, should not influence the trend estimates because the data have been harmonized (see Sect. 2.1) and thus corrected for such effects. The harmonization also corrects for possible effects due to changes in the temporal resolution (from 1 h to 30 min).

In the upper stratosphere (above 2 hPa), the GROMOS trend estimates are mostly insignificant but negative. This is probably influenced by the negative trend observed in the mesosphere. A negative ozone trend in the mesosphere is consistent with theory because increased methane emissions lead to an enhanced ozone loss cycle above 45 km (WMO, 2014). However, this is not further investigated in the present study because of the small mesospheric measurement response in the GROMOS filter bench data (before 2009).

In the middle and lower stratosphere (below 5 hPa), using different anomaly corrections results in largest trend differences, with trends ranging from $2\% \text{ decade}^{-1}$ to $3\% \text{ decade}^{-1}$. This result suggests that the GROMOS anomalies mostly affect these altitudes between 30 and 5 hPa. The corrected GROMOS trend (case III) is not significantly different from zero below 23 hPa, but cases I (uncorrected) and II (corrected by S_y) show significant trends. Compared to other studies, the GROMOS trends in the lower stratosphere are slightly larger than trends of most merged satellite data sets.

In summary, correcting the GROMOS trend with our anomaly approach leads to a trend profile of $\sim 2\% \text{ decade}^{-1}$ to $2.5\% \text{ decade}^{-1}$ in the lower and middle stratosphere. This is consistent with satellite-based trends from recent studies in the middle stratosphere but is still larger than most satellite trends in the lower stratosphere. The GROMOS trends are almost not affected by anomalies at 4 hPa (≈ 37 km), sug-

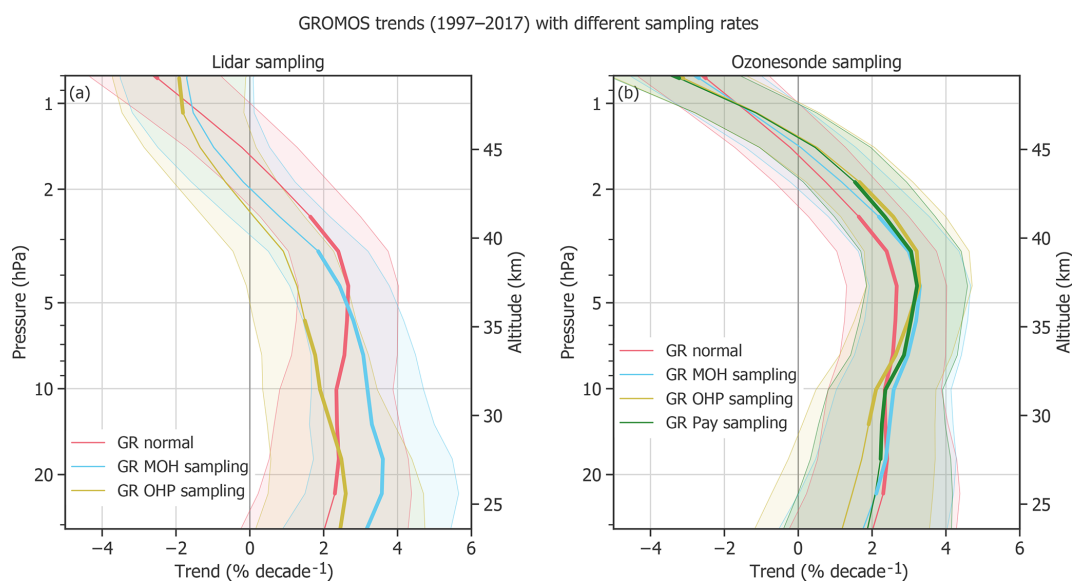


Figure 8. GROMOS (GR) trends from January 1997 to December 2017 using its high temporal resolution (normal data set with correction for anomalies) as well as the temporal sampling rate of the different lidars (a) and ozonesondes (b). The shaded areas show the 2σ uncertainties, and bold lines identify trends that are significantly different from zero.

gesting a robust ozone recovery of $2.5\% \text{ decade}^{-1}$ at this altitude. At lower altitudes, trends are more affected by the detected anomalies, and the corrected trend estimate shows a trend of $2\% \text{ decade}^{-1}$. The larger uncertainties in the lower stratosphere, the dependency on anomalies, and the insignificance of the corrected trend show that this positive trend in the lower stratosphere is less robust than the trend at higher altitudes.

4.3.1 Influence of temporal sampling on trends

Stratospheric ozone at northern mid-latitudes has a strong seasonal cycle of $\sim 16\%$ (Moreira et al., 2016) and a moderate diurnal cycle of 3% to 6% (Schanz et al., 2014; Studer et al., 2014). The sampling rate of ozone data is thus important for trend estimates because measurement dependencies on season or time of the day might influence the resulting trends. An important characteristic of microwave radiometers is their measurement continuity, being able to measure during day and night as well as during almost all weather conditions (except for an opaque atmosphere) and thus during all seasons. Other ground-based instruments such as lidars are temporally more restricted because they typically acquire data during clear-sky nights only. Clear-sky situations are more frequent during high-pressure events which vary with season and location (Steinbrecht et al., 2006; Hatzaki et al., 2014). The lidar measurements thus do not only depend on the daily cycle, but also on location and season. The seasonal dependency for ozonesondes might be smaller, but they are only launched during daytime.

Figure 8 gives an example of how the measurement sampling rate can influence resulting trends. The GROMOS time

series is used for these trend estimates, once using only measurements at the time of lidar measurements and once only at the time of ozonesonde launches. The differences to the trend that uses the complete GROMOS sampling are not significant but still important, especially between 35 and 40 km and in the lower stratosphere. Using the sampling of the MOH lidar leads to larger trends ($\sim 3\% \text{ decade}^{-1}$) than using the normal sampling ($\sim 2\% \text{ decade}^{-1}$) below 5 hPa. The OHP lidar sampling, however, leads to smaller trends than the normal sampling above 13 hPa. This suggests that selecting different night measurements within a month can lead to trend differences.

All three ozonesonde samplings result in a larger trend than normal or lidar sampling above 5 hPa. Even if ozonesondes are not measuring at those altitudes, the result shows that measuring with an ozonesonde sampling (e.g. only at noon) might influence the trend at these altitudes. Our findings suggest that the time of the measurement (day or night) or the number and the timing of measurements within a month can influence the resulting trend estimates. Results concerning the time dependences of trends based on SOMORA data can be found in Maillard Barras et al. (2019). We conclude that sampling differences have to be kept in mind when comparing trend estimates from instruments with different sampling rates or measurement times.

4.3.2 Influence of time period on trends

An important factor that influences trend estimates is the length and starting year of the trend period. Several studies have shown that the choice of start or end point affects the resulting trend substantially (Harris et al., 2015;

Weber et al., 2018). Further, the number of years in the trend period is crucial for the trend estimate (Vyushin et al., 2007; Millán et al., 2016). We investigate how the GROMOS trends change when the regression starts in different years. For this, we average the GROMOS trends over three altitude ranges and determine the trend for periods of different lengths, all ending in December 2017 but starting in different years (Fig. 9). As expected, the uncertainties increase with decreasing period length, and trends starting after 2010 are thus not even shown. Consequently, trends become insignificant for short trend periods. In the lower and middle stratosphere, more than 11 years is needed to detect a significant positive trend (at a 95 % confidence level) in the GROMOS data, whereas the 23 years considered is not enough to detect a significant trend in the upper stratosphere (above 3 hPa). Weatherhead et al. (2000) and Vyushin et al. (2007) state that at least 20 to 30 years is needed to detect a significant trend at mid-latitudes, but their results apply to total column ozone, which can not directly be compared with our ozone profiles. In general we observe that the magnitude of the trend estimates highly depends on the starting year. Furthermore, the trends start to increase in 1997 (middle stratosphere) or 1998 (lower stratosphere), probably due to the turning point in ODSs. The later the trend period starts after this turning point, the larger the trend estimate is, which has also been observed by Harris et al. (2015). Starting the trend, for example, in the year 2000, as is done in other studies (e.g. Steinbrecht et al., 2017; SPARC/IO3C/GAW, 2019), increases the GROMOS trend by almost 2 % decade⁻¹ compared to the trend that starts in 1997. The trend magnitudes depend on the starting year of the regression, which is controversial to the definition of a linear trend that does not change with time. This illustrates that the true trend might not be linear or that some interannual variations or anomalies are not captured by the trend model. Nevertheless, our findings demonstrate that it is important to consider the starting year and the trend period length when comparing trend estimates from different instruments or different studies.

4.4 Trend comparison

The GROMOS trend profile (corrected as described above) and trend profiles for all instruments at the other measurement stations (uncorrected) are shown in Fig. 10. The trend profiles agree on a positive trend in the upper stratosphere, whereas they differ at lower altitudes. Due to the given uncertainties, most of the trend profiles are not significantly different from zero at a 95 % confidence interval. Only GROMOS, the lidars, and the ozonesonde at OHP show significant trends in some parts of the stratosphere (bold lines in Fig. 10).

We observe that all instruments that measure in the upper stratosphere show a trend maximum between ~ 4 and ~ 1.8 hPa (between ~ 37 and 43 km), which indicates that ozone is recovering at these altitudes. The trend max-

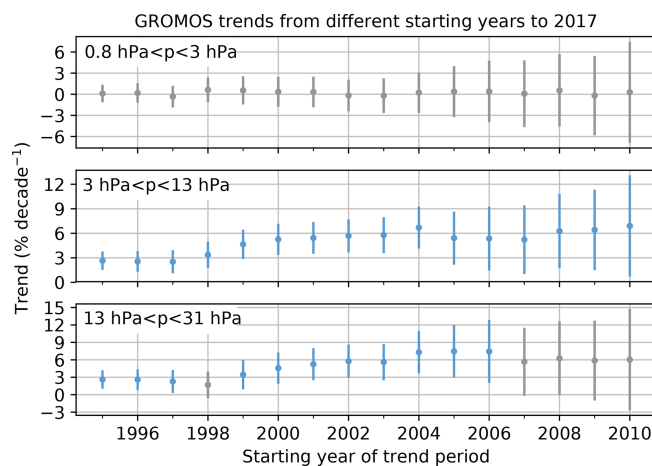


Figure 9. GROMOS trends averaged over three altitude ranges starting in different years, all ending in December 2017. The error bars show the 2σ uncertainties. Trend estimates that are not significantly different from zero at a 95 % confidence interval are shown in grey.

ima range from ~ 1 % decade⁻¹ to 3 % decade⁻¹, which is comparable with recent, mainly satellite-based ozone trends for northern mid-latitudes (e.g. Ball et al., 2017; Frith et al., 2017; Sofieva et al., 2017; Steinbrecht et al., 2017; SPARC/IO3C/GAW, 2019). Only the lidar trend at MOH is larger throughout the whole stratosphere, with ~ 3 % decade⁻¹ in the middle stratosphere and 4 % decade⁻¹ to 5 % decade⁻¹ between 5 and 2 hPa. Nair et al. (2015) observed similar trend results for the MOH lidar, even if they consider 5 fewer years with a trend period ranging from 1997 to 2012. Steinbrecht et al. (2006) found that lidar data at MOH and OHP deviate from reference satellite data above 35 km before 2003, with less ozone at MOH and more ozone at OHP compared to SAGE satellite data (Stratospheric Aerosol and Gas Experiment; McCormick et al., 1989). Opposite drifts are reported by Eckert et al. (2014) after 2002 compared to MIPAS satellite data (Michelson Interferometer for Passive Atmospheric Sounding; Fischer et al., 2008). Combining those drifts might explain our large MOH trends and smaller OHP trends. The distance of ~ 600 km between the MOH and OHP stations might also explain some differences between the lidar trends. Furthermore, our sampling results show that the lidar sampling at MOH leads to a larger trend in the lower stratosphere than using a continuous sampling, whereas OHP lidar sampling leads to a lower trend in the middle stratosphere. The large lidar trend at MOH and the comparable low OHP lidar trend might therefore also be partly explained by the sampling rate of the lidars. The GROMOS trend peaks at slightly lower altitudes than the trends of the other instruments. This difference might be related to the averaging kernels of GROMOS, which indicate that GROMOS retrieves information from higher altitudes than expected (~ 2 km difference).

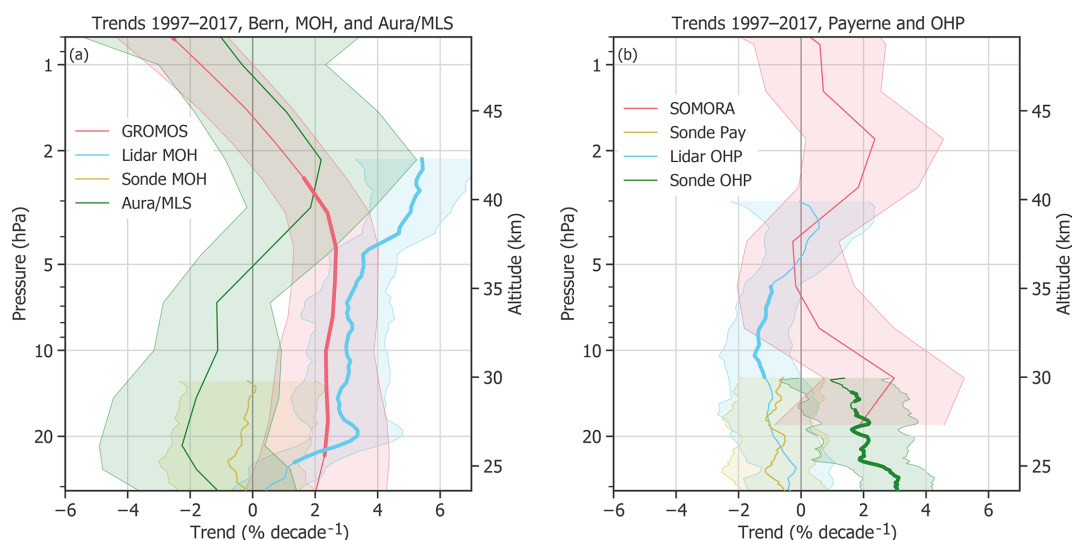


Figure 10. Ozone trends of different ground-based instruments in central Europe and Aura/MLS (over Bern, Switzerland). The 2σ uncertainties are shown by shaded areas. Bold lines indicate trends that are significantly different from zero (at a 95 % confidence interval). The trends at Bern and MOH as well as the Aura/MLS trend are shown in (a), whereas (b) shows the trends from data sets at Payerne and OHP.

In the middle and lower stratosphere, at altitudes below 5 hPa (≈ 36 km), the estimated trends differ from each other. The microwave radiometers and the MOH lidar report trends of 0 \% decade^{-1} to 3 \% decade^{-1} , and also the ozonesonde at OHP confirms this positive trend. However, the ozonesondes at MOH and Payerne as well as Aura/MLS and the OHP lidar report a trend of around 0 \% decade^{-1} to $-2 \text{ \% decade}^{-1}$ below 5 hPa. Some of these observed trend differences can be explained by instrumental changes or differences in processing algorithms and instrument setup. The discrepancy between ozonesonde and lidar trends at OHP, for example, are possibly due to the change of the pressure–temperature radiosonde manufacturer in 2007, which resulted in a step change in bias between ozonesonde and lidar observations. A thorough harmonization would be necessary to correct the trend for this change. The SOMORA trend shows a positive peak at 30 km, which is probably due to homogenization problems that are corrected in the new retrieval version of SOMORA, which is, however, not yet used in our analyses (Maillard Barras et al., 2019). Furthermore, we have shown that sampling rates and starting years have an important effect on the resulting trend. The trend period lengths differ between SOMORA, Aura/MLS, and the other data sets, which might also partly explain differences in trend estimates. To explain the remaining trend differences in the lower stratosphere, further corrections, e.g. for anomalies, instrumental changes, or sampling rates, would be necessary. In brief, trends in the lower stratosphere are not yet clear. For some instruments, significant positive trends are reported, but for many other instruments, trends are negative and mostly not significantly different from zero. This result reflects the currently ongoing discussion about lower stratospheric ozone

trends (e.g. Ball et al., 2018; Chipperfield et al., 2018; Stone et al., 2018).

In summary, our ground-based instrument data agree that ozone is recovering around 3 hPa (≈ 39 km), with trends ranging between 1 \% decade^{-1} and 3 \% decade^{-1} for most data sets. In the lower and middle stratosphere between 24 and 37 km (≈ 31 and 4 hPa), however, the trends disagree, suggesting that further research is needed to explain the differences between ground-based trends in the lower stratosphere.

5 Conclusions

Our study emphasizes that natural or instrumental anomalies in a time series affect ground-based stratospheric ozone trends. We found that the ozone time series from the GROMOS radiometer (Bern, Switzerland) shows some unexplained anomalies. Accounting for these anomalies in the trend estimation can substantially improve the resulting trends. We further compared different ground-based ozone trend profiles and found an agreement on ozone recovery at around 40 km over central Europe. At the same time, we observed trend differences ranging between $-2 \text{ \% decade}^{-1}$ and 3 \% decade^{-1} at lower altitudes.

We compared the GROMOS time series with data from other ground-based instruments in central Europe and found that they generally agree within $\pm 10 \text{ \%}$. Periods with larger discrepancies have been identified and confirmed to be anomalies in the GROMOS time series. We did not find the origins of these anomalies and assume that they are due to instrumental issues of GROMOS. The identified anomalies have been considered in the GROMOS trend estimations be-

cause they can distort the trend. By testing this approach first on a theoretical time series and then with the real GROMOS data, we have shown that identifying anomalies in a time series and considering them in the trend analysis makes the resulting trend estimates more accurate. With this method, we propose an approach of advanced trend analysis based on the work of von Clarmann et al. (2010) that may also be applied to other ground- or satellite-based data sets to obtain more consistent trend results.

Comparing the GROMOS trend with other ground-based trends in central Europe suggests that ozone is recovering in the upper stratosphere between around 4 and 1.8 hPa (\approx 37 and 43 km). This result confirms recent, mainly satellite-based studies. At other altitudes, we have observed contrasting trend estimates. We have shown that the observed differences can partly be explained by different sampling rates and starting years. Other reasons might be instrumental changes or nonconformity in measurement techniques, instrumental systems, or processing approaches. Further, the spatial distance between some stations might explain some trend differences because different air masses can be measured, especially in winter when polar air extends over parts of Europe. Accounting for anomalies in the different data sets as proposed in the present study might be a first step to improve trend estimates. Combined with further corrections, e.g. for sampling rates or instrumental differences, this approach may help to decrease discrepancies between trend estimates from different instruments. In many other studies, the observed trend differences are less apparent because the ground-based data are averaged over latitudinal bands (e.g. WMO, 2014; Harris et al., 2015; Steinbrecht et al., 2017). Nevertheless, it is important to be aware that ground-based trend estimates differ considerably, especially in the lower stratosphere. Exploring the origin of the differences and improving the trend profiles in a similar way as we did for GROMOS may be an important further step on the way to monitoring the development of the ozone layer. To summarize, we have shown that anomalies in time series need to be considered when estimating trends. Our ground-based results confirm that ozone is recovering in the upper stratosphere above central Europe and emphasize the urgency to further investigate lower stratospheric ozone changes. The presented approach to improve trend estimates can help in this endeavour.

Data availability. All ground-based data used in this study are available at <ftp://ftp.cpc.ncep.noaa.gov/ndacc>. The MLS data from the Aura satellite are available at https://disc.gsfc.nasa.gov/datasets/ML2O3_V004/summary (Schwartz, 2015).

Author contributions. LB and KH designed the concept and the methodology. LB carried out the analysis and prepared the manuscript. TvC provided the trend model. All co-authors con-

tributed to the manuscript preparation and the interpretation of the results.

Competing interests. The authors declare that they have no competing interests. Thomas von Clarmann is co-editor of Atmospheric Chemistry and Physics, but he is not involved in the evaluation of this paper.

Acknowledgements. The authors thank the Aura/MLS team for providing the satellite data. This study has been funded by the Swiss National Science Foundation, grant number 200021-165516.

Review statement. This paper was edited by Jens-Uwe Groö and reviewed by two anonymous referees.

References

- Bai, K., Chang, N.-B., Shi, R., Yu, H., and Gao, W.: An inter-comparison of multi-decadal observational and re-analysis data sets for global total ozone trends and variability analysis, *J. Geophys. Res.-Atmos.*, 122, 1–21, <https://doi.org/10.1002/2016JD025835>, 2017.
- Ball, W. T., Alsing, J., Mortlock, D. J., Rozanov, E. V., Tummon, F., and Haigh, J. D.: Reconciling differences in stratospheric ozone composites, *Atmos. Chem. Phys.*, 17, 12269–12302, <https://doi.org/10.5194/acp-17-12269-2017>, 2017.
- Ball, W. T., Alsing, J., Mortlock, D. J., Staehelin, J., Haigh, J. D., Peter, T., Tummon, F., Stübi, R., Stenke, A., Anderson, J., Bourassa, A., Davis, S. M., Degenstein, D., Frith, S. M., Froidevaux, L., Roth, C., Sofieva, V., Wang, R., Wild, J., Yu, P., Ziemke, J. R., and Rozanov, E. V.: Evidence for continuous decline in lower stratospheric ozone offsetting ozone layer recovery, *Atmos. Chem. Phys.*, 18, 1379–1394, <https://doi.org/10.5194/acp-18-1379-2018>, 2018.
- Bates, B. C., Chandler, R. E., and Bowman, A. W.: Trend estimation and change point detection in individual climatic series using flexible regression methods, *J. Geophys. Res.-Atmos.*, 117, 1–9, <https://doi.org/10.1029/2011JD017077>, 2012.
- Bourassa, A. E., Roth, C. Z., Zawada, D. J., Rieger, L. A., McLinden, C. A., and Degenstein, D. A.: Drift-corrected Odin-OSIRIS ozone product: Algorithm and updated stratospheric ozone trends, *Atmos. Meas. Tech.*, 11, 489–498, <https://doi.org/10.5194/amt-11-489-2018>, 2018.
- Brewer, A. W. and Milford, J. R.: The Oxford-Kew Ozone Sonde, in: *Proc. R. Soc. Lond. Ser. A, Mathematical and Physical Sciences*, vol. 256, Royal Society, 470–495, <http://www.jstor.org/stable/2413928> (last access: 28 March 2019), 1960.
- Calisesi, Y.: The stratospheric ozone monitoring radiometer SOMORA: NDSC application document, Research report no. 2003-11, Institute of Applied Physics, University of Bern, Switzerland, 2003.
- Calisesi, Y., Soebijanta, V. T., and van Oss, R.: Regridding of remote soundings: Formulation and application to ozone profile comparison, *J. Geophys. Res.*, 110, D23306, <https://doi.org/10.1029/2005JD006122>, 2005.

- Chipperfield, M. P., Dhomse, S., Hossaini, R., Feng, W., Santee, M. L., Weber, M., Burrows, J. P., Wild, J. D., Loyola, D., and Coldewey-Egbers, M.: On the Cause of Recent Variations in Lower Stratospheric Ozone, *Geophys. Res. Lett.*, 45, 5718–5726, <https://doi.org/10.1029/2018GL078071>, 2018.
- Chubachi, S.: A special ozone observation at Syowa station, Antarctica from February 1982 to January 1983, in: *Atmos. Ozone, Proc. Quadrenn. Ozone Symp.*, edited by: Zerefos, C. S. and Ghazi, A., Halkidiki, Greece, 285–286, 1984.
- Connor, B. J., Parrish, A., and Tsou, J.-J.: Detection of stratospheric ozone trends by ground-based microwave observations, in: *Proc. SPIE 1491, Remote Sens. Atmos. Chem.*, edited by: McElroy, James L. and McNeal, R. J., vol. 1491, International Society for Optics and Photonics, Orlando, FL, USA, 218–230, <https://doi.org/10.1117/12.46665>, 1991.
- Damadeo, R. P., Zawodny, J. M., Remsberg, E. E., and Walker, K. A.: The impact of nonuniform sampling on stratospheric ozone trends derived from occultation instruments, *Atmos. Chem. Phys.*, 18, 535–554, <https://doi.org/10.5194/acp-18-535-2018>, 2018.
- Eckert, E., von Clarmann, T., Kiefer, M., Stiller, G. P., Lossow, S., Glatthor, N., Degenstein, D. A., Froidevaux, L., Godin-Beekmann, S., Leblanc, T., McDermid, S., Pastel, M., Steinbrecht, W., Swart, D. P. J., Walker, K. A., and Bernath, P. F.: Drift-corrected trends and periodic variations in MIPAS-IMK/IAA ozone measurements, *Atmos. Chem. Phys.*, 14, 2571–2589, <https://doi.org/10.5194/acp-14-2571-2014>, 2014.
- Eriksson, P., Jiménez, C., and Buehler, S. A.: Qpack, a general tool for instrument simulation and retrieval work, *J. Quant. Spectrosc. Ra.*, 91, 47–64, <https://doi.org/10.1016/j.jqsrt.2004.05.050>, 2005.
- Eriksson, P., Buehler, S., Davis, C., Emde, C., and Lemke, O.: ARTS, the atmospheric radiative transfer simulator, version 2, *J. Quant. Spectrosc. Ra.*, 112, 1551–1558, <https://doi.org/10.1016/j.jqsrt.2011.03.001>, 2011.
- Farman, J. C., Gardiner, B. G., and Shanklin, J. D.: Large losses of total ozone in Antarctica reveal seasonal ClO_x/NO_x interaction, *Nature*, 315, 207–210, <https://doi.org/10.1038/315207a0>, 1985.
- Favaro, G., Jeannot, P., and Stübi, R.: Re-evaluation and trend analysis of the Payerne ozone soundings, Scientific report no. 63, MeteoSwiss, Zürich, Switzerland, 2002.
- Fischer, H., Birk, M., Blom, C., Carli, B., Carlotti, M., Von Clarmann, T., Delbouille, L., Dudhia, A., Ehnhalt, D., Endemann, M., Flaud, J. M., Gessner, R., Kleinert, A., Koopman, R., Langen, J., López-Puertas, M., Mosner, P., Nett, H., Oelhaf, H., Perron, G., Remedios, J., Ridolfi, M., Stiller, G., and Zander, R.: MIPAS: An instrument for atmospheric and climate research, *Atmos. Chem. Phys.*, 8, 2151–2188, <https://doi.org/10.5194/acp-8-2151-2008>, 2008.
- Frith, S. M., Stolarski, R. S., Kramarova, N. A., and McPeters, R. D.: Estimating uncertainties in the SBUV Version 8.6 merged profile ozone data set, *Atmos. Chem. Phys.*, 17, 14695–14707, <https://doi.org/10.5194/acp-17-14695-2017>, 2017.
- Gaudel, A., Ancellet, G., and Godin-Beekmann, S.: Analysis of 20 years of tropospheric ozone vertical profiles by lidar and ECC at Observatoire de Haute Provence (OHP) at 44° N, 6.7° E, *Atmos. Environ.*, 113, 78–89, <https://doi.org/10.1016/j.atmosenv.2015.04.028>, 2015.
- Godin, S., Mégie, G., and Pelon, J.: Systematic lidar measurements of the stratospheric ozone vertical distribution, *Geophys. Res. Lett.*, 16, 547–550, 1989.
- Godin, S., Carswell, A. I., Donovan, D. P., Claude, H., Steinbrecht, W., McDermid, I. S., McGee, T. J., Gross, M. R., Nakane, H., Swart, D. P., Bergwerff, H. B., Uchino, O., von der Gathen, P., and Neuber, R.: Ozone differential absorption lidar algorithm intercomparison, *Appl. Opt.*, 38, 6225–6236, <https://doi.org/10.1364/AO.38.006225>, 1999.
- Godin-Beekmann, S., Porteneuve, J., and Garnier, A.: Systematic DIAL lidar monitoring of the stratospheric ozone vertical distribution at Observatoire de Haute-Provence (43.92° N, 5.71° E), *J. Environ. Monit.*, 5, 57–67, <https://doi.org/10.1039/b205880d>, 2003.
- Guirlet, M., Keckhut, P., Godin, S., and Mégie, G.: Description of the long-term ozone data series obtained from different instrumental techniques at a single location: The Observatoire de Haute-Provence (43.9° N, 5.7° E), *Ann. Geophys.*, 18, 1325–1339, <https://doi.org/10.1007/s00585-000-1325-y>, 2000.
- Harris, N. R. P., Hudson, R., and Phillips, C.: SPARC/IOC/GAW, Assessment of trends in the vertical distribution of ozone, SPARC Report No. 1, WMO Ozone Research and Monitoring Project Report No. 43, Geneva, Switzerland, 1998.
- Harris, N. R. P., Hassler, B., Tummon, F., Bodeker, G. E., Hubert, D., Petropavlovskikh, I., Steinbrecht, W., Anderson, J., Bhartia, P. K., Boone, C. D., Bourassa, A., Davis, S. M., Degenstein, D., Delcloo, A., Frith, S. M., Froidevaux, L., Godin-Beekmann, S., Jones, N., Kurylo, M. J., Kyrölä, E., Laine, M., Leblanc, S. T., Lambert, J.-C., Liley, B., Mahieu, E., Maycock, A., de Mazzière, M., Parrish, A. D., Querel, R., Rosenlof, K. H., Roth, C., Sioris, C., Staehelin, J., Stolarski, R. S., Stübi, R., Tamminen, J., Vigouroux, C., Walker, K. A., Wang, H. J., Wild, J., and Zawodny, J. M.: Past changes in the vertical distribution of ozone – Part 3: Analysis and interpretation of trends, *Atmos. Chem. Phys.*, 15, 9965–9982, <https://doi.org/10.5194/acp-15-9965-2015>, 2015.
- Hatzaki, M., Flocas, H. A., Simmonds, I., Kouroutzoglou, J., Keay, K., and Rudeva, I.: Seasonal aspects of an objective climatology of anticyclones affecting the mediterranean, *J. Clim.*, 27, 9272–9289, <https://doi.org/10.1175/JCLI-D-14-00186.1>, 2014.
- Hubert, D., Lambert, J.-C., Verhoelst, T., Granville, J., Keppens, A., Baray, J. L., Bourassa, A. E., Cortesi, U., Degenstein, D. A., Froidevaux, L., Godin-Beekmann, S., Hoppel, K. W., Johnson, B. J., Kyrölä, E., Leblanc, T., Lichtenberg, G., Marchand, M., McElroy, C. T., Murtagh, D., Nakane, H., Portafaix, T., Querel, R., Russell, J. M., Salvador, J., Smit, H. G. J., Stebel, K., Steinbrecht, W., Strawbridge, K. B., Stübi, R., Swart, D. P. J., Taha, G., Tarasick, D. W., Thompson, A. M., Urban, J., Van Gijssel, J. A. E., Van Malderen, R., Von Der Gathen, P., Walker, K. A., Wolfram, E., and Zawodny, J. M.: Ground-based assessment of the bias and long-term stability of 14 limb and occultation ozone profile data records, *Atmos. Meas. Tech.*, 9, 2497–2534, <https://doi.org/10.5194/amt-9-2497-2016>, 2016.
- Hubert et al.: The temporal and spatial homogeneity of ozone profile data records obtained by ozonesonde, lidar and microwave radiometer networks, in preparation, 2019.
- Jeannot, P., Stübi, R., Levrat, G., Viatte, P., and Staehelin, J.: Ozone balloon soundings at Payerne (Switzerland): Reevaluation of the time series 1967–2002 and trend analysis, *J. Geophys. Res.*

- Atmos., 112, D11302, <https://doi.org/10.1029/2005JD006862>, 2007.
- Jones, A., Urban, J., Murtagh, D. P., Sanchez, C., Walker, K. A., Livesey, N. J., Froidevaux, L., and Santee, M. L.: Analysis of HCl and ClO time series in the upper stratosphere using satellite data sets, *Atmos. Chem. Phys.*, 11, 5321–5333, <https://doi.org/10.5194/acp-11-5321-2011>, 2011.
- Kämpfer, N.: Microwave remote sensing of the atmosphere in Switzerland, *Opt. Eng.*, 34, 2413–2424, 1995.
- Keppens, A., Lambert, J. C., Granville, J., Miles, G., Siddans, R., Van Peet, J. C., Van Der A, R. J., Hubert, D., Verhoelst, T., Delcloo, A., Godin-Beekmann, S., Kivi, R., Stübi, R., and Zehner, C.: Round-robin evaluation of nadir ozone profile retrievals: Methodology and application to MetOp-A GOME-2, *Atmos. Meas. Tech.*, 8, 2093–2120, <https://doi.org/10.5194/amt-8-2093-2015>, 2015.
- Komhyr, W. D.: Electrochemical concentration cells for gas analysis, *Ann. Geophys.*, 25, 203–210, 1969.
- Kuttippurath, J. and Nair, P. J.: The signs of Antarctic ozone hole recovery, *Sci. Rep.*, 7, 585 pp., <https://doi.org/10.1038/s41598-017-00722-7>, 2017.
- Maillard Barras, E., Ruffieux, D., and Hocke, K.: Stratospheric ozone profiles over Switzerland measured by SOMORA, ozonesonde and MLS/AURA satellite, *Int. J. Remote Sens.*, 30, 4033–4041, <https://doi.org/10.1080/01431160902821890>, 2009.
- Maillard Barras, E., Haefele, A., Stübi, R., and Ruffieux, D.: A method to derive the Site Atmospheric State Best Estimate (SASBE) of ozone profiles from radiosonde and passive microwave data, *Atmos. Meas. Tech. Discuss.*, 8, 3399–3422, <https://doi.org/10.5194/amt-d-8-3399-2015>, 2015.
- Maillard Barras et al.: Trends of stratospheric ozone daily cycle, in preparation, 2019.
- McCormick, M., Zawodny, J., Veiga, R., Larsen, J., and Wang, P.: An overview of SAGE I and II ozone measurements, *Planet. Space Sci.*, 37, 1567–1586, [https://doi.org/10.1016/0032-0633\(89\)90146-3](https://doi.org/10.1016/0032-0633(89)90146-3), 1989.
- Millán, L. F., Livesey, N. J., Santee, M. L., Neu, J. L., Manney, G. L., and Fuller, R. A.: Case studies of the impact of orbital sampling on stratospheric trend detection and derivation of tropical vertical velocities: solar occultation vs. limb emission sounding, *Atmos. Chem. Phys.*, 16, 11521–11534, <https://doi.org/10.5194/acp-16-11521-2016>, 2016.
- Molina, M. J. and Rowland, F. S.: Stratospheric sink for chlorofluoromethanes: chlorine atom-catalysed destruction of ozone, *Nature*, 249, 810–812, <https://doi.org/10.1038/249810a0>, 1974.
- Moreira, L.: Trends and oscillations in middle atmospheric ozone observed by a ground-based microwave radiometer, Phd. thesis, University of Bern, Switzerland, 2017.
- Moreira, L., Hocke, K., Eckert, E., Von Clarmann, T., and Kämpfer, N.: Trend analysis of the 20-year time series of stratospheric ozone profiles observed by the GROMOS microwave radiometer at Bern, *Atmos. Chem. Phys.*, 15, 10999–11009, <https://doi.org/10.5194/acp-15-10999-2015>, 2015.
- Moreira, L., Hocke, K., Navas-Guzmán, F., Eckert, E., von Clarmann, T., and Kämpfer, N.: The natural oscillations in stratospheric ozone observed by the GROMOS microwave radiometer at the NDACC station Bern, *Atmos. Chem. Phys.*, 16, 10455–10467, <https://doi.org/10.5194/acp-16-10455-2016>, 2016.
- Moreira, L., Hocke, K., and Kämpfer, N.: Comparison of ozone profiles and influences from the tertiary ozone maximum in the night-to-day ratio above Switzerland, *Atmos. Chem. Phys.*, 17, 10259–10268, <https://doi.org/10.5194/acp-17-10259-2017>, 2017.
- Nair, P. J., Godin-Beekmann, S., Pazmiño, A., Hauchecorne, A., Ancellet, G., Petropavlovskikh, I., Flynn, L. E., and Froidevaux, L.: Coherence of long-term stratospheric ozone vertical distribution time series used for the study of ozone recovery at a northern mid-latitude station, *Atmos. Chem. Phys.*, 11, 4957–4975, <https://doi.org/10.5194/acp-11-4957-2011>, 2011.
- Nair, P. J., Godin-Beekmann, S., Froidevaux, L., Flynn, L. E., Zawodny, J. M., Russell, J. M., Pazmiño, A., Ancellet, G., Steinbrecht, W., Claude, H., Leblanc, T., McDerimid, S., Van Gijssel, J. A. E., Johnson, B., Thomas, A., Hubert, D., Lambert, J.-C., Nakane, H., and Swart, D. P. J.: Relative drifts and stability of satellite and ground-based stratospheric ozone profiles at NDACC lidar stations, *Atmos. Meas. Tech.*, 5, 1301–1318, <https://doi.org/10.5194/amt-5-1301-2012>, 2012.
- Nair, P. J., Godin-Beekmann, S., Kuttippurath, J., Ancellet, G., Goutail, F., Pazmiño, A., Froidevaux, L., Zawodny, J. M., Evans, R. D., Wang, H. J., Anderson, J., and Pastel, M.: Ozone trends derived from the total column and vertical profiles at a northern mid-latitude station, *Atmos. Chem. Phys.*, 13, 10373–10384, <https://doi.org/10.5194/acp-13-10373-2013>, 2013.
- Nair, P. J., Froidevaux, L., Kuttippurath, J., Zawodny, J. M., Russell, J. M., Steinbrecht, W., Claude, H., Leblanc, T., Van Gijssel, J. A., Johnson, B., Swart, D. P., Thomas, A., Querel, R., Wang, R., and Anderson, J.: Subtropical and midlatitude ozone trends in the stratosphere: Implications for recovery, *J. Geophys. Res.-Atmos.*, 120, 7247–7257, <https://doi.org/10.1002/2014JD022371>, 2015.
- National Research Council of Canada: Latest Solar Radio Flux Report from DRAO, Penticton, <http://www.spaceweather.ca/solarflux/sx-4-en.php>, last access: 12 March 2019.
- NDACC: Network for the Detection of Atmospheric Composition Change, <http://www.ndaccdemo.org>, last access: 12 March 2019.
- Newchurch, M. J., Yang, E.-S., Cunnold, D. M., Reinsel, G. C., Zawodny, J. M., and Russell, J. M.: Evidence for slowdown in stratospheric ozone loss: First stage of ozone recovery, *J. Geophys. Res.-Atmos.*, 108, 4507, <https://doi.org/10.1029/2003JD003471>, 2003.
- Parkinson, C. L., Ward, A., and King, M. D. (Eds.): *Earth Science Reference Handbook – A Guide to NASA’s Earth Science Program and Earth Observing Satellite Missions*, National Aeronautics and Space Administration, Washington, DC, 2006.
- Pazmiño, A., Godin-Beekmann, S., Hauchecorne, A., Claud, C., Khaykin, S., Goutail, F., Wolfram, E., Salvador, J., and Quel, E.: Multiple symptoms of total ozone recovery inside the Antarctic vortex during austral spring, *Atmos. Chem. Phys.*, 18, 7557–7572, <https://doi.org/10.5194/acp-18-7557-2018>, 2018.
- Peter, R.: *The Ground-based Millimeter-wave Ozone Spectrometer – GROMOS*, Research report no. 97-13, Institute of Applied Physics, University of Bern, Switzerland, 1997.
- Ramaswamy, V., Chanin, M.-L., Angell, J., Barnett, J., Gaffen, D., Gelman, M., Keckhut, P., Koshelkov, Y., Labitzke, K., Lin, J.-J. R., O’Neill, A., Nash, J., Randel, W., Rood, R., Shine, K., Shiotani, M., and Swinbank, R.: Stratospheric temperature trends: Observations and model simulations, *Rev. Geophys.*, 39, 71–122, <https://doi.org/10.1029/1999RG000065>, 2001.

- Reinsel, G. C., Miller, A. J., Weatherhead, E. C., Flynn, L. E., Nagatani, R. M., Tiao, G. C., and Wuebbles, D. J.: Trend analysis of total ozone data for turnaround and dynamical contributions, *J. Geophys. Res.-Atmos.*, 110, D16306, <https://doi.org/10.1029/2004JD004662>, 2005.
- Rodgers, C. D.: *Inverse Methods for Atmospheric Sounding: Theory and Practice*, World Scientific Publishing Co. Pte. Ltd, Singapore, 2000.
- Rodgers, C. D. and Connor, B. J.: Intercomparison of remote sounding instruments, *J. Geophys. Res.*, 108, 46–48, <https://doi.org/10.1029/2002JD002299>, 2003.
- Schanz, A., Hocke, K., and Kämpfer, N.: Daily ozone cycle in the stratosphere: Global, regional and seasonal behaviour modelled with the Whole Atmosphere Community Climate Model, *Atmos. Chem. Phys.*, 14, 7645–7663, <https://doi.org/10.5194/acp-14-7645-2014>, 2014.
- Schotland, R. M.: Errors in the Lidar Measurement of Atmospheric Gases by Differential Absorption, *J. Appl. Meteorol.*, 13, 71–77, [https://doi.org/10.1175/1520-0450\(1974\)013<0071:EITLMO>2.0.CO;2](https://doi.org/10.1175/1520-0450(1974)013<0071:EITLMO>2.0.CO;2), 1974.
- Schwartz, M., Froidevaux, L., Livesey, N. and Read, W.: MLS/Aura Level 2 Ozone (O₃) Mixing Ratio V004, Greenbelt, MD, USA, Goddard Earth Sciences Data and Information Services Center (GES DISC), available at: https://disc.gsfc.nasa.gov/datasets/ML2O3_V004/summary (last accessed: 5 February 2018), 2015.
- Shepherd, T. G., Plummer, D. A., Scinocca, J. F., Hegglin, M. I., Fioletov, V. E., Reader, M. C., Remsberg, E., von Clarmann, T., and Wang, H. J.: Reconciliation of halogen-induced ozone loss with the total-column ozone record, *Nat. Geosci.*, 7, 443–449, <https://doi.org/10.1038/ngeo2155>, 2014.
- Smit, H. G. J. and ASOPOS Panel: Quality Assurance and Quality Control for Ozone Sonde Measurements in GAW, World Meteorological Organization, Global Atmosphere Watch, GAW Report No. 201, Geneva, Switzerland, 2013.
- Smit, H. G. J. and Kley, D.: Jülich Ozone Sonde Intercomparison Experiment (JOSIE), World Meteorological Organization, Global Atmosphere Watch, Report No. 130, 1996.
- Sofieva, V. F., Kyrölä, E., Laine, M., Tamminen, J., Degenstein, D., Bourassa, A., Roth, C., Zawada, D., Weber, M., Rozanov, A., Rahpoe, N., Stiller, G., Laeng, A., von Clarmann, T., Walker, K. A., Sheese, P., Hubert, D., van Roozendaal, M., Zehner, C., Damadeo, R., Zawodny, J., Kramarova, N., and Bhartia, P. K.: Merged SAGE II, Ozone_cci and OMPS ozone profile dataset and evaluation of ozone trends in the stratosphere, *Atmos. Chem. Phys.*, 17, 12533–12552, <https://doi.org/10.5194/acp-17-12533-2017>, 2017.
- Solomon, S., Ivy, D. J., Kinnison, D., Mills, M. J., Neely, R. R., and Schmidt, A.: Emergence of healing in the Antarctic ozone layer, *Science*, 353, 269–274, <https://doi.org/10.1126/science.aae0061>, 2016.
- SPARC/IO3C/GAW: SPARC/IO3C/GAW Report on Long-term Ozone Trends and Uncertainties in the Stratosphere, edited by: Petropavlovskikh, I., Godin-Beekmann, S., Hubert, D., Damadeo, R., Hassler, B., and Sofieva, V., SPARC Report No. 9, GAW Report No. 241, WCRP-17/2018, <https://doi.org/10.17874/f899e57a20b>, 2019.
- Steinbrecht, W., Claude, H., Schöenborn, F., McDermid, I. S., Leblanc, T., Godin, S., Song, T., Swart, D. P. J., Meijer, Y. J., Bodeker, G. E., Connor, B. J., Kämpfer, N., Hocke, K., Calisei, Y., Schneider, N., de la Noë, J., Parrish, A. D., Boyd, I. S., Brühl, C., Steil, B., Giorgetta, M. A., Manzini, E., Thomason, L. W., Zawodny, J. M., McCormick, M. P., Russell, J. M., Bhartia, P. K., Stolarski, R. S., and Hollandsworth-Frith, S. M.: Long-term evolution of upper stratospheric ozone at selected stations of the Network for the Detection of Stratospheric Change (NDSC), *J. Geophys. Res.-Atmos.*, 111, D10308, <https://doi.org/10.1029/2005JD006454>, 2006.
- Steinbrecht, W., Claude, H., Schöenborn, F., McDermid, I. S., Leblanc, T., Godin-Beekmann, S., Keckhut, P., Hauchecorne, A., Van Gijssel, J. A. E., Swart, D. P. J., Bodeker, G. E., Parrish, A. D., Boyd, I. S., Kämpfer, N., Hocke, K., Stolarski, R. S., Frith, S. M., Thomason, L. W., Remsberg, E. E., von Savigny, C., Rozanov, A., and Burrows, J. P.: Ozone and temperature trends in the upper stratosphere at five stations of the Network for the Detection of Atmospheric Composition Change, *Int. J. Remote Sens.*, 30, 3875–3886, <https://doi.org/10.1080/01431160902821841>, 2009a.
- Steinbrecht, W., McGee, T. J., Twigg, L. W., Claude, H., Schöenborn, F., Sumnicht, G. K., and Silbert, D.: Intercomparison of stratospheric ozone and temperature profiles during the October 2005 Hohenpeißenberg Ozone Profiling Experiment (HOPE), *Atmos. Meas. Tech.*, 2, 125–145, <https://doi.org/10.5194/amt-2-125-2009>, 2009b.
- Steinbrecht, W., Köhler, U., Schöenborn, F., Adelwart, M., Petersen, D., Heinen, M., Munier, H., Claude, H., Steiner, S., and Attmannspacher, W.: 50 Years of Routine Ozone Soundings at Hohenpeißenberg, Quadrennial Ozone Symposium of the International Ozone Commission, Edinburgh, UK, 4–9 September 2016, QOS2016-28-1, 2016.
- Steinbrecht, W., Froidevaux, L., Fuller, R., Wang, R., Anderson, J., Roth, C., Bourassa, A., Degenstein, D., Damadeo, R., Zawodny, J., Frith, S. M., McPeters, R., Bhartia, P., Wild, J., Long, C., Davis, S., Rosenlof, K., Sofieva, V., Walker, K., Rahpoe, N., Rozanov, A., Weber, M., Laeng, A., von Clarmann, T., Stiller, G., Kramarova, N., Godin-Beekmann, S., Leblanc, T., Querel, R., Swart, D., Boyd, I., Hocke, K., Kämpfer, N., Mailard Barras, E., Moreira, L., Nedoluha, G., Vigouroux, C., Blumenstock, T., Schneider, M., García, O., Jones, N., Mahieu, E., Smale, D., Kotkamp, M., Robinson, J., Petropavlovskikh, I., Harris, N., Hassler, B., Hubert, D., and Tummon, F.: An update on ozone profile trends for the period 2000 to 2016, *Atmos. Chem. Phys.*, 17, 10675–10690, <https://doi.org/10.5194/acp-17-10675-2017>, 2017.
- Stiller, G. P., von Clarmann, T., Haenel, F., Funke, B., Glatthor, N., Grabowski, U., Kellmann, S., Kiefer, M., Linden, A., Lossow, S., and López-Puertas, M.: Observed temporal evolution of global mean age of stratospheric air for the 2002 to 2010 period, *Atmos. Chem. Phys.*, 12, 3311–3331, <https://doi.org/10.5194/acp-12-3311-2012>, 2012.
- Stolarski, R. S. and Frith, S. M.: Search for evidence of trend slowdown in the long-term TOMS/SBUV total ozone data record: the importance of instrument drift uncertainty, *Atmos. Chem. Phys.*, 6, 4057–4065, <https://doi.org/10.5194/acp-6-4057-2006>, 2006.
- Stone, K. A., Solomon, S., and Kinnison, D. E.: On the Identification of Ozone Recovery, *Geophys. Res. Lett.*, 45, 5158–5165, <https://doi.org/10.1029/2018GL077955>, 2018.
- Strahan, S. E. and Douglass, A. R.: Decline in Antarctic Ozone Depletion and Lower Stratospheric Chlorine Determined

- From Aura Microwave Limb Sounder Observations, *Geophys. Res. Lett.*, 45, 382–390, <https://doi.org/10.1002/2017GL074830>, 2018.
- Studer, S., Hocke, K., Schanz, A., Schmidt, H., and Kämpfer, N.: A climatology of the diurnal variations in stratospheric and mesospheric ozone over Bern, Switzerland, *Atmos. Chem. Phys.*, 14, 5905–5919, <https://doi.org/10.5194/acp-14-5905-2014>, 2014.
- Tsou, J. J., Connor, B. J., Parrish, A. D., McDermid, I. S., and Chu, W. P.: Ground-based microwave monitoring of middle atmosphere ozone: Comparison to lidar and Stratospheric and Gas Experiment II satellite observations, *J. Geol.*, 100, 3005–3016, 1995.
- von Clarmann, T., Grabowski, U., and Kiefer, M.: On the role of non-random errors in inverse problems in radiative transfer and other applications, *J. Quant. Spectrosc. Ra.*, 71, 39–46, [https://doi.org/10.1016/S0022-4073\(01\)00010-3](https://doi.org/10.1016/S0022-4073(01)00010-3), 2001.
- von Clarmann, T., Stiller, G. P., Grabowski, U., Eckert, E., and Orphal, J.: Technical note: Trend estimation from irregularly sampled, correlated data, *Atmos. Chem. Phys.*, 10, 6737–6747, <https://doi.org/10.5194/acp-10-6737-2010>, 2010.
- Vyushin, D. I., Fioletov, V. E., and Shepherd, T. G.: Impact of long-range correlations on trend detection in total ozone, *J. Geophys. Res.*, 112, D14307, <https://doi.org/10.1029/2006JD008168>, 2007.
- Wargan, K., Orbe, C., Pawson, S., Ziemke, J. R., Oman, L. D., Olsen, M. A., Coy, L., and Emma Knowland, K.: Recent Decline in Extratropical Lower Stratospheric Ozone Attributed to Circulation Changes, *Geophys. Res. Lett.*, 45, 5166–5176, <https://doi.org/10.1029/2018GL077406>, 2018.
- Waters, J. W., Froidevaux, L., Harwood, R. S., Jarnot, R. F., Pickett, H. M., Read, W. G., Siegel, P. H., Cofield, R. E., Filipiak, M. J., Flower, D. A., Holden, J. R., Lau, G. K., Livesey, N. J., Manney, G. L., Pumphrey, H. C., Santee, M. L., Wu, D. L., Cuddy, D. T., Lay, R. R., Loo, M. S., Perun, V. S., Schwartz, M. J., Stek, P. C., Thurstans, R. P., Boyles, M. A., Chandra, K. M., Chavez, M. C., Chen, G. S., Chudasama, B. V., Dodge, R., Fuller, R. A., Girard, M. A., Jiang, J. H., Jiang, Y., Knosp, B. W., Labelle, R. C., Lam, J. C., Lee, K. A., Miller, D., Oswald, J. E., Patel, N. C., Pukala, D. M., Quintero, O., Scaff, D. M., Van Snyder, W., Tope, M. C., Wagner, P. A., and Walch, M. J.: The Earth Observing System Microwave Limb Sounder (EOS MLS) on the aura satellite, *IEEE Trans. Geosci. Remote Sens.*, 44, 1075–1092, <https://doi.org/10.1109/TGRS.2006.873771>, 2006.
- Weatherhead, E. C., Reinsel, G. C., Tiao, G. C., Jackman, C. H., Bishop, L., Hollandsworth, S. M., Deluisi, J., Keller, T., Oltmans, S. J., Fleming, E. L., Wuebbles, D. J., Kerr, J. B., Miller, A. J., Herman, J., McPeters, R., Nagatani, R. M., and Frederick, J. E.: Detecting the recovery of total column ozone, *J. Geophys. Res.*, 105, 22201–22210, <https://doi.org/10.1029/2000JD900063>, 2000.
- Weber, M., Coldewey-Egbers, M., Fioletov, V. E., Frith, S. M., Wild, J. D., Burrows, J. P., Long, C. S., and Loyola, D.: Total ozone trends from 1979 to 2016 derived from five merged observational datasets – the emergence into ozone recovery, *Atmos. Chem. Phys.*, 18, 2097–2117, <https://doi.org/10.5194/acp-18-2097-2018>, 2018.
- Werner, J., Rothe, K. W., and Walther, H.: Monitoring of the stratospheric ozone layer by laser radar, *Appl. Phys. B*, 32, 113–118, <https://doi.org/10.1007/BF00688815>, 1983.
- WMO: Scientific Assessment of Ozone Depletion: 2014, World Meteorological Organization, Global Ozone Research and Monitoring Project – Report No. 55, Geneva, Switzerland, p. 416, 2014.
- WMO: Scientific Assessment of Ozone Depletion: 2018, World Meteorological Organization, Global Ozone Research and Monitoring Project – Report No. 58, Geneva, Switzerland, p. 588, 2018.
- Wolter, K. and Timlin, M. S.: Measuring the strength of ENSO events: How does 1997/98 rank?, *Weather*, 53, 315–324, <https://doi.org/10.1002/j.1477-8696.1998.tb06408.x>, 1998.
- Zanis, P., Maillard, E., Staehelin, J., Zerefos, C., Kosmidis, E., Tourpali, K., and Wohltmann, I.: On the turnaround of stratospheric ozone trends deduced from the reevaluated Umkehr record of Arosa, Switzerland, *J. Geophys. Res.-Atmos.*, 111, D22307, <https://doi.org/10.1029/2005JD006886>, 2006.

A.2 STUDY ON OZONE TRENDS IN LAUDER, NEW ZEALAND






The following article was submitted to *Remote Sensing* in October 2020.

FULL CITATION:

L. Bernet, I. Boyd, G. Nedoluha, R. Querel, D. Swart and K. Hocke (2020a). Validation and trend analysis of stratospheric ozone data from ground-based observations at Lauder, New Zealand. In: *Remote Sensing* in review, pp. 1–14

Article

Validation and Trend Analysis of Stratospheric Ozone Data from Ground-Based Observations at Lauder, New Zealand

Leonie Bernet ^{1,2,*} , Ian Boyd ³ , Gerald Nedoluha ⁴, Richard Querel ⁵ , Daan Swart ⁶  and Klemens Hocke ^{1,2} 

¹ Institute of Applied Physics, University of Bern, 3012 Bern, Switzerland

² Oeschger Centre for Climate Change Research, University of Bern, 3012 Bern, Switzerland

³ BC Scientific Consulting LLC, Stony Brook, NY, USA

⁴ Naval Research Laboratory, Remote Sensing Division, Washington, DC, USA

⁵ National Institute of Water and Atmospheric Research, Lauder, New Zealand

⁶ National Institute for Public Health and the Environment (RIVM), Bilthoven, The Netherlands

* Correspondence: leonie.bernet@iap.unibe.ch

Version October 23, 2020 submitted to Remote Sens.

Abstract: Changes in stratospheric ozone have to be assessed continuously to evaluate the effectiveness of the Montreal Protocol. In the southern hemisphere, few ground-based observational datasets exist, making measurements at the NDACC (Network for the Detection of Atmospheric Composition Change) station at Lauder, New Zealand invaluable. Investigating these datasets in detail is essential to derive realistic ozone trends. We compared lidar data and microwave radiometer data with collocated Aura Microwave Limb sounder (MLS) satellite data and ERA5 reanalysis data. The detailed comparison makes it possible to assess inhomogeneities in the data. We find good agreement between the datasets but also some possible biases, especially in the ERA5 data. The data uncertainties and the inhomogeneities were then considered when deriving trends. Using two regression models from the Long-term Ozone Trends and Uncertainties in the Stratosphere (LOTUS) project and from the Karlsruhe Institute of Technology (KIT), we estimated resulting ozone trends. Further, we assessed how trends are affected by data uncertainties and inhomogeneities. We find positive ozone trends throughout the stratosphere between 0% and 5% per decade and show that considering data uncertainties and inhomogeneities in the regression affects the resulting trends.

Keywords: stratospheric ozone; trends; ozone profiles; microwave radiometry; lidars

1. Introduction

Changes in stratospheric ozone have to be assessed continuously to verify how it reacts to the decline of ozone-depleting substances (ODSs) and to a changing climate. Anthropogenic ODS emissions caused a strong decrease in stratospheric ozone observed from the 1960s. The Montreal Protocol (1987) succeeded in reducing ODS emissions. Consequently, concentrations of stratospheric chlorine have been decreasing since 1997 [1], and stratospheric ozone generally stopped declining in the late 1990s [e.g. 2]. However, an increase in stratospheric ozone has proved difficult to detect, and global positive ozone trends have recently been recorded only in the upper stratosphere [e.g. 3–5].

Stable long-term measurements of stratospheric ozone are indispensable to assessing changes in stratospheric ozone. In the southern hemisphere (SH) mid-latitudes, continuous stratospheric ozone measurements are rare. Ozone observations at Lauder, New Zealand are therefore invaluable to derive stratospheric ozone trends at southern mid-latitudes. The Lauder ozone measurements are part of the Network for the Detection of Atmospheric Composition Change [6] and have provided

29 stable, continuous measurements since the early 1980s. Recently, Lauder stratospheric ozone data
30 have been used in several trend studies and reports, such as Steinbrecht *et al.*'s [2017] study and the
31 comprehensive report on Long-term Ozone Trends and Uncertainties in the Stratosphere (LOTUS) [3].
32 However, the collocated time series of various ground-based instruments at Lauder have not been
33 compared in detail. Investigating the time series in detail is required to assess their suitability for trend
34 estimations.

35 The aim of the present study is to investigate ozone time series at Lauder and to verify whether
36 they are suitable for trend estimation. For this purpose, we compare coincident measurements of
37 microwave radiometer, lidar, ERA5 reanalysis data, and satellite data from the Aura Microwave Limb
38 Sounder (Aura MLS) at Lauder to identify possible inhomogeneities. Particularly, we investigate
39 whether the datasets agree. If one dataset deviates from the others, it might be the result of
40 measurement failures, which are then considered in the trend estimation. Further, we compare
41 two trend analysis methods, the LOTUS regression [3] and the KIT model developed at the Karlsruhe
42 Institute of Technology (KIT) [7]. Both models are based on multiple linear regression. The KIT model
43 considers data uncertainties by default, but these have not been considered in the LOTUS model for
44 ground-based data so far [3]. Finally, we assess how inhomogeneities in the time series and data
45 uncertainties affect the trend estimates.

46 2. Ozone Datasets

47 We use stratospheric ozone data (1997 to 2019) from a microwave radiometer (MWR) and a lidar,
48 both located at Lauder, New Zealand (45° S, 169.7° E, 370 m above sea level (a.s.l.)). Both instruments
49 are part of NDACC, and the data are archived on the NDACC website [6]. In addition, we use ozone
50 profiles from the MLS on the Aura satellite [8] and ERA5 reanalysis data [9]. We limit our analyses to
51 altitudes from 14 to 50 km and refer for convenience to the lower stratosphere (14 to 20 km), the middle
52 stratosphere (20 to 30 km), the upper-middle stratosphere (30 to 39 km), and the upper stratosphere (39
53 to 50 km).

54 2.1. Microwave Radiometer

55 The Microwave Ozone Profiling Instrument (MOPI) is an MWR that measured stratospheric
56 ozone at Lauder from 1992 to 2016. It measures ozone emission of ozone molecules due to rotational
57 transitions at 110.836 GHz at a 20-minute resolution. The measured spectra are then used to retrieve
58 ozone volume mixing ratio (VMR) profiles from 20 to 68 km, with a vertical resolution of around 7
59 to 8 km at 10 hPa [10]. Measurements are performed in clear-sky and some overcast conditions and
60 are averaged to obtain up to two daytime and two nighttime retrievals per day [10]. We use the most
61 recently retrieved MWR data (version 6) that are available on NDACC [6] (last access: 01.04.2020) and
62 at <https://doi.org/10.21336/gen.bpqv-7z42> [11]. The MOPI instrument and data have been described
63 by Nedoluha *et al.* [10], and basic technical details about the measurements and the instrument are
64 given in Parrish *et al.*'s [1992] and Parrish's [1994] studies. The data have been validated by Boyd *et al.*
65 [14], showing a general agreement within 5% with Aura MLS data.

66 2.2. Lidar

67 The stratospheric ozone lidar at Lauder is a differential absorption lidar (DIAL) that has been
68 measuring since November 1994. It emits laser pulses at wavelengths of 308 and 353 nm, of which the
69 first is strongly absorbed by ozone molecules. The ratio of the backscattered signal at both wavelengths
70 and the signal travel time provides information about the vertical ozone distribution. The system has
71 been described in Swart *et al.* [15]. Very good agreement with ozonesonde and satellite data has been
72 shown by Keckhut *et al.* [16]. Further, the lidar data have been validated within multiple NDACC
73 intercomparison studies [e.g. 17–19]. We use the lidar data available on NDACC (2020) (processing
74 version 8.3, last access: 31.03.2020) and at <https://doi.org/10.21336/gen.0x48-sm13> [20]. The lidar
75 retrieves ozone during clear sky nights, with an average of five profiles per month within our study

76 period. The sparse sampling might result in the distortion of monthly means. For trend estimation,
77 we therefore applied a seasonal fitting on daily lidar means. We then show trend estimates of both
78 monthly lidar time series. We use the term "lidar fit" when referring to the lidar data with seasonal fit,
79 whereas "full lidar" refers to regular monthly lidar means. For the seasonal fit, a seasonal model is fit to
80 the 15th of each month at each altitude level using a specific window length, following [Wilhelm *et al.*'s](#)
81 [\[2019\]](#) method as described in [Bernet *et al.* \[22\]](#). Instead of their proposed window length of 2 years,
82 we used a length of 1.5 years. We judged this to be sufficient for the lidar data, which is generally well
83 distributed within a month. Monthly means were excluded wherever less than 50 measurements were
84 available in the window.

85 Lidar ozone profiles were initially given in number density and converted with coincident ERA5
86 pressure and temperature profiles to VMR. We limited the lidar data to altitudes from 14.2 to 38.6 km,
87 where the averaged measurement uncertainty within our study period remains below 5%. To compare
88 the vertically highly resolved lidar profiles with less resolved MWR profiles, the lidar data were
89 convolved with the MWR averaging kernels according to [Connor *et al.* \[23\]](#). To do this, the rows of
90 the averaging kernels were interpolated to the highly resolved lidar grid and scaled to conserve the
91 measurement response [\[24\]](#).

92 2.3. Aura MLS

93 The Microwave Limb Sounder (MLS) on board the Aura satellite has been providing profiles of
94 stratospheric ozone since August 2004 [\[25\]](#). It retrieves ozone from radiance measurements at 240 GHz.
95 The ozone data have been validated by [Froidevaux *et al.* \[26\]](#). We use Aura MLS data version 4.2. [\[8\]](#),
96 which is described in detail by [Livesey *et al.* \[27\]](#). The satellite crosses Lauder twice a day at a spatial
97 coincidence of $\pm 1^\circ$ latitude and $\pm 8^\circ$ longitude.

98 2.4. ERA5

99 ERA5 is the atmospheric reanalysis from the European Centre for Medium Range Weather
100 Forecasts (ECMWF) [\[28\]](#). We derived six hourly ozone VMR profiles on model levels from
101 ERA5-complete ozone mass mixing ratio profiles provided by Copernicus Climate Change Service
102 (C3S) [\[9\]](#). The reanalysis model assimilates various ozone satellite measurements to derive ozone
103 profiles, as described by [Hersbach *et al.* \[28\]](#). When comparing ERA5 profiles with MWR profiles, the
104 ERA5 profiles were convolved with MWR averaging kernels as described above.

105 3. Time Series Comparison

106 Deseasonalized MWR, lidar, and ERA5 data show that stratospheric ozone at Lauder varies
107 naturally within around 10% in the middle and upper stratosphere (Figure 1a to c). Occasionally, larger
108 anomalies are observed, especially in the lower stratosphere (Figure 1d). All datasets agree on specific
109 natural anomalies. This includes, for example, increased ozone between 30 and 40 km from 2009 to
110 2013, as also reported by [Nedoluha *et al.* \[10\]](#), an ozone minimum in November 1997 [\[29\]](#), and an
111 ozone minimum in 2007 between 20 and 30 km. Aura MLS and ERA5 agree closely, which is expected
112 because Aura MLS data is assimilated in ERA5. However, we also observe some differences between
113 the datasets. For example, the MWR deviates from ERA5 in the middle stratosphere from 2011 to 2014,
114 and the lidar differs from ERA5 after 2015 in the lower and middle stratosphere.

115 To better evaluate such differences, we compared monthly means of MWR and lidar profiles with
116 coincident ERA5 profiles with a time coincidence of ± 3 hours. In addition, we compared monthly
117 means of the two ground-based instruments (MWR and lidar), with a time coincidence of ± 6 hours.
118 These relative differences are shown in Figure 2. The MWR and lidar data mostly agree well, with
119 slightly more MWR ozone in the middle stratosphere and more ozone observed by the lidar in the
120 upper-middle stratosphere to upper stratosphere (Figure 2a). However, ERA5 strongly underestimates
121 ozone in the upper stratosphere compared to MWR (Figure 2b). Further, ERA5 reports slightly larger
122 ozone values than MWR in the upper-middle stratosphere, except from 2009 to 2014. The same pattern

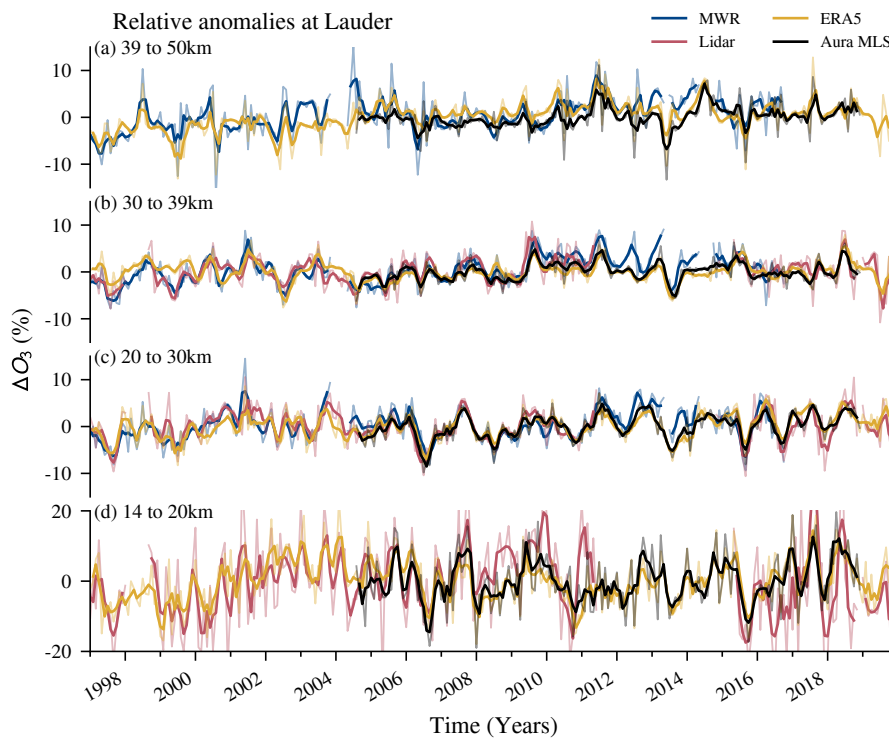


Figure 1. Relative anomalies of ozone volume mixing ratio (VMR) at Lauder, New Zealand. Relative anomalies are shown, describing the deviation from the monthly mean climatology (1997 to 2019) for the microwave radiometer (MWR), the lidar, ERA5 reanalysis data and Aura MLS (2004 to 2019), averaged over four altitude ranges, representing approximately (a) the upper stratosphere, (b) the upper-middle stratosphere, (c) the middle stratosphere, and (d) the lower stratosphere. Bold lines show smoothed data with a moving window of three months; unsmoothed monthly means are shown by thin pale lines.

123 is also observed when comparing ERA5 with lidar data (Figure 2c): ERA5 underestimates ozone in
 124 the upper stratosphere and overestimates ozone in the upper-middle stratosphere. For lidar data,
 125 we further observe that the difference compared to ERA5 increases after the data gap in 2014 in the
 126 lower stratosphere. This might be due to potential lidar changes after the data gap, but also due to
 127 increased ERA5 anomalies after 2015, which are also reported by Hersbach *et al.* [28]. Changes in lower
 128 stratospheric lidar data in 2018 might be related to the addition of two low-altitude channels in the
 129 lidar retrieval in October 2018. Further, a change in lidar is observed compared to ERA5 in 2004, with
 130 better agreement in the middle stratosphere after 2004. This change is not observed in the comparison
 131 between lidar and MWR data (Figure 2a), which suggests that it is due to a change in ERA5 data. This
 132 confirms ERA5 anomalies observed by Hersbach *et al.* [28], who attribute the change to the assimilation
 133 of Aura MLS measurements in ERA5 ozone data from that time.

134 4. Trend Estimations

135 4.1. Trend Models

136 We use two multiple linear regression models and compare the trend estimates using both
 137 methods. The first model is the LOTUS regression model (available at [https://arg.usask.ca/docs/](https://arg.usask.ca/docs/LOTUS_regression/)
 138 [LOTUS_regression/](https://arg.usask.ca/docs/LOTUS_regression/)), which was developed within the LOTUS activity on stratospheric ozone trends
 139 and uncertainties and is described in detail in SPARC/IO3C/GAW [3]. The second model is a
 140 multiple linear trend model developed at the Karlsruhe Institute of Technology (KIT), described by
 141 von Clarmann *et al.* [7]. Both trend models account for autocorrelation between residuals within an

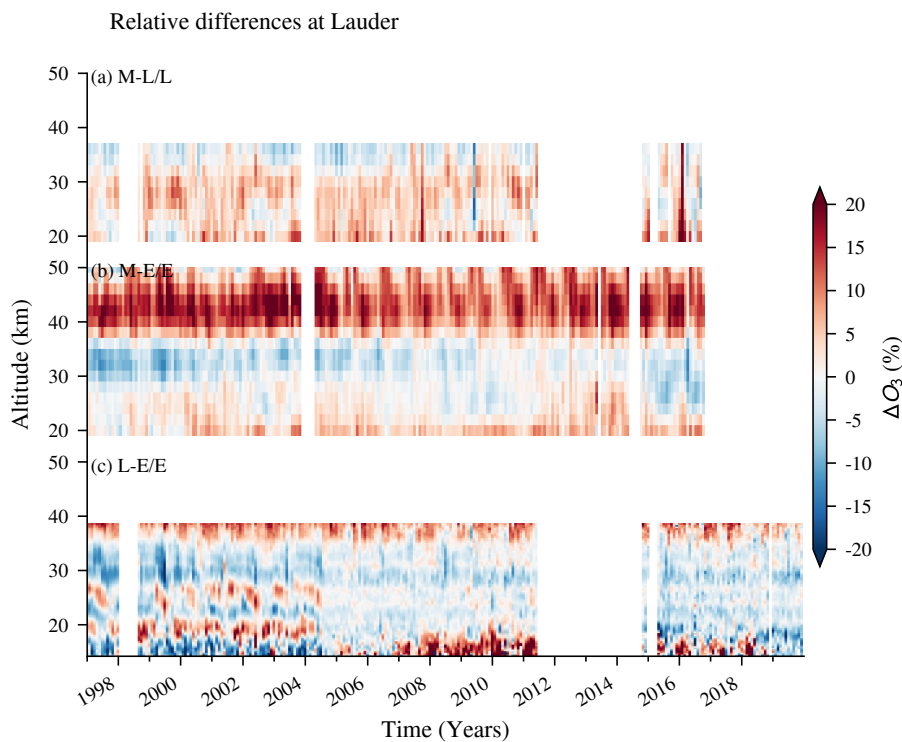


Figure 2. Relative ozone differences between (a) MWR (M) and lidar (L) data, (b) MWR and ERA5 (E) data, and (c) lidar and ERA5 data. Lidar and ERA5 profiles in (a) and (b) have been convolved with MWR averaging kernels.

142 iterative process and use similar predictors: the Quasi biannual oscillation (QBO), the El Niño Southern
 143 Oscillation (ENSO), solar activity as well as four periodic oscillations to account for seasonality [3,30].
 144 The LOTUS model uses two additional predictors, tropopause pressure and aerosol optical depth
 145 (AOD). The latter is, however, negligible in our study period. For the LOTUS regression, we use a
 146 piecewise linear term (PWL) as predictor, using the year 1997 as inflection point [3].

147 We determine linear trends by fitting the regression functions to monthly ozone data. We start
 148 the trend estimates in 1997, when a turnaround due to decreasing ODSs is expected [1]. MWR data is
 149 not available after 2016, so we limit the trend estimates to that year to compare trends in all datasets
 150 over the same period. Trends are considered to be significantly different from zero at 95% confidence
 151 intervals when they exceed twice their standard deviation.

152 4.1.1. Weighted Regression

153 The KIT model uses the uncertainties of the monthly means to weight the regression [7,30].
 154 This improves the regression fit and results in more realistic trend uncertainties. The feature of
 155 weighted regression is also available in the LOTUS model but has not been used for final trend
 156 results in SPARC/IO3C/GAW [3] due to the difficulty of correcting for unknown variances in the
 157 data (heteroscedasticity correction). This is mainly problematic when using merged datasets in which
 158 the sampling frequency and thus the monthly standard errors change over time [3]. In our case,
 159 the sampling frequency is rather constant over time, and we therefore apply the weighted LOTUS
 160 regression to the ozone time series to compare it with the unweighted regression.

161 To weight the regression, the diagonal elements of the covariance matrix are set to the monthly
 162 uncertainties of the data. We estimate monthly uncertainties in the MWR data using the square root
 163 of the sum of the squared measurement uncertainty (random and systematic error) and the squared
 164 standard error (monthly standard deviation divided by measurements per month). We estimate
 165 uncertainties for the fitted lidar monthly means with the systematic measurement uncertainty (from

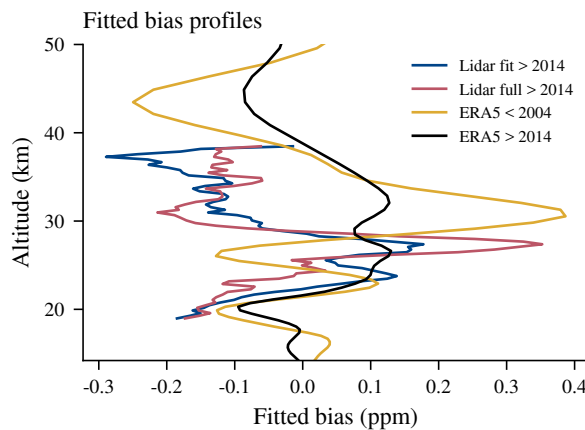


Figure 3. Bias profiles as estimated by the KIT regression for lidar and ERA5 data. The lidar bias compares to data before 2014, whereas the data block from 2004 to 2015 is the reference for ERA5 biases.

166 photon-counting statistics), the standard error, and an additional error term resulting from the seasonal
 167 fit. For ERA5 data, the standard error is small due to the high temporal resolution. To our knowledge,
 168 no comprehensive ozone cross-comparisons have yet been published of the new ERA5 data that derive
 169 systematic uncertainties. We therefore add a systematic uncertainty of 5% to the standard error of each
 170 ERA5 monthly mean. This corresponds approximately to the averaged difference between ERA5 and
 171 MWR profiles in our study period.

172 4.1.2. Bias Correction

173 An additional feature of the KIT model is the possibility of accounting for biases within the
 174 trend estimation. This is helpful if the data shows some jumps or inhomogeneities, for example after
 175 instrumental changes. A fully correlated block is then added to the error covariance matrix in the
 176 weighted regression. The block, corresponding to the biased subset, is filled with the square of the
 177 estimated bias uncertainty. This enables a fit of the bias and is mathematically equivalent to adding
 178 the bias as an independent fit variable [31]. The bias can thus be estimated from the data itself and
 179 does not depend on an a priori choice of bias [32]. The bias uncertainty chosen determines how much
 180 freedom the programme has when estimating the bias from the data. Following Bernet *et al.*'s [2019]
 181 suggestion, we use an altitude-independent bias uncertainty of 5 ppm. They assessed this value to be
 182 appropriate for fitting the bias from the data independently of the a priori zero bias.

183 We fit the bias in this way to the lidar and ERA5 time series, for which we identified
 184 inhomogeneities, as described in Sect. 3. As soon as a change point is set in the data due to observed
 185 inhomogeneities, a bias is fitted from the data in the subsequent block. We considered a change point
 186 in the lidar data after the instrumental break in 2014, when we identified anomalies in the lower
 187 stratosphere compared to previous data. For ERA5, we consider change points in 2004 and in 2015
 188 that have been identified by Hersbach *et al.* [28] and confirmed in our comparison with the lidar data
 189 (see Sect. 3). At each altitude, the programme estimates a bias for the biased block, leading to the bias
 190 profiles shown in Figure 3. Note that to obtain the corrected time series, these bias profiles have to be
 191 subtracted from the original time series in the biased subsets.

192 4.1.3. Artificial Test Case

193 To illustrate weighted regression, we present an artificial test case in Figure 4. The artificial time
 194 series has a trend of 0.1 ppm per decade. We added anomalies to the summer months of 2012, 2014,
 195 and 2015. Such anomalies could represent for example months with few measurements and larger
 196 uncertainties. The trend of this biased time series is then overestimated (case B), with a trend estimate

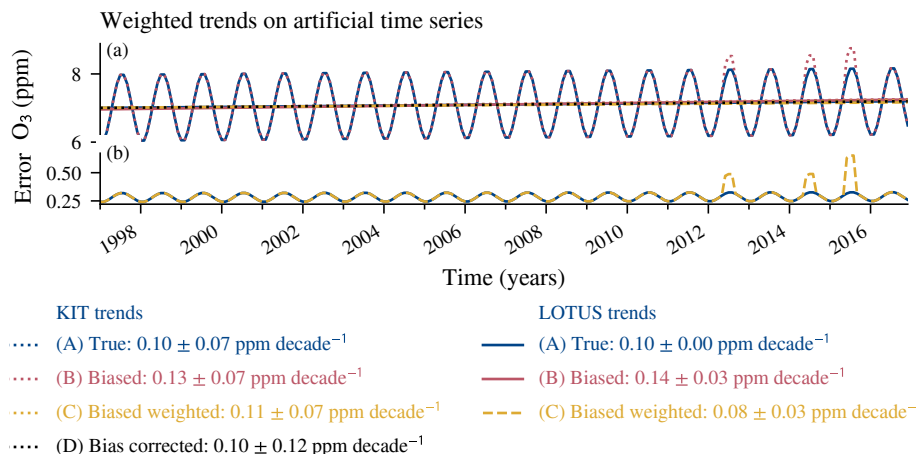


Figure 4. Artificial time series with a trend of 0.1 ppm per decade (case A) and with added anomalies in 2012, 2014, and 2015. Trends for the biased time series are shown, weighted with the regular uncertainties (case B) and with the adapted uncertainties (case C). In case D, a bias was fitted within the KIT model for the anomalous periods.

197 of 0.13 ppm (KIT) or 0.14 ppm (LOTUS) per decade instead of the true trend of 0.1 ppm per decade.
 198 We therefore adapted the uncertainties for these months to weight the regression, as shown in Figure
 199 4b. Considering the adapted uncertainties in the covariance matrix changes the trend fit for both
 200 models (case C), which is then closer to the true trend. The weighted LOTUS trend (case C) is slightly
 201 overcorrected, suggesting that further investigations might be necessary to use the LOTUS weighting
 202 with confidence. When the bias fit in the KIT model is applied (case D), the trend corresponds to the
 203 true trend, which has also been demonstrated by Bernet *et al.* [30].

204 Further, we found that the weighting is less effective if a data jump with a subsequent biased
 205 block is added to the artificial time series (not shown). In such a case, the KIT bias fitting corrects
 206 the trend estimate, as shown by Bernet *et al.* [22]. The simple weighting, however, is not sufficient
 207 to correct for such a jump. Moreover, we found that the LOTUS model would require additional
 208 adjustments to estimate trends with a data jump, including for example a heteroscedasticity correction
 209 to account for the varying residuals, as described by Damadeo *et al.* [33] and SPARC/IO3C/GAW [3].
 210 Further investigations would be necessary to derive solid conclusions about such corrections in the
 211 LOTUS model.

212 We conclude that using weighted regression changes trend fits in both regression models.
 213 Depending upon the model being used, the trend may differ by 0.06 ppm per decade in this case.

214 4.2. Ozone Trend Estimates

215 Trend profiles have been estimated using the LOTUS regression (Figure 5) and the KIT regression
 216 model (Figure 6). Both trend models report generally positive ozone trends between 0% and 5% per
 217 decade in the middle and upper stratosphere. Only ERA5 shows a negative trend peak at 30 km, which
 218 seems to be a data artefact. MWR trends are almost zero between 25 and 30 km, and peak in the upper
 219 stratosphere. Lidar trends vary between 0% and 3% per decade in the middle stratosphere. They are
 220 negative (lidar full) or close to zero (lidar fit) at 20 km and increase strongly in the lower stratosphere.
 221 Differences between the full lidar trends (lidar full) and trends using lidar data with the seasonal fit
 222 (lidar fit) are small in the middle stratosphere, and larger in the lower stratosphere.

223 When using weighted LOTUS regression (Figure 5b), MWR and fitted lidar trends are consistent
 224 in the middle stratosphere. They agree better than the unweighted trends (Figure 5a), suggesting that
 225 the weighting improves the lidar trend estimate. Further, the negative lidar trend peak when using
 226 full lidar data at 20 km is not visible in the weighted trend estimate. The weighted trends for full lidar
 227 data are noisier throughout the stratosphere than the fitted lidar data. This might be due to the larger

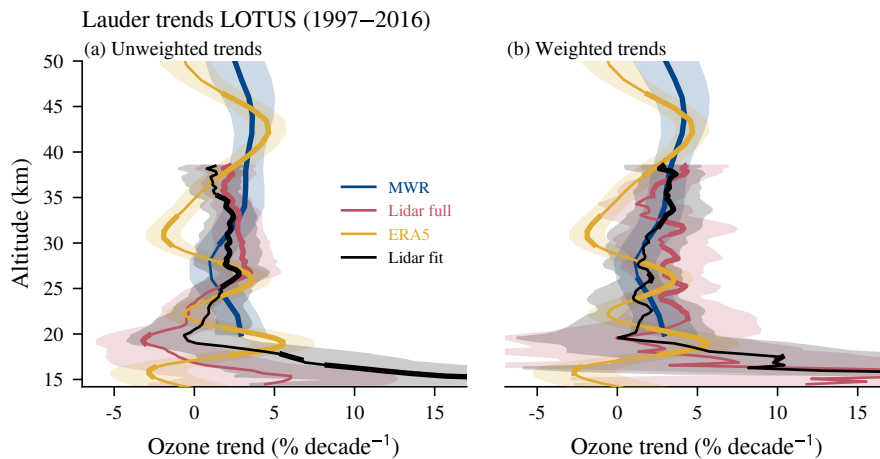


Figure 5. Ozone trends at Lauder from January 1997 to December 2016 for MWR, full lidar data (lidar full), ERA5 data, and lidar data where a seasonal fit was applied (lidar fit). The trends have been estimated using the LOTUS regression model. Panel (a) shows the unweighted trend estimates, whereas monthly means have been weighted by their uncertainties in the regression fit in (b). Shaded areas represent 2-standard-deviation (σ) uncertainties, and bold lines mark trends that are significantly different from zero at 95% confidence intervals ($|\text{trend}| > 2\sigma$).

228 variability of the full lidar monthly means and uncertainties compared to the fitted lidar data. The
 229 seasonality of the uncertainties might also affect the weighted trends. In the lower stratosphere, the
 230 weighted lidar trends are high at the lowest altitude levels. Weighted ERA5 and MWR LOTUS trends
 231 do not differ much from the unweighted LOTUS trends.

232 The KIT trend profiles (Figure 6a) are similar to the LOTUS trends (Figure 5). However, small
 233 differences in the middle stratospheric lidar trends exist, which might be related to different model
 234 setups including differences in predictors. Further, the KIT full lidar trend profile is less variable than
 235 the weighted LOTUS profile which suggests differences in the weighting procedures for uncertainties
 236 which are more variable in time.

237 To account for inhomogeneities in the time series, the lidar and ERA5 trend profiles were corrected
 238 for observed anomalies as described in Sect. 4.1.2. The bias-corrected lidar and ERA5 trend profiles are
 239 shown in Figure 6b. The corrected lidar profiles differ from the uncorrected trend profiles (Figure 6a)
 240 mainly in the lower stratosphere, with a better agreement to the MWR profile between approximately
 241 20 and 25 km. This corresponds to the altitudes where the bias was observed (Figure 2c), suggesting
 242 that the bias was successfully considered in the corrected trend estimate. In the corrected ERA5 trend
 243 profile, the negative ERA5 trends at 30 km and in the lower stratosphere are reduced, and the corrected
 244 ERA5 profile agrees more closely with the MWR and lidar trend profiles.

245 5. Discussion of Results

246 We have shown that the Lauder ozone datasets agree remarkably well on ozone anomalies from
 247 1997 to 2019. Further, the two ground-based ozone datasets at Lauder agree well, with differences
 248 mostly below 10%. The good agreement proves the quality of both ground-based datasets. Differences
 249 from ERA5 are larger, especially in the upper stratosphere, where ERA5 strongly underestimates
 250 ozone compared to MWR and lidar data. By comparing the various Lauder datasets, we identified
 251 data-specific inhomogeneities, especially in ERA5 data. Such data inhomogeneities in the time series
 252 may impact trend estimates and their uncertainties. We observe inhomogeneities in ERA5 data in 2004
 253 and 2015. For the lidar, we observe small changes in the data after pausing measurements in 2014.
 254 Whereas the lidar and MWR can be considered suitable for trend estimations, the ERA5 data requires
 255 corrections for biases when estimating trends. Indeed, trends from reanalysis data should generally be
 256 handled with care because of unconsidered changes in observing systems of assimilated data [e.g. 34].

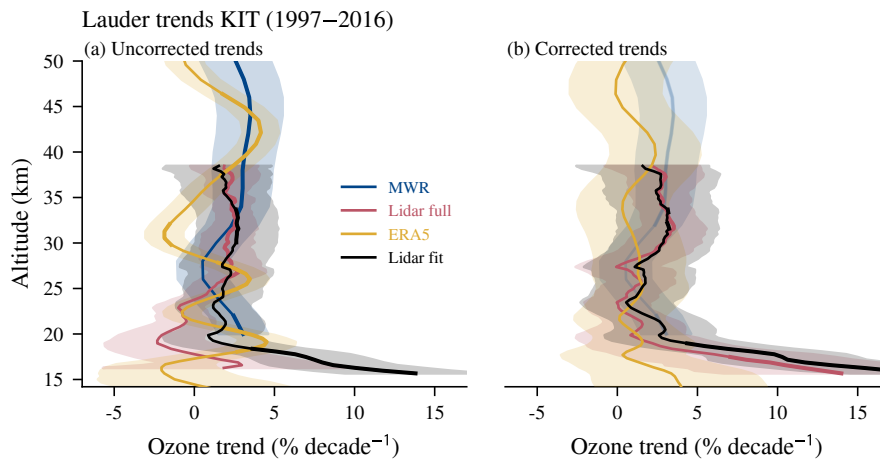


Figure 6. Ozone trends estimated with the KIT regression model for MWR, full lidar, ERA5, and seasonal lidar data (1997 to 2016). Trends are weighted but uncorrected with respect to biases in panel (a). Panel (b) shows weighted bias corrected trends for lidar and ERA5. Uncorrected MWR trends are also shown in (b) (pale color) for comparison.

257 To improve the lidar trend, we also considered the change observed after the instrumental break in
 258 2014 by fitting a bias to the anomalous period using the trend model from von Clarmann *et al.* [7].

259 We have presented two regression models and determined trends using unweighted, weighted,
 260 and bias-corrected regression. Unweighted lidar and MWR trends agree well in the middle stratosphere
 261 and differ in the lower stratosphere, whereas unweighted ERA5 trends disagree in the middle
 262 stratosphere, apparently as the result of biases in the data. In most stratospheric ozone trend
 263 studies, data uncertainties are not considered when estimating trends [3]. However, considering the
 264 uncertainties of the time series can improve the trend estimates and their uncertainties. We therefore
 265 use weighted regression with the KIT model and apply weighted regression within the LOTUS trend
 266 model to account for the time dependence of data uncertainties. Logically, the weighted regression
 267 should be more reliable than the unweighted regression, as also shown with our artificial time series.
 268 However, the weighted LOTUS full lidar trends show larger variability with altitude, suggesting that
 269 additional model adjustments might be required when weighting with varying uncertainties. Further
 270 investigations might be necessary to derive sound conclusions about the use of the LOTUS model
 271 with the option of weighted regression. For example, a heteroscedasticity correction, as suggested
 272 by SPARC/IO3C/GAW [3] and presented by Damadeo *et al.* [33], might improve the weighted trend
 273 estimates. Bias-corrected trends are presented using the KIT regression. For this, we corrected lidar
 274 and ERA5 trends by fitting a bias to anomalous periods. This bias correction affects the lidar trend
 275 estimate, which then agrees more closely with the MWR trend profile in the lower-middle stratosphere.
 276 Moreover the bias-corrected ERA5 trend profile agrees more closely with the MWR and lidar trends
 277 than the uncorrected profile. Our trend results generally show that weighted and corrected trend
 278 estimates change the trend values and their uncertainties slightly. Nevertheless, the changes mostly lie
 279 within the trend uncertainties.

280 Our lidar and MWR trends in the middle and upper stratosphere agree on values between 2%
 281 and 3% per decade. Further, all our datasets report positive stratospheric ozone trends, with the
 282 exception of a negative trend peak reported by the uncorrected ERA5 trend profile at around 30 km
 283 and a negative trend when using full lidar data at 20 km. However, this negative lidar trend is not
 284 visible in the weighted LOTUS and bias-corrected KIT trend, suggesting that it is caused by data
 285 inhomogeneities. Depending on the regression model used, trends are significantly positive in the
 286 middle and the upper stratosphere. Our trends in the middle and upper stratosphere are consistent
 287 with other studies. In the upper stratosphere, significant positive trends were reported at Lauder from
 288 Fourier transform infrared (FTIR) observations (2001 to 2012, Vigouroux *et al.* [35]). Similar trends were

289 also reported from combined ground- and space-based data at Lauder by Nair *et al.* [36] (1997 to 2012)
290 and from various Lauder instruments presented in SPARC/IO3C/GAW [3]. In the lower stratosphere,
291 negative to near-zero trends are reported by SPARC/IO3C/GAW [3] for SH mid-latitudes using a
292 range of satellite records. Further, ozonesonde and FTIR observations at Lauder [3] indicate negative
293 lower-stratospheric trends, which are also reported by Zerefos *et al.* [37] based on Solar Backscattered
294 Ultraviolet (SBUV) satellite data (1998 to 2015). These results are consistent with our negative to
295 near-zero ERA5 trend in the lower stratosphere, but conflicts with our strong positive lidar trend.
296 These conflicting results might be due to unconsidered inhomogeneities in lower-stratospheric lidar
297 data, but they also indicate that further analyses are required to derive lower-stratospheric ozone
298 trends with confidence. Indeed, whether lower-stratospheric ozone concentrations increase or continue
299 to decrease is an ongoing discussion [38–41].

300 Our study concentrates on lidar and MWR datasets with high spatial or temporal resolutions in
301 the middle stratosphere and on ERA5 reanalysis data at Lauder. Other ozone measurements at Lauder
302 from ozonesondes, FTIR, and Umkehr are available, but provide data with limited altitude range
303 (ozonesonde) or with smaller vertical resolution (Umkehr and FTIR). Nevertheless, comparing lidar
304 and MWR data with these datasets might be useful to further identify possible data inhomogeneities.
305 The same is true for additional comparison with merged satellite datasets. In future studies, the use of
306 corrected trend estimates could be further improved by automatizing the detection of inhomogeneities.
307 This could be achieved, for example, by defining thresholds of differences when comparing multiple
308 datasets [30], or by constructing an ozone composite using a comprehensive Bayesian approach as
309 presented by Ball *et al.* [42].

310 6. Conclusions

311 We presented stratospheric ozone time series from a microwave radiometer (MWR), a lidar,
312 Aura MLS satellite data, and ERA5 reanalysis data from Lauder, New Zealand. We investigated and
313 compared the time series to verify whether they can be used for trend estimation. We then presented
314 ozone trend estimates using two regression models with weighted and unweighted regression.

315 The lidar and MWR data at Lauder agree well and were judged to be suitable for trend estimation.
316 Nevertheless, accounting for small instrumental changes in the lidar data might improve the trend
317 estimates. In contrast, the ERA5 data show some biases and have to be corrected when estimating
318 trends. The LOTUS and the KIT regression methods have both been tested to obtain best estimates
319 of the true ozone trend. Considering data uncertainties by using weighted regression changes trend
320 estimates, but further investigations might be required for the use of the weighted LOTUS regression
321 model. We identified data inhomogeneities and recommend considering them in the trend estimation
322 to obtain optimal trend estimates. The ozone data at Lauder report positive ozone trends throughout
323 the middle and upper stratosphere between 0% and 5%, which confirms ozone recovery at these
324 altitudes.

325 In summary, our study compares ozone datasets at the Lauder site and shows that they are
326 generally suitable for trend estimation. The agreement of observed ozone anomalies from the four
327 datasets is remarkable and indicates that lidar, MWR, Aura MLS, and ERA5 data at Lauder are highly
328 reliable. However, we also show that some inhomogeneities in the data influence the trend estimates
329 and that differences in how data uncertainties are treated will affect the calculated trend. The results of
330 our study are useful for other ozone trend studies that aim to understand differences in stratospheric
331 ozone trend estimates.

332 **Author Contributions:** Conceptualization, Leonie Bernet and Klemens Hocke; Data curation, Ian Boyd, Gerald
333 Nedoluha, Richard Querel and Daan Swart; Formal analysis, Leonie Bernet; Resources, Ian Boyd, Gerald Nedoluha,
334 Richard Querel and Daan Swart; Supervision, Klemens Hocke; Visualization, Leonie Bernet; Writing – original
335 draft, Leonie Bernet; Writing – review editing, Leonie Bernet, Ian Boyd, Gerald Nedoluha, Richard Querel, Daan
336 Swart and Klemens Hocke.

337 **Funding:** This research was funded by the Swiss National Science Foundation, grant number 200021-165516.

338 **Acknowledgments:** We thank the LOTUS group for the LOTUS regression model, Thomas von Clarmann for
 339 providing the KIT trend model, Gunter Stober for the seasonal fitting programme, and Simon Milligan for the
 340 language support. We also thank Sophie Godin-Beekmann and Daan Hubert from the LOTUS group for the
 341 motivation and ideas for the study.

342 **Conflicts of Interest:** The authors declare no conflict of interest. The funders had no role in the design of the
 343 study; in the collection, analyses, or interpretation of data; in the writing of the manuscript, or in the decision to
 344 publish the results.

345 References

- 346 [1] Jones, A.; Urban, J.; Murtagh, D.P.; Sanchez, C.; Walker, K.A.; Livesey, N.J.; Froidevaux, L.; Santee, M.L.
 347 Analysis of HCl and ClO time series in the upper stratosphere using satellite data sets. *Atmos. Chem. Phys.*
 348 **2011**, *11*, 5321–5333. doi:10.5194/acp-11-5321-2011.
- 349 [2] Steinbrecht, W.; Hegglin, M.I.; Harris, N.; Weber, M. Is global ozone recovering? *Comptes Rendus - Geosci.*
 350 **2018**, *350*, 368–375. doi:10.1016/j.crte.2018.07.012.
- 351 [3] SPARC/IO3C/GAW. SPARC/IO3C/GAW Report on Long-term Ozone Trends and Uncertainties in the
 352 Stratosphere; SPARC Report No. 9, GAW Report No. 241, WCRP-17/2018, 2019. doi:10.17874/f899e57a20b.
- 353 [4] WMO. Scientific Assessment of Ozone Depletion: 2018; World Meteorological Organization, Global Ozone
 354 Research and Monitoring Project - Report No. 58: Geneva, Switzerland, 2018; p. 588.
- 355 [5] Steinbrecht, W.; Froidevaux, L.; Fuller, R.; Wang, R.; Anderson, J.; Roth, C.; Bourassa, A.; Degenstein, D.;
 356 Damadeo, R.; Zawodny, J.; Frith, S.M.; McPeters, R.; Bhartia, P.; Wild, J.; Long, C.; Davis, S.; Rosenlof,
 357 K.; Sofieva, V.; Walker, K.; Rahpoe, N.; Rozanov, A.; Weber, M.; Laeng, A.; von Clarmann, T.; Stiller, G.;
 358 Kramarova, N.; Godin-Beekmann, S.; Leblanc, T.; Querel, R.; Swart, D.; Boyd, I.; Hocke, K.; Kämpfer, N.;
 359 Maillard Barras, E.; Moreira, L.; Nedoluha, G.; Vigouroux, C.; Blumenstock, T.; Schneider, M.; García, O.;
 360 Jones, N.; Mahieu, E.; Smale, D.; Kotkamp, M.; Robinson, J.; Petropavlovskikh, I.; Harris, N.; Hassler, B.;
 361 Hubert, D.; Tummon, F. An update on ozone profile trends for the period 2000 to 2016. *Atmos. Chem. Phys.*
 362 **2017**, *17*, 10675–10690. doi:10.5194/acp-17-10675-2017.
- 363 [6] NDACC. Network for the Detection of Atmospheric Composition Change. <http://www.ndaccdemo.org>,
 364 accessed on 2020-04-01.
- 365 [7] von Clarmann, T.; Stiller, G.P.; Grabowski, U.; Eckert, E.; Orphal, J. Technical note: Trend
 366 estimation from irregularly sampled, correlated data. *Atmos. Chem. Phys.* **2010**, *10*, 6737–6747.
 367 doi:10.5194/acp-10-6737-2010.
- 368 [8] Schwartz, M.; Froidevaux, L.; Livesey, N.; Read, W. *MLS/Aura Level 2 Ozone (O3) Mixing Ratio V004*;
 369 Goddard Earth Sciences Data and Information Services Center (GES DISC): Greenbelt, MD, USA, 2020.
 370 doi:10.5067/Aura/MLS/DATA2017.
- 371 [9] Copernicus Climate Change Service (C3S). *ERA5 hourly data on pressure levels from 1979 to present*;
 372 Copernicus Climate Change Service Climate Data Store (CDS), 2020. doi:10.24381/cds.bd0915c6.
- 373 [10] Nedoluha, G.E.; Boyd, I.S.; Parrish, A.; Gomez, R.M.; Allen, D.R.; Froidevaux, L.; Connor, B.J.; Querel, R.R.
 374 Unusual stratospheric ozone anomalies observed in 22 years of measurements from Lauder, New Zealand.
 375 *Atmos. Chem. Phys.* **2015**, *15*, 6817–6826. doi:10.5194/acp-15-6817-2015.
- 376 [11] Nedoluha, G.; Parrish, A.; Boyd, I.; Gomez, R.M. *NDACC Version 6 ozone Microwave dataset from NIWA*
 377 *Lauder atmospheric research station available at the NDACC and EVDC Data Handling Facilities*; NDACC -
 378 Network for the Detection of Atmospheric Composition Change / EVDC - ESA Atmospheric Validation
 379 Data Centre, 2016. doi:10.21336/gen.bpqv-7z42.
- 380 [12] Parrish, A.D.; Connor, B.J.; Tsou, J.J.; McDermid, I.S.; Chu, W.P. Ground-based microwave monitoring of
 381 stratospheric ozone. *J. Geophys. Res. Atmos.* **1992**, *97*, 2541–2546. doi:10.1029/91JD02914.
- 382 [13] Parrish, A. Millimeter-wave remote sensing of ozone and trace constituents in the stratosphere. *Proc. IEEE*
 383 **1994**, *82*, 1915–1929. doi:10.1109/5.338079.
- 384 [14] Boyd, I.S.; Parrish, A.D.; Froidevaux, L.; von Clarmann, T.; Kyrölä, E.; Russell, J.M.; Zawodny, J.M.
 385 Ground-based microwave ozone radiometer measurements compared with Aura-MLS v2.2 and other
 386 instruments at two Network for Detection of Atmospheric Composition Change sites. *J. Geophys. Res.*
 387 *Atmos.* **2007**, *112*, 1–10. doi:10.1029/2007JD008720.

- 388 [15] Swart, D.P.; Spakman, J.; Bergwerff, H.B. RIVM's Stratospheric Ozone Lidar for NDSC Station Lauder:
389 System Description and First Results. Abstracts of Papers of the 17th International Laser Radar Conference;
390 Laser Radar Society of Japan: Sendai, Japan, 1994; Number 28D2, pp. 405–408.
- 391 [16] Keckhut, P.; McDermid, S.; Swart, D.; McGee, T.; Godin-Beekmann, S.; Adriani, A.; Barnes, J.; Baray, J.L.;
392 Bencherif, H.; Claude, H.; di Sarra, A.G.; Fiocco, G.; Hansen, G.; Hauchecorne, A.; Leblanc, T.; Lee, C.H.;
393 Pal, S.; Megie, G.; Nakane, H.; Neuber, R.; Steinbrecht, W.; Thayer, J. Review of ozone and temperature lidar
394 validations performed within the framework of the Network for the Detection of Stratospheric Change. *J.*
395 *Environ. Monit.* **2004**, *6*, 721–733. doi:10.1039/b404256e.
- 396 [17] McDermid, I.S.; Bergwerff, J.B.; Bodeker, G.; Boyd, I.S.; Brinksma, E.J.; Connor, B.J.; Farmer, R.; Gross, M.R.;
397 Kimvilakani, P.; Matthews, W.A.; McGee, T.J.; Ormel, F.T.; Parrish, A.; Singh, U.; Swart, D.P.; Tsou, J.J.; Wang,
398 P.H.; Zawodny, J. OPAL: Network for the detection of stratospheric change ozone profiler assessment
399 at Lauder, New Zealand 1. Blind intercomparison. *J. Geophys. Res. Atmos.* **1998**, *103*, 28683–28692.
400 doi:10.1029/98JD02706.
- 401 [18] Godin, S.; Carswell, A.I.; Donovan, D.P.; Claude, H.; Steinbrecht, W.; McDermid, I.S.; McGee, T.J.; Gross,
402 M.R.; Nakane, H.; Swart, D.P.; Bergwerff, H.B.; Uchino, O.; von der Gathen, P.; Neuber, R. Ozone differential
403 absorption lidar algorithm intercomparison. *Appl. Opt.* **1999**, *38*, 6225–6236. doi:10.1364/AO.38.006225.
- 404 [19] Brinksma, E.J.; Bergwerff, J.B.; Bodeker, G.E.; Boersma, K.F.; Boyd, I.S.; Connor, B.J.; De Haan, J.F.;
405 Hogervorst, W.; Hovenier, J.W.; Parrish, A.; Tsou, J.J.; Zawodny, J.M.; Swart, D.P. Validation of 3 years
406 of ozone measurements over Network for the Detection of Stratospheric Change station Lauder, New
407 Zealand. *J. Geophys. Res. Atmos.* **2000**, *105*, 17291–17306. doi:10.1029/2000JD900143.
- 408 [20] Querel, R.; Swart, D. NDACC ozone LIDAR data data sets from NIWA Lauder atmospheric research
409 station available at the NDACC and EVDC Data Handling Facilities; NDACC - Network for the Detection
410 of Atmospheric Composition Change / EVDC - ESA Atmospheric Validation Data Centre, 2020.
411 doi:10.21336/gen.0x48-sm13.
- 412 [21] Wilhelm, S.; Stober, G.; Brown, P. Climatologies and long-term changes in mesospheric wind and wave
413 measurements based on radar observations at high and mid latitudes. *Ann. Geophys.* **2019**, *37*, 851–875.
414 doi:10.5194/angeo-37-851-2019.
- 415 [22] Bernet, L.; Brockmann, E.; von Clarmann, T.; Kämpfer, N.; Mahieu, E.; Mätzler, C.; Stober, G.; Hocke, K.
416 Trends of atmospheric water vapour in Switzerland from ground-based radiometry, FTIR and GNSS data.
417 *Atmos. Chem. Phys.* **2020**, *20*, 11223–11244. doi:10.5194/acp-20-11223-2020.
- 418 [23] Connor, B.J.; Parrish, A.; Tsou, J.J. Detection of stratospheric ozone trends by ground-based microwave
419 observations. Remote Sensing of Atmospheric Chemistry; McElroy, J.L.; McNeal, R.J., Eds. International
420 Society for Optics and Photonics, SPIE, 1991, Vol. 1491, pp. 218 – 230. doi:10.1117/12.46665.
- 421 [24] Keppens, A.; Lambert, J.C.; Granville, J.; Miles, G.; Siddans, R.; Van Peet, J.C.; Van Der A, R.J.; Hubert, D.;
422 Verhoelst, T.; Delcloo, A.; Godin-Beekmann, S.; Kivi, R.; Stübi, R.; Zehner, C. Round-robin evaluation of
423 nadir ozone profile retrievals: Methodology and application to MetOp-A GOME-2. *Atmos. Meas. Tech.*
424 **2015**, *8*, 2093–2120. doi:10.5194/amt-8-2093-2015.
- 425 [25] Waters, J.W.; Froidevaux, L.; Harwood, R.S.; Jarnot, R.F.; Pickett, H.M.; Read, W.G.; Siegel, P.H.; Cofield,
426 R.E.; Filipiak, M.J.; Flower, D.A.; Holden, J.R.; Lau, G.K.; Livesey, N.J.; Manney, G.L.; Pumphrey, H.C.;
427 Santee, M.L.; Wu, D.L.; Cuddy, D.T.; Lay, R.R.; Loo, M.S.; Perun, V.S.; Schwartz, M.J.; Stek, P.C.; Thurstans,
428 R.P.; Boyles, M.A.; Chandra, K.M.; Chavez, M.C.; Chen, G.S.; Chudasama, B.V.; Dodge, R.; Fuller, R.A.;
429 Girard, M.A.; Jiang, J.H.; Jiang, Y.; Knosp, B.W.; Labelle, R.C.; Lam, J.C.; Lee, K.A.; Miller, D.; Oswald, J.E.;
430 Patel, N.C.; Pukala, D.M.; Quintero, O.; Scaff, D.M.; Van Snyder, W.; Tope, M.C.; Wagner, P.A.; Walch, M.J.
431 The Earth Observing System Microwave Limb Sounder (EOS MLS) on the aura satellite. *IEEE Trans. Geosci.*
432 *Remote Sens.* **2006**, *44*, 1075–1092. doi:10.1109/TGRS.2006.873771.
- 433 [26] Froidevaux, L.; Jiang, Y.B.; Lambert, A.; Livesey, N.J.; Read, W.G.; Waters, J.W.; Browell, E.V.; Hair, J.W.;
434 Avery, M.A.; McGee, T.J.; Twigg, L.W.; Sumnicht, G.K.; Jucks, K.W.; Margitan, J.J.; Sen, B.; Stachnik, R.A.;
435 Toon, G.C.; Bernath, P.F.; Boone, C.D.; Walker, K.A.; Filipiak, M.J.; Harwood, R.S.; Fuller, R.A.; Manney,
436 G.L.; Schwartz, M.J.; Daffer, W.H.; Drouin, B.J.; Cofield, R.E.; Cuddy, D.T.; Jarnot, R.F.; Knosp, B.W.; Perun,
437 V.S.; Snyder, W.V.; Stek, P.C.; Thurstans, R.P.; Wagner, P.A. Validation of Aura Microwave Limb Sounder
438 stratospheric ozone measurements. *J. Geophys. Res.* **2008**, *113*, D15S20. doi:10.1029/2007JD008771.
- 439 [27] Livesey, N.J.; Read, W.G.; Wagner, P.A.; Froidevaux, L.; Lambert, A.; Manney, G.L.; Valle, L.F.M.; Pumphrey,
440 H.C.; Santee, M.L.; Schwartz, M.J.; Wang, S.; Fuller, R.A.; Jarnot, R.F.; Knosp, B.W.; Martinez, E.; Lay, R.R.;

- 441 Rev, E.; Microwave, A.; Sounder, L. Earth Observing System (EOS) Aura Microwave Limb Sounder (MLS)
 442 Version 4.2x Level 2 data quality and description document. Technical report, Jet Propulsion Laboratory,
 443 California Institute of Technology, Pasadena, California, 2020.
- 444 [28] Hersbach, H.; Bell, B.; Berrisford, P.; Hirahara, S.; Horányi, A.; Muñoz-Sabater, J.; Nicolas, J.; Peubey, C.;
 445 Radu, R.; Schepers, D.; Simmons, A.; Soci, C.; Abdalla, S.; Abellan, X.; Balsamo, G.; Bechtold, P.; Biavati,
 446 G.; Bidlot, J.; Bonavita, M.; Chiara, G.; Dahlgren, P.; Dee, D.; Diamantakis, M.; Dragani, R.; Flemming, J.;
 447 Forbes, R.; Fuentes, M.; Geer, A.; Haimberger, L.; Healy, S.; Hogan, R.J.; Hólm, E.; Janisková, M.; Keeley, S.;
 448 Laloyaux, P.; Lopez, P.; Lupu, C.; Radnoti, G.; Rosnay, P.; Rozum, I.; Vamborg, F.; Villaume, S.; Thépaut,
 449 J. The ERA5 global reanalysis. *Quarterly Journal of the Royal Meteorological Society* **2020**, *146*, 1999–2049.
 450 doi:10.1002/qj.3803.
- 451 [29] Brinksma, E.J. Five years of observations of ozone profiles over Lauder, New Zealand. *J. Geophys. Res.*
 452 **2002**, *107*, 1–11. doi:10.1029/2001jd000737.
- 453 [30] Bernet, L.; von Clarmann, T.; Godin-Beekmann, S.; Ancellet, G.; Maillard Barras, E.; Stübi, R.; Steinbrecht,
 454 W.; Kämpfer, N.; Hocke, K. Ground-based ozone profiles over central Europe: incorporating anomalous
 455 observations into the analysis of stratospheric ozone trends. *Atmos. Chem. Phys.* **2019**, *19*, 4289–4309.
 456 doi:10.5194/acp-19-4289-2019.
- 457 [31] von Clarmann, T.; Grabowski, U.; Kiefer, M. On the role of non-random errors in inverse problems
 458 in radiative transfer and other applications. *J. Quant. Spectrosc. Radiat. Transf.* **2001**, *71*, 39–46.
 459 doi:10.1016/S0022-4073(01)00010-3.
- 460 [32] Stiller, G.P.; von Clarmann, T.; Haedel, F.; Funke, B.; Glatthor, N.; Grabowski, U.; Kellmann, S.; Kiefer, M.;
 461 Linden, A.; Lossow, S.; López-Puertas, M. Observed temporal evolution of global mean age of stratospheric
 462 air for the 2002 to 2010 period. *Atmos. Chem. Phys.* **2012**, *12*, 3311–3331. doi:10.5194/acp-12-3311-2012.
- 463 [33] Damadeo, R.P.; Zawodny, J.M.; Thomason, L.W. Reevaluation of stratospheric ozone trends from SAGE
 464 II data using a simultaneous temporal and spatial analysis. *Atmos. Chem. Phys.* **2014**, *14*, 13455–13470.
 465 doi:10.5194/acp-14-13455-2014.
- 466 [34] Dee, D.P.; Uppala, S.M.; Simmons, A.J.; Berrisford, P.; Poli, P.; Kobayashi, S.; Andrae, U.; Balmaseda, M.A.;
 467 Balsamo, G.; Bauer, P.; Bechtold, P.; Beljaars, A.C.; van de Berg, L.; Bidlot, J.; Bormann, N.; Delsol, C.;
 468 Dragani, R.; Fuentes, M.; Geer, A.J.; Haimberger, L.; Healy, S.B.; Hersbach, H.; Hólm, E.V.; Isaksen, I.;
 469 Kållberg, P.; Köhler, M.; Matricardi, M.; McNally, A.P.; Monge-Sanz, B.M.; Morcrette, J.J.; Park, B.K.; Peubey,
 470 C.; de Rosnay, P.; Tavolato, C.; Thépaut, J.N.; Vitart, F. The ERA-Interim reanalysis: Configuration and
 471 performance of the data assimilation system. *Q. J. R. Meteorol. Soc.* **2011**, *137*, 553–597. doi:10.1002/qj.828.
- 472 [35] Vigouroux, C.; Blumenstock, T.; Coffey, M.; Errera, Q.; García, O.; Jones, N.B.; Hannigan, J.W.; Hase, F.; Liley,
 473 B.; Mahieu, E.; Mellqvist, J.; Notholt, J.; Palm, M.; Persson, G.; Schneider, M.; Servais, C.; Smale, D.; Thölix,
 474 L.; De Mazière, M. Trends of ozone total columns and vertical distribution from FTIR observations at eight
 475 NDACC stations around the globe. *Atmos. Chem. Phys.* **2015**, *15*, 2915–2933. doi:10.5194/acp-15-2915-2015.
- 476 [36] Nair, P.J.; Froidevaux, L.; Kuttippurath, J.; Zawodny, J.M.; Russell, J.M.; Steinbrecht, W.; Claude, H.; Leblanc,
 477 T.; Van Gijssels, J.A.; Johnson, B.; Swart, D.P.; Thomas, A.; Querel, R.; Wang, R.; Anderson, J. Subtropical
 478 and midlatitude ozone trends in the stratosphere: Implications for recovery. *J. Geophys. Res. Atmos.* **2015**,
 479 *120*, 7247–7257. doi:10.1002/2014JD022371.
- 480 [37] Zerefos, C.; Kapsomenakis, J.; Eleftheratos, K.; Tourpali, K.; Petropavlovskikh, I.; Hubert, D.;
 481 Godin-Beekmann, S.; Steinbrecht, W.; Frith, S.; Sofieva, V.; Hassler, B. Representativeness of single
 482 lidar stations for zonally averaged ozone profiles, their trends and attribution to proxies. *Atmos. Chem.*
 483 *Phys.* **2018**, *18*, 6427–6440. doi:10.5194/acp-18-6427-2018.
- 484 [38] Ball, W.T.; Alsing, J.; Mortlock, D.J.; Staehelin, J.; Haigh, J.D.; Peter, T.; Tummon, F.; Stübi, R.; Stenke,
 485 A.; Anderson, J.; Bourassa, A.; Davis, S.M.; Degenstein, D.; Frith, S.M.; Froidevaux, L.; Roth, C.;
 486 Sofieva, V.; Wang, R.; Wild, J.; Yu, P.; Ziemke, J.R.; Rozanov, E.V. Evidence for continuous decline in
 487 lower stratospheric ozone offsetting ozone layer recovery. *Atmos. Chem. Phys.* **2018**, *18*, 1379–1394.
 488 doi:10.5194/acp-18-1379-2018.
- 489 [39] Chipperfield, M.P.; Dhomse, S.; Hossaini, R.; Feng, W.; Santee, M.L.; Weber, M.; Burrows, J.P.; Wild,
 490 J.D.; Loyola, D.; Coldewey-Egbers, M. On the Cause of Recent Variations in Lower Stratospheric Ozone.
 491 *Geophys. Res. Lett.* **2018**, *45*, 5718–5726. doi:10.1029/2018GL078071.

- 492 [40] Ball, W.T.; Alsing, J.; Staehelin, J.; Davis, S.M.; Froidevaux, L.; Peter, T. Stratospheric ozone trends
493 for 1985-2018: sensitivity to recent large variability. *Atmos. Chem. Phys. Discuss.* **2019**, pp. 1–27.
494 doi:10.5194/acp-2019-243.
- 495 [41] Wargan, K.; Orbe, C.; Pawson, S.; Ziemke, J.R.; Oman, L.D.; Olsen, M.A.; Coy, L.; Emma Knowland, K.
496 Recent Decline in Extratropical Lower Stratospheric Ozone Attributed to Circulation Changes. *Geophys.*
497 *Res. Lett.* **2018**, *45*, 5166–5176. doi:10.1029/2018GL077406.
- 498 [42] Ball, W.T.; Alsing, J.; Mortlock, D.J.; Rozanov, E.V.; Tummon, F.; Haigh, J.D. Reconciling differences in
499 stratospheric ozone composites. *Atmos. Chem. Phys.* **2017**, *17*, 12269–12302. doi:10.5194/acp-2017-142.

500 **Sample Availability:** Lidar data are available at <https://doi.org/10.21336/gen.0x48-sm13> [20] and microwave
501 radiometer data at <https://doi.org/10.21336/gen.bpqv-7z42> [11]. Both datasets are also available at [http://www.
502 ndaccdemo.org/](http://www.ndaccdemo.org/) [6]. Aura MLS data are available at <https://doi.org/10.5067/Aura/MLS/DATA2017> [8]. ERA5
503 data can be downloaded from <https://doi.org/10.24381/cds.bd0915c6> [9]. The LOTUS regression can be obtained
504 from https://arg.usask.ca/docs/LOTUS_regression/, and the KIT model is available on request.

505 **Publisher's Note:** MDPI stays neutral with regard to jurisdictional claims in published maps and institutional
506 affiliations.

507 © 2020 by the authors. Submitted to *Remote Sens.* for possible open access publication
508 under the terms and conditions of the Creative Commons Attribution (CC BY) license
509 (<http://creativecommons.org/licenses/by/4.0/>).

A.3 STUDY ON WATER VAPOUR TRENDS IN SWITZERLAND

The following article was published in *Atmospheric Chemistry and Physics* in October 2020 (<https://doi.org/10.5194/acp-20-11223-2020>).

FULL CITATION:

L. Bernet, E. Brockmann, T. von Clarmann, N. Kämpfer, E. Mahieu, C. Mätzler, G. Stober and K. Hocke (2020c). Trends of atmospheric water vapour in Switzerland from ground-based radiometry, FTIR and GNSS data. In: *Atmospheric Chemistry and Physics* 20.19, pp. 11223–11244. DOI: [10.5194/acp-20-11223-2020](https://doi.org/10.5194/acp-20-11223-2020)

Atmos. Chem. Phys., 20, 11223–11244, 2020
<https://doi.org/10.5194/acp-20-11223-2020>
 © Author(s) 2020. This work is distributed under
 the Creative Commons Attribution 4.0 License.



Atmospheric
 Chemistry
 and Physics
 Open Access
 EGU

Trends of atmospheric water vapour in Switzerland from ground-based radiometry, FTIR and GNSS data

Leonie Bernet^{1,2}, Elmar Brockmann³, Thomas von Clarmann⁴, Niklaus Kämpfer^{1,2}, Emmanuel Mahieu⁵, Christian Mätzler^{1,2}, Gunter Stober^{1,2}, and Klemens Hocke^{1,2}

¹Institute of Applied Physics, University of Bern, Bern, Switzerland

²Oeschger Centre for Climate Change Research, University of Bern, Bern, Switzerland

³Federal Office of Topography, swisstopo, Wabern, Switzerland

⁴Institute of Meteorology and Climate Research, Karlsruhe Institute of Technology, Karlsruhe, Germany

⁵Institute of Astrophysics and Geophysics, University of Liège, Liège, Belgium

Correspondence: Leonie Bernet (leonie.bernet@iap.unibe.ch)

Received: 25 January 2020 – Discussion started: 24 February 2020

Revised: 27 August 2020 – Accepted: 4 September 2020 – Published: 1 October 2020

Abstract. Vertically integrated water vapour (IWV) is expected to increase globally in a warming climate. To determine whether IWV increases as expected on a regional scale, we present IWV trends in Switzerland from ground-based remote sensing techniques and reanalysis models, considering data for the time period 1995 to 2018. We estimate IWV trends from a ground-based microwave radiometer in Bern, from a Fourier transform infrared (FTIR) spectrometer at Jungfraujoch, from reanalysis data (ERA5 and MERRA-2) and from Swiss ground-based Global Navigation Satellite System (GNSS) stations. Using a straightforward trend method, we account for jumps in the GNSS data, which are highly sensitive to instrumental changes. We found that IWV generally increased by 2 % per decade to 5 % per decade, with deviating trends at some GNSS stations. Trends were significantly positive at 17 % of all GNSS stations, which often lie at higher altitudes (between 850 and 1650 m above sea level). Our results further show that IWV in Bern scales to air temperature as expected (except in winter), but the IWV–temperature relation based on reanalysis data in the whole of Switzerland is not clear everywhere. In addition to our positive IWV trends, we found that the radiometer in Bern agrees within 5 % with GNSS and reanalyses. At the Jungfraujoch high-altitude station, we found a mean difference of 0.26 mm (15 %) between the FTIR and coincident GNSS data, improving to 4 % after an antenna update in 2016. In general, we showed that ground-based GNSS data are highly valuable for climate monitoring, given that the data have been homo-

geneously reprocessed and that instrumental changes are accounted for. We found a response of IWV to rising temperature in Switzerland, which is relevant for projected changes in local cloud and precipitation processes.

1 Introduction

Atmospheric water vapour is a key component in the climate system. It is the most abundant greenhouse gas and is responsible for a strong positive feedback that enhances temperature increase induced by other greenhouse gases (e.g. IPCC, 2013; Stocker et al., 2001). Furthermore, water vapour is involved in important tropospheric processes such as cloud formation and precipitation; it influences size, composition and optical properties of aerosols; and it is responsible for atmospheric energy and heat transport via evaporation and condensation (Kämpfer, 2013). Measuring changes in atmospheric water vapour is thus important because they reflect externally forced temperature changes in the climate system and can be an indicator for changes in involved processes such as cloud formation and precipitation. Concentrating here on regional changes is of special interest because water vapour is spatially variable and the relation between water vapour, temperature and precipitation shows spatial dependencies.

Temperature and water vapour are closely linked as expected from the Clausius–Clapeyron relation. Several stud-

ies have revealed spatial correlation between mass changes in vertically integrated water vapour (IWV) and changes in temperature, especially over oceans (e.g. Wentz and Schabel, 2000; Trenberth et al., 2005; Wang et al., 2016). Nevertheless, it has also been shown that water vapour does not scale to temperature everywhere as expected and that large regional differences exist (e.g. O’Gorman and Muller, 2010; Chen and Liu, 2016; Wang et al., 2016). Over continental areas, correlations between surface temperature and IWV changes are smaller than over oceans, even showing opposite trends in some regions (Wagner et al., 2006). Also, temperature climate feedbacks may have regional dependencies (Armour et al., 2013). Regional analyses of changes in water vapour and the relation to temperature changes are thus required.

Most of the atmospheric water vapour resides in the troposphere. Measuring IWV, vertically integrated over the whole atmospheric column, is therefore representative of tropospheric water vapour. The IWV can be measured by different techniques. Nadir sounding satellite techniques provide global data sets of IWV that have been used for global trend analyses in multiple studies (e.g. Trenberth et al., 2005; Santer et al., 2007; Wentz et al., 2007; Mieruch et al., 2008; Hartmann et al., 2013; Ho et al., 2018; Zhang et al., 2018). Most of these studies found global IWV trends between 1 % per decade and 2 % per decade, with large spatial differences. However, these satellite data sets have some limitations for regional IWV trend analyses. First, missing homogenization across multiple satellite platforms can make satellite trend studies difficult (Hartmann et al., 2013; John et al., 2011). Second, visible and infrared satellite techniques are limited to clear-sky measurements. Furthermore, satellite products from passive microwave sensors are restricted to oceans only, because the well-known ocean surface emissivity makes retrievals generally easier over oceans than over land surfaces (Urban, 2013). Stable and long-term station measurements from ground are therefore more appropriate for regional IWV trend analyses over land. From ground, IWV can be measured by radiosondes (Ross and Elliot, 2001), sun photometers (precision filter radiometers, PFRs, Ingold et al., 2000; Wehrli, 2000), Fourier transform infrared (FTIR) spectrometers (Sussmann et al., 2009; Schneider et al., 2012) or microwave radiometers (Morland et al., 2009). Radiosondes provide the longest time series, but the homogeneity of the records can be problematic due to changes in instrumentation or observational routines (Ross and Elliot, 2001), and the temporal sampling is sparse (usually twice a day). PFR and FTIR instruments measure during day and clear-sky conditions only, whereas microwave radiometers can measure in almost all weather conditions during day and night with high temporal resolution. However, no dense measurement network exists for these techniques. Another technique that provides data in all weather situations is the use of ground-based receivers of the Global Navigation Satellite System (GNSS). The advantage of GNSS receivers is the high spatial resolu-

tion due to dense networks. In the present study we combine the microwave and FTIR techniques at two Swiss measurement stations with data from the ground-based GNSS network in Switzerland to analyse IWV trends.

Several studies use GNSS measurements to derive global IWV trends over land (e.g. Chen and Liu, 2016; Wang et al., 2016; Parracho et al., 2018). Chen and Liu (2016) report GNSS-derived IWV trends at mid-latitudes of 1.46 % per decade, and Parracho et al. (2018) found IWV trends in the Northern Hemisphere of approximately 2.6 % per decade based on GNSS and reanalysis data. The high spatial resolution of some regional GNSS networks makes them a valuable data set for regional trend analyses of IWV. For Europe, IWV trends based on GNSS data have been presented, for example, for Germany (Alshawaf et al., 2017) and Scandinavia (Nilsson and Elgered, 2008), reporting a large trend variability between different stations.

To the best of our knowledge, no regional analysis of IWV trends covering the whole area of Switzerland has been published so far. Some studies presented IWV trends at single Swiss stations (Morland et al., 2009; Sussmann et al., 2009; Hocke et al., 2011, 2016; Nyeki et al., 2019), but most of them cover shorter time periods than available today. Morland et al. (2009) and Hocke et al. (2011, 2016) presented IWV trends at Bern using the same microwave radiometer that we use in the present study. However, they use time series of a maximum of 13 years, whereas a time series of 24 years (1995–2018) is available now. Given that Switzerland experienced strong warming in the last decade, an update is of particular interest. Indeed, 9 of the warmest 10 years in Switzerland (from 1864 to 2018) have occurred in the last two decades, and 6 of the years lie in the last decade (NCCS, 2018). A recent study by Nyeki et al. (2019) presents GNSS-based trends for longer time series (until 2015), but they concentrate only on four Swiss stations. In fact, none of the mentioned studies presents IWV trends in the whole of Switzerland.

Our study presents a complete trend analysis of IWV in Switzerland based on data from the Swiss GNSS station network, a microwave radiometer located in Bern, an FTIR spectrometer located at Jungfraujoeh and from reanalysis models. We present IWV trends for time series of 24 years (radiometer, FTIR and reanalyses) or 19 years (GNSS) and analyse how they are related to observed changes in temperature. To avoid artificial trends, homogenized radiometer data have been used in the present study (Morland et al., 2009; Hocke et al., 2011). For the GNSS data, possible jumps due to instrumental changes have been considered in the trend analysis by using the feature of bias fitting in the trend programme of von Clarmann et al. (2010). The goal of our study is to present trends of IWV in Switzerland, to detect potential regional differences and to verify if water vapour increases as expected from the observed temperature rise.

2 Water vapour data sets

We compare IWV data from a microwave radiometer located in Bern and an FTIR spectrometer at Jungfraujoch with Swiss GNSS ground stations and reanalysis data (ERA5 and MERRA-2). Radiometer data are available from 1995 onwards. We therefore define our study period from January 1995 to December 2018, even though GNSS data are available only after 2000 (see Table 1). IWV is often given as the total mass of water vapour per square metre (kg m^{-2}). However, we provide IWV data in millimetres, taking the density of water into account, which is often referred to as “total precipitable water vapour”. Evidently not all of the water vapour is actually precipitable. To avoid confusion, we prefer the term integrated water vapour (IWV) and provide the amount in the more convenient unit of millimetres, where 1 mm corresponds to 1 kg m^{-2} .

2.1 Microwave radiometer

The Tropospheric Water Vapour Radiometer (TROWARA) is a microwave radiometer that has been retrieving IWV and integrated liquid water (ILW) since November 1994 in Bern, Switzerland (46.95° N , 7.44° E ; 575 m above sea level, a.s.l.). It measures the thermal microwave emission at the frequencies of 21.39, 22.24 and 31.5 GHz with a time resolution of several seconds and an elevation angle of 40° . The measured signal is used to infer the atmospheric opacity, using the Rayleigh–Jeans approximation of the radiative transfer equation as described in Mätzler and Morland (2009) and In-gold et al. (1998).

The opacity linearly depends on the water content in the atmosphere and can therefore be used to derive IWV and ILW (Mätzler and Morland, 2009; Hocke et al., 2017):

$$\tau_i = a_i + b_i \text{IWV} + c_i \text{ILW}, \quad (1)$$

where τ_i is the opacity of the i th frequency channel of the radiometer. The coefficients a_i and b_i are statistically derived from nearby radiosonde measurements and fine-tuned with clear-sky measurements (Mätzler and Morland, 2009). The coefficient c_i is the Rayleigh mass absorption coefficient of liquid water.

The initial instrument setup and measurement principle is presented in Peter and Kämpfer (1992). To improve the measurement stability and data availability, the instrument was upgraded in 2002 and 2004 and a new radiometer model was developed (Morland, 2002; Morland et al., 2006). Furthermore, it was moved into an indoor laboratory in November 2002, which made it possible to measure IWV even during light-rain conditions (Morland, 2002). However, to maintain consistency with the measurements before 2002, data observed during rainy conditions were excluded in the present study as soon as the ILW exceeded 0.5 mm or rain was detected by the collocated weather station (Morland et al., 2009). We use hourly IWV data

from the STARTWAVE database (<http://www.iapmw.unibe.ch/research/projects/STARTWAVE/>, last access: 29 September 2020) which were derived from the opacities at 21.39 and 31.5 GHz. Before 2008, we use TROWARA data in which data gaps were filled with data derived from a collocated radiometer as described by Hocke et al. (2011) and Gerber (2009). Furthermore, change points in TROWARA data due to instrumental changes have been detected and corrected by a careful comparison of the TROWARA time series before 2008 with simultaneous measurements from other techniques (Morland et al., 2009). No instrumental changes have been performed in recent years. We therefore presume that the data are well homogenized and suitable for trend estimation.

2.2 Fourier transform infrared spectrometer

A ground-based solar Fourier transform infrared (FTIR) spectrometer is located at the high-altitude observatory Jungfraujoch in Switzerland (46.55° N , 7.98° E ; 3580 m a.s.l.). Water vapour information is retrieved from absorption in the solar spectrum at three spectral intervals within 11.7 and 11.9 μm . The optimized IWV retrieval for FTIR spectrometry is described by Sussmann et al. (2009), and instrumental details are given in Zander et al. (2008). FTIR measurements at Jungfraujoch provide water vapour data since 1984. For consistency with our study period, we use data only from 1995 to 2018. In this period, two FTIR instruments were installed at Jungfraujoch, with overlapping measurements from 1995 to 2001. Sussmann et al. showed that the bias between both instruments is negligible. We therefore compute monthly means of a merged time series including both instruments. FTIR measurements are weather dependent (cloud-free conditions are required) and thus provide irregularly sampled data at Jungfraujoch, with on average eight measurement days per month in our study period. This sparse sampling can be problematic when calculating monthly means. We therefore apply the resampling method proposed by Wilhelm et al. (2019) when calculating monthly means of FTIR-derived IWV. For this, the background IWV data are determined by fitting a seasonal model to daily IWV means. The seasonal model is given by a mean IWV_0 , the first two seasonal harmonics with periods $T_n = 365.25/n$, and the fit coefficients a_n and b_n :

$$\text{IWV}(t) = \text{IWV}_0 + \sum_{n=1}^2 \left(a_n \cdot \sin\left(\frac{2\pi}{T_n} \cdot t\right) + b_n \cdot \cos\left(\frac{2\pi}{T_n} \cdot t\right) \right). \quad (2)$$

This seasonal model is fitted to the 15th of each month using a window length of 2 years. Due to the sparsity of the FTIR data, the model fit to each month provides a more robust estimate compared to the statistical monthly means, which might be based on only 1 or 2 d of observations at the beginning

Table 1. Swiss GNSS stations used in the present study. Stations marked in bold were directly compared with radiometer and reanalysis data at Bern (latitude = $46.95 \pm 0.5^\circ$, longitude = $7.44 \pm 1^\circ$, altitude = 575 ± 200 m).

Abbreviation	Station name	Altitude m a.s.l.	Data available	Change points yyyy-mm	Remark
ANDE	Andermatt	2318	2000 to 2010	2000-09, 2002-08, 2007-06, 2010-02	
ARDE	Ardez	1497	2002 to 2018		
BOUR	Bourrignon	891	2002 to 2018		
DAVO	Davos	1597	2000 to 2018		
EPFL	EPF Lausanne	411	2000 to 2018	2000-03, 2000-04, 2000-06, 2003-10, 2006-05, 2007-06, 2015-04	
ERDE	Erde	731	2007 to 2018		No AGNES station
ETHZ	ETH Zurich	548	2000 to 2018	2000-03, 2000-08, 2000-09, 2003-05, 2015-05	
EXWI	Exakte Wissenschaften Bern	578	2001 to 2016		No AGNES station
FALE	Falera	1296	2002 to 2018	2007-06, 2010-02	
FHNW_M	Fachhochschule Nord- westschweiz Muttenz	347	2000 to 2018	2007-06, 2015-05, 2018-09	Merged with FHBB (329 m) in 2018
FRIC	Frick	678	2001 to 2018	2008-12, 2015-04	
GENE_M	Geneva	422	2001 to 2018	2007-07, 2009-05, 2015-04	Merged with AIGE (424 m) in 2009
HABG	Hasliberg	1098	2007 to 2018	2007-06, 2010-02	
HOHT	Hohtenn	934	2001 to 2018		
HUTT	Huttwil	731	2002 to 2018	2007-06, 2009-01, 2015-04	
JUJO_M	Jungfrauojoch	3584	2000 to 2018	2015-06, 2016-10	Merged with JUJ2 (3585 m) in 2016
KREU	Kreuzlingen	483	2002 to 2018	2006-07, 2006-09, 2007-06, 2015-04	
LOMO	Locarno-Monti	389	2000 to 2018	2007-06, 2015-05	
LUZE	Lucerne	494	2001 to 2018	2007-07, 2008-04, 2015-03	
MART_M	Martigny	594	2002 to 2018	2002-06, 2008-06, 2009-05, 2013-08	Merged with MAR2 (593 m) in 2008
NEUC	Neuchâtel	455	2000 to 2018	2000-09, 2007-06, 2015-04	
PAYE	Payerne	499	2001 to 2018	2000-09, 2007-06, 2015-04	
SAAN	Saanen	1370	2002 to 2018		
SAME_M	Samedan	1709	2003 to 2018	2007-06, 2010-02, 2012-08, 2016-03	Merged with SAM2 (1712 m) in 2016
SANB	San Bernardino	1653	2002 to 2018	2007-06, 2010-02	
SARG_M	Sargans	1211	2002 to 2018	2007-06, 2011-10, 2014-10, 2015-03	Merged with SAR2 (1218 m) in 2011
SCHA	Schaffhausen	590	2001 to 2018	2007-06, 2015-04	
STAB_M	Stabio	371	2002 to 2018	2007-12, 2015-05	Merged with STA2 (371 m) in 2007
STCX	Sainte-Croix	1105	2002 to 2018	2007-06, 2010-02, 2013-11	
STGA	St. Gallen	707	2001 to 2018	2007-06, 2007-08, 2015-04	
VARE	Varen	652	2006 to 2018		No AGNES station
WAB1	Wabern	611	2006 to 2018	2005-08, 2009-09, 2016-05	No AGNES station
WEHO	Wetterhorn	2916	2007 to 2018		No AGNES station
ZERM	Zermatt	1879	2006 to 2018	2007-06, 2010-02	
ZIMM	Zimmerwald	908	2000 to 2018		

or end of a month that are not necessarily representative as a monthly mean. The measurement uncertainties of the obtained monthly mean values are derived from the covariance matrix of the model fit. Furthermore, we also tested a seasonal model with higher seasonal harmonics. However, due to the sparse FTIR measurements it appeared not to be useful to improve the obtained monthly mean IWV estimates.

2.3 GNSS ground stations

The signal of GNSS satellites is delayed when passing through the atmosphere. This so-called zenith total delay (ZTD) can be used to infer information about the atmospheric water vapour content. Various studies explain the method to derive IWV from the measured ZTD (e.g. Bevis et al., 1992; Hagemann et al., 2002; Guerova et al., 2003;

Heise et al., 2009). We briefly summarize the procedure that we used in our study. The ZTD can be written as the sum of (i) the zenith hydrostatic delay (ZHD) due to refraction by the dry atmosphere and (ii) the zenith wet delay (ZWD) due to refraction by water vapour (Davis et al., 1985):

$$\text{ZTD} = \text{ZHD} + \text{ZWD}. \quad (3)$$

The ZHD (in metres) is calculated from the surface pressure at each GNSS station as proposed by Elgered et al. (1991):

$$\text{ZHD} = (2.2768 \pm 0.024) \times 10^{-3} \frac{p_s}{f(\lambda, H)}, \quad (4)$$

with surface pressure p_s in hectopascals. The dependency of the gravitational acceleration on latitude and altitude is con-

sidered in the function f (Saastamoinen, 1972):

$$f(\lambda, H) = 1 - 0.00266 \cos\left(2 \frac{\lambda\pi}{180}\right) - 0.00028 H, \quad (5)$$

where λ is the station latitude in degrees and H is the station altitude in kilometres. With the measured ZTD and the calculated ZHD, we obtain the ZWD (Eq. 3), which can then be used to infer information about the IWV in millimetres. It is calculated according to Bevis et al. (1992) with

$$\text{IWV} = \kappa \text{ZWD} \frac{1}{\rho_{\text{H}_2\text{O}}}, \quad (6)$$

where $\rho_{\text{H}_2\text{O}}$ is the density of liquid water ($\rho_{\text{H}_2\text{O}} = 1000 \text{ kg m}^{-3}$). The factor κ is given by

$$\frac{1}{\kappa} = R_v \left(\frac{k_3}{T_m} + k'_2 \right) 10^{-6}, \quad (7)$$

with the constants k_3 and k'_2 as derived by Davis et al. (1985) from Thayer (1974) ($k_3 = (3.776 \pm 0.004) \times 10^5 \text{ K}^2 \text{ hPa}^{-1}$ and $k'_2 = 17 \pm 10 \text{ K hPa}^{-1}$). The required estimate of the mean atmospheric temperature T_m is linearly approximated from the surface temperature T_s (damped with the daily mean) as proposed by Bevis et al. (1992) ($T_m = 70.2 \text{ K} + 0.72 T_s$). Another possibility would be to estimate T_m from reanalysis data. However, GNSS estimates would then depend on reanalyses, which would make validation of GNSS with reanalyses problematic. Furthermore, Alshawaf et al. (2017) showed that the use of reanalyses temperature and pressure data can lead to a bias in IWV compared to the use of surface measurements, especially in mountainous regions in Germany. We therefore follow their recommendation to use the Bevis approximation derived from surface temperature. The pressure p_s and the surface temperature T_s at the GNSS station are vertically interpolated from pressure and temperature measurements at the closest meteorological station, assuming hydrostatic equilibrium and an adiabatic lapse rate of 6.5 K km^{-1} .

We use hourly ZTD data from the Automated GNSS Network for Switzerland (AGNES), containing 41 antennas (at 31 locations), as well as data from a few stations that are part of the COGEAR network (<https://mpg.igp.ethz.ch/research/geomonitring/cogear-gnss-monitoring.html>, last access: 29 September 2020) and from two additional stations in Bern. The AGNES network was established in 2001 (Schneider et al., 2000; Brockmann, 2001; Brockmann et al., 2001a, b), and it is maintained by the Swiss Federal Office of Topography (swisstopo). A monitor web page shows the current status of all stations (Swisstopo, 2019). In 2008, most of the antennas and receivers were enhanced from GPS only to GPS and GLONASS (Russian global navigation satellite system). Since spring 2015, AGNES has been a multi-GNSS network (Brockmann et al., 2016) also using data from Galileo (European global navigation satellite system) and

GNSS stations in Switzerland

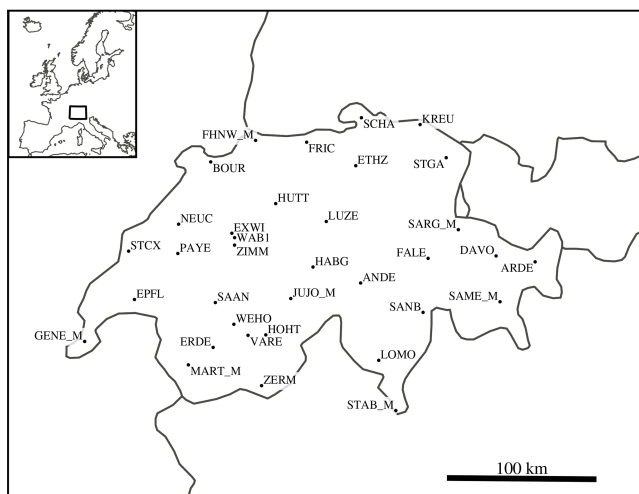


Figure 1. Map of Swiss Global Navigation Satellite System (GNSS) stations used in this study.

BeiDou (Chinese navigation satellite system). All European GNSS data were reprocessed in 2014 within the second EUREF (International Association of Geodesy Reference Frame Sub-Commission for Europe) Permanent Network (EPN) reprocessing campaign as described in Pacione et al. (2017). In the present study, only the reprocessed ZTD products of swisstopo are used (Brockmann, 2015).

The stations used in our study are shown in Fig. 1 and listed in Table 1. We only use stations that provide measurements for more than 10 years. At some GNSS stations, a new antenna and receiver were installed at the same or nearby location, replacing the older ones after an overlapping measurement period. An antenna change often leads to a small height difference, which can lead to a jump in the ZTD time series. It is therefore important to decide how to handle such instrumental changes for trend analyses. In cases of antenna and receiver replacements, we merged these stations to a single time series by calculating the mean value for overlapping periods. They are marked by “_M” (for “merged”) in their station abbreviation (Table 1), and a potential jump was considered in the trend estimation (see Sect. 3.1). At nine stations, new multi-GNSS receivers and antennas were installed at an additional location nearby, but the old GPS-only receivers and antennas are still operating. Swisstopo installed such twin stations to ensure a best possible long-term consistency. Simply replacing antennas at all stations would not guarantee continuous time series, even if the phase centres of the antennas were individually calibrated. Furthermore, no calibrations have been available for the tracked satellite systems Galileo and BeiDou until today. In the case of twin stations, we only used the old, continuous GPS-only station, because the stability is better suited for trend calculations than merged time series with potential data jumps.

2.4 Reanalysis data

IWV, relative humidity (RH) and temperature data from two reanalysis products are used in the present study, the ERA5 and the MERRA-2 reanalyses. The Modern-Era Retrospective Analysis for Research and Applications, version 2 (MERRA-2), is an atmospheric reanalysis from NASA's Global Modeling and Assimilation Office (GMAO), described in Gelaro et al. (2017). The MERRA-2 product used in the present study for IWV data contains monthly means of vertically integrated values of water vapour (Global Modeling and Assimilation Office (GMAO), 2015) with a grid resolution of 0.5° latitude \times 0.625° longitude. The ERA5 reanalysis is the latest atmospheric reanalysis from the European Centre for Medium Range Weather Forecasts (ECMWF) (Hersbach et al., 2018). In the present study, we use an ERA5 product providing integrated water vapour (Copernicus CDS, 2019a) and another product providing RH and temperature profiles (Copernicus CDS, 2019b), both with a grid resolution of 0.25° latitude \times 0.25° longitude (Copernicus Climate Change Service (C3S), 2017). Reanalysis models assume a smooth topography that can deviate from the real topography, especially in mountainous regions (Bock et al., 2005; Bock and Parracho, 2019). For validation of reanalysis data with specific station data (e.g. GNSS), the reanalysis IWV value would need to be corrected for altitude differences as proposed by for example Bock et al. (2005) or Parracho et al. (2018). For linear trends, however, such a linear correction is not relevant. We therefore use uncorrected reanalysis data, which might lead to some differences in IWV when comparing reanalysis IWV directly with IWV measured from the radiometer or at a GNSS station.

When using reanalysis data for trend estimates, one has to keep in mind their limitations. Due to changes in observing systems of the assimilated data, the use of reanalyses for trend studies has been debated (e.g. Bengtsson et al., 2004; Sherwood et al., 2010; Dee et al., 2011; Parracho et al., 2018). The recent reanalysis products contain some improvements in handling possible steps in assimilated data. For example, the bias correction of assimilated data in ERA5 has been extended to more observation systems (Hersbach et al., 2018) and MERRA-2 reduced certain biases in water cycle data (Gelaro et al., 2017). Nevertheless, future studies have to assess whether these improvements affect the reliability of reanalysis data for trend estimates. We exclude MERRA-2 lower-tropospheric-temperature trends in our study because we found unexpected large trends in some Alpine grids. They seem to be related to a bias in tropospheric temperature in some grids after 2017, but further investigations would be required to understand the origin of the observed trends. In this study, we therefore concentrate on ERA5 data for the temperature-related analyses in Sects. 4.2 and 6.2.

3 Methodology

We used a multilinear parametric trend model from von Clarman et al. (2010) to fit monthly means of IWV to the following regression function:

$$y(t) = a + b \cdot t + \sum_{n=1}^4 \left(c_n \cdot \sin\left(\frac{2\pi}{l_n} \cdot t\right) + d_n \cdot \cos\left(\frac{2\pi}{l_n} \cdot t\right) \right), \quad (8)$$

with the estimated IWV time series $y(t)$, the time vector of monthly means t , and the fit coefficients a to d . We account for annual ($l_1 = 12$ months) and semi-annual ($l_2 = 6$ months) oscillations, as well as for two additional overtones of the annual cycle ($l_3 = 4$ months and $l_4 = 3$ months). For the FTIR trends, the solar activity is additionally fitted by using F10.7 solar flux data measured at a wavelength of 10.7 cm (National Research Council of Canada, 2019). Uncertainties of the time series $y(t)$ are considered in a full error covariance matrix \mathbf{S}_y . The estimated trend depends on the uncertainty characterization of the observational data set, both in terms of random uncertainties and the systematic uncertainties. Thus it is of utmost importance to use the best possible independent information available to characterize these uncertainties in \mathbf{S}_y . As monthly uncertainties σ_{mon} , we use for TROWARA and GNSS data

$$\sigma_{\text{mon}} = \sqrt{\sigma_{\bar{x}}^2 + \sigma_{\text{sys}}^2}, \quad (9)$$

where σ_{sys} is a systematic error and $\sigma_{\bar{x}}$ is the standard error of the monthly mean, given by

$$\sigma_{\bar{x}} = \sigma n^{-\frac{1}{2}}, \quad (10)$$

with σ the standard deviation of the monthly measurements and n the number of measurements per month. The systematic error σ_{sys} is estimated to be 1 mm for TROWARA and 0.7 mm for GNSS data. These values are based on results from Ning et al. (2016a), who assessed IWV uncertainties from a radiometer and GNSS observations in Sweden. Our monthly uncertainties used for TROWARA and GNSS are on average 8 % for TROWARA and around 5 % for a typical GNSS station. FTIR uncertainties (around 25 %) are based on the model fit of daily means as described in Sect. 2.2. For reanalysis data, we use a monthly uncertainty of 10 %. This value has been chosen because it is slightly larger than the mean relative difference of reanalysis data and TROWARA data at Bern (≈ 5 %). Furthermore, it corresponds to the variability proposed by Parracho et al. (2018) for ERA-Interim and MERRA-2 that is due to model and assimilation differences. In addition to IWV trends, we determine ERA5 trends of RH and temperature. We use monthly uncertainties of 10 % to estimate RH trends, whereas the standard error of each averaged temperature profile (below 500 hPa) is used as monthly temperature uncertainties (around 2.5 K).

We generally express trends in percent per decade that are derived from the regression model output in millimetres per decade by dividing it for each data set by its mean IWV value of the whole period. A trend is declared to be significantly different from zero at the 95 % confidence interval as soon as its absolute value exceeds twice its uncertainty.

3.1 Bias fitting in the trend model

The trend model is able to consider jumps in the time series by assuming a bias for a given subset of the data. For this, a fully correlated block is added to the part of S_y that corresponds to the biased subset. For each subset, the block in S_y is set to the square of the estimated bias uncertainty of this block. The block with the most data points (longest block) is set as a reference block in which no bias is assumed. This possibility of bias fitting in the trend estimation has been presented in von Clarmann et al. (2010) and is mathematically explained in von Clarmann et al. (2001). The method has been applied for example by Eckert et al. (2014) to consider a data jump after retrieval changes in a satellite product. It is also described in Bernet et al. (2019), in which it has been applied on ozone data to consider data irregularities in a time series due to instrumental anomalies.

3.1.1 Bias fitting with an artificial time series

The approach of bias fitting is illustrated with an example case (Fig. 2). We used an artificial time series with a trend of 0.5 mm per decade and added three change points with a constant bias for each subset. The biases added to the time series are illustrated in Fig. 2b, showing that the longest block (third block) was set as a reference block with a bias of zero. The change points represent for example an instrumental update that leads to a constant bias in the following data. The biased time series has a trend of 1.19 ± 0.06 mm per decade, which is too large compared to the true trend of 0.5 ± 0.06 mm per decade. To improve the trend estimate, we add a fully correlated block in S_y for each biased subset, assuming a bias uncertainty of 5 %. We obtain a corrected trend of 0.52 ± 0.17 mm, which corresponds within its uncertainties to the true trend of the unbiased time series. This demonstrates that the approach can reconstruct the true trend from a biased time series, with slightly increased trend uncertainties.

3.1.2 Bias fitting for GNSS trends

In the present study, we use the bias fitting on GNSS data sets to account for instrumental changes. Analysing IWV trends from GNSS data is challenging because the measurements are highly sensitive to changes in the setup (mainly concerning antennas and radomes, but also receivers and cables) or in the environment (Pacione et al., 2017). The presented method is a straightforward way to obtain reliable IWV trend estimates despite possible data jumps due to instru-

mental changes. We consider each instrumental change in the trend programme, requiring as single information the dates when changes have been performed at the GNSS stations and an estimate of the bias uncertainty. We introduced change points in the trend programme as soon as a possible jump in the GNSS height data was recorded by swisstopo (available at http://pnac.swisstopo.admin.ch/restxt/pnac_sta.txt, last access: 12 July 2019), which was mostly due to antenna updates.

After such antenna changes, we assume a bias uncertainty of 5 % of the averaged IWV value for each biased subset. The bias uncertainty of 5 % was chosen based on our example case at Neuchâtel (Fig. 3), in which we observed a bias of 4 % after an antenna change. This is also consistent with results from Gradinarsky et al. (2002) and Vey et al. (2009), who found IWV jumps of around 1 mm due to antenna changes or changes in the number of observations and the elevation cut-off angles. For a typical Swiss station with averaged IWV values of around 16 mm, this corresponds to a bias of around 6 %. Ning et al. (2016b) found IWV biases due to GNSS antenna changes mostly between 0.2 and 1 mm, which corresponds to a bias of 1 % to 6 %, confirming our choice of 5 % bias uncertainty. In addition to the antenna updates, we added change points in the GNSS time series when a new antenna and receiver was added to replace an older system nearby (see Table 1). This can lead to larger biases, and we therefore assume a bias uncertainty of 10 % due to this data merging. For some antenna updates, jumps were observed back to a data level of a previous period. These subsets were then considered as unbiased to each other. Otherwise, we assumed the longest data block to be the unbiased reference block.

The trend programme and the bias correction are illustrated by an example case of the GNSS station in Neuchâtel, Switzerland (Fig. 3). Figure 3a shows the monthly IWV time series of GNSS data in Neuchâtel with antenna updates in the years 2000, 2007 and 2015 (vertical red dotted lines). Figure 3b shows the deseasonalized anomalies of the IWV time series, divided by the overall mean value of each month, illustrating the interannual variability. The anomalies are less variable from 2007 to 2012, but it is not clear whether this is related to the antenna update in 2007. Furthermore, the relative difference compared to ERA5 ($(\text{ERA5} - \text{GNSS})/\text{GNSS}$) reveals a data jump after the antenna change in 2015 (Fig. 3b). After this antenna update to multi-GNSS, the mean difference compared to ERA5 was reduced, suggesting that the antenna update improved the measurements. The jump corresponds to a bias in IWV of 0.66 mm (4 %) compared to the data before the change. Such a jump can falsify the resulting trend. In the corrected trend fit, the trend model therefore accounts for possible biases for each antenna update. When the bias is considered in the trend model, the jump in the difference compared to ERA5 is reduced (Fig. 3b). Furthermore, we obtain a larger bias-corrected trend (0.78 ± 0.89 mm per decade) compared to the trend of

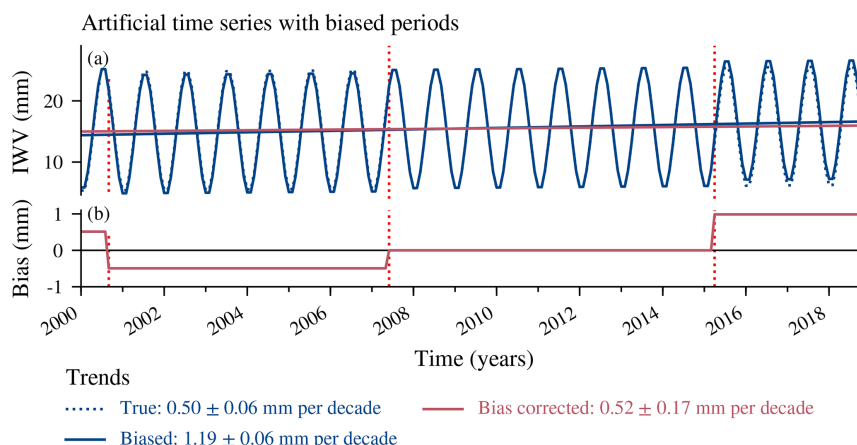


Figure 2. Artificial time series (a) and added biases (b). The linear trends for the true (unbiased) data, the biased data and the bias-corrected data are given with 1-standard-deviation uncertainties.

the initial data (0.33 ± 0.44 mm per decade) (Fig. 3c and d), suggesting that IWV was overestimated in earlier years. In general, the trend fit (Fig. 3c) reproduces the IWV time series well. For both model fits, 90 % of the residuals (Fig. 3d) lie within 2 mm, which corresponds to differences between observed data and model fit below 17 %. The regression model explains 93 % of the variability of the IWV time series at this station. As described above, the resulting trend depends on the assumed bias uncertainties and random observational error. However, respective tests have shown that different observation error covariance matrices, where these quantities were varied within realistic bounds, lead to trend estimates within the error margin of the original trend estimate.

4 Integrated water vapour around Bern

IWV measurements from the TROWARA radiometer in Bern are compared to surrounding GNSS stations and reanalysis data. Figure 4 shows monthly means of TROWARA and reanalyses, as well as the averaged monthly means of seven GNSS stations close to Bern. The selected GNSS stations lie within $\pm 0.5^\circ$ latitude and $\pm 1^\circ$ longitude around Bern, with a maximum altitude difference of 200 m (see Table 1). The altitude restriction has been chosen to avoid the inclusion of the two higher-altitude stations (Zimmerwald and Bourrignon) that are close to Bern but show larger IWV variability due to their higher elevation.

Generally, we observe a good agreement between the data sets, with interannual variability that is captured by all data sets (Fig. 4b). The data sets agree well with TROWARA, with averaged differences smaller than 0.6 mm ($\sim 5\%$). Only the stations in Bern (WAB1 and EXWI) show a bias compared to TROWARA (not shown). The Huttwil (HUTT) station reports less IWV than TROWARA, which is probably due to the higher station altitude. The GNSS stations around Bern

agree well with TROWARA after 2013 and show larger winter differences before 2008 (Fig. 4c).

ERA5 agrees generally well with TROWARA, whereas MERRA-2 differs slightly more. Especially in the last decade, the MERRA-2 difference compared to TROWARA shows a strong seasonal behaviour with larger differences in winter, which is not visible in the other data sets. Correcting the reanalysis data for a possible altitude mismatch due to wrong topography assumptions (Bock and Parracho, 2019) might partly reduce discrepancies between reanalyses and observations.

4.1 IWV trends around Bern

Trends of IWV for the different data sets around Bern are shown in Fig. 5 and Table 2. IWV measured by the radiometer TROWARA increased significantly by 4.8 % per decade from 1995 to 2018. This trend value is similar to the bias-corrected trends from GNSS stations in Lausanne (EPFL), Huttwil (HUTT), Lucerne (LUZE), Neuchâtel (NEUC) and Wabern next to Bern (WAB1), which all report trends around 5 % per decade (Fig. 5 and Table 2). We observe a slightly larger trend in Payerne (PAYE, 7.0 % per decade). The GNSS station in Bern, located on the roof of the university building of exact sciences (EXWI), shows a trend of nearly zero (0.1 % per decade). Unfortunately, the site EXWI has not been operation since September 2017. Reanalysis IWV at Bern increases significantly by 3.7 % per decade for MERRA-2 and by 2.3 % per decade for ERA5 data, both for the period from 1995 to 2018. With the exception of Payerne, all GNSS trends are not significantly different from zero at the 95 % confidence interval. The larger GNSS trend uncertainties compared to TROWARA and reanalysis trends are mainly due to the bias correction, which adds some uncertainty to the trend estimates. Furthermore, all GNSS trends result from a shorter time period than TROWARA and reanalysis trends (see Table 1), which also increases the trend

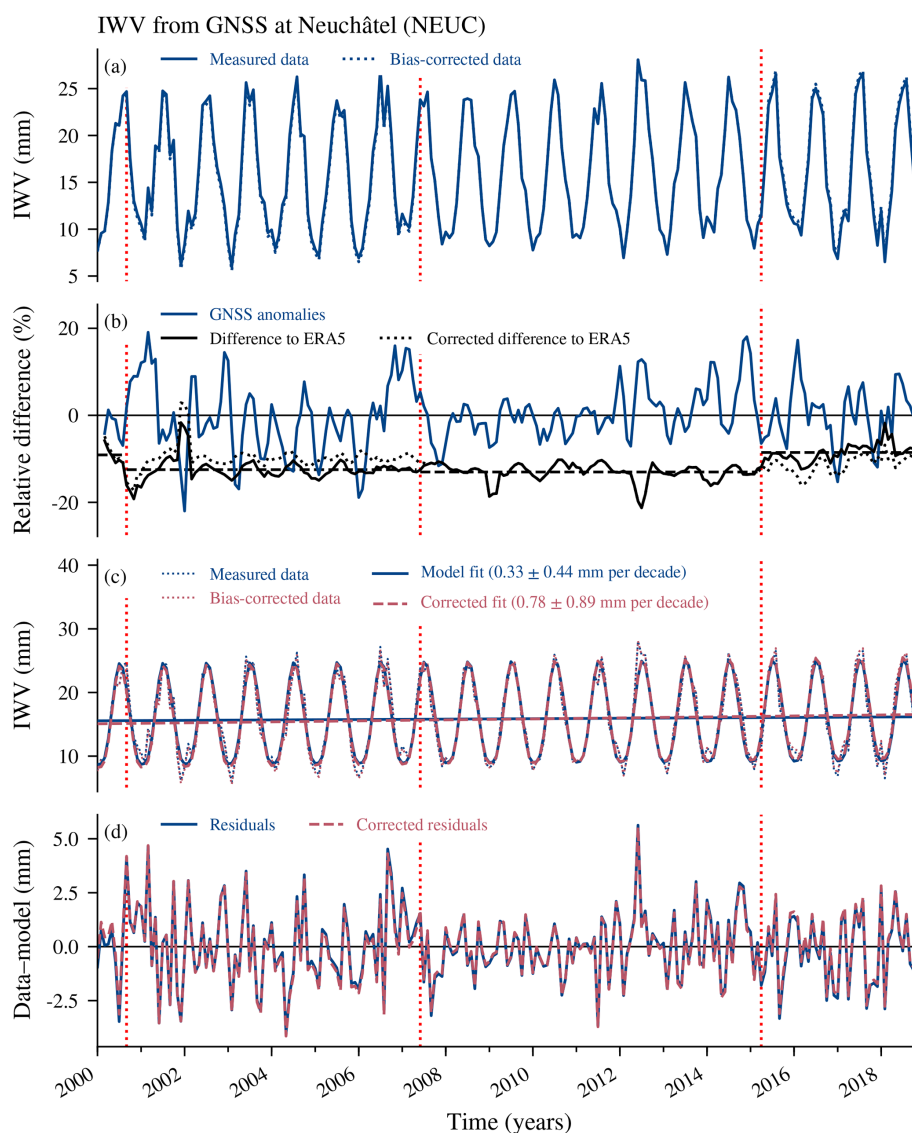


Figure 3. (a) Monthly means of integrated water vapour (IWV) from the GNSS station at Neuchâtel (NEUC), Switzerland. Changes in antenna types are indicated in all panels by vertical red dotted lines. (b) Anomalies from the climatology ($(\text{data} - \text{climatology}) / \text{climatology}$) of the GNSS data at Neuchâtel and relative difference compared to ERA5 data at the same location ($(\text{ERA5} - \text{GNSS}) / \text{GNSS}$), both smoothed with a 3-month moving mean window. The horizontal black dashed lines show the averaged difference compared to ERA5 for each antenna change. The relative difference of the bias-corrected GNSS data to ERA5 is also shown (dotted line). (c) Regression model fit and (d) residuals of the model without bias correction and with correction by considering data jumps in the trend model. The given trend uncertainties correspond to 2 standard deviations (σ).

uncertainty and may lead to some trend differences. For comparison, the GNSS trends without bias correction are also shown in Table 2. They are generally smaller than the bias-corrected trends, suggesting that GNSS trends are mostly underestimated when biases are not accounted for. Furthermore, their uncertainties are smaller, reflecting the additional uncertainty when biases are considered.

In brief, most of the GNSS stations around Bern report positive trends of approximately 5 % per decade. However, two of the GNSS stations around Bern (EXWI and PAYE) re-

port different trends. The near-zero trend at the EXWI station is less reliable than the other trends because the EXWI station is not part of the AGNES network and therefore does not fulfil the same quality requirements. The large GNSS trend in Payerne results from the bias correction. If the bias correction in the trend fit (as described in Sect. 3) is not applied, the trend in Payerne is only 2 % per decade (0.32 mm per decade), whereas it increases to 7.0 % per decade (1.09 mm per decade) when accounting for antenna changes. Nyeki et al. (2019) found IWV trends in Payerne from GNSS mea-

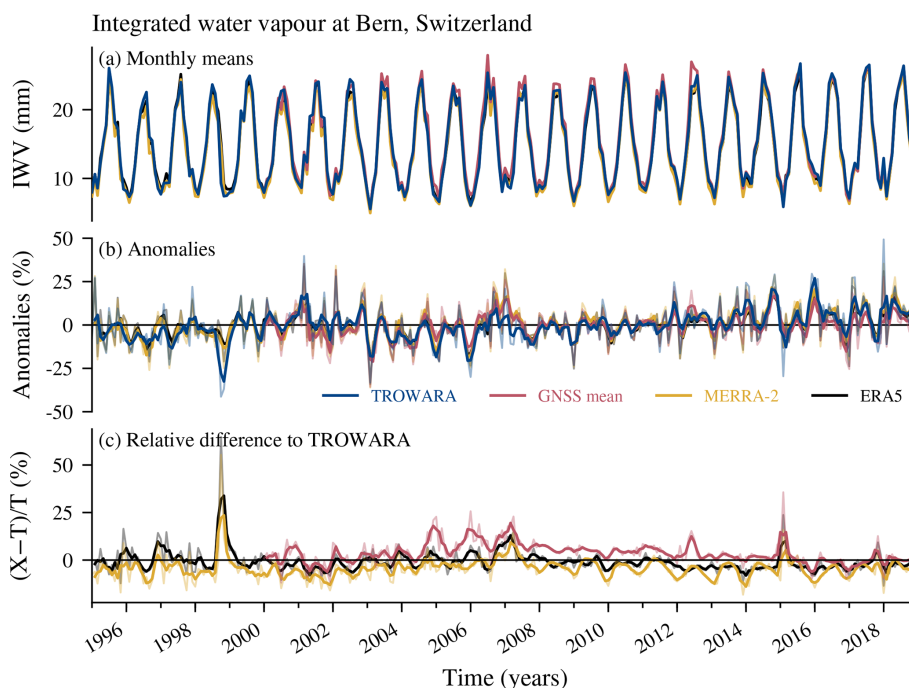


Figure 4. (a) Monthly means of IWV from the microwave radiometer TROWARA in Bern (Switzerland), from GNSS stations close to Bern and from reanalysis grids (MERRA-2 and ERA5) at Bern. (b) Anomalies from the climatology ($(\text{data} - \text{climatology})/\text{climatology}$) for each of the mentioned data sets. (c) Relative differences of the mentioned data set X to TROWARA (T) data $((X - T)/T)$. The bold lines in (b) and (c) show the data smoothed with a moving mean window of 3 months; the thin pale lines show the unsmoothed monthly data.

Table 2. IWV trends for TROWARA in Bern, GNSS stations close to Bern and reanalysis grids (MERRA-2 and ERA5) at Bern, with 2σ uncertainties. GNSS trends have been bias corrected in the case of antenna updates. The uncorrected trends for these stations are given in brackets. Trends that are significantly different from zero at the 95 % confidence interval are shown in bold.

Location	Data set	Trend	Trend
		% per decade	mm per decade
Bern	TROWARA	4.8 ± 2.0	0.72 ± 0.30
Bern	MERRA-2	3.7 ± 1.7	0.53 ± 0.25
Bern	ERA5	2.3 ± 1.5	0.34 ± 0.23
EPFL	GNSS	4.7 ± 5.1	0.75 ± 0.81
		(4.0 ± 2.7)	(0.65 ± 0.43)
EXWI	GNSS	0.1 ± 4.5	0.01 ± 0.68
HUTT	GNSS	4.4 ± 6.4	0.63 ± 0.92
		(1.0 ± 3.9)	(0.15 ± 0.56)
LUZE	GNSS	4.6 ± 6.1	0.74 ± 0.99
		(1.6 ± 2.7)	(0.25 ± 0.43)
NEUC	GNSS	4.9 ± 5.6	0.78 ± 0.89
		(2.1 ± 2.8)	(0.33 ± 0.44)
PAYE	GNSS	7.0 ± 6.3	1.09 ± 0.98
		(2.0 ± 2.9)	(0.32 ± 0.46)
WAB1	GNSS	5.4 ± 8.2	0.94 ± 1.41
		(3.4 ± 3.9)	(0.59 ± 0.68)

measurements of 0.8 mm per decade, which lie between our corrected and uncorrected trends. This suggests that the instrumental changes in Payerne play an important role but might be overcorrected in our case. The recent study by Hicks-Jalali et al. (2020) reports similar IWV trends in Payerne using nighttime radiosonde measurements (6.36 % per decade) and even larger trends using clear-night lidar data (8.85 % per decade) in the period from 2009 to 2019, suggesting that IWV in Payerne was strongly increasing, especially in recent years. However, comparing their trend results with ours has to be done with care, because their trend time period is short and the lidar trends might contain a clear-sky bias.

The trend from the TROWARA radiometer of 4.8 % per decade (0.72 mm per decade) slightly differs from the TROWARA trends reported by Morland et al. (2009) and Hocke et al. (2011, 2016). It is larger than TROWARA's 1996 to 2007 trend of 3.9 % per decade (0.56 mm per decade) (Morland et al., 2009). Hocke et al. (2011) found no significant TROWARA trend for the period 1994 to 2009, which suggests that our larger IWV trends are mainly due to a strong IWV increase in the last decade. This is also confirmed by Hocke et al. (2016), who observed larger trends for recent years (1.5 mm per decade for 2004 to 2015). However, care has to be taken when comparing these TROWARA trends of different trend period lengths.

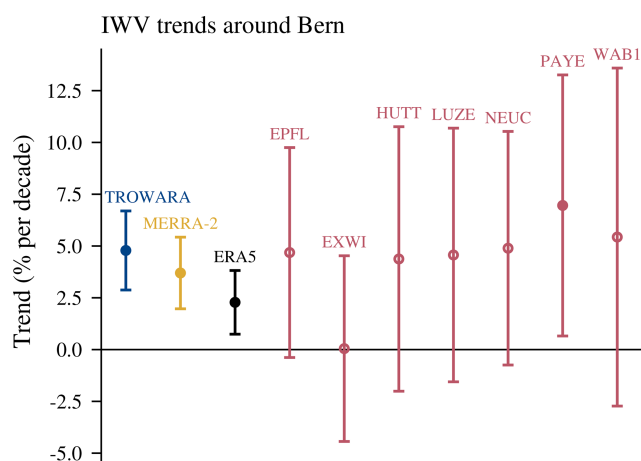


Figure 5. IWV trends for TROWARA in Bern, reanalysis (MERRA-2 and ERA5) grid points at Bern and GNSS stations close to Bern. The error bars show 2σ uncertainties. Filled dots represent trends that are significantly different from zero at the 95 % confidence interval.

To summarize, IWV trends around Bern from TROWARA and GNSS data generally lie around 5 % per decade, whereas reanalysis trends for the Bern grid are slightly smaller.

Seasonal IWV trends around Bern

To study the seasonal differences of the IWV trends around Bern, we analysed trends for each month of the year (Fig. 6). The absolute trends (Fig. 6a) are largest in summer months due to more IWV in summer. The trends in percent (Fig. 6b) account for the seasonal cycle in IWV, leading to more uniform trends throughout the year. However, differences between winter trends might sometimes be overweighted when calculating trends in percent: a small trend difference in winter will be more important when expressed in percent than the same difference in summer trends because of less water vapour in winter. Nevertheless, we will concentrate on trends in percent per decade in the following, which facilitates comparing relative changes in IWV in different seasons.

Our monthly trends in Bern mostly agree on the largest and significant trends in June ($\sim 7\%$ per decade to 9% per decade) and in November ($\sim 8\%$ per decade to 10% per decade) as well on minimal but insignificant trends in February and October (Fig. 6b). Furthermore, all data sets report a special pattern of low trends in October, with again larger trends in November. However, the differences between those monthly trends are significant only at the 68 % confidence level. The mean trend (arithmetic mean) of the GNSS stations around Bern agrees with the other data sets in summer but shows an offset to the other trends in several months, especially in March and in autumn. We further found that MERRA-2 trends are slightly larger in summer than trends from the other data sets, whereas TROWARA trends differ from the other trends in the winter months of December and

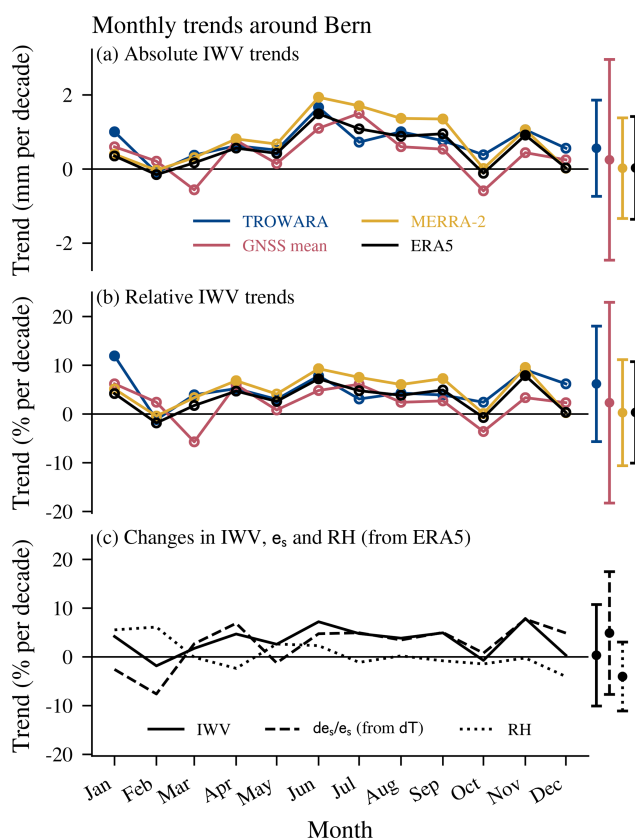


Figure 6. Trends of IWV for different months for TROWARA in Bern, GNSS stations close to Bern (arithmetic mean) and reanalysis grids (MERRA-2 and ERA5) at Bern. Uncertainty bars show the maximum range of 2σ uncertainties of each data set. Filled dots represent trends that are significantly different from zero at the 95 % confidence interval. Monthly IWV trends are given in (a) as absolute trends in millimetres per decade and in panel (b) as relative trends in percent per decade. Panel (c) presents again the monthly IWV trends from ERA5, as well as the relative humidity (RH) trends and the theoretical change in saturation vapour pressure e_s due to the observed temperature change from ERA5 data (both averaged below 500 hPa).

January. This larger disagreement between TROWARA and reanalysis trends in December and January is consistent with the larger winter biases of TROWARA starting in 2008 in Fig. 4c.

Previous studies analysed TROWARA seasonal trends using shorter time periods. Morland et al. (2009) and Hocke et al. (2011) observed significant positive summer trends and negative winter trends for TROWARA. Our TROWARA trends confirm positive summer trends (significant in June and August) but do not confirm negative winter trends. The observed autumn peak (minimum trend in October and a trend peak in November) has also been reported by Morland et al. (2009) and Hocke et al. (2011). However, their trend peak was shifted by 2 months, with a minimum in August and a subsequent maximum in September. The 10 additional

years that we use in our study compared to their data might be responsible for this shift. Morland et al. (2009) proposed that this autumn trend peak might be related to precipitation changes, but such a relationship has not been verified for the present study. Nevertheless, we showed that the IWV trend peak is consistent with November temperature trends, suggesting that those trends are temperature driven (see Sect. 4.2 and Fig. 6c).

In summary, Bern data sets generally agree on the annual trend distribution, with the largest trends in June and in November. However, the monthly trends of GNSS stations around Bern disagree with the other data sets in spring and in autumn, whereas TROWARA deviates in December and January. Positive summer trends are reported by all data sets.

4.2 Changes in IWV and temperature around Bern

To examine the relationship between IWV trends and changing temperature, we present the theoretical change in water vapour in the atmosphere due to observed changes in temperature (Fig. 6c). For this, we determined the temperature-dependent change in saturation vapour pressure for the time period 1995 to 2018. The saturation vapour pressure e_s describes the equilibrium pressure of water between the condensed and the vapour phase. It increases rapidly with increasing temperature (Held and Soden, 2000). In cases where the water vapour pressure e is smaller than e_s , the available water is in the vapour phase, whereas for $e \geq e_s$ it condenses. With increasing temperature, e_s increases, which leads to an increase in e for a given relative humidity (RH). Changes in e_s can therefore directly be compared to changes in the amount of water vapour, assuming that RH remains constant (Möller, 1963; Held and Soden, 2000):

$$\text{RH} = \frac{e}{e_s} \approx \text{constant}. \quad (11)$$

A change in e_s is then directly reflected in a change in e and therefore in IWV:

$$\frac{de_s}{e_s} \approx \frac{de}{e} = \frac{d\text{IWV}}{\text{IWV}}. \quad (12)$$

The fractional change in e_s for a given change in temperature can be approximated by the Clausius–Clapeyron equation:

$$\frac{de_s}{e_s} \approx \frac{L_v}{R_v T^2} dT, \quad (13)$$

where L_v is the latent heat of evaporation ($L_v = 2.5 \times 10^6 \text{ J kg}^{-1}$), R_v is the gas constant for water vapour ($R_v = 461 \text{ J K}^{-1} \text{ kg}^{-1}$), dT is the change in temperature and T is the actual temperature. To obtain the tropospheric temperature change dT , we derived the temperature trend (1995 to 2018) from ERA5 temperature profiles, averaged below 500 hPa. This limit was chosen because around 95 % of IWV resides below 500 hPa for the averaged ERA5 profiles in our

study period. The resulting temperature trend (in kelvin per decade) is then used for dT in Eq. (13) to determine the change in e_s in percent per decade. For the actual temperature T we used the mean of ERA5 temperature profiles below 500 hPa for the same time period.

The fractional changes in ERA5 e_s for the Bern grid for different months are shown in Fig. 6c. These temperature-induced changes in e_s agree generally well with the observed trends in IWV. They agree especially well with TROWARA and reanalysis trends in spring (March and April), late summer and autumn (July to November), but they agree less in the winter months and in May and June. Furthermore, they agree less with GNSS trends from September to March. Generally, the good agreement between the change in e_s and the IWV trends indicates that observed IWV changes around Bern can mostly be explained by temperature changes. However, the changes in e_s do not confirm our observed IWV winter trends, especially in January and February. This discrepancy can be related to changes in RH, which was assumed to be constant (Eq. 11). Indeed, our trends of ERA5 RH for the Bern grid (Fig. 6c) show that RH was not constant in those months, especially in winter but also in May and June. Even though the RH trends are not significantly different from zero, these results suggest that assuming RH to be constant may not be valid during all seasons, especially in winter. This makes the attribution of IWV trends to changes in temperature more challenging. Furthermore, other factors than temperature might be responsible for IWV changes in winter, such as changes in dynamical patterns and the horizontal transport of humid air. Indeed, Hocke et al. (2019) showed that evaporation of surface water plays a minor role in winter, with a latent heat flux that is 6 to 7 times smaller than in summer in Bern, suggesting that, in winter, horizontal transport of humid air is more important than evaporation.

We conclude that IWV in Bern changes as expected from temperature changes in early spring, late summer and autumn, but other processes might also be responsible for IWV changes, especially in winter.

5 Integrated water vapour at Jungfraujoch

We compare IWV at Jungfraujoch from a GNSS antenna and an FTIR spectrometer (Fig. 7). Due to the sparser FTIR sampling, we compare FTIR data not only with the full GNSS time series, but also with coincident GNSS data, i.e. pairwise data limited to clear-sky weather conditions. Monthly means of these sparser data have been computed by a seasonal fitting as described in Sect. 2.2. This leads to some missing data at the edges of the coincident GNSS time series (Fig. 7a, c) because a specific number of data points is required for the seasonal fitting. For the FTIR time series, no data are missing at the edges because data were available beyond the dates of our study period.

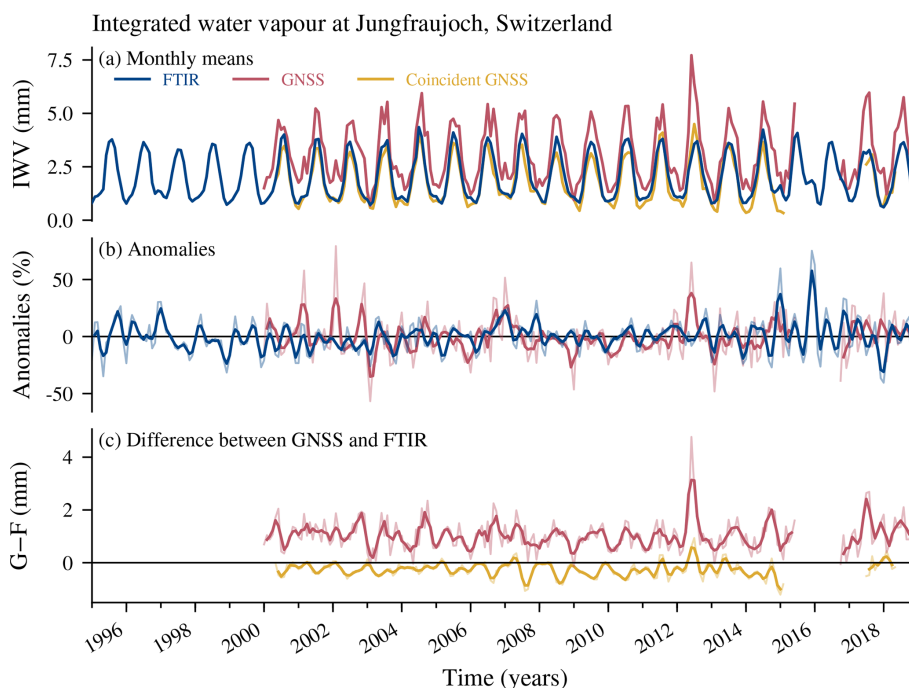


Figure 7. (a) Monthly means of IWV from the FTIR spectrometer and the GNSS station at Jungfraujoch (Switzerland). Shown are GNSS means once using the full hourly sampling and once using data only at the same time as the FTIR measured (coincident GNSS). The monthly means of FTIR and coincident GNSS have been resampled to correspond to the 15th of each month. (b) Anomalies from the climatology ((data – climatology)/climatology) for FTIR data and fully sampled GNSS data. (c) Differences between GNSS (G) and FTIR (F) data, using the full GNSS data and GNSS data coincident with the FTIR. The bold lines in (b) and (c) show the data smoothed with a moving mean window of 3 months; the thin pale lines show the unsmoothed monthly data.

We observe less IWV at Jungfraujoch than at Bern due to the high altitude of the station, with a mean IWV from GNSS of 3 mm (Fig. 7a). The deseasonalized anomalies (Fig. 7b) show that the interannual variability of IWV at Jungfraujoch is larger than in Bern, with anomalies larger than 50 % for some months. Monthly means of coincident GNSS data have a mean dry bias of -0.26 ± 0.3 mm compared to FTIR ($\text{GNSS}_{\text{coincident}} - \text{FTIR}$) (Fig. 7c). This corresponds to a bias of 15 % when referring to the long-term average of GNSS coincident IWV data. Furthermore, monthly means of fully sampled GNSS have a bias of 1.05 ± 0.61 mm compared to FTIR ($\text{GNSS} - \text{FTIR}$), which corresponds to a bias of 34 % (using the mean of the fully sampled GNSS as reference). This larger bias illustrates the sampling effect of the FTIR measurements, leading to a dry bias of FTIR compared to GNSS data. Indeed, the difference results from the restriction that FTIR measurements require clear-sky conditions, preventing measurements during the wettest days.

The remaining bias of -0.26 mm when using coincident GNSS measurements indicates that GNSS measures slightly less IWV than FTIR. This is consistent with results from Schneider et al. (2010), who report that GNSS at the high-altitude Izaña Observatory (Tenerife) systematically underestimates IWV in dry conditions (< 3.5 mm). Furthermore, a dry bias has also been observed in previous studies that

compared Jungfraujoch GNSS data with precision filter radiometer (PFR) data (Guerova et al., 2003; Haeferle et al., 2004; Nyeki et al., 2005; Morland et al., 2006). Guerova et al. (2003) attributed this bias to incorrect modelling of the antenna phase centre and Haeferle et al. (2004) to unmodelled multi-path effects of the Jungfraujoch antenna. Brockmann et al. (2019) stated that the old GPS-only antenna used at Jungfraujoch until 2016 was never calibrated. Due to the special radome construction (with circulating warm air to avoid icing), the standard antenna phase centre calibration is not appropriate for use with the Jungfraujoch data. From this point of view the achieved results are good and a possible offset is not relevant for trend analyses as long as it is constant over the whole trend period. The use of this antenna was stopped in summer 2015, and it was replaced by a new multi-GNSS antenna in October 2016 (Brockmann et al., 2016). Furthermore, the complete antenna-radome construction was individually calibrated for GPS and GLONASS signals (Galileo and BeiDou are assumed to be identical to GPS). We found that the bias to FTIR has been reduced to $-0.07 \text{ mm} \pm 0.28$ (4 %) after the antenna change in 2016, suggesting that the GNSS antenna update improved the consistency of the measurements at Jungfraujoch.

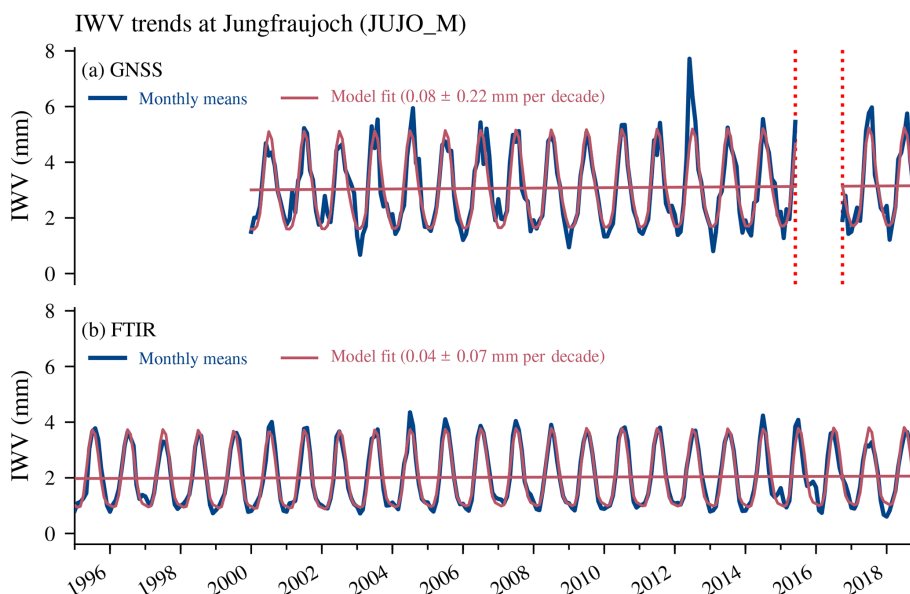


Figure 8. Monthly means and their trend fits for (a) GNSS and (b) FTIR data at Jungfraujoch. The given trend uncertainty corresponds to 2σ uncertainties. GNSS antenna changes are indicated by vertical red dotted lines.

IWV trends at Jungfraujoch

The IWV trends at the Jungfraujoch station from FTIR and fully sampled GNSS data are presented in Fig. 8. The GNSS antenna update has been considered in the trend estimate as described in Sect. 3.1.2. We observe IWV trends of 0.08 mm per decade (2.6 % per decade) for GNSS and 0.04 mm per decade (1.8 % per decade) for FTIR. However, both trends are insignificant. The difference between both trends can partly be explained by the dry sampling bias of the FTIR spectrometer, which measures only during clear-sky day conditions. Indeed, the absolute GNSS trend is comparable with the FTIR trend when we use GNSS data coincident with FTIR measurements, with 0.05 mm per decade (not shown). Our IWV trends at Jungfraujoch are similar to the trend by Sussmann et al. (2009), who reported insignificant FTIR trends at the same station of 0.08 mm per decade in the time period 1996 to 2008. In contrast to these results, Nyeki et al. (2019) found larger trends at Jungfraujoch that were significantly different from zero. They decided not to use GNSS IWV data from Jungfraujoch due to the high IWV variability and the missing calibration of the antenna before the replacement in 2016. Therefore, they derived their trends from IWV data based on a parameterization from surface temperature and relative humidity measurements. However, they admit that this approximation is prone to large uncertainties (Gubler et al., 2012), which might explain parts of the differences compared to our trends.

6 IWV trends in Switzerland

6.1 Swiss GNSS trends

The GNSS data generally report positive IWV trends throughout Switzerland (Fig. 9). Using data for the whole year (Fig. 9a), 50 % of the stations show trends between 2.3 % per decade and 5.1 % per decade (0.27 and 0.74 mm per decade). The trends of all stations range between 0.1 % per decade and 7.2 % per decade (0.01 mm per decade and 1.09 mm per decade), with exception of three stations that show negative trends (ANDE, HOHT and MART_M). The mean trend value of all GNSS stations is 3.6 % per decade (0.49 mm per decade), and the median is 4.4 % per decade (0.57 mm per decade).

Only three stations (9 % of all stations) show negative IWV trends and none of them is significantly different from zero at the 95 % confidence interval. Significant positive trends are reported at 17 % of the stations (six stations), being generally stations with long time series and lying mostly in western and south-eastern Switzerland. Most significant trends are observed in summer (Fig. 9d), with significant positive trends at five stations. In winter, only two north-eastern Swiss station trends are significant (Fig. 9b). In spring (Fig. 9c) and autumn (Fig. 9e), none of the IWV trends are significantly different from zero. Autumn trends tend to be negative, especially in the south-western part (Rhône valley in the canton of Valais), but they are all insignificant.

Our trend range covered by all GNSS stations is consistent with results from Nilsson and Elgered (2008), who observed in Sweden and Finland IWV trends between -0.2 and 1 mm per decade. However, they concluded that their

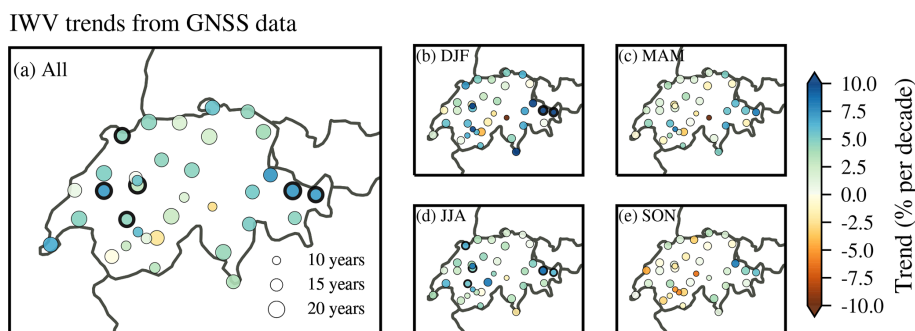


Figure 9. Trends of IWV in Switzerland for the different GNSS stations for (a) the whole year, (b) winter (December, January, February), (c) spring (March, April, May), (d) summer (June, July, August) and (e) autumn (September, October, November). The length of the GNSS time series (Table 1) is indicated by the size of the markers. Stations with trends that are significantly different from zero at the 95 % confidence interval are marked with a bold edge.

study period was too short (10 years) to obtain stable trends. Our trends also lie within the range of trends observed in Germany by Alshawaf et al. (2017). Their trends vary even more between different stations, with trends ranging between -1.5 and 2.3 mm per decade. Note, however, that both studies use different trend period lengths than in our study, which makes trend comparisons difficult. The recent study by Nyeki et al. (2019) reports IWV trends from GNSS data at three Swiss stations for the period 2001 to 2015. Using Sen's slope trend method, they found positive all-sky trends in Davos (0.89 mm per decade), Locarno (0.42 mm per decade) and Payerne (0.80 mm per decade).

Our GNSS trends for these stations are slightly different (Davos: 0.71 mm per decade, Locarno: 0.72 mm per decade, Payerne: 1.09 mm per decade), which might be due to the three additional years in our analysis, but also due to our bias correction in the trend model. Furthermore, our GNSS-derived ZTD data were reprocessed until 2014 (see Sect. 2.3), whereas Nyeki et al. (2019) still used the old GNSS data.

Note that most bias-corrected GNSS trends are larger than the uncorrected trends. This suggests that earlier GNSS data overestimate IWV compared to recent measurements. A possible explanation might be the enhancement from GPS-only to multi-GNSS antennas that was performed on AGNES stations in spring 2015. In our example case (Fig. 3b), this update improved GNSS IWV measurements compared to ERA5 data, suggesting that IWV was overestimated by GNSS in earlier years. This overestimation would then lead to a smaller trend, whereas the trend would increase when the jump is corrected in the trend estimation.

The altitude dependence of the GNSS trends is shown in Fig. 10. We observe that most of the stations that show significant positive trends lie at higher altitudes. Indeed, 83 % of the stations showing significant trends lie at altitudes above 850 m a.s.l., whereas less than half of the stations lie above 850 m. This is consistent with the expectation of Pepin et al. (2015) that the rate of warming is larger at higher altitudes.

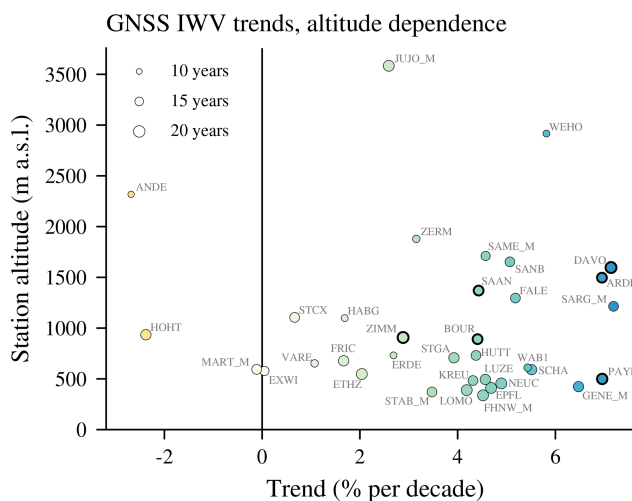


Figure 10. IWV trends from GNSS stations in Switzerland with the station altitude. For merged stations (see Table 1), the averaged altitude of both stations is used. The colours correspond to the trend in percent per decade and are the same as in Fig. 9; the length of the time series is indicated by the size of the markers. Trends that are significantly different from zero are shown with bold edges. The station abbreviations are explained in Table 1.

Due to the direct link between temperature and water vapour content, an increased warming at higher altitudes would lead to larger IWV trends. The increasing significance with altitude provides some observational evidence for this suggestion. However, the altitude dependence is less visible in absolute trends (not shown), which indicates that, due to less IWV at higher altitudes, these trends are more sensitive to changes when calculating trends in percent. Also, the IWV trends of the six stations with highest altitudes (> 1650 m a.s.l.) are not significantly different from zero.

We conclude that Swiss GNSS stations generally show positive IWV trends, with a mean value of 3.6 % per decade

(0.49 mm per decade) and a tendency for more significant percentage trends at higher altitudes.

6.2 Swiss reanalysis trends

Reanalysis trends of IWV for Switzerland are presented in Figs. 11 and 12. The trends are on average 2.6 % per decade (0.35 mm per decade) for ERA5 (Fig. 11a) and 3.6 % per decade (0.52 mm per decade) for MERRA-2 (Fig. 12a). Both reanalysis trends show only small spatial variability. The seasonal trends are positive, with the largest values in summer (Figs. 11d and 12d). This is consistent with our observed GNSS trends, which are mostly positive in summer. The smallest and partly negative reanalysis trends are observed in winter (Figs. 11b and 12b), which contrasts with our GNSS trends that showed the smallest (but insignificant) trends in autumn and not in winter. In spring and autumn, the reanalysis trends are spatially more variable. Both data sets report slightly larger autumn trends in south-eastern Switzerland and northern Italy (Figs. 11e and 12e). In spring, ERA5 shows larger IWV trends in south-western Switzerland.

The averaged MERRA-2 trend agrees with our averaged GNSS trend (both 3.6 % per decade), which is slightly larger than the averaged ERA5 trend (2.6 % per decade). However, the reanalyses do not resolve small-scale variability, which can explain the differences compared to some GNSS station trends. Furthermore, the GNSS point measurements are generally more variable than the gridded reanalyses data. Alshawaf et al. (2017) also observed larger differences in mountainous regions between GNSS-derived IWV and reanalyses data in Germany. Our mean ERA5 trend for Switzerland of 0.35 mm per decade is consistent with IWV trends from ERA-Interim in Germany reported by Alshawaf et al. (2017) (0.34 mm per decade). The MERRA-2 trends are generally slightly larger than the ERA5 trends. Parracho et al. (2018) also found larger IWV trends for MERRA-2 compared to ERA-Interim reanalysis trends on a global scale, especially in summer.

To determine the relationship between temperature changes and IWV trends for the whole of Switzerland, we present changes in saturation vapour pressure e_s derived from ERA5 temperature changes below 500 hPa (as described in Sect. 4.2). The fractional change in ERA5 e_s , which corresponds to the change in IWV (Eq. 12), is presented in Fig. 13. The averaged changes in ERA5 e_s of 2.9 % per decade are similar to our ERA5 IWV trends described before (2.6 % per decade), which indicates that IWV is on average following the temperature change as expected from the Clausius–Clapeyron equation. The ERA5 e_s changes are spatially more uniform than the ERA5 IWV trends but agree well in all seasons, except in winter (Figs. 13b and 11b). ERA5 e_s is decreasing in winter, whereas ERA5 IWV winter trends are increasing. These conflicting results indicate that factors other than temperature might dominate IWV changes in winter, as already discussed in Sect. 4.2. Furthermore, it indicates that

the assumption of constant relative humidity might not be valid in winter. This is confirmed by the ERA5 RH trends (Fig. 14), which are around zero for the whole of Switzerland in all seasons but slightly positive in winter. Even though these positive winter RH trends are not significantly different from zero, they raise the question of whether it is justified to assume RH to be constant.

The partly negative winter changes in e_s are surprising because they result from a decrease in reanalysis winter temperature. Such a decrease in winter temperature is not consistent with long-term temperature observations in Switzerland, which report a temperature increase also in winter (Begert and Frei, 2018). This difference is due to our short study period. A few cold winters in the past 15 years have hidden the overall positive temperature trend when looking only at the relatively short period from 1995 to 2018 (MeteoSwiss, Federal Institute for Meteorology and Climatology, 2019).

To summarize, the ERA5 IWV trends follow on average the changes expected from temperature changes. The reanalysis IWV trends generally agree well with GNSS trends in Switzerland, but the spatial trend variability is not resolved by the reanalyses. Local measurements of IWV such as microwave radiometer, FTIR or GNSS measurements are therefore crucial to monitor changes in IWV, especially in mountainous regions such as Switzerland.

7 Conclusions

Our study presents trends of integrated water vapour (IWV) in Switzerland from a ground-based microwave radiometer, an FTIR spectrometer, GNSS stations and reanalysis data. We found that IWV generally increased by around 2 % per decade to 5 % per decade from 1995 to 2018. Using a straightforward trend approach that accounts for jumps due to instrumental changes, we found significant positive IWV trends for some GNSS stations in western and eastern Switzerland. Furthermore, our data show that trend significance tends to be larger in summer and to increase with altitude (up to 1650 m a.s.l.).

Comparing IWV from the radiometer in Bern with GNSS and reanalyses showed a good agreement, with differences within 5 %. The FTIR spectrometer at the high-altitude station Jungfraujoch revealed a constant clear-sky bias of 1 mm compared to GNSS data. Nevertheless, the IWV data and also the trends of both data sets at Jungfraujoch agree within their uncertainties when only coincident measurements are used. We further found that the IWV trends of the Swiss GNSS station network agree on average with the Swiss reanalysis trends (2.6 % per decade to 3.6 % per decade) but that the reanalyses are not able to capture regional variability, especially in the Alps. We conclude that GNSS data are reliable for the detection of climatic IWV trends. However, a few stations may require further quality control and harmonization in the trend analysis.

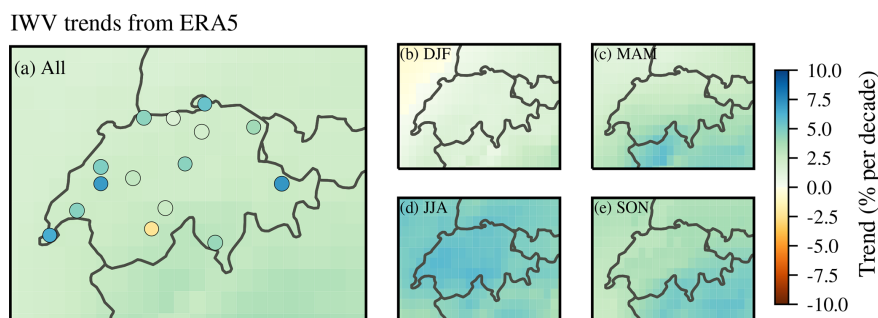


Figure 11. IWV trends from ERA5 reanalysis data in Switzerland from 1995 to 2018 for the whole year (a) and for the different seasons (b to e). GNSS trends are additionally shown in panel (a) (same as in Fig. 9a but restricted to stations with longest time series of 18 and 19 years).

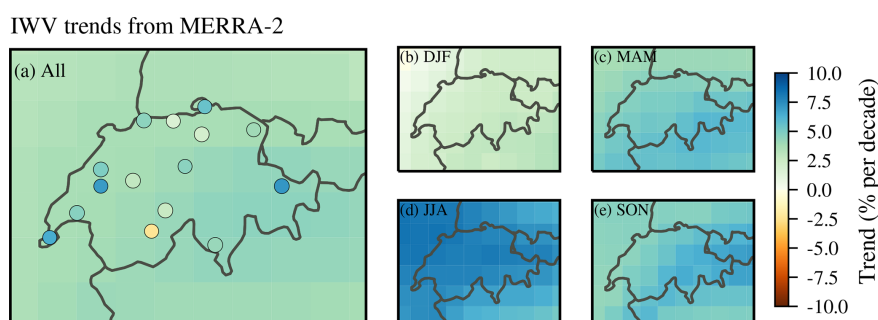


Figure 12. Same as Fig. 11 but for MERRA-2 reanalysis data (1995–2018).

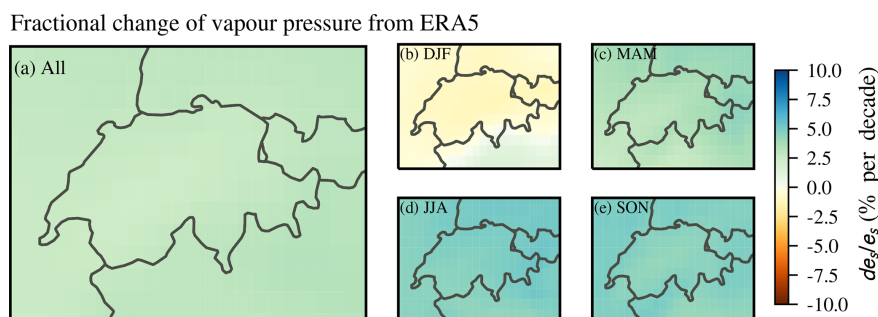


Figure 13. Fractional change in water vapour pressure (e_s) derived from temperature trends from ERA5 (1995–2018) for the whole year (a) and different seasons (b to e). The temperature data were averaged below 500 hPa.

Measurements in Bern reveal that the IWV trends follow observed temperature changes according to the Clausius–Clapeyron equation. Still, they do not scale to temperature as expected in some months, especially in winter, suggesting that other processes such as changes in dynamical patterns are responsible for IWV changes in winter. However, these winter trends are not significantly different from zero, which prevents us from drawing robust conclusions about temperature-related IWV changes in winter. Also, several colder winters in our study period might hide the long-term winter temperature increase in Switzerland. Nevertheless, ERA5 confirms the departure from Clausius–Clapeyron scaling in winter during our study period.

We did not use lower tropospheric temperature from MERRA-2 in this study because we observed biases in some Alpine grids that we could not explain so far. This reflects the difficulty of using reanalysis data for trend estimates and illustrates that reanalysis data have to be handled with care due to possible changes in observing systems or assimilated data.

Another reason for observed inconsistencies between temperature and IWV changes might be changes in relative humidity (RH). Our temperature–IWV relation assumes that the relative humidity remains constant. However, we found positive RH trends in winter using lower-tropospheric ERA5 data. Even though the RH trends are not significant, they

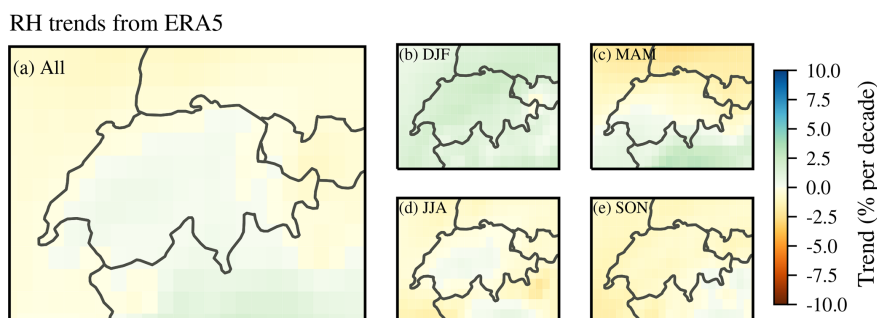


Figure 14. Relative humidity (RH) trends from ERA5 reanalysis data in Switzerland from 1995 to 2018 (averaged below 500 hPa) for the whole year (a) and for the different seasons (b to e).

might partly explain the disagreement between observed winter temperature and IWV changes. Wang et al. (2016) states that RH may not be constant because of limited moisture availability over land surfaces. Some studies even found a decrease in relative humidity with increasing temperature at mid-latitudes (O’Gorman and Muller, 2010) or in the subtropics (Dessler et al., 2008). Further analyses with additional data sets would be required to provide more insights into possible RH trends in Switzerland.

It would be necessary to analyse temperature-induced changes at more stations to draw robust conclusions about correlations between temperature and IWV changes. The problem of hidden long-term temperature trends in our study might be solved by using longer temperature time series, but longer IWV time series are sparse. Comparing regional IWV changes with tropospheric temperature changes from observations (e.g. radiosondes) rather than from reanalyses might be another approach to improve understanding of regional temperature–IWV relations. Nevertheless, it is generally difficult to attribute observed climate changes to unambiguous sources and feedbacks (Santer et al., 2007). Only complex attribution studies with multiple model runs can clarify this issue, as done for example by Santer et al. (2007) for IWV over oceans. However, global climate models lack feedbacks on the regional level (Sherwood et al., 2010), and studies based on regional observations are thus necessary.

In summary, our results confirm the increase in water vapour with global warming on a regional scale, stressing the importance of the water vapour feedback. Furthermore, the results emphasize the importance of regional IWV analyses by showing that regional trend differences can be large, especially in mountainous areas. The spatial coverage of long-term IWV measurements from ground stations is sparse. We have shown that homogeneously reprocessed GNSS data have the potential to fill this gap and that they enable monitoring of regional water vapour trends in a changing climate. We further found that water vapour increase follows temperature changes as expected, except in winter. In a changing climate, it is therefore important to assess both regional changes in temperature and water vapour to understand and project pos-

sible changes in precipitation patterns and cloud formation on a regional scale.

Data availability. TROWARA and GNSS-derived IWV data are provided by the STARTWAVE database (<http://www.iapmw.unibe.ch/research/projects/STARTWAVE/>, STARTWAVE, 2020). The gap-filled TROWARA data used before 2008 are available on request. The Jungfrauoch FTIR data are publicly available from the Network for the Detection of Atmospheric Composition Change (NDACC) at <ftp://ftp.cpc.ncep.noaa.gov/ndacc/station/jungfrau/hdf/ftir/> (NDACC, 2019). MERRA-2 data are available online through the NASA Goddard Earth Sciences Data Information Services Center (GES DISC) at <https://doi.org/10.5067/KVTU1A8BWFSJ> (Global Modeling and Assimilation Office, 2015). ERA5 data are available through the Copernicus Climate Change Service Climate Data Store (CDS) at <https://doi.org/10.24381/cds.f17050d7> (Copernicus CDS, 2019a) and <https://doi.org/10.24381/cds.6860a573> (Copernicus CDS, 2019b).

Author contributions. The study concept was designed by LB and KH. LB analysed the data and prepared the manuscript. TvC provided the trend programme and GS provided the monthly resampling programme. EM was responsible for the FTIR data, EB for the GNSS data, and CM, NK and KH for the TROWARA data. All co-authors contributed to the manuscript preparation and the interpretation of the results.

Competing interests. The authors declare that they have no conflict of interest.

Acknowledgements. Leonie Bernet was funded by the Swiss National Science Foundation. We thank the technicians and engineers from the Institute of Applied Physics, University of Bern, who have kept TROWARA working for many years. The University of Liège’s involvement has primarily been supported by the F.R.S.–FNRS (Fonds de la Recherche Scientifique) and the Belgian Federal Science Policy Office (BELSPO), both in Brussels, as well as by the GAW-CH programme of MeteoSwiss. The Fédération Wal-

lonie Bruxelles contributed to supporting observational activities. Emmanuel Mahieu is supported by a F.R.S.–FNRS research associate fellowship. We thank the International Foundation High Altitude Research Stations Jungfrauoch and Gornergrat (HFSJG, Bern) for supporting the facilities needed to perform the FTIR observations and the many colleagues who contributed to FTIR data acquisition at that site. The 10.7 cm solar radio flux data were provided as a service by the National Research Council of Canada and distributed in partnership with Natural Resources Canada. Elmar Brockmann from swisstopo provided the GNSS-derived ZTD data (operationally and reprocessed) for all Swiss stations.

Financial support. This research has been supported by the Swiss National Science Foundation (grant no. 200021-165516).

Review statement. This paper was edited by Geraint Vaughan and reviewed by two anonymous referees.

References

- Alshawaf, F., Balidakis, K., Dick, G., Heise, S., and Wickert, J.: Estimating trends in atmospheric water vapor and temperature time series over Germany, *Atmos. Meas. Tech.*, 10, 3117–3132, <https://doi.org/10.5194/amt-10-3117-2017>, 2017.
- Armour, K. C., Bitz, C. M., and Roe, G. H.: Time-Varying Climate Sensitivity from Regional Feedbacks, *J. Climate*, 26, 4518–4534, <https://doi.org/10.1175/JCLI-D-12-00544.1>, 2013.
- Begert, M. and Frei, C.: Long-term area-mean temperature series for Switzerland—Combining homogenized station data and high resolution grid data, *Int. J. Climatol.*, 38, 2792–2807, <https://doi.org/10.1002/joc.5460>, 2018.
- Bengtsson, L., Hagemann, S., and Hodges, K. I.: Can climate trends be calculated from reanalysis data?, *J. Geophys. Res.–Atmos.*, 109, D11111, <https://doi.org/10.1029/2004JD004536>, 2004.
- Bernet, L., von Clarmann, T., Godin-Beekmann, S., Ancellet, G., Maillard Barras, E., Stübi, R., Steinbrecht, W., Kämpfer, N., and Hocke, K.: Ground-based ozone profiles over central Europe: incorporating anomalous observations into the analysis of stratospheric ozone trends, *Atmos. Chem. Phys.*, 19, 4289–4309, <https://doi.org/10.5194/acp-19-4289-2019>, 2019.
- Bevis, M., Businger, S., Herring, T. A., Rocken, C., Anthes, R. A., and Ware, R. H.: GPS meteorology: Remote sensing of atmospheric water vapor using the global positioning system, *J. Geophys. Res.*, 97, 15787–15801, <https://doi.org/10.1029/92JD01517>, 1992.
- Bock, O. and Parracho, A. C.: Consistency and representativeness of integrated water vapour from ground-based GPS observations and ERA-Interim reanalysis, *Atmos. Chem. Phys.*, 19, 9453–9468, <https://doi.org/10.5194/acp-19-9453-2019>, 2019.
- Bock, O., Keil, C., Richard, E., Flamant, C., and Bouin, M. N.: Validation for precipitable water from ECMWF model analyses with GPS and radiosonde data during the MAP SOP, *Q. J. Roy. Meteor. Soc.*, 131, 3013–3036, <https://doi.org/10.1256/qj.05.27>, 2005.
- Brockmann, E.: Positionierungsdienste und Geodaten des Schweizerischen Bundesamtes für Landestopographie, in: Tagungsband – POSNAV 2001, DGON-Symposium Positionierung und Navig. 6. bis 8. März 2001, Dresden, DGON, Bonn, 2001.
- Brockmann, E.: Reprocessed GNSS tropospheric products at swisstopo, GNSS4SWEC workshop, 11–14 May 2015, Thessaloniki, 2015.
- Brockmann, E., Grünig, S., Hug, R., Schneider, D., Wiget, A., and Wild, U.: National Report of Switzerland Introduction and first applications of a Real-Time Precise Positioning Service using the Swiss Permanent Network, in: Subcomm. Eur. Ref. Fram. (EU-REF), EUREF Publ. No. 10, edited by: Torres, J. and Hornik, H., 272–276, Mitteilungen des Bundesamtes für Kartographie und Geodäsie, Vol. 23, Frankfurt am Main 2002, available at: http://www.euref.eu/symposia/book2001/nr_28.PDF (last access: 29 September 2020), 2001a.
- Brockmann, E., Guerova, G., and Troller, M.: Swiss Activities in Combining GPS with Meteorology, in: Subcomm. Eur. Ref. Fram. (EUREF), EUREF Publ. No. 10, edited by: Torres, J. and Hornik, H., 95–99, Mitteilungen des Bundesamtes für Kartographie und Geodäsie, Vol. 23, Frankfurt am Main 2002, available at: http://www.euref.eu/symposia/book2001/2_6.pdf (last access: 29 September 2020), 2001b.
- Brockmann, E., Andrey, D., Ineichen, D., Kislig, L., Liechti, J., Lutz, S., Misslin, C., Schaer, S., and Wild, U.: Automated GNSS Network Switzerland (AGNES), International Foundation HFSJG, Activity Report 2016, available at: https://www.hfsjg.ch/reports/2016/pdf/137_Swisstopo_Brockmann.pdf (last access: 29 September 2020), 2016.
- Brockmann, E., Andrey, D., Ineichen, D., Kislig, L., Liechti, J., Lutz, S., and Wild, U.: Automated GNSS Network Switzerland (AGNES), International Foundation HFSJG, Activity Report 2019, available at: https://www.hfsjg.ch/reports/2019/pdf/125_Swisstopo_Brockmann.pdf (last access: 29 September 2020), 2019.
- Chen, B. and Liu, Z.: Global water vapor variability and trend from the latest 36 year (1979 to 2014) data of ECMWF and NCEP reanalyses, radiosonde, GPS, and microwave satellite, *J. Geophys. Res.*, 121, 11442–11462, <https://doi.org/10.1002/2016JD024917>, 2016.
- Copernicus CDS: ERA5 monthly averaged data on single levels from 1979 to present, <https://doi.org/10.24381/cds.f17050d7>, 2019a.
- Copernicus CDS: ERA5 monthly averaged data on pressure levels from 1979 to present, <https://doi.org/10.24381/cds.6860a573>, 2019b.
- Copernicus Climate Change Service (C3S): ERA5: Fifth generation of ECMWF atmospheric reanalyses of the global climate, available at: <https://cds.climate.copernicus.eu/cdsapp#!/home> (last access: 29 September 2020), 2017.
- Davis, J. L., Herrinch, T. A., Shapiro, I. I., Rogers, A. E. E., and Elgered, G.: Geodesy by radio interferometry: Effects of atmospheric modeling errors on estimates of baseline length, *Radio Sci.*, 20, 1593–1607, 1985.
- Dee, D. P., Uppala, S. M., Simmons, A. J., Berrisford, P., Poli, P., Kobayashi, S., Andrae, U., Balmaseda, M. A., Balsamo, G., Bauer, P., Bechtold, P., Beljaars, A. C., van de Berg, L., Bidlot, J., Bormann, N., Delsol, C., Dragani, R., Fuentes, M., Geer, A. J., Haimberger, L., Healy, S. B., Hersbach, H., Hólm, E. V., Isaksen, I., Kållberg, P., Köhler, M., Matricardi, M., McNally, A. P., Monge-Sanz, B. M., Morcrette, J. J., Park, B. K., Peubey, C.,

- de Rosnay, P., Tavolato, C., Thépaut, J. N., and Vitart, F.: The ERA-Interim reanalysis: Configuration and performance of the data assimilation system, *Q. J. Roy. Meteor. Soc.*, 137, 553–597, <https://doi.org/10.1002/qj.828>, 2011.
- Dessler, A. E., Yang, P., Lee, J., Solbrig, J., Zhang, Z., and Minschwaner, K.: An analysis of the dependence of clear-sky top-of-atmosphere outgoing longwave radiation on atmospheric temperature and water vapor, *J. Geophys. Res.*, 113, D17102, <https://doi.org/10.1029/2008JD010137>, 2008.
- Eckert, E., von Clarmann, T., Kiefer, M., Stiller, G. P., Lossow, S., Glatthor, N., Degenstein, D. A., Froidevaux, L., Godin-Beekmann, S., Leblanc, T., McDermid, S., Pastel, M., Steinbrecht, W., Swart, D. P. J., Walker, K. A., and Bernath, P. F.: Drift-corrected trends and periodic variations in MIPAS IMK/IAA ozone measurements, *Atmos. Chem. Phys.*, 14, 2571–2589, <https://doi.org/10.5194/acp-14-2571-2014>, 2014.
- Elgered, G., Davis, J. L., Herring, T. A., and Shapiro, I. I.: Geodesy by Radio Interferometry: Water Vapor Radiometry for Estimation of the Wet Delay, *J. Geophys. Res.*, 96, 6541–6555, 1991.
- Gelaro, R., McCarty, W., Suárez, M. J., Todling, R., Molod, A., Takacs, L., Randles, C. A., Darmenov, A., Bosilovich, M. G., Reichle, R., Wargan, K., Coy, L., Cullather, R., Draper, C., Akella, S., Buchard, V., Conaty, A., da Silva, A. M., Gu, W., Kim, G. K., Koster, R., Lucchesi, R., Merkova, D., Nielsen, J. E., Partyka, G., Pawson, S., Putman, W., Rienecker, M., Schubert, S. D., Sienkiewicz, M., and Zhao, B.: The Modern-Era Retrospective Analysis for Research and Applications, version 2 (MERRA-2), *J. Climate*, 30, 5419–5454, <https://doi.org/10.1175/JCLI-D-16-0758.1>, 2017.
- Gerber, C.: Combining measurements from the microwave radiometers TROWARA and GROMOS for improved trend analysis of the integrated water vapour, Bachelor thesis, University of Bern, 2009.
- Global Modeling and Assimilation Office (GMAO): MERRA-2 instM_2d_int_Nx: 2d, Monthly mean, Instantaneous, Single-Level, Assimilation, Vertically Integrated Diagnostics V5.12.4, Goddard Earth Sciences Data and Information Services Center (GES DISC), Greenbelt, MD, USA, <https://doi.org/10.5067/KVTU1A8BWFSJ>, 2015.
- Gradinarsky, L. P., Johansson, J. M., Bouma, H. R., Scherneck, H. G., and Elgered, G.: Climate monitoring using GPS, *Phys. Chem. Earth*, 27, 335–340, [https://doi.org/10.1016/S1474-7065\(02\)00009-8](https://doi.org/10.1016/S1474-7065(02)00009-8), 2002.
- Gubler, S., Gruber, S., and Purves, R. S.: Uncertainties of parameterized surface downward clear-sky shortwave and all-sky longwave radiation., *Atmos. Chem. Phys.*, 12, 5077–5098, <https://doi.org/10.5194/acp-12-5077-2012>, 2012.
- Guerova, G., Brockmann, E., Quiby, J., Schubiger, F., and Mätzler, C.: Validation of NWP Mesoscale Models with Swiss GPS Network AGNES, *J. Appl. Meteorol.*, 42, 141–150, [https://doi.org/10.1175/1520-0450\(2003\)042<0141:vonmmw>2.0.co;2](https://doi.org/10.1175/1520-0450(2003)042<0141:vonmmw>2.0.co;2), 2003.
- Haefele, P., Martin, L., Becker, M., Brockmann, E., Morland, J., Nyeki, S., Mätzler, C., and Kirchner, M.: Impact of radiometric water vapor measurements on troposphere and height estimates by GPS, in: Proc. 17th Int. Tech. Meet. Satell. Div. Inst. Navig. ION GNSS 2004, 2289–2302, Long Beach, CA, 2004.
- Hagemann, S., Bengtsson, L., and Gendt, G.: On the determination of atmospheric water vapour from GPS measurements, Tech. Rep. 340, Max Planck Institute for Meteorology, Hamburg, Germany, 2002.
- Hartmann, D., Tank, A. K., Rusticucci, M., Alexander, L., Brönnimann, S., Charabi, Y., Dentener, F., Dlugokencky, E., Easterling, D., Kaplan, A., Soden, B., Thorne, P., Wild, M., and Zhai, P. M.: Observations: Atmosphere and Surface, in: Clim. Chang. 2013 Phys. Sci. Basis. Contrib. Work. Gr. I to Fifth Assess. Rep. Intergov. Panel Clim. Chang., edited by: Stocker, T., Qin, D., Plattner, G.-K., Tignor, M., Allen, S., Boschung, J., Nauels, A., Xia, Y., Bex, V., and Midgley, P., chap. 2, 159–254, Cambridge University Press, Cambridge, <https://doi.org/10.1017/CBO9781107415324.008>, 2013.
- Heise, S., Dick, G., Gendt, G., Schmidt, T., and Wickert, J.: Integrated water vapor from IGS ground-based GPS observations: initial results from a global 5-min data set, *Ann. Geophys.*, 27, 2851–2859, <https://doi.org/10.5194/angeo-27-2851-2009>, 2009.
- Held, I. M. and Soden, B. J.: Water Vapor Feedback and Global Warming, *Annu. Rev. Energy Environ.*, 25, 441–475, <https://doi.org/10.1146/annurev.energy.25.1.441>, 2000.
- Hersbach, H., De Rosnay, P., Bell, B., Schepers, D., Simmons, A., Soci, C., Abdalla, S., Balmaseda, A., Balsamo, G., Bechtold, P., Berrisford, P., Bidlot, J., De Boissésou, E., Bonavita, M., Browne, P., Buizza, R., Dahlgren, P., Dee, D., Dragani, R., Diamantakis, M., Flemming, J., Forbes, R., Geer, A., Haiden, T., Hólm, E., Haimberger, L., Hogan, R., Horányi, A., Janisková, M., Laloyaux, P., Lopez, P., Muñoz-Sabater, J., Peubey, C., Radu, R., Richardson, D., Thépaut, J.-N., Vitart, F., Yang, X., Zsótér, E., and Zuo, H.: Operational global reanalysis: progress, future directions and synergies with NWP including updates on the ERA5 production status, in: ERA Rep. Ser. No. 27, European Centre for Medium Range Weather Forecasts (ECMWF), Reading, England, <https://doi.org/10.21957/tkic6g3wm>, 2018.
- Hicks-Jalali, S., Sica, R. J., Martucci, G., Maillard Barras, E., Voirin, J., and Haefele, A.: A Raman lidar tropospheric water vapour climatology and height-resolved trend analysis over Payerne, Switzerland, *Atmos. Chem. Phys.*, 20, 9619–9640, <https://doi.org/10.5194/acp-20-9619-2020>, 2020.
- Ho, S.-P., Peng, L., Mears, C., and Anthes, R. A.: Comparison of global observations and trends of total precipitable water derived from microwave radiometers and COSMIC radio occultation from 2006 to 2013, *Atmos. Chem. Phys.*, 18, 259–274, <https://doi.org/10.5194/acp-18-259-2018>, 2018.
- Hocke, K., Kämpfer, N., Gerber, C., and Mätzler, C.: A complete long-term series of integrated water vapour from ground-based microwave radiometers, *Int. J. Remote Sens.*, 32, 751–765, <https://doi.org/10.1080/01431161.2010.517792>, 2011.
- Hocke, K., Navas Guzmán, F., Cossu, F., and Mätzler, C.: Cloud Fraction of Liquid Water Clouds above Switzerland over the Last 12 Years, *Climate*, 4, 48, <https://doi.org/10.3390/cli4040048>, 2016.
- Hocke, K., Navas-Guzmán, F., Moreira, L., Bernet, L., and Mätzler, C.: Oscillations in atmospheric water above Switzerland, *Atmos. Chem. Phys.*, 17, 12121–12131, <https://doi.org/10.5194/acp-17-12121-2017>, 2017.
- Hocke, K., Bernet, L., Hagen, J., Murk, A., Renker, M., and Mätzler, C.: Diurnal cycle of short-term fluctuations of integrated water vapour above Switzerland, *Atmos. Chem. Phys.*, 19, 12083–12090, <https://doi.org/10.5194/acp-19-12083-2019>, 2019.

- Ingold, T., Peter, R., and Kämpfer, N.: Weighted mean tropospheric temperature and transmittance determination at millimeter-wave frequencies for ground-based applications, *Radio Sci.*, 33, 905–918, <https://doi.org/10.1002/zaac.200400263>, 1998.
- Ingold, T., Schmid, B., Mätzler, C., Demoulin, P., and Kämpfer, N.: Modeled and empirical approaches for retrieving columnar water vapor from solar transmittance measurements in the 0.72, 0.82, and 0.94 μm absorption bands, *J. Geophys. Res.*, 105, 24327–24343, 2000.
- IPCC: Summary for Policymakers, in: *Clim. Chang. 2013 Phys. Sci. Basis. Contrib. Work. Gr. I to Fifth Assess. Rep. Intergov. Panel Clim. Chang.*, edited by: Stocker, T., Qin, D., Plattner, G.-K., Tignor, M., Allen, S., Boschung, J., Nauels, A., Xia, Y., Bex, V., and Midgley, P., Cambridge University Press, Cambridge, United Kingdom and New York, NY, USA, <https://doi.org/10.1017/CBO9781107415324.004>, 2013.
- John, V. O., Holl, G., Allan, R. P., Buehler, S. A., Parker, D. E., and Soden, B. J.: Clear-sky biases in satellite infrared estimates of upper tropospheric humidity and its trends, *J. Geophys. Res.-Atmos.*, 116, D14108, <https://doi.org/10.1029/2010JD015355>, 2011.
- Kämpfer, N.: Introduction, in: *Monit. Atmos. Water Vapour. Ground-Based Remote Sens. In-situ Methods*, edited by: Kämpfer, N., chap. 1, 1–7, Springer New York, New York, NY, https://doi.org/10.1007/978-1-4614-3909-7_1, 2013.
- Mätzler, C. and Morland, J.: Refined physical retrieval of integrated water vapor and cloud liquid for microwave radiometer data, *IEEE T. Geosci. Remote Sens.*, 47, 1585–1594, <https://doi.org/10.1109/TGRS.2008.2006984>, 2009.
- MeteoSwiss (Federal Institute for Meteorology and Climatology): Temperature and precipitation trends, available at: https://www.meteoswiss.admin.ch/home/climate/climate-change-in-switzerland/temperature-and-precipitation-trends.html?filters=ths200m0_swiss_djf_1864-smoother (last access: 29 September 2020), 2019.
- Mieruch, S., Noël, S., Bovensmann, H., and Burrows, J. P.: Analysis of global water vapour trends from satellite measurements in the visible spectral range, *Atmos. Chem. Phys.*, 8, 491–504, <https://doi.org/10.5194/acp-8-491-2008>, 2008.
- Möller, F.: On the influence of changes in the CO_2 concentration in air on the radiation balance of the Earth's surface and on the climate, *J. Geophys. Res.*, 68, 3877–3886, <https://doi.org/10.1029/jz068i013p03877>, 1963.
- Morland, J.: TROWARA – Tropospheric Water Vapour Radiometer. Radiometer review and new calibration model, Tech. rep., University of Bern, Bern, Switzerland, 2002.
- Morland, J., Deuber, B., Feist, D. G., Martin, L., Nyeki, S., Kämpfer, N., Mätzler, C., Jeannot, P., and Vuilleumier, L.: The STARTWAVE atmospheric water database, *Atmos. Chem. Phys.*, 6, 2039–2056, <https://doi.org/10.5194/acp-6-2039-2006>, 2006.
- Morland, J., Collaud Coen, M., Hocke, K., Jeannot, P., and Mätzler, C.: Tropospheric water vapour above Switzerland over the last 12 years, *Atmos. Chem. Phys.*, 9, 5975–5988, <https://doi.org/10.5194/acp-9-5975-2009>, 2009.
- National Research Council of Canada: Latest Solar Radio Flux Report from DRAO, Penticton, available at: <https://www.spaceweather.gc.ca/solarflux/sx-5-mavg-en.php> (last access: 19 December 2019), 2019.
- NCCS: CH2018 – Climate Scenarios for Switzerland, p. 271, Technical Report, National Centre for Climate Services, Zurich, 2018.
- NDACC: Network for the Detection of Atmospheric Composition Change, NDACC, Measurements at the Jungfraujoeh, Switzerland Station, FTIR Spectrometer, available at: <ftp://ftp.cpc.ncep.noaa.gov/ndacc/station/jungfrau/hdf/ftir/>, last access: 8 November 2019.
- Nilsson, T. and Elgered, G.: Long-term trends in the atmospheric water vapor content estimated from ground-based GPS data, *J. Geophys. Res.-Atmos.*, 113, D19101, <https://doi.org/10.1029/2008JD010110>, 2008.
- Ning, T., Wang, J., Elgered, G., Dick, G., Wickert, J., Bradke, M., Sommer, M., Querel, R., and Smale, D.: The uncertainty of the atmospheric integrated water vapour estimated from GNSS observations, *Atmos. Meas. Tech.*, 9, 79–92, <https://doi.org/10.5194/amt-9-79-2016>, 2016a.
- Ning, T., Wickert, J., Deng, Z., Heise, S., Dick, G., Vey, S., and Schöne, T.: Homogenized time series of the atmospheric water vapor content obtained from the GNSS reprocessed data, *J. Climate*, 29, 2443–2456, <https://doi.org/10.1175/JCLI-D-15-0158.1>, 2016b.
- Nyeki, S., Vuilleumier, L., Morland, J., Bokoye, A., Viatte, P., Mätzler, C., and Kämpfer, N.: A 10-year integrated atmospheric water vapor record using precision filter radiometers at two high-alpine sites, *Geophys. Res. Lett.*, 32, L23803, <https://doi.org/10.1029/2005GL024079>, 2005.
- Nyeki, S., Wacker, S., Aebi, C., Gröbner, J., Martucci, G., and Vuilleumier, L.: Trends in surface radiation and cloud radiative effect at four Swiss sites for the 1996–2015 period, *Atmos. Chem. Phys.*, 19, 13227–13241, <https://doi.org/10.5194/acp-19-13227-2019>, 2019.
- O’Gorman, P. A. and Muller, C. J.: How closely do changes in surface and column water vapor follow Clausius-Clapeyron scaling in climate change simulations?, *Environ. Res. Lett.*, 5, 025207, <https://doi.org/10.1088/1748-9326/5/2/025207>, 2010.
- Pacione, R., Araszkievicz, A., Brockmann, E., and Dousa, J.: EPN-Repro2: A reference GNSS tropospheric data set over Europe, *Atmos. Meas. Tech.*, 10, 1689–1705, <https://doi.org/10.5194/amt-10-1689-2017>, 2017.
- Parracho, A. C., Bock, O., and Bastin, S.: Global IWV trends and variability in atmospheric reanalyses and GPS observations, *Atmos. Chem. Phys.*, 18, 16213–16237, <https://doi.org/10.5194/acp-18-16213-2018>, 2018.
- Pepin, N., Bradley, R. S., Diaz, H. F., Baraer, M., Caceres, E. B., Forsythe, N., Fowler, H., Greenwood, G., Hashmi, M. Z., Liu, X. D., Miller, J. R., Ning, L., Ohmura, A., Palazzi, E., Rangwala, I., Schöner, W., Severskiy, I., Shahgedanova, M., Wang, M. B., Williamson, S. N., and Yang, D. Q.: Elevation-dependent warming in mountain regions of the world, *Nat. Clim. Chang.*, 5, 424–430, <https://doi.org/10.1038/nclimate2563>, 2015.
- Peter, R. and Kämpfer, N.: Radiometric Determination of Water Vapor and Liquid Water and Its Validation With Other Techniques, *J. Geophys. Res.*, 97, 18173–18183, 1992.
- Ross, R. J. and Elliot, W. P.: Radiosonde-based Northern Hemisphere tropospheric water vapor trends, *J. Climate*, 14, 1602–1612, [https://doi.org/10.1175/1520-0442\(2001\)014<1602:RBNHTW>2.0.CO;2](https://doi.org/10.1175/1520-0442(2001)014<1602:RBNHTW>2.0.CO;2), 2001.
- Saastamoinen, J.: Atmospheric Correction for the Troposphere and Stratosphere in Radio Ranging Satellites, in: *Use Artif. Satell.*

- Geod., edited by: Henriksen, S. W., Mancini, A., and Chovitz, B. H., Vol. 15, 247–251, Geophys. Monogr. Ser., Washington, D.C., <https://doi.org/10.1029/GM015p0247>, 1972.
- Santer, B. D., Mears, C., Wentz, F. J., Taylor, K. E., Gleckler, P. J., Wigley, T. M. L., Barnett, T. P., Boyle, J. S., Bruggemann, W., Gillett, N. P., Klein, S. A., Meehl, G. A., Nozawa, T., Pierce, D. W., Stott, P. A., Washington, W. M., and Wehner, M. F.: Identification of human-induced changes in atmospheric moisture content, *P. Natl. Acad. Sci. USA*, 104, 15248–15253, <https://doi.org/10.1073/pnas.0702872104>, 2007.
- Schneider, D., Brockmann, E., Marti, U., Schlatter, A., and Wild, U.: National Report of Switzerland Introduction of a Precise Swiss Positioning Service “swipos” and Progress in the Swiss National Height Network “LHN95”, in: Rep. Symp. IAG Subcomm. Eur. held Tromsø, 22–24 June 2000, edited by: Torres, J., 315–322, 2000.
- Schneider, M., Romero, P. M., Hase, F., Blumenstock, T., Cuevas, E., and Ramos, R.: Continuous quality assessment of atmospheric water vapour measurement techniques: FTIR, Cimel, MFRSR, GPS, and Vaisala RS92, *Atmos. Meas. Tech.*, 3, 323–338, <https://doi.org/10.5194/amt-3-323-2010>, 2010.
- Schneider, M., Barthlott, S., Hase, F., González, Y., Yoshimura, K., García, O. E., Sepúlveda, E., Gomez-Pelaez, A., Gisi, M., Kohlhepp, R., Dohe, S., Blumenstock, T., Wiegeler, A., Christner, E., Strong, K., Weaver, D., Palm, M., Deutscher, N. M., Warneke, T., Notholt, J., Lejeune, B., Demoulin, P., Jones, N., Griffith, D. W. T., Smale, D., and Robinson, J.: Ground-based remote sensing of tropospheric water vapour isotopologues within the project MUSICA, *Atmos. Meas. Tech.*, 5, 3007–3027, <https://doi.org/10.5194/amt-5-3007-2012>, 2012.
- Sherwood, S. C., Roca, R., Weckwerth, T. M., and Andronova, N. G.: Tropospheric water vapor, convection, and climate, *Rev. Geophys.*, 48, RG2001, <https://doi.org/10.1029/2009RG000301>, 2010.
- STARTWAVE: Studies in Atmospheric Radiative Transfer and Water Vapour Effects, University of Bern, available at: <http://www.iapmw.unibe.ch/research/projects/STARTWAVE/>, last access: 29 September 2020.
- Stocker, T. F., Clarke, G., Treut, H. L., Lindzen, R., Meleshko, V., Mugara, R., Palmer, T., Pierrehumbert, R., Sellers, P., Trenberth, K., and Willebrand, J.: Physical Climate Processes and Feedbacks, in: *Clim. Chang. 2001 Sci. Basis. Contrib. Work. Gr. I to Third Assess. Rep. Intergov. Panel Clim. Chang.*, edited by: Houghton, J., Ding, Y., Griggs, D., Noguer, M., van der Linden, P., Dai, X., Maskell, K., and Johnson, C., chap. 7, 417–470, Cambridge University Press, Cambridge, United Kingdom and New York, NY, USA, 2001.
- Sussmann, R., Borsdorff, T., Rettinger, M., Camy-Peyret, C., Demoulin, P., Duchatelet, P., Mahieu, E., and Servais, C.: Technical Note: Harmonized retrieval of column-integrated atmospheric water vapor from the FTIR network – first examples for long-term records and station trends, *Atmos. Chem. Phys.*, 9, 8987–8999, <https://doi.org/10.5194/acp-9-8987-2009>, 2009.
- Swisstopo: Automated GNSS Network for Switzerland (AGNES), available at: <http://pnac.swisstopo.admin.ch/pages/en/agnes.html> (last access: 29 September 2020), 2019.
- Thayer, G. D.: An improved equation for the radio refractive index of air, *Radio Sci.*, 9, 803–807, <https://doi.org/10.1029/RS009i010p00803>, 1974.
- Trenberth, K. E., Fasullo, J., and Smith, L.: Trends and variability in column-integrated atmospheric water vapor, *Clim. Dynam.*, 24, 741–758, <https://doi.org/10.1007/s00382-005-0017-4>, 2005.
- Urban, J.: Satellite Sensors Measuring Atmospheric Water Vapour, in: *Monit. Atmos. Water Vapour. Ground-Based Remote Sens. In-situ Methods*, edited by: Kämpfer, N., chap. 9, 175–214, Springer New York, New York, NY, <https://doi.org/10.1007/978-1-4614-3909-7>, 2013.
- Vey, S., Dietrich, R., Fritsche, M., Rülke, A., Steigenberger, P., and Rothacher, M.: On the homogeneity and interpretation of precipitable water time series derived from global GPS observations, *J. Geophys. Res.-Atmos.*, 114, D10101, <https://doi.org/10.1029/2008JD010415>, 2009.
- von Clarmann, T., Grabowski, U., and Kiefer, M.: On the role of non-random errors in inverse problems in radiative transfer and other applications, *J. Quant. Spectrosc. Ra.*, 71, 39–46, [https://doi.org/10.1016/S0022-4073\(01\)00010-3](https://doi.org/10.1016/S0022-4073(01)00010-3), 2001.
- von Clarmann, T., Stiller, G., Grabowski, U., Eckert, E., and Orphal, J.: Technical Note: Trend estimation from irregularly sampled, correlated data, *Atmos. Chem. Phys.*, 10, 6737–6747, <https://doi.org/10.5194/acp-10-6737-2010>, 2010.
- Wagner, T., Beirle, S., Grzegorski, M., and Platt, U.: Global trends (1996–2003) of total column precipitable water observed by Global Ozone Monitoring Experiment (GOME) on ERS-2 and their relation to near-surface temperature, *J. Geophys. Res.-Atmos.*, 111, D12102, <https://doi.org/10.1029/2005JD006523>, 2006.
- Wang, J., Dai, A., and Mears, C.: Global water vapor trend from 1988 to 2011 and its diurnal asymmetry based on GPS, radiosonde, and microwave satellite measurements, *J. Climate*, 29, 5205–5222, <https://doi.org/10.1175/JCLI-D-15-0485.1>, 2016.
- Wehrli, C.: Calibrations of filter radiometers for determination of atmospheric optical depth, *Metrologia*, 37, 419–422, <https://doi.org/10.1088/0026-1394/37/5/16>, 2000.
- Wentz, F. J. and Schabel, M.: Precise climate monitoring using complementary satellite data sets, *Nature*, 403, 414–416, <https://doi.org/10.1038/35000184>, 2000.
- Wentz, F. J., Ricciardulli, L., Hilburn, K., and Mears, C.: How much more rain will global warming bring?, *Science*, 317, 233–235, <https://doi.org/10.1126/science.1140746>, 2007.
- Wilhelm, S., Stober, G., and Brown, P.: Climatologies and long-term changes in mesospheric wind and wave measurements based on radar observations at high and mid latitudes, *Ann. Geophys.*, 37, 851–875, <https://doi.org/10.5194/angeo-37-851-2019>, 2019.
- Zander, R., Mahieu, E., Demoulin, P., Duchatelet, P., Roland, G., Servais, C., Mazière, M. D., Reimann, S., and Rinsland, C. P.: Our changing atmosphere: Evidence based on long-term infrared solar observations at the Jungfraujoch since 1950, *Sci. Total Environ.*, 391, 184–195, <https://doi.org/10.1016/j.scitotenv.2007.10.018>, 2008.
- Zhang, Y., Xu, J., Yang, N., and Lan, P.: Variability and Trends in Global Precipitable Water Vapor Retrieved from COSMIC Radio Occultation and Radiosonde Observations, *Atmosphere*, 9, 174, <https://doi.org/10.3390/atmos9050174>, 2018.

B.1 LIST OF PUBLICATIONS

ARTICLES

- Bernet, L.**, I. Boyd, G. Nedoluha, R. Querel, D. Swart and K. Hocke (2020a). Validation and trend analysis of stratospheric ozone data from ground-based observations at Lauder, New Zealand, submitted to Earth Syst. Sci. Data.
- Bernet, L.**, E. Brockmann, T. von Clarmann, N. Kämpfer, E. Mahieu, C. Mätzler, G. Stober and K. Hocke (2020b). Trends of atmospheric water vapour in Switzerland from ground-based radiometry, FTIR and GNSS data. In: *Atmospheric Chemistry and Physics* 20.19, pp. 11223–11244. DOI: [10.5194/acp-20-11223-2020](https://doi.org/10.5194/acp-20-11223-2020).
- Bernet, L.**, F. Navas-Guzmán and N. Kämpfer (2017d). The effect of cloud liquid water on temperature retrievals from microwave measurements. In: *Atmospheric Measurement Techniques* 10.11, pp. 4421–4437. DOI: [10.5194/amt-10-4421-2017](https://doi.org/10.5194/amt-10-4421-2017).
- Bernet, L.**, T. von Clarmann, S. Godin-Beekmann, G. Ancellet, E. Maillard Barras, R. Stübi, W. Steinbrecht, N. Kämpfer and K. Hocke (2019c). Ground-based ozone profiles over central Europe: incorporating anomalous observations into the analysis of stratospheric ozone trends. In: *Atmospheric Chemistry and Physics* 19.7, pp. 4289–4309. ISSN: 1680-7324. DOI: [10.5194/acp-19-4289-2019](https://doi.org/10.5194/acp-19-4289-2019).
- Hocke, K., M. Lainer, **L. Bernet** and N. Kämpfer (2018). Mesospheric inversion layers at mid-latitudes and coincident changes of ozone, water vapour and horizontal wind in the middle atmosphere. In: *Atmosphere* 9.5, 171. ISSN: 20734433. DOI: [10.3390/atmos9050171](https://doi.org/10.3390/atmos9050171).
- Hocke, K., **L. Bernet**, J. Hagen, A. Murk, M. Renker and C. Mätzler (2019). Diurnal cycle of short-term fluctuations of integrated water vapour above Switzerland. In: *Atmospheric Chemistry and Physics* 19.19, pp. 12083–12090. DOI: [10.5194/acp-19-12083-2019](https://doi.org/10.5194/acp-19-12083-2019).
- Hocke, K., F. Navas-Guzmán, L. Moreira, **L. Bernet** and C. Mätzler (2017a). Diurnal Cycle in Atmospheric Water over Switzerland. In: *Remote Sensing* 9.9, 909. ISSN: 2072-4292. DOI: [10.3390/rs9090909](https://doi.org/10.3390/rs9090909).
- (2017b). Oscillations in atmospheric water above Switzerland. In: *Atmospheric Chemistry and Physics* 17.19, pp. 12121–12131. DOI: [10.5194/acp-17-12121-2017](https://doi.org/10.5194/acp-17-12121-2017).
- Maillard Barras, E., A. Haefele, L. Nguyen, F. Tummon, W. Ball, E. Rozanov, R. Rüfenacht, K. Hocke, **L. Bernet**, N. Kämpfer, G. Nedoluha and I. Boyd (2020). Study of the dependence of stratospheric ozone long-term trends on local solar time. In: *Atmospheric Chemistry and Physics* 20, pp. 8453–8471. ISSN: 1680-7316. DOI: [10.5194/acp-20-8453-2020](https://doi.org/10.5194/acp-20-8453-2020).

PRESENTATIONS

- Bernet, L.** (2020a). Disparities in ground-based ozone data and challenges in their trend estimation. 1st ISSI team on "Towards a Universal Framework for Merging

- Atmospheric Observations from the Ground and Space". 10.02.-14.02.2020, Bern, Switzerland.
- Bernet, L.** (2020b). Ground-based measurements of stratospheric ozone: A "supersite" trend comparison. Third LOTUS Workshop. 28.05.-29.05.2020, online meeting.
- Bernet, L., N. Kämpfer and K. Hocke** (2018b). Stratospheric ozone profiles from the GROMOS microwave radiometer at Bern: intercomparison, trends and their uncertainties. EGU General Assembly 2018. 08.04.-13.04.2018, Vienna, Austria.
- (2018c). Stratospheric ozone recovery at mid-latitudes: improved ground-based time series and trend estimations. SPARC General Assembly 2018. 01.10.-05.10.2018, Kyoto, Japan.
 - (2018d). Stratospheric ozone recovery at mid-latitudes: improved ground-based time series and trend estimations. Microwave and Atmospheric Physics Seminar. 02.11.2018, Bern, Switzerland.
 - (2018e). Stratospheric ozone recovery at mid-latitudes: improved ground-based time series and trend estimations. Swiss Geoscience Meeting 2018. 30.11.-01.12.2018, Bern, Switzerland.
- Bernet, L., C. Mätzler, E. Brockmann, N. Kämpfer and K. Hocke** (2019a). Atmospheric water vapour trends in Switzerland based on data from ground-based microwave radiometry and GNSS ground stations. EGU General Assembly 2019. 06.04.-12.04.2019, Vienna, Austria.
- Bernet, L., T. von Clarmann, S. Godin-Beekmann, G. Ancellet, E. Maillard Barras, R. Stübi, W. Steinbrecht, N. Kämpfer and K. Hocke** (2019d). Stratospheric ozone recovery at mid-latitudes: incorporating anomalous observations into ground-based ozone trends. Invited talk. Seminar at KIT, IMK. 14.06.2019, Karlsruhe, Germany.

POSTERS

- Bernet, L., E. Brockmann, T. von Clarmann, N. Kämpfer, E. Mahieu, C. Mätzler, G. Stober and K. Hocke** (2020c). Water vapour trends in Switzerland from radiometry, FTIR and GNSS ground stations. Poster. 5th Virtual Alpine Observatory Symposium. 04.02.- 06.02.2020, Bern, Switzerland.
- (2020d). Water vapour trends in Switzerland from radiometry, FTIR and GNSS ground stations. Poster. EGU General Assembly 2020. 04.05.-08.05.2020, Sharing Geoscience Online.
- Bernet, L., F. N. Guzmán and N. Kämpfer** (2016). Cloud Effect on Temperature Profiles from Microwave Radiometry. Poster. AGU Fall Meeting 2016. 12.11.-16.11.2016, San Francisco, USA.
- (2017a). Cloud effect on temperature profiles from microwave radiometry. Awarded poster. 18th Swiss Global Change Day. 11.04.2017, Bern, Switzerland.
 - (2017b). The effect of cloud liquid water on temperature retrievals from microwave measurements. EGU General Assembly 2017. 23.04.-28.04.2017, Vienna, Austria.
- Bernet, L., K. Hocke and N. Kämpfer** (2017c). Longterm trends in stratospheric ozone over Western Europe. Poster. 16th International Swiss Climate Summer School. 03.09.-08.09.2017, Ascona, Switzerland.
- (2018a). Stratospheric ozone profiles from the GROMOS microwave radiometer at Bern: intercomparison, trends and their uncertainties. Poster. Second LOTUS Workshop. 17.09.-19.09.2018, Geneva, Switzerland.
- Bernet, L., C. Mätzler, E. Brockmann, N. Kämpfer and K. Hocke** (2019b). Water vapour trends in Switzerland based on data from ground-based microwave radiometry and GNSS ground stations. Poster. 7th international colloquium on scientific and fundamental aspects of GNSS. 04.09.-06.09.2019, Zurich, Switzerland.

B.2 DECLARATION OF CONSENT

Erklärung

gemäss Art. 18 PromR Phil.-nat. 2019

Name/Vorname: Leonie Bernet

Matrikelnummer: 11-203-403

Studiengang: PhD of Science in Climate Sciences
Bachelor Master Dissertation

Titel der Arbeit: Detecting trends of stratospheric ozone and tropospheric water vapour at mid-latitudes using measurements from multiple techniques

Leiter der Arbeit: PD Dr. Klemens Hocke

Ich erkläre hiermit, dass ich diese Arbeit selbständig verfasst und keine anderen als die angegebenen Quellen benutzt habe. Alle Stellen, die wörtlich oder sinngemäss aus Quellen entnommen wurden, habe ich als solche gekennzeichnet. Mir ist bekannt, dass andernfalls der Senat gemäss Artikel 36 Absatz 1 Buchstabe r des Gesetzes über die Universität vom 5. September 1996 und Artikel 69 des Universitätsstatuts vom 7. Juni 2011 zum Entzug des Dokortitels berechtigt ist. Für die Zwecke der Begutachtung und der Überprüfung der Einhaltung der Selbständigkeitserklärung bzw. der Reglemente betreffend Plagiate erteile ich der Universität Bern das Recht, die dazu erforderlichen Personendaten zu bearbeiten und Nutzungshandlungen vorzunehmen, insbesondere die Doktorarbeit zu vervielfältigen und dauerhaft in einer Datenbank zu speichern sowie diese zur Überprüfung von Arbeiten Dritter zu verwenden oder hierzu zur Verfügung zu stellen.

Bern, den 2. Oktober 2020

Leonie Bernet

